Mixed Metal Oxides for Sustainable Fuel Production via Solar Thermochemical Routes

Asim Riaz

February 2021

A THESIS SUBMITTED FOR THE DEGREE OF DOCTOR OF PHILOSOPHY OF

THE AUSTRALIAN NATIONAL UNIVERSITY

Research School of Electrical, Energy and Materials Engineering

College of Engineering and Computer Science

The Australian National University

Declaration

This dissertation reports the research I conducted from February 2017 to July 2020 at the Research School of Electrical, Energy and Materials Engineering, College of Engineering and Computer Science, the Australian National University, Canberra, Australian Capital Territory, Australia.

To the best of my knowledge, the materials included in this thesis are originally my own work except were acknowledged and referenced in appropriate manner. They have not been previously published by others or submitted in whole or in part for the purpose of obtaining a degree from any university or tertiary education institution.

Asim Riaz

2020

Abstract

The overall solar-to-fuel efficiency of the synthesis gas production *via* solar-driven thermochemical splitting of CO_2 and H_2O reactions is highly dependent on the energy required to break down the strong molecules such as CH_4, CO_2 and H_2O. To maximize the syngas production yields, designing new redox materials and optimizing the reactor designs and receiver models are of great importance. Redox materials mediate the thermochemical process by exchanging oxygen with the reactant gases and their performance is mainly assessed by the oxygen exchange capacity, syngas yields and structural stability. In this thesis, a range of redox materials including $LaSrMnO_3$ perovskites and cerium-vanadium mixed/doped metal oxides are studied for syngas production *via* cyclic H_2O and CO_2 splitting coupled with methane partial oxidation and high temperature inert gas reduction.

The effects of reducing atmospheres such as Ar and CH_4 on the structural features in $La_xSr_{1-x}MnO_3$ perovskites are investigated. The $La_{0.5}Sr_{0.5}MnO_3$ powders composed of nano-crystalline particles are considered as the best performing Perovskites with premium structural stability and a 117% higher initial syngas production rate than that of pure $SrMnO_3$ and $LaMnO_3$ structures. The overall syngas production rates are 9 times faster during the chemical looping reforming of methane when compared to those of inert gas reduction. It is demonstrated that lanthanum incorporation prevents the structural breakdown caused by CH_4 and up to 65–100% of the initial perovskite structure is regenerated. Notably, H_2 purity of up to 93% is achieved by lanthanum-rich LSM structures during the H_2O splitting redox cycles coupled with an efficient methane reforming reaction. These findings provide a robust set of physiochemical properties of $LaSrMnO_3$ systems that can be utilized for enhanced solar fuel production *via* thermochemical redox cycles.

The effects of vanadium (V) and cerium (Ce) concentrations (each varying in the 0–100% range) in CeO_2–$CeVO_4$ mixed-phase, Ce^{4+}-doped V_2O_5 and V^{5+}-doped CeO_2 redox materials are explored for synthesis gas production *via* thermochemical redox cycling of CO_2 and H_2O splitting coupled to methane partial oxidation reactions. In particular, an optimum mixture of CeO_2 and $CeVO_4$ is achieved by 25 wt% of vanadium incorporation in the CeO_2 powders, which produce up to 68% higher syngas yields than that of pure ceria. It is observed that V^{5+} provides more reducing states for the hydrocarbon oxidation, while cerium ions act as an oxygen buffer for the re-oxidation reaction. Notably, doping of vanadium increases the cycle capacity of ceria by 400% and the activation temperature of the methane reforming reaction is lowered by up to 178°C, while doping the V_2O_5 lattice with large cerium cations results in a V_2O_5-to-V_2O_3 phase transition and produces up to 100 times higher syngas production rates when compared to the pure V_2O_5. Finally, these findings suggest that a facile combination of the extraordinary catalytic properties of vanadia and superior oxygen ion mobility of ceria can be a powerful approach for an efficient and effective solar thermochemical fuel production.

Acknowledgements

In the name of Allah, the most Beneficent, the most Merciful

I would like to firstly acknowledge my primary supervisor A/Prof. Adrian Lowe and my co-supervisors Prof. Wojciech Lipiński and A/Prof. Takuya Tsuzuki, who invested their time and efforts in guiding me to shape the scope of my field and morally supported me to throughout my candidature. Their continuous involvement in the numerous discussions helped me to secure the technological foundations of my research field and endowed me to become an independent researcher. I would also like to acknowledge Dr. Peter Kreider and Dr. Mahesh Venkataraman for their useful technical advice on the research issues I encountered and the experimental expertise they provide.

I would also extend my gratitude to my local and international collaborators, including Dr. Suchinda Sattayaporn from the Synchrotron Light Research Institute institute located in Thailand, Dr. Tak Kim from Grifith University, Dr. Felipie Kremer from Centre of Advance Microscopy, ANU, and Mr Muhammad Umair and Dr Hassina Tabbassum from Peking University. Their assistance significantly improved the quality of my research and notable outcomes could have been possible with the resources they provided.

I also acknowledge the assistance provided by our technical support staff, Colin Carvolth, Cavin Carvolth and Jason Chen, which greatly reduced the time for setting up the equipment used in experimentations.

I would like to thank the Research Training Program of the Australian Government for providing the scholarship support, without which none of my endeavours would have been possible.

Finally, I would like to thank my family especially my parents and wife, for their never-ending support and prayers, which boosted my moral throughout my PhD journey. I would also like to thank the valuable and overwhelming existence of my friends, whose moral support greatly helped me to go through my hardships.

List of Publications

1. **Asim Riaz**, P. Kreider, F. Kremer, H. Tabassum, JS. Yeoh, W. Lipiński and A. Lowe, (2019) *Electrospun Manganese-Based Perovskites as Efficient Oxygen Exchange Redox Materials for Improved Solar Thermochemical CO_2 Splitting.* ACS Appl. Energy Mater. 2, 2494−2505.
2. **Asim Riaz**, MU. Ali, W. Lipiński and A. Lowe, (2019), *Enhanced oxygen exchange capacity in nanostructured ceria–vanadia multi-phase oxygen carriers for solar thermal fuel production*, Journal of Materials Chemistry A, 7, 27349-27360
3. **Asim Riaz**, MU. Ali, TG. Enge, T. Tsuzuki, A. Lowe and W. Lipiński, *Concentration -Dependent Solar Thermochemical CO_2/H_2O Splitting Performance by Vanadia-Ceria Multi-Phase Metal Oxide Systems,* Research, 3049534
4. **Asim Riaz**, Felipe Kermer, Suchinda Sattayaporn, Muhammad Umair Ali, Takuya Tsuzuki, Wojciech Lipiński, Adrian Lowe, *Structural re-arrangement in LSM perovskites for enhanced syngas production via solar thermochemical redox cycles*, ACS Catalysis, 10, 8263-8276
5. **Asim Riaz**, Felipe Kermer, Suchinda Sattayaporn, Takuya Tsuzuki, Wojciech Lipiński, Adrian Lowe, *an experimental demonstration of Vanadium doped nanostructured ceria for enhanced solar thermochemical syngas production*. Nano Energy, 81, 105639.
6. **Asim Riaz**, Takuya Tsuzuki, Wojciech Lipiński, Adrian Lowe, *Successful utilization of a VO/V_2O_3 redox pair for efficient solar thermochemical CO_2 and H_2O splitting*. Under Review in ACS Catalysis
7. **Asim Riaz**, Wojciech Lipiński, Adrian Lowe, *$LaSrMnO_3$ perovskites for efficient CO_2 splitting via thermochemical redox cycles*, 10th International Conference on Materials for Advanced Technologies (ICMAT 2019).

8. **Asim Riaz**, Wojciech Lipiński, Adrian Lowe, *Cerium-vanadium oxides for enhanced syngas production via chemical looping reforming of methane*, Nature Conference on Solar Fuels (2019).
9. **Asim Riaz**, Takuya Tsuzuki, Adrian Lowe, Wojciech Lipiński, *Cerium–vanadium Metal Oxides or Syngas Production Via Solar Thermochemical Redox Cycles*, American Institute for Chemical Engineers (AlChE 2019).

Table of Contents

Chapter One

Solar Thermochemical Routes for Syngas Production

1.1 Introduction

Solar energy is the most abundant renewable resource, technically capable of supplying all the world's energy by utilizing just a small portion of earth exposed by solar radiation.[1,2] With the ever increasing global energy and fuel demands, it is imperative to develop sustainable processes by utilizing this plentiful energy source.[3,4] With this in mind, employing solar energy for large-scale non-fossil fuel production is a sustainable route. Such synthetic fuels (termed "solar fuels" or "synfuels") are the liquid hydrocarbon fuels, produced via solar energy-driven conversion techniques. The global alarm around greenhouse gas emissions by fossil fuels drives society towards a swift integration of solar fuels into existing fossil fuel-derived commodities and relevant infrastructures.[5] The typically high average market values of fossil fuels is a strong economic justification for the commercial-scale production of solar fuels.

So far, numerous chemical pathways have been developed for an upscaled production of solar fuels. In particular, thermochemical redox reactions driven by concentrated solar radiation are environmentally friendly and economically viable processes for the production of syngas (a combination of H_2 and CO) which consequently is converted into solar fuels via an industrially established "Fischer-Tropsch" technique.[6,7] Thermochemical redox cycles and chemical looping methane reforming techniques have been extensively investigated for high solar-to-fuel efficiencies and fuel selectivity because of the thermodynamically favorable reactions carried out on oxygen carrier materials.[5] Typically, oxygen carrier materials utilize the thermal energy harnessed from concentrated solar radiation to carryout highly endothermic reduction and reforming of methane, followed by splitting of H_2O and CO_2 to produce syngas. Flexible material choice with a wide variety of physiochemical and redox properties for these thermochemical processes is widely appreciated for solar reactor designs. Currently, the

limited materials studies reported on these redox materials suggest that advanced characterization of the physiochemical evolutions during syngas production is required.[8]

1.2 Fundamentals of solar thermochemical syngas production

The term "solar fuel" is often referred to the final liquid hydrocarbon commodity, synthesized from the universal feedstock "syngas"; a product of solar energy-driven electrochemical, photochemical, and thermochemical processes. Solar thermochemical processes are categorized as H_2O/CO_2 splitting and decarbonization techniques depending on the feedstock (Figure 1).[9]

H_2O/CO_2 splitting is a non-carbonaceous feedstock-based process, further categorized as (i) solar thermolysis and (ii) solar thermochemical redox cycling techniques. Solar thermolysis is a single-step approach to dissociate H_2O/CO_2 into syngas at temperatures above 2200°C. This technique requires an efficient separation step to avoid the recombination of H_2/CO with oxygen.[10–14] while thermochemical H_2O/CO_2 splitting cycles are independent of the separation step and can be operated at relatively lower temperatures than that of thermolysis.[15–18]

The decarbonization technique is carried out with a carbonaceous feedstock and is further categorized as solar cracking, solar reforming, and solar gasification methods. Solar cracking involves the solar thermal decomposition of hydrocarbons such as natural gas and oils etc. into H_2 or syngas, depending on chemical composition of the feedstock, as shown in Reaction 1.1.

$$C_xH_y = xC(s) + \frac{y}{2}H_2 \quad (1.1)$$

It is likely that by-products in Reaction 1.1 will form due to possible impurities present in reactants. The reforming and gasification processes involve the oxidation of feedstock

hydrocarbons and gasification of the carbonaceous materials, respectively. A generic net reaction of solar thermochemical reforming and gasification can be seen in Reaction 1.2.

$$C_xH_yO_z + (x-z)H_2O = (\frac{y}{2} + x - z)H_2 + xCO \quad (1.2)$$

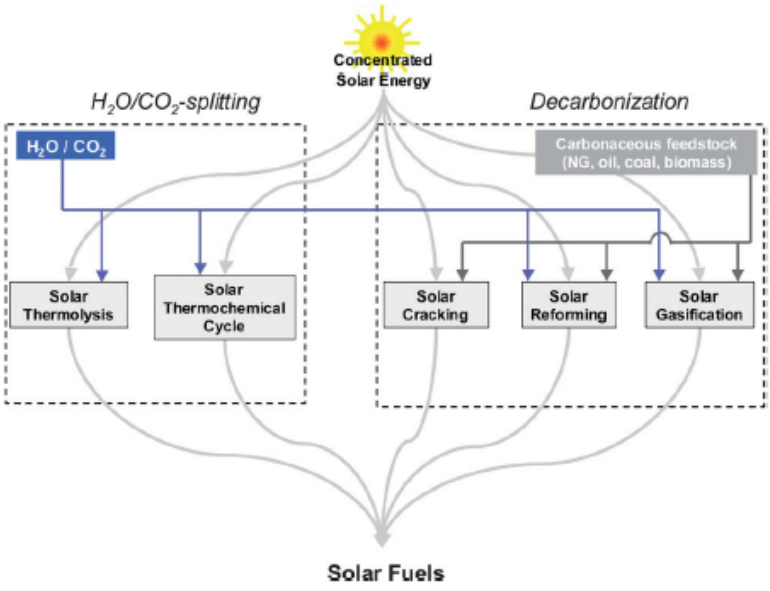

Figure 1.1. Categories of solar thermochemical syngas production techniques.[9]

Incorporation of an oxygen carrier into Reaction 1.2 and thermochemical cycles results in a two-step step chemical looping process, where oxygen carriers are reduced by the carbonaceous feedstocks or the inert atmosphere/vacuum at high temperatures and re-oxidized by CO_2/H_2O. Currently, the solar thermochemical redox cycles (STRC) and solar thermal chemical looping reforming (STCLR) are commonly utilized for the solar syngas production. Both processes are carried out in two separate reduction/oxidation steps utilizing a meal oxide (MO) redox pair as an intermediate active material. In the next sections, chemical and thermodynamic aspects of STRC and STCLR will be discussed and the advancements in the MO performance for syngas production will be analysed.

1.2.1 Thermochemical redox cycles via inert gas sweeping

Process overview

Solar thermochemical redox cycles consist of a two-step reduction and oxidation of oxygen carriers, as shown in Reactions 1.3–1.5.[5]

$$\text{Reduction: } MO + \Delta H = MO_{1-\delta} + \frac{\delta}{2}O_2(g) \quad (1.3)$$

$$\text{WS: } MO_{1-\delta} + (\delta - \alpha)H_2O(g) = MO + (\delta - \alpha)H_2(g) \quad (1.4)$$

$$\text{CDS: } MO_{1-\delta} + \alpha CO_2(g) - \Delta H = MO + \delta CO(g) \quad (1.5)$$

The first step involves an endothermic reduction of metal oxide to a lower valance state driven by concentrated solar radiation. An inert atmosphere is maintained in this step to avoid Reaction 1.3 going in a reverse direction by the recombination of reduced MO and released oxygen. The reduced MO is re-oxidized to its original valance state during CO_2 splitting (CDS) or H_2O splitting (WS) reactions at temperatures equal to or lower than T_{red}. The two-step solar thermal redox cycle process is explained graphically in Figure 1.2.

Solar reduction occurs at temperatures as high as $T_{red} > 1000°C$ which is achieved with solar concentrated energy (Q_{solar}). The reduction of metal oxide in inert atmospheres requires high energies to draw oxygen from its lattice, which in result demand a high temperature. For instance, the temperature at which ceria can be reduced efficiently to its lower valance state is greater than 1500°C and solar-to-fuel efficiency may increase up to a certain point. However, cyclic temperature swing between T_{ox} and T_{red} at high temperatures demands high energy during the heating and cooling cycles of the thermochemical redox reactions. In addition, designing reactors to sustain high temperatures is also of a concern.[5,8,10,19,20] Indeed, efficiency of reaction 1.3 depends on high reduction extents of the redox material, which are achievable at high temperatures.

While the amount of H_2/CO produced in reaction 1.4 and 1.5 counts on the concentration of oxygen vacancies formed in MO during Reaction 1.3.[8,21]

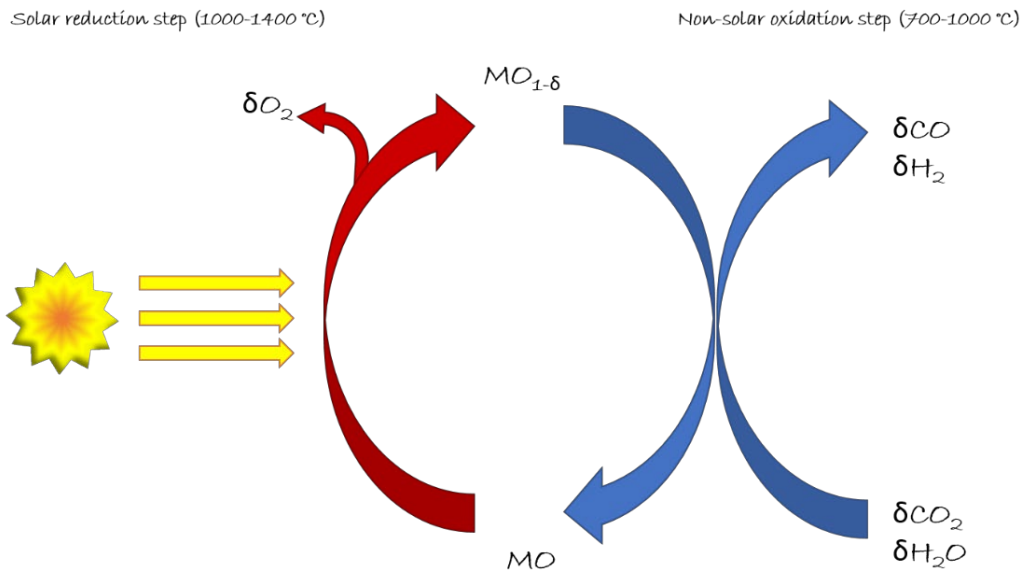

Figure 1.2. Schematic diagram of a generic thermochemical redox cycle with a solar reduction and non-solar oxidation step.

Although reduction in inert atmosphere requires high temperatures, high purity product gases can be achieved during the solar thermochemical redox reactions as compared to that of methane assisted reduction of redox materials. The reduction of metal oxides by carbonaceous feedstocks results in carbon formation onto the redox material, which is not the case observed during the reduction via inert gas sweeping methods. Furthermore, H_2/CO and O_2 are produced in separate steps, which makes this independent of the high temperature separation steps that are required by the thermolysis process.

Key performance factors

The solar-to-fuel efficiency ($\eta_{\text{solar-to-fuel}}$) of thermochemical redox cycles is defined as the ratio of chemical energy produced (ΔH_{fuel}) to the solar thermal energy input (Q_{solar}), (Reaction 1.6).[5,11]

$$\eta_{\text{solar-to-fuel}} = \frac{\Delta H_{\text{fuel}}}{Q_{\text{solar}}} \qquad (1.6)$$

This is associated with the fact that solar thermochemical processes utilize thermal energy of the entire solar spectrum for a thermodynamically favourable path to produce synthetic fuel via reduction and oxidation reactions. The deviation from stoichiometry δ, known as the oxygen exchange/storage capacity of metal oxides, is the determining factor for high process efficiencies of STRC ($\eta_{solar\text{-}to\text{-}fuel}$ α δ/Q_{solar}), where the quantity of produced fuel is reflected by the number of oxygen moles exchanged during the reduction and oxidation reactions. As the thermochemical redox cycles are mostly governed by the temperature swing between T_{red} and T_{ox}, redox materials with efficient oxygen exchange capacity are preferred.[22]

1.2.2 Chemical looping reforming of methane

Process overview

Solar thermal chemical looping methane reforming is operated on the same principles of drawing energy (Q_{solar}) from concentrated solar radiation. The first step of a STCLR process involves the partial oxidation of methane (MPO) with the oxygen evolved from oxygen carriers. The better reducing capabilities of methane allows an efficient removal of oxygen from metal oxides at relatively low temperatures.[3,23] The ideal H_2/CO ratio for the methane partial oxidation reaction is 2.0, which can be influenced by the CH_4:O_2 ratios, operating temperatures and a material's inertness towards carbon. A two-step MPO–CDS and MPO–WS redox cycle is expressed in Reactions 1.7–1.9.

$$\text{Reduction: MO} + \delta\text{CH}_4\ (g) + \Delta H = \text{MO}_{1-\delta} + \delta(2\text{H}_2 + \text{CO})(g) \quad (1.7)$$

$$\text{WS: MO}_{1-\delta} + (\delta - \alpha)\text{H}_2\text{O}(g) = \text{MO} + (\delta - \alpha)\text{H}_2(g) \quad (1.8)$$

$$\text{CDS: MO}_{1-\delta} + \alpha\text{CO}_2(g) - \Delta H = \text{MO} + \alpha\text{CO}(g) \quad (1.9)$$

The endothermic reduction of metal oxides can be carried out at temperatures as low as $T_{red} \leq 800°C$, while the oxidation can be isothermal or at $T_{ox} < T_{red}$, Figure 1.3. Consequently, the complications of elevated reduction temperatures and repeated heating

and cooling cycles can be avoided in STCLR-based reactors. However, syngas selectivity and deactivation of material are the persisting challenges linked to the CLR process.

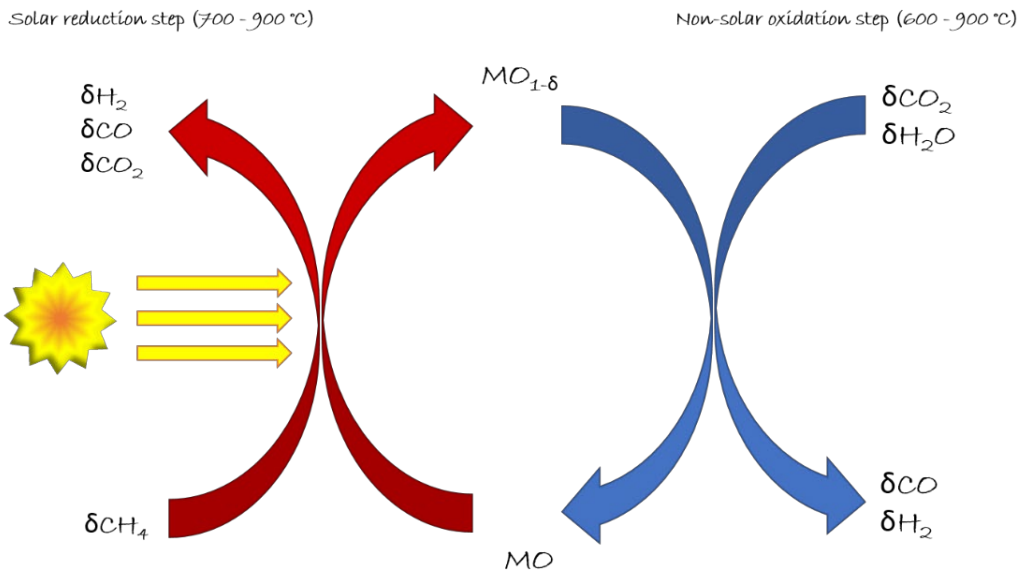

Figure 1.3. Schematic illustration of a solar thermal chemical looping reforming of methane followed by H_2O/CO_2 splitting reactions.

Chemical thermodynamics

The product distribution of an efficient methane partial oxidation reaction consists of CO, and H_2, while CO_2, H_2O, solid carbon and unreacted O_2 are the by-products. The equilibrium product distribution for Reaction 1.7 at 1 bar is shown in Figure 1.4. At temperatures higher than 870°C, the mole fraction of oxygen significantly increases. The amounts of oxygen carrier and reactant gas influence the H_2:CO ratios (ideal = 2) and a non-proportional oxygen to feedstock (CH_4:O_2) balance may result in C, CO_2 and H_2O as by-products in Reaction 1.7.

The CH_4:O_2 ratios quantify the available oxygen per gram of material for the partial oxidation of methane.[23,24,33,25–32] For instance, a CH_4:O_2 ratio of 1:1 results in combustion of methane and results in high H_2:CO ratios because considerable amounts of CO_2 are produced, as shown in Figure 1.5a. While CH_4:O_2 ratios greater than 2 leads to methane cracking which produces solid carbon and high concentrations of H_2. Carbon formation

is commonly observed during the STCLR process in fixed bed reactors when significant amount of oxygen is consumed from the metal oxide, as illustrated in Figure 1.5b.[3,34–36]

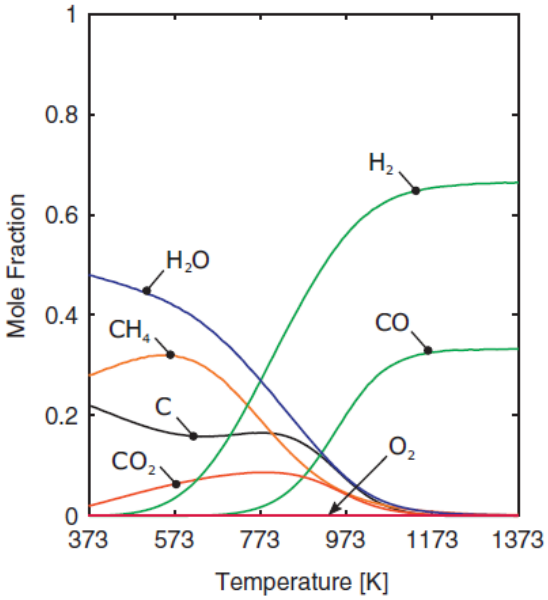

Figure 1.4. Equilibrium product distribution of the methane partial oxidation reaction with a ratio of CH_4:O_2 = 2.[3]

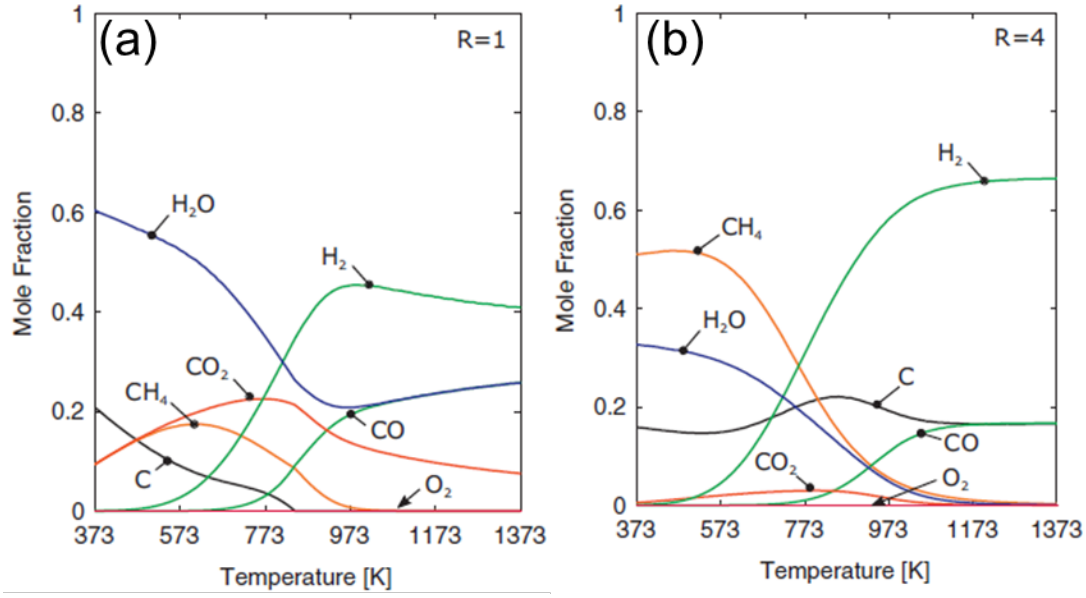

Figure 1.5. Equilibrium product distribution for methane partial oxidation with (a) CH_4:O_2 (R) = 1 and (b) CH_4:O_2 (R) = 4.[3]

The presence of solid carbon reportedly causes the deactivation of oxygen carriers by blocking the active oxide sites available for the detailed in reactions 1.7, which significantly suppresses its recyclability and consequently lowers the yields of fuel over the number of cycles.[37–41] In addition, reduced metal oxides cannot be sufficiently re-oxidized because the oxygen from steam or carbon dioxide is utilized to oxidize surface carbon species. Hence the ratio of methane-to-oxygen carrier must be carefully adjusted to avoid inefficient methane partial oxidation.[3]

Key performance parameters

The methane conversion (X_{CH4}), hydrogen selectivity (S_{H2}), CO selectivity (S_{CO}), moles of deposited carbon (n_C), carbon selectivity (S_C) and oxidizer conversion (X_{OX}) are the key metrics for efficient MPO/CDS/WS reactions. The mathematical expressions for these key metrics are shown as follows:

$$X_{CH_4} = \frac{n_{\mathrm{CH_4,IN}} - n_{\mathrm{CH_4,OUT}}}{n_{\mathrm{CH_4,IN}}} \tag{1.10}$$

$$S_{\mathrm{CO}} = \frac{n_{\mathrm{CO,OUT}}}{2X_{\mathrm{CH_4}} \times n_{\mathrm{CH_4,IN}}} \tag{1.11}$$

$$S_{\mathrm{H_2}} = \frac{n_{\mathrm{H_2,OUT}}}{2X_{\mathrm{CH_4}} \times n_{\mathrm{CH_4,IN}}} \tag{1.12}$$

$$n_{\mathrm{C}} = \frac{n_{\mathrm{CH_4,IN}} - n_{\mathrm{CH_4,OUT}} - n_{\mathrm{CO_2}} - n_{\mathrm{CO}}}{n_{\mathrm{CH_4,IN}}} \tag{1.13}$$

$$S_{\mathrm{C}} = \frac{n_{\mathrm{C}}}{X_{\mathrm{CH_4}} \times n_{\mathrm{CH_4,IN}}} \tag{1.14}$$

$$X_{\mathrm{OX}} = \frac{n_{\mathrm{OX,IN}} - n_{\mathrm{OX,OUT}}}{n_{\mathrm{OX,IN}}} \tag{1.15}$$

Here, $n_{CH4.IN}$ is the amount of methane flowing into reactor and $n_{CH4.OUT}$, $n_{CO.OUT}$, n_{CO2} are the moles of CO, CO_2 and CH_4 measured by the gas analyzer at the outlet of reactor. The degree of carbon deposition primarily depends on the moles of CO produced

by methane partial oxidation and is negligible when the H_2:CO ratios are close to 2. A material with high ionic and electronic conductivities displays a strong resistance to carbon deposition.[22,42,43]

High purity of hydrogen is also a challenging aspect to consider while estimating the overall solar-to-fuel efficiency of the WS reaction, because oxidation of deposited carbon releases CO into the product stream and may increase the cost of the overall process with an additional CO separation step required to achieve high H_2 purity.[21,44] The purity of hydrogen (ϕ) produced during the water splitting step can be quantified from the ratio of volumes (V) of H_2 to the sum of volumes of H_2, CO and CO_2, Reaction 1.16.

$$\phi = \frac{V_{H_2}}{V_{H_2} + V_{CO} + V_{CO_2}} \tag{1.16}$$

Potential reasons for methane cracking include the high temperatures >900°C[22] and catalytic activity of oxygen carriers.[41,45,46] Lowering the reduction temperatures and adjusting methane concentration, has been reported as a potential solution to reduce carbon formation.[37,47–50] Also, addition of alkaline metal or alkaline-earth metal oxide hinders the carbon deposition on oxygen carriers. Moreover, duration and CH_4:O_2 ratio significantly affects the overall equilibrium products in the MPO reaction.[34,51] In the following sections, performance of various groups of redox materials in the solar thermochemical processes will be discussed.

1.3 Materials for syngas production

Various redox materials have been investigated via computational and experimental efforts to optimize their oxygen exchange capacity for an upscale production of syngas through H_2O and CO_2 splitting via thermochemical redox cycles[26,33,60–69,52,70–79,53,80–89,54,90–99,55,100–109,56,110–119,57,120,121,58,59] and solar chemical looping reforming of methane (STCLR).[15,16,122–131,34,132–141,41,142–151,43,152–161,49,162,84,89,90,113]

Comprehensive reviews on the process and chemical thermodynamics of these redox materials have also been reported since their potential for solar fuel became apparent. Reviews of syngas production via STRC[5,6,20,147,163] and STCLR cycles[3,164–167] report recent advances in oxygen carriers, process parameters, thermodynamics and reactor developments, so before a detailed overview and advancement of this technology are presented in this thesis, the key performance factors of these redox materials are listed below:

High oxygen exchange capacity: Redox materials with this feature can release and absorbing high concentrations of oxygen and increase the syngas production yields.[20,168]

Fast and stable reaction kinetics: Fast and stable reaction kinetics enable the redox materials to produce large amounts of syngas per gram for long term cycling, which will reduce the cost associated with frequent materials replacement.

Carbon inertness: Carbon deposition suppresses the gas-solid transfer and syngas yield, so carbon inert materials are considered successful in the partial oxidation of methane reaction.[42,160]

Low temperature oxygen exchange: Metal oxides are considered as an efficient oxygen carrier if a considerable amount of oxygen can be exchanged at low temperatures, which decreases the overall fuel cost due to low Q_{solar} requirements.

High fuel selectivity: Redox materials with high fuel selectivity produce syngas without any by-products, which bypass the need of an additional separation step.

Structural stability: Redox materials must retain their microstructural properties during the long-term oxygen exchange at high temperatures and harsh atmospheres to ensure long term production of syngas.

Low cost: The intermediate materials must be abundant and easily up scalable to the industrial level with the lowest possible cost.

Environmentally friendly: Materials need to be non-toxic and must not pose any threat/harm to the environment.

Developments in process dynamics has led the family of the redox pairs to be classified into two distinct groups known as volatile and non-volatile redox pairs, as shown in Figure 1.6. This classification is based on different chemical and structural compositions, physical properties, and oxygen exchange mechanisms.

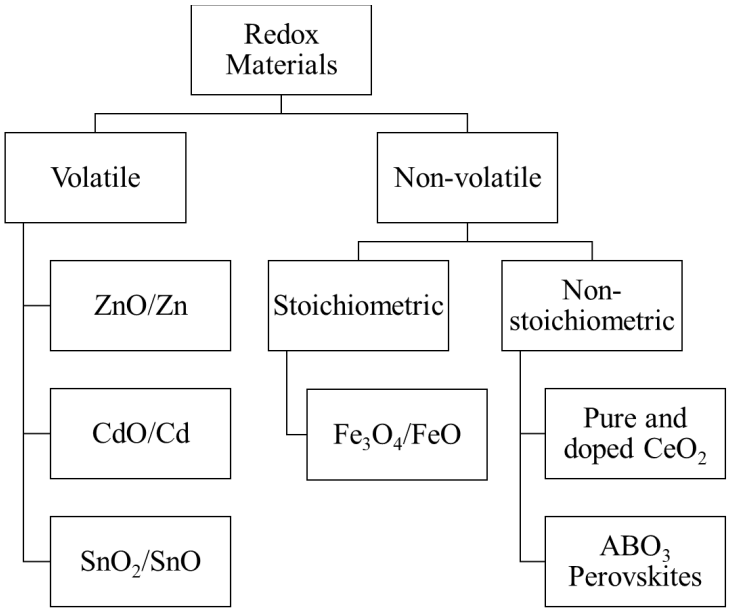

Figure 1.6. Classification of redox materials for syngas production.

1.3.1 Volatile metal oxides:

Such redox materials have decomposition temperatures lower than the operating temperatures of the thermochemical cycles and undergo a solid-to-gas transition. This transition can be in the metallic form or a low-valance metal oxide. However, as this transition results in high entropy, recombination of these reduced species is problematic for the thermochemical processes and requires separation of product gases via a quenching process, which adds to the total cost of the fuel. The most extensively studied volatile stoichiometric metal oxides are discussed in the following sections.

i. ZnO/Zn cycle

ZnO/Zn redox pairs have been extensively studied during the initial-phase research for solar fuel production via thermochemical redox cycles and solar methane reforming.[6,167] Zinc has a high affinity towards water and a high mass-specific energy density, which make ZnO/Zn an attractive redox pair for syngas production.[169] However, the low boiling point (903°C) of Zn lowers the O_2 partial pressure due to the recombination of gaseous Zn and the released oxygen, which leads to low reaction kinetics. The thermochemical aspects of ZnO dissociation are studied by the research group at Swiss Federal Institute of Technology/Paul Scherrer Institute (ETH/PSI), focusing on its utilization for syngas production via WS and CDS.[122,170] A maximum energy conversion efficiency of 39% is achieved during the thermochemical WS/CDS cycles driven by concentrated solar energy. [121] The two step reduction and oxidation are formulated in the Reactions 1.17 and 1.18.[5,171,172]

$$ZnO = Zn + \frac{1}{2}O_2 \quad (H = 478\ kJmol^{-1}) \tag{1.17}$$

$$Zn + H_2O = ZnO + H_2 \quad (H = -104\ kJmol^{-1}) \tag{1.18}$$

ii. SnO_2/SnO cycle

SnO_2/SnO is another volatile stoichiometric thermochemical cycle achieving a SnO_2 to SnO conversion at 1200°C under low oxygen partial pressures.[173] At temperatures higher than 1200°C SnO_2 is reduced into either SnO or disproportionation of SnO is observed.[174]

$$2SnO = SnO_2 + Sn \tag{1.19}$$

However, the SnO_2-to-SnO conversion is simpler and considered more practical for the syngas production when compared to that of SnO_2-to-Sn conversion because the oxidation of SnO is thermodynamically more favourable when compared to that of Sn.[175] The hydrolysis of SnO nanoparticles produces H_2 yields of up to 95% at 523–623°C, while the CO_2 splitting by SnO requires higher temperatures than those required for the

hydrolysis reaction. In addition, SnO is sensitive to carbon contamination during CO_2 splitting reactions, which decreases the overall reaction kinetics. Kodama et.al. reported a 25% of methane conversion and a 91% CO selectivity by a SnO_2/SnO cycle, which is twice the production rate by the ZnO/Zn cycle.

1.3.2 Non-volatile metal oxides

Such metal oxides remain condensed during the redox cycles which effectively bypass the recombination issue found in the volatile materials.[20,176] Since these materials remain in solid state, the physiochemical characteristics such as surface area, porosity and particle size are of prime importance for efficient thermochemical cycling. Certain synthesis techniques have demonstrated the desired properties. However, maintaining such properties for long-term cycling in a real solar driven operation is the main issue to address. Hence, a detailed study of redox mechanisms aligned with the physical properties must be carried out via advanced characterization techniques for screening suitable redox materials. Depending upon the difference in redox mechanisms, non-volatile metal oxides are characterized as stoichiometric and non-stoichiometric (e.g., Ceria and its derivatives and perovskites).

Stoichiometric metal oxides undergo a full reduction to their metallic components and form a solid solution. Iron oxide, ferrites and hercynites are the stoichiometric metal oxides that will be discussed in the following sections. In contrast to stoichiometric oxygen carriers, nonstoichiometric metal oxides such as pure/doped ceria, and perovskites follow an O–vacancy mechanism. This results in lower oxygen exchange capacity than that of achieved in the stoichiometric materials. The simplified chemical equations of non-stoichiometric thermochemical reduction and oxidation reactions are presented in Reactions 1.26 and 1.27.[163]

$$\text{Reduction: } MO_{x-\delta_{OX}} = MO_{x-\delta_{red}} + \frac{\Delta\delta}{2} O_2 \qquad (1.26)$$

$$\text{Oxidation: } MO_{x-\delta_{red}} + \Delta\delta H_2O = MO_{x-\delta_{OX}} + \Delta\delta H_2 \quad (1.27)$$

$$\Delta\delta = \delta_{red} - \delta_{ox}$$

Methane reforming over non-stoichiometric oxide pairs appeared to be kinetically limited, despite of the high oxygen diffusion through the lattice.[3,34,49,177] However, high specific surface area increases the syngas production rates.[22,34,89,168,177,178] The methane oxidation path is demonstrated by the modified Mars-van Krevelen mechanism, 3,34,184,230 as shown in Reactions 1.28–1.32.

$$CH_4 + 5[*] = CH_3* + H* + 3[*] = C* + 4H* \quad (1.28)$$

$$C* + O* \text{ (surface)} = CO* + [*] = CO\ (g) + 2[*] \quad (1.29)$$

$$C* + 2O* \text{ (surface)} = CO_2* + 2[*] = CO_2\ (g) + 3[*] \quad (1.30)$$

$$2H* = H_2* + [*] = H_2\ (g) + 2[*] \quad (1.31)$$

$$2H* + O* \text{ (surface)} = H_2O* + 2[*] = H_2O\ (g) + 3[*] \quad (1.32)$$

Initially, the high concentration of surface oxygen rapidly oxidizes the chemisorbed species (*) such as hydrogen and carbon, which results in high methane conversion. After a few cycles, methane conversion depends on the bulk lattice oxygen, which slows down the kinetics. Consequently, high concentrations of hydrogen and carbon deactivate the material when 80% of its oxygen is consumed. 3,34,36,57 The mechanism of for re-oxidation of reduced metal oxide by steam can be mathematically expressed via Reactions 1.33 and 1.34:

$$2H_2O\ (g) + 2[*] = H_2O* + [*] = H_2* + O* \text{ (surface)} \quad (1.33)$$

$$H_2* = H_2\ (g) + [*] \quad (1.34)$$

$$O* \text{ (surface)} = O \text{ (bulk)}$$

The re-oxidation reaction (1.34) starts with fast oxidizer splitting with high initial concentrations of oxygen vacancies followed by slow oxygen transport from the surface to the bulk vacancies. Here, the composition and morphology of oxygen carriers along

with the reaction conditions greatly influence methane/oxidizer conversion and syngas selectivity. Oxygen carriers with high oxygen exchange capacity, surface area, and weak M-O bonds results in high syngas yields with fast kinetics.

i. Iron oxides and ferrites

Iron based oxide materials have been extensively investigated for solar fuel production via thermochemical redox cycles and chemical looping reforming methods. The in-depth study of the chemistry of Fe_3O_4/FeO cycles is carried out to evaluate the complexities of reactions involving cyclic conversion of Fe_3O_4 to FeO at high temperatures. The endothermic reduction of Fe_3O_4 results its melting at temperatures higher than 1700°C, while the resulting FeO melts at 1370°C.[43,179] Figure 1.7 shows the equilibrium composition of the Fe/O system in a temperature range of 500–2500°C.[70] Thermal reduction of Fe_3O_4 to $Fe_{0.95}O$ can be carried out at 1300°C and 1000°C if the oxygen partial pressure is decreased up to 10^{-11} and 10^{-15} atm, respectively. This method can produce a stable wustite (FeO) structure with a varying stoichiometric chemistry from $Fe_{0.85}O$ to $Fe_{0.95}O$ at high temperatures. However, a mixed phase of FeO–Fe_3O_4 is achieved at lower temperatures resulting low extents of reduction, as shown in Figure 1.9. The simplified reduction of iron oxide can be formulated in Reaction 1.20.

$$Fe_3O_4 = 3FeO + \frac{1}{2}O_2 \qquad (1.20)$$

Several methods including stabilizing with inert support materials and doping with transition metals have been proposed to obtain stable redox kinetics over the Fe_3O_4/FeO cycle at high temperatures. Zirconia-supported Fe_3O_4 showed a maximum conversion of 60% after reduction at 1600°C during the thermochemical WS redox reactions.[180] Kodama et.al. presented a first demonstration of yttrium-stabilized zirconia (YSZ)-supported Fe_3O_4 for hydrogen production via two-step thermochemical WS reactions.[78] Zhu et.al. explored the evolution of structure and reducibility of CeO_2–Fe_2O_3 oxygen

carriers during hydrogen production via chemical looping reforming of methane followed by water splitting reactions. A simplified thermochemical reduction of ferrite is given by the Reaction 1.21.[123]

$$M_xFe_{3-x}O_4 = xMO + (3-x)FeO \quad (1.21)$$

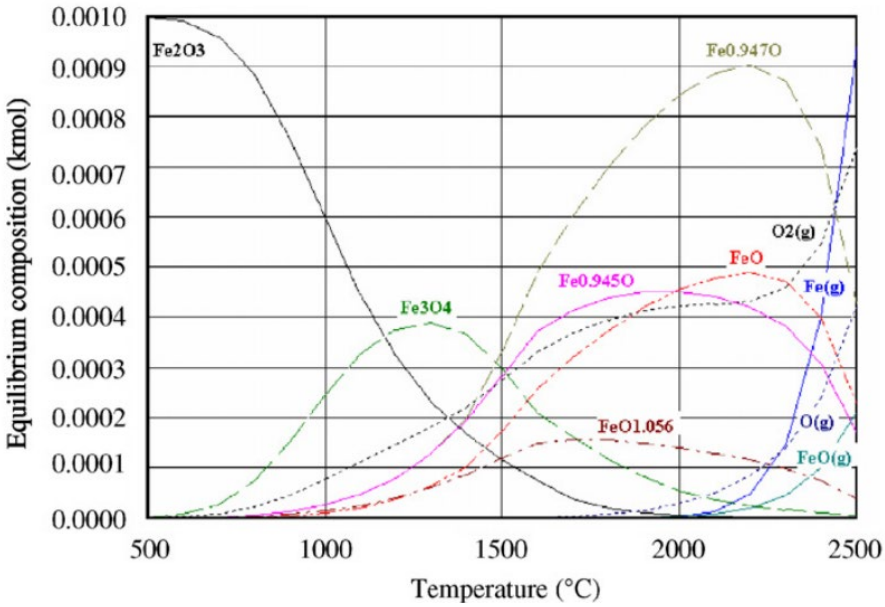

Figure 1.7. Equilibrium composition of a Fe/O system in a temperature range of 500–2500°C.[70]

Interactions between Ce and Fe species during the methane reforming and water splitting steps were investigated.[158]The CeO_2–Fe_2O_3 oxygen carriers were reduced at 950°C under CH_4 flow in a fixed bed quartz tube reactor, followed by purging with N_2/steam. The water splitting step was carried out at 500°C in a separate reactor powered by an electric furnace. The output gasses were quantified by GC equipment coupled to reactor outlets. Three distinct phases of CeO_2, Fe_3O_4 and $CeFeO_4$ were observed in the Ce–Fe–O equilibrium phase distribution. The oxygen mobility was intensified by the formation of $CeFeO_4$ and morphological transformation due to the Ce–Fe chemical interactions. Methane conversion, H_2/CO selectivity, H_2/CO ratios and amounts of H_2/CO/CO_2 produced are evaluated during the CLR and WS steps, as detailed in Figure 1.8.[158]

A series of doped ferrites have been experimentally tested for syngas production. Doping the A cites with metal cations including Mn, Zn, Ni, Zr, Ce and Co has been reported.[80,82,140–143,145,154,181] Substitution of these transition metal ions potentially increases the oxygen storage capacity of pure iron oxide.[182] In addition, the reduction extent also increases due to a low thermodynamic potential for oxygen in doped-ferrites. Various synthesis techniques including solid state reaction, sol-gel,[183] co-precipitation,[184] aerial oxidation of aqueous suspensions,[123,125] combustion synthesis,[123,185] and atomic layer deposition,[186] are utilized for the development of these ferrites.

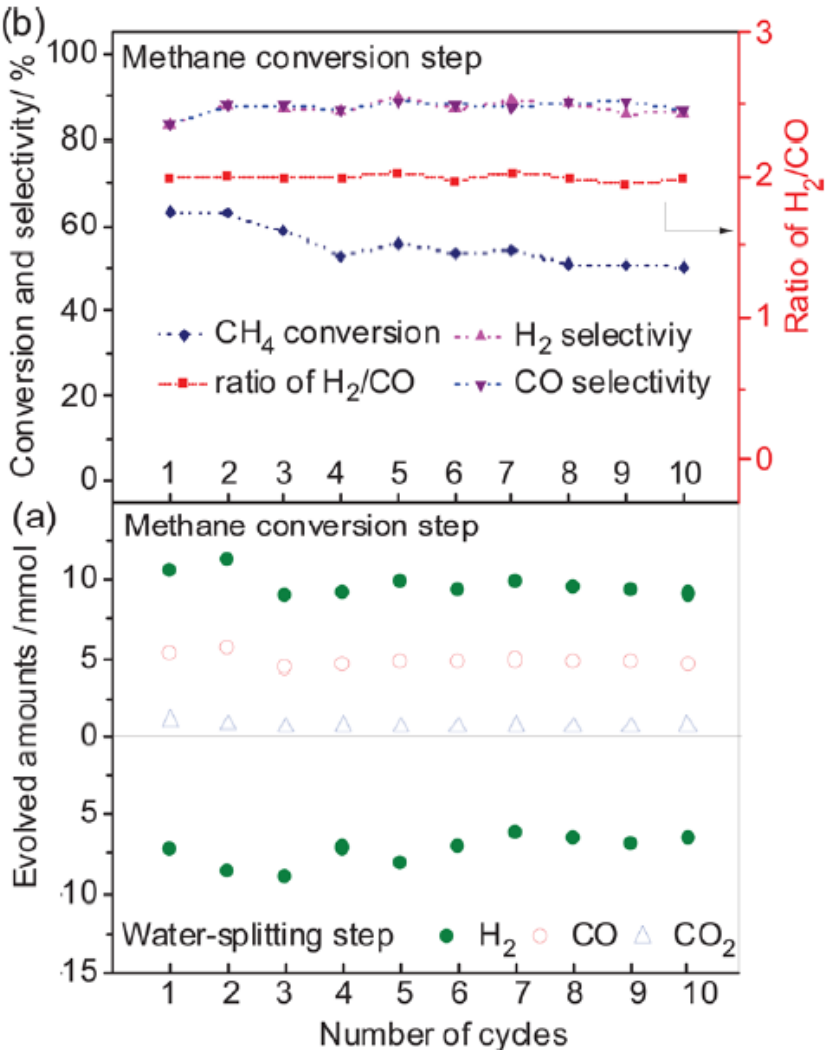

Figure 1.8. (a) Yields of syngas and hydrogen produced and (b) methane conversion, H_2/CO ratios, and syngas selectivity, during the STCLR–WS process over CeO_2–Fe_2O_3 redox materials.[158]

Despite of improved oxygen exchange capacity, some thermodynamic challenges still exist in the ferrite structures. For instance, the thermodynamic potential for oxidation is decreased in cobalt ferrites.[5] While, Zn and Sn doped ferrites are impractical to use in high temperature redox cycles because of the recombination problems.[20,187] The reduction extent in not affected by Mn doping and instead decrease the oxidation rates.[188] However, these mixed metal oxide systems are promising than that of volatile metal oxide pairs.

ii. Hercynite

Combination of ferrites with a second metal oxide i.e. aluminium oxide (Al_2O_3), reversibly transforms into multiple oxides during the reduction and oxidation reactions, Reactions 1.22 and 1.23.[25,189,190]

$$Fe_3O_4 + 3Al_2O_3 = 3FeAl_2O_4 \quad (1.22)$$

$$M_xFe_{3-x}O_4 + 3Al_2O_3 = (3-x)FeAl_2O_{4-x} + xMAl_2O_4 \quad (1.23)$$

The reaction of metal ferrite with the alumina support reduces Fe^{3+} to Fe^{2+} and forms metal/iron aluminate with the release of oxygen, Reaction 1.24. This mixed oxide system is transformed into metal ferrites and alumina during CDS and WS reactions, Reaction 1.25. These hercynite cycles can be performed at low reduction temperatures with high specific H_2 and CO yields because alumina reduces the thermodynamic barrier for the reduction of metal ferrites.

$$CoFe_2O_4 + Al_2O_3 = CoAl_2O_4 + 2FeAl_2O_4 + \frac{1}{2}O_2(g) \quad (1.24)$$

$$CoAl_2O_4 + 2FeAl_2O_4 + H_2O = CoFe_2O_4 + 3Al_2O_3 + H_2(g) \quad (1.25)$$

The first demonstration of the hercynite cycle was carried out by Scheffe et al. for hydrogen production. The $CoFe_2O_4/Al_2O_3$ system was reduced between 1200–1400°C and produced higher H_2 yields as compared to that of $CoFe_2O_4$.[189] Arifin et al. compared the reaction kinetics of bulk iron oxide structures with the $CoFe_2O_4$ deposited by atomic

layer deposition (ALD) on Al_2O_3. Rapid reaction kinetics were achieved with high surface area Al_2O_3 supported-ferrites as compared to bulk iron oxides.[190] The isothermal hercynite cycle at 1253°C studied by Muhich et al. showed more than 3 folds higher H_2 yields than the traditional hercynite cycle carried out between 1000–1253°C.[25] This finding unveiled the improved local oxygen activity near the material's surface which enhances the oxidation rates during isothermal thermochemical redox cycles. Although the doped hercynite cycle has demonstrated better fuel production yield than the traditional doped ferrites, not much of experimental work has been reported yet.

iii. Ceria-based mixed metal oxides

Ceria is one of the most investigated oxygen carriers for solar fuel production via thermochemical redox cycles and methane reforming cycles. The redox kinetics, reaction temperatures, structural features, and stoichiometric chemistry of ceria have been thoroughly documented in recently published reviews.[3,5,6,164,166,191] After the first demonstration of the stoichiometric transition of CeO_2 to Ce_2O_3,[15] many studies reported the nonstoichiometric reduction of CeO_2 to $CeO_{2-\delta}$ [38] and successfully utilized ceria-based solar reactors for simultaneous H_2O and CO_2 splitting cycles.[27,192] The non-stoichiometry and defect chemistry of ceria reflects its low oxygen exchange capacity and high ionic conductivity. [26,38,194–198,43,60,81,85,95,125,192,193] Reaction 1.35 is a mathematical representation of the oxygen vacancy formation mechanism in ceria structures according to Kroger-Vink notations.[60,199]

$$2Ce^{\times}_{Ce} + O^{\times}_{o}\ (T, \rho_{O_2}) \leftrightarrow Ce^{'}_{Ce} + V^{\bullet\bullet}_{O} + \frac{1}{2}O_2 \qquad (1.35)$$

Where, $Ce^{\times}_{Ce}$, $O^{\times}_{O}$, $Ce`_{Ce}$, $V^{\bullet\bullet}_{O}$ are Ce^{4+}, lattice oxygen, Ce_{3+} and oxygen vacancy, respectively. The electrostatic interactions dominate in the defect cluster formation due to high oxygen vacancy concentrations. Hence, the effects of interactions between defects are negligible and Reaction 1.45 can be expressed according to Reaction 1.36.[60,200]

$$2Ce^{\times}_{Ce} + V^{\bullet\bullet}_{O} \leftrightarrow (Ce'_{Ce}\ V^{\bullet\bullet}_{O}\ Ce'_{Ce})^{\times} \quad (1.36)$$

The expression $(Ce`_{Ce}\ V\ ¨_{O}\ Ce`_{Ce})^{\times}$ refers to an electron-vacancy cluster. The experimental studies suggest that oxygen non-stoichiometry of ceria is specific to temperature and oxygen partial pressure.[199] Simplified chemical equations for the reduction and oxidation reactions seen in ceria during STRC and STCLR processes are presented in Reactions 1.37–1.39.

$$\text{Inert gas sweeping: } CeO_{2-\delta_{OX}} = CeO_{2-\delta_{red}} + (\frac{\delta_{red} - \delta_{OX}}{2})O_2 \quad (1.37)$$

$$\text{MPO: } CeO_{2-\delta_{OX}} + CH_4 = CeO_{2-\delta_{red}} + (\frac{\delta_{red} - \delta_{OX}}{2})(CO + 2H_2) \quad (1.38)$$

$$\text{WS: } CeO_{2-\delta_{red}} + (\delta_{red} - \delta_{OX})H_2O = CeO_{2-\delta_{OX}} + (\delta_{red} - \delta_{OX})H_2 \quad (1.39)$$

Redox capacity and thermal stability as a function of morphology and ceria structure have been studied for thermochemical cycles at various temperatures. Different ceria (pure and doped) structures have been synthesized via various methods such as sol-gel, hydrothermal, flame spray, pechini, solid state reaction, co-precipitation, and combustion methods. The aim was to lower the reduction temperatures of ceria with high surface area and structural stability for an efficient and repeatable syngas production at elevated temperatures over multiple cycles. Gao et al, reported a direct dependency of structural parameters (specific surface area, morphology and particle size) on the redox kinetics and fuel yields, during the isothermal splitting of CO_2 at 900°C.[22]

In this regard, reticulated porous ceria structures embedded in solar reactors have been investigated to improve the solar-to-fuel efficiency.[201–203] These porous ceramic foams provided an upscale production of active material-imbedded solar reactors without any need of a support structure, (Figure 1.9).[204]

Marxer et.al. demonstrated simultaneous water and CO_2 splitting redox cycles using ceria RPC in a cavity-type solar reactor, Figure 1.10. The overall syngas yield was 700 L

during 291 redox cycles, Figure 1.11.[192] Moreover, heat and gas flow was significantly increased in RPC-imbedded reactors unlikely to that of fixed bed and fluidized reactors. Typically, RPCs are synthesized by a replication method, in which organic polyurethane sponges are immersed into a slurry of active oxide materials.[201] The porosity of these ceramics can be tuned by modifying the solid to liquid ratios with variable pore density of polymeric foam templates. Furthermore, a variety of structures with single and dual scale porosity can by synthesized by utilizing spherical carbon pore-forming agent particles.

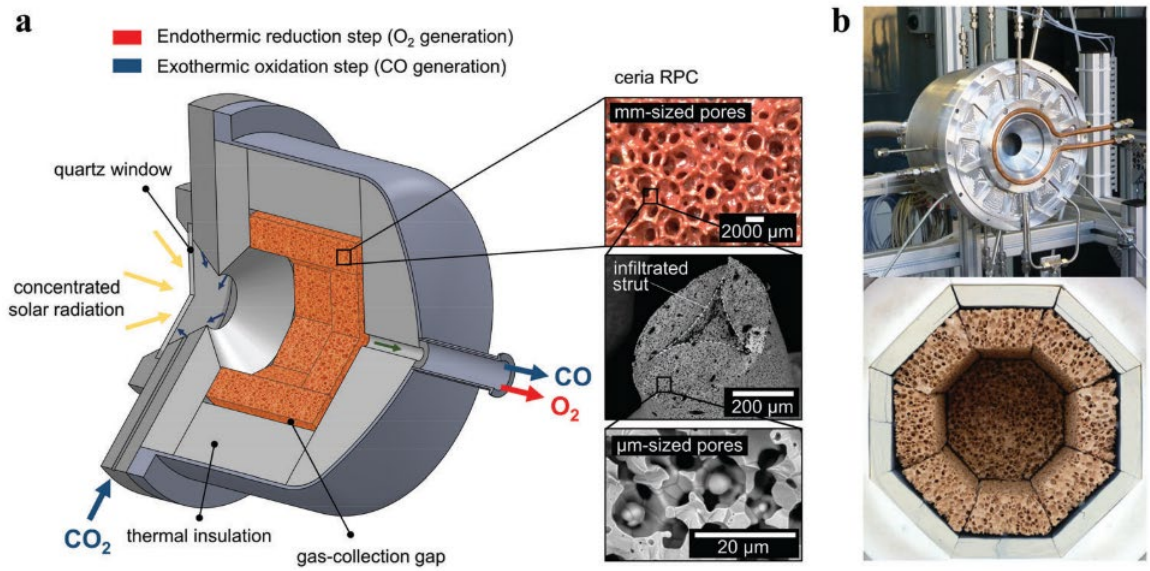

Figure 1.9. (a) Schematic and (b) photographs of the reticulated porous ceria-RPC-embedded solar reactor for thermochemical CO_2 splitting cycles.[204]

Furler et al. demonstrated simultaneous splitting of CO_2 and H_2O in a solar reactor incorporated with RPC ceria bricks, reduced at a temperature range of 1460–1647°C and re-oxidized at 927°C. A non-stoichiometry of $\delta = 0.044$ and fuel yield of 5.9 ml g^{-1} were achieved during the redox reactions. In another study, Furler et al. utilized reticulated foams of ceria with dual scale porosities during thermochemical CO_2 splitting cycles. Samples were reduced at 1500°C and CO_2 splitting was carried out at temperatures in a range of 500–1000°C. It was observed that with 0.44 strut porosity, ceria outperformed the non-porous strut ceria foams by ten times for the CO production yield per cycle.

Testing the dual porous RPC ceria foams under high-flux thermal radiation (up to 3015 suns) showed a shorter cycle time with an average solar-to-fuel energy conversion efficiency up to 1.72%, Figure 1.12.[27]

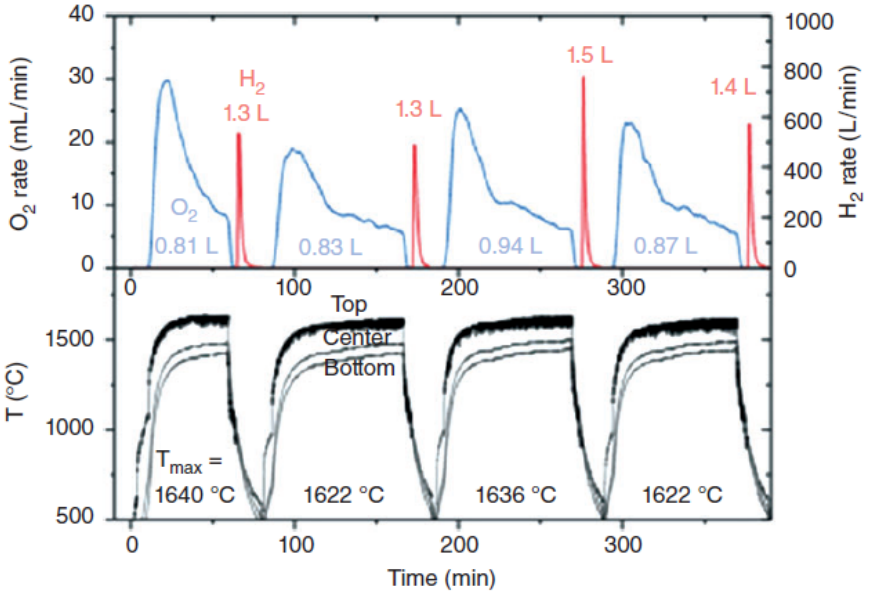

Figure 1.10. Temperature variance between top, center and bottom layers of a cavity-type solar reactor and rates of H_2 and O_2 produced during the reduction and oxidation stpes of thermochemical WS cycles.[192]

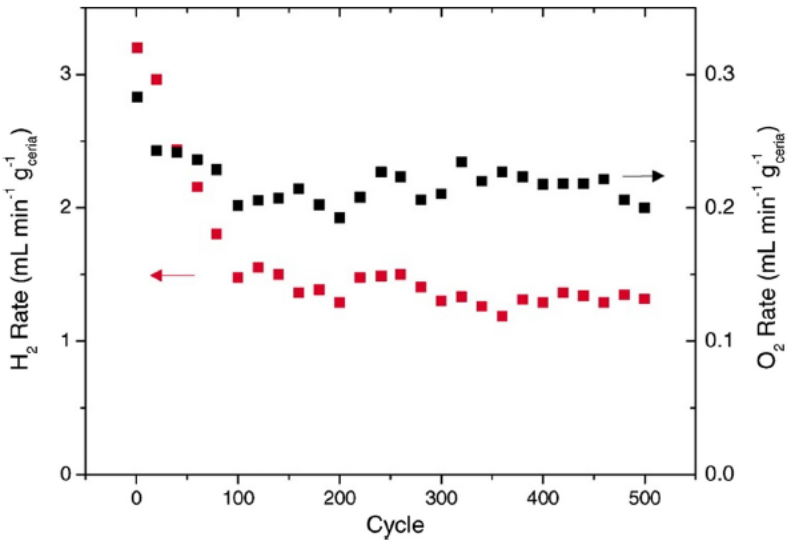

Figure 1.11. Rates of H_2 and O_2 produced during 500 cycles of thermochemical WS splitting reactions.[192]

Ackermann et al. performed numerical and experimental analysis of RPCs for the thermochemical CO_2/H_2O splitting. Behaviour of the RPC ceria foams under

concentrated solar radiation is investigated by a transient heat and mass transfer model. Samples with different porosities representing variable optical thickness were studied under high flux solar radiation. It was observed that structures with moderate optical thickness showed better absorption of solar radiation, which leads to uniform heat transfer and high specific oxygen exchange capacity.[202]

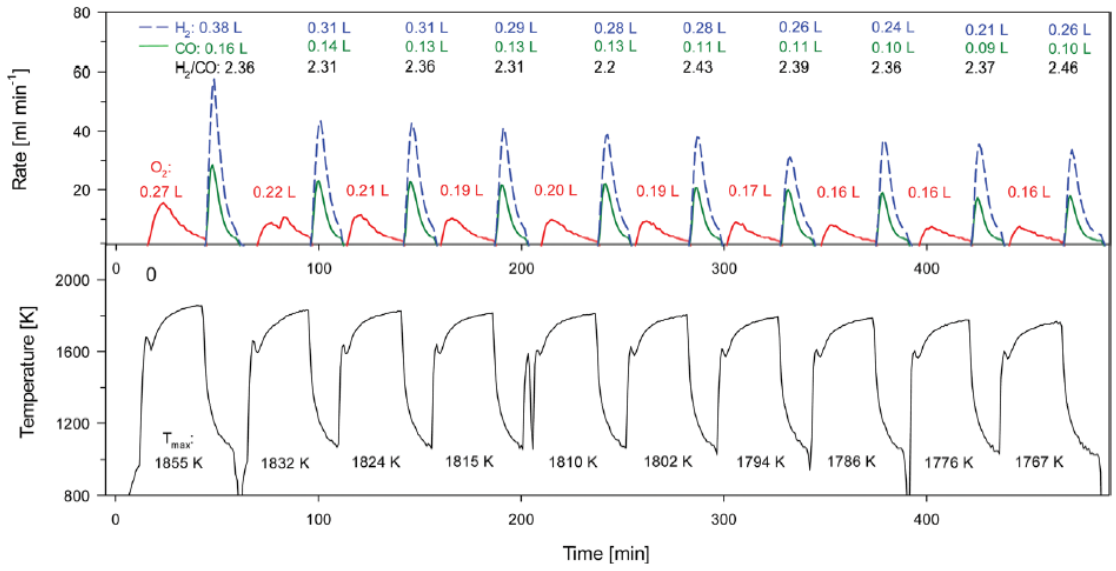

Figure 1.12. Temperature variance in ceria felt, syngas production rates/yields and H_2:CO molar ratios during 10 consecutive thermochemical simultaneous CO_2/H_2O splitting cycles.[27]

Doping with transition metal cations has been vastly investigated to improve the solar fuel production performance of ceria structures. Various binary and ternary oxides containing ceria with variable concentrations of dopant e.g. Mn, Co, Fe, Ni, Li, Zr, Si, Ti, Nb, Sm, Mg, Sc, Hf, Pr, Ta, La, Gd, Zn, Y, Sn, Ca, Dy, Rh, Al and Cr, are studied for syngas production. [19,22,168,205–210,23,25,58,59,84,147,151,159] In the following paragraphs, the best ceria derivatives are highlighted.

CeO_2–ZrO_2 solid solutions are one of the most successful derivatives of ceria for improved solar thermochemical redox activity. Miller et al. first reported the CeO_2–ZrO_2 monolithic structures for 4 consecutive thermochemical H_2O and CO_2 splitting cycles at 1100°C. The monolithic structure underwent sever sintering which reduced the overall

splitting performance after several cycles.[163] Abanades et.al. demonstrated the effect of Ce:Zr ratios on water splitting performance at different oxidation temperatures. Where, Ce:Zr ratio (3:1) showed the highest level of H_2 yields at 1045°C.[52] In extension of this study, Le Gal et.al. evaluated the effects of synthesis method on the thermochemical redox performance of oxygen carriers. Samples were prepared by co-precipitation, hydrothermal, sol-gel and Pechini method and three thermochemical tests were performed at T_{red} = 1400°C and T_{ox} = 1000°C, 1100°C and 1200°C. The Ceria-zirconia derivative prepared by Pechini method showed the highest CO and H_2 production yields at T_{ox} = 1000°C and 1200°C.[192,211]

Considering the importance of materials structural properties, Venstrom et.al. studied the thermochemical redox performance of three-dimensionally ordered microporous (3-DOM) Ce-Zr structures. The 3-DOM Ce-Zr structures ($Ce_{1-x}Zr_xO_2$) produced higher yields of H_2 than the 3-DOM pure ceria at 825°C. Efforts were made to investigate metal (M) doped CeO_2-ZrO_2 binary oxides for thermochemical H_2O and CO_2 splitting reactions. Only magnesium doping showed improvements in the thermochemical activities of CeO_2–ZrO_2 binary oxide systems during the CO_2 splitting reactions at 1100°C.

Doping Fe^{3+} has reportedly influenced the redox properties of ceria.[3,84,197,205] High concentrations of Fe^{3+} cations facilitates the methane conversions[151,159,212–214] and leads to high syngas yields.[178,212,213] Li et.al. reported higher syngas selectivity over Fe^{3+} doped CeO_2 than that of Zr^{4+} doped ceria powders.[215] While, co-doping of Fe^{3+} and Zr^{4+} improves the methane conversion with high syngas selectivity.[178] Recently, Gao et.al. reported efficient redox activities of Mn_3O_4 with Ce^{4+} as a dopant, during CDS cycles coupled to the methane partial oxidation reaction. However, carbon deposition is still a persisting challenge to overcome.[168,206]

iv. Perovskites

Perovskites with a general formula ABO_3 are a class of non-stoichiometric redox materials that have been investigated for an alternative to ceria for syngas production. Single and multiple dopants can be substituted on A and B site of these materials which outcomes in a wide range of potential perovskites configurations.[5] In addition, perovskite oxides exhibit better thermal stability and oxygen capacity at lower temperatures than the pure ceria.[57,83–85,93,95,99,203,216]

The non-stoichiometric reduction and oxidation of ABO_3 type perovskites can be mathematically expressed in Reactions 1.50–1.52.

$$\text{Inert gas sweeping: } ABO_{3-\delta_{OX}} = ABO_{3-\delta_{red}} + \left(\frac{\delta_{red} - \delta_{OX}}{2}\right)O_2 \quad (1.50)$$

$$\text{MPO: } ABO_{3-\delta_{OX}} + CH_4 = ABO_{3-\delta_{red}} + \left(\frac{\delta_{red} - \delta_{OX}}{2}\right)(CO + H_2) \quad (1.51)$$

$$\text{WS: } ABO_{3-\delta_{red}} + (\delta_{red} - \delta_{OX})H_2O = ABO_{3-\delta_{OX}} + (\delta_{red} - \delta_{OX})H_2 \quad (1.52)$$

A range of perovskites oxides with doping of Ba, Ca, Ce, Dy, Gd, La, Nd, Sm, Sr, Y on A-sites and Al, Co, Cr, Fe, Mg, Mn on B-sites, are studied for syngas production via thermochemical redox cycles and chemical looping reforming reactions.[89,90,223–232,149,233–238,216–222] Manganese based perovskites oxides are the most investigated oxygen carriers for its high syngas selectivity and oxygen exchange capacity.[3,89,90,219] The substitution of La and Sr on A-site and Mn on B-site doping ($La_{1-x}Sr_xMnO_{3-x}$; LSM) demonstrated reduction extents twice higher than that of pure ceria at 1500°C.[95] Moreover, despite the slow oxidation kinetics, the reduced LSM species are capable to produce higher CO yields than that of pure ceria, during CDS cycles.[85] Compared to ceria, the $SrLaMnAlO_3$ perovskites oxides produced up to a staggering 9-fold and 6-folds higher H_2 and CO yields respectively, at T_{red} = 1250°C and T_{ox} = 1000°C. The oxidation behaviour of SLMA during the CO_2 and H_2O splitting reaction is compared with the pure ceria in Figure 1.13.[85]

The partial substitution of Cr and Fe on B-sites improved the methane and oxidizer conversion of LSM perovskites, while H_2 selectivity remained unchanged.[90] A double perovskite system ($CaMnNiFeO_3$) and ($BaMnNiFeO_3$) enhanced the syngas selectivity with fast initial redox kinetics.[226] Another study summarized the effects of A-site doping of Sr^{2+}, Ca^{2+}, Ba^{2+}, Y^{3+}, La^{3+}, Nd^{3+}, Sm^{3+}, Gd^{3+} and Dy^{3+}, on the redox performance of $LaMnO_3$ perovskites.[57,95,96,99,216] The orthorhombic $LaCaMnO_3$ perovskites showed higher reduction extents than that of rhombohedral $LaSrMnO_3$ perovskites.[83,99,203] Manganese and iron-based perovskites showed poor water splitting and overall fuel production despite having high total O_2 yields.[216] Despite the good redox performance, perovskites oxides are yet to be studied in an actual reactor.

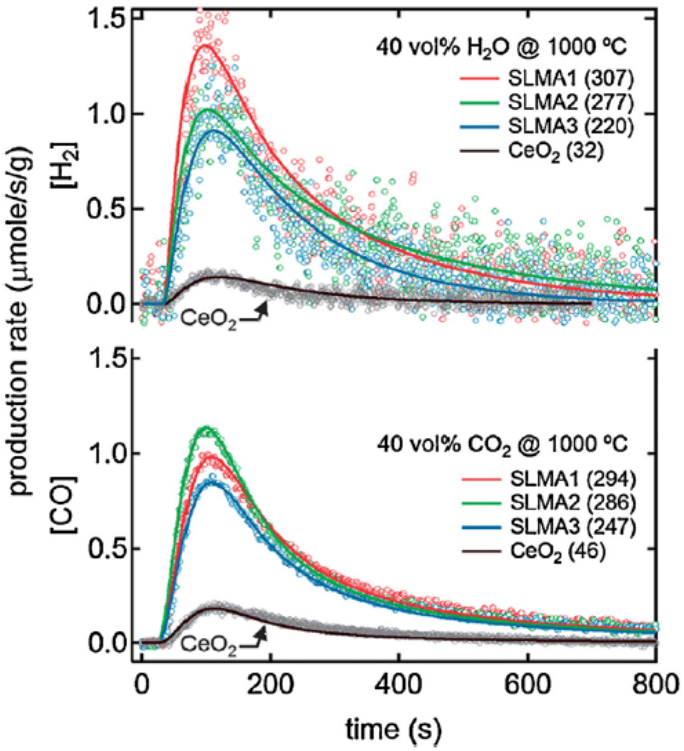

Figure 1. 13. A comparison of H_2 and CO production rates during H_2O and CO_2 splitting cycles at 1250°C, between $SrLaMnAlO_x$ Perovskites and pure ceria.[85]

1.3.3. Summary

The solar-to-fuel efficiencies have been investigated experimentally and theoretically. So far, low energy conversion efficiencies of current redox materials is still considerably

lower than the benchmark values for a commercial, large-scale implementation of STRC and STCLR processes. The pros and cons of different groups of redox materials for solar fuel production can be summarize in Table 1.1:

Table 1.1. Comparison of pros and cons of various groups of redox materials for syngas production via solar thermochemcial redox cycles and chemical looping reforming of methane processes.

Redox materials	**Pros**	**Cons**
ZnO/Zn, SnO_2/SnO	High oxygen exchange capacity	Low thermal stability Recombination needs an extra separation step
Fe_3O_4/FeO	High thermal stability No need for separation	Sintering Non-consistent redox kinetics
Ferrites	High structural stability Low operating temperatures	Low fuel selectivity and yields
Ceria	High ion conductivity High syngas yields and selectivity. High structural and phase stability	Low oxygen exchange capacity High temperature requirements
Doped ceria	Improved oxygen exchange capacity Low reduction temperatures	Inconsistent redox kinetics Low ion conductivity

Perovskites	High oxygen exchange capacity High reduction extents Flexible doping conditions	Slow oxidation kinetics Low structural stability with hydrocarbons

1.4. Scope of thesis

In this thesis, the redox mechanisms in ceria-vanadia and LSM perovskites redox materials have been explored for solar thermochemical redox cycles and chemical looping dry/steam reforming of methane for syngas production. Current research trends focusing on the oxygen exchange capacity, redox kinetics, and structural stability of various metal oxide materials with unique chemical identities have also been detailed. Recent research has resulted in considerable improvement in cyclic redox performance of oxygen carriers, where structural features and chemical identities play a vital role in the enhancement of syngas production kinetics and yields over hundreds of cycles. Nevertheless, the challenge to search for an efficient and low-cost sustainable redox material for thermochemical processes is still there. The seamless transition of this technology into the global energy market to supply synthetic fuels is highly dependent on the scalability and low cost of redox material. Rigorous and decisive selection criteria to achieve high redox features demands an expansion of research and development efforts in materials engineering. With this in mind, this thesis aims to achieve a benchmark performance of mass production of syngas over selected redox materials, engineered by facile and effective ionic substitution methods. Moreover, aims to highlight the key physiochemical evolutions of thermochemical redox cycles and chemical looping methane reforming processes via advanced materials studies.

In Chapter 2, synthesis of a family of redox materials including vanadium-ceria (V–CeO_2) and lanthanum strontium manganite (LSM) perovskite structures, via

electrospinning and liquid precursor combustion methods are introduced. A facile stoichiometric substitution of metal cations in structurally engineered metal oxides is elucidated. The experimental procedures for structural and chemical characterization of these redox materials before and after the thermochemical process are also discussed. Materials characterization using X-ray diffraction, X-ray photoelectron, X-ray absorption near edge, Raman spectroscopy, scanning and transmission electron microscopy and energy dispersive spectroscopy techniques is undertaken. Key process parameters for thermochemical redox cycling and chemical looping methane reforming are investigated for syngas production.

In Chapter 3, the redox characteristics of $La_xSr_{1-x}MnO_3$ (LSM, x = 0…1) nanostructures are investigated for syngas production via solar thermochemical redox cycles and chemical looping methane reforming processes. In particular, the composition of resulting powders, advanced characterization of their structural evolution and syngas production performance are undertaken and observed as a function of lanthanum concentration. The Sr-rich LSM nanopowders revealed a high oxygen non-stoichiometry associated with a high degree of sintering at high reduction temperatures. Key performance parameters that are studied here, include high structural and phase stability, oxygen vacancies, chemical composition and ionic mobility are critical for the utilization of LSM perovskites oxides in syngas production via inert gas sweeping and chemical looping reforming techniques.

In Chapter 4, vanadium-doped ceria nanostructures with efficient redox properties are developed via a facile liquid phase precursor combustion method. The Effect of vanadium concentration on the reduction temperatures and structural stability of ceria is evaluated over 200 H_2O/CO_2 splitting cycles coupled to a methane partial oxidation reaction. A redox mechanism of Ce^{4+}/V^{5+} ions was proposed based on the information acquired from the advanced characterization of powders before and after the cycling. XPS analysis

revealed the migration of vanadium ions from the interior to the surface of ceria nanopowders, which exhibited different attributes towards the feedstocks and led to variable redox kinetics and fuel selectivity. This work can potentially lead the research community in exploring new redox materials for large-scale synthesis of solar fuels via thermochemical processes.

In Chapter 5, an efficient and stable redox pair Ce-doped V_2O_5 mechanism is developed. This is achieved by fractional incorporation of cerium ions into a V_2O_5 lattice, which activated it in relation to fast redox kinetics with an extraordinary oxygen exchange capacity. Structural analysis revealed that cerium chemically reacted with the surface vanadium cations to form segregated $CeVO_4$ phase, which is thermodynamically stable at the operating temperatures in contrast to the pure V_2O_5 with a melting point of ~650°C. Moreover, the V_2O_5 lattice expansion by large Ce cations expelled oxygen species and led to a +5 to +3 transition in vanadium oxidation states with a resultant V_2O_3 phase. Despite the initially slow activation, Ce-doped V_2O_5 systems demonstrated an excellent redox performance for over 200 cycles, with a combined catalytic and chemical looping reforming mechanism to produce syngas from natural hydrocarbon feedstocks.

In Chapter 6, enhanced oxygen exchange capacity in nano-structured V_2O_5–CeO_2 multi-phase metal oxides system was studied for syngas production via solar thermochemical looping reforming of methane and H_2O/CO_2 splitting cycles. The addition of 25% vanadium resulted in an optimum mixture of CeO_2 and $CeVO_4$ with high structural stability. Structural studies revealed that surface vanadium plays a crucial role in enhancing the cycle capacity of ceria because of high oxygen vacancies created by V^{5+}. Introducing a CO_2 splitting step after H_2O splitting substantially increased oxidation potential of the redox materials and increased fuel selectivity in the subsequent methane reforming reaction. These useful insights relating to Ce–V doped oxides and CeO_2–$CeVO_4$ multiphase oxides should generate interest in evaluating the full range of suitable

stoichiometric concentrations among the multi-cationic oxide systems for thermochemical applications.

In Chapter 7, a summary of these outcomes and their contribution towards the field of solar driven thermochemical routes, is presented. The prospects and potential for this field of research are briefly discussed.

Chapter Two

Materials and Methods

2.1 Synthesis of metal oxides

This section covers the synthesis of $LaSrMnO_3$ Perovskites and V–Ce doped and mixed metal oxides via electrospinning and liquid-phase precursor combustion techniques, respectively.

2.1.1 $LaSrMnO_3$ perovskites

Lanthanum strontium manganite Perovskites (LSM) oxides were prepared via an electrospinning technique. Lanthanum (III) chloride $LaCl_3 \cdot 7H_2O$ (Sigma Aldrich), strontium carbonate $SrCO_3$ (Sigma Aldrich) and manganese (II) acetate ($C_6H_9MnO_6.4(H_2O)$) (Ajax Finechem) were the main precursor materials for the synthesis of LSM oxides, while polyvinyl pyrollidone (PVP) (Sigma Aldrich, M_w $1.3x10^6$) was used as a fibre forming polymer. Commercial Mn_3O_4 (Sigma Aldrich) was used for the purpose of comparing CDS performance and material structure. De-ionized (DI) water, absolute ethanol (Ajax Finechem) and acetic acid (Ajax Finechem) were used as solvents.

LSM Perovskites were synthesized by a standard electrospinning technique as reported elsewhere.[239] This technique was utilized to obtain structural and stoichiometric uniformity of the LSM structures, with low setup cost, batch production capability and morphology control. In addition, the interconnected woven fibrous features avoid extensive structural damage during the high temperature thermochemical cycling, which significantly helps in retaining the syngas production performance for long-term stability tests. Whereas extensive sintering in nanoparticles synthesized by other liquid phase preparation techniques e.g., sol-gel and hydrothermal methods hinders the solid to gas transfer and deteriorates the syngas production rates after a few cycles. In addition, these techniques involve use of expensive and toxic precursors and solvents. Volume shrinkage and difficulty in morphology control is another disadvantage in sol-gel methods. In addition, formation of the gel is a slow process and extra steps for by-products/solvent

removal and gel-cleaning make the sol-gel method complicated for perovskite production.[240] The hydrothermal process utilizes expensive equipment and crystal growth cannot be observed during the reaction.[241]

First, the precursor materials with the required cation stoichiometric ratios (Table 2.1) were dissolved in a combination of solvents and stirred for 18 hours. The combination of solvents used for $C_6H_9MnO_6.4(H_2O)$ precursor was a 3:1 mix of DI water and ethanol, while a 3:2 mix of DI water and acetic acid was used to dissolve $LaCl_3$ and $SrCO_3$ in separate containers. The two solutions were mixed and PVP was added with a molar ratio of 1:10 to the precursor material and stirred until a homogenized sol was achieved. The molar ratios of PVP were carefully adjusted to achieve a suitably viscous sol, which was then transferred into a syringe.

Table 2.1. Elemental composition of $La_xSr_{1-x}MnO_3$ for sample synthesis determined by stoichiometric analysis vs measured composition of as-prepared samples using energy-dispersive X-ray spectroscopy. The measurement errors represent 95%-confidence intervals about the mean.

Sample	x	Molar fraction							
		Stoichiometric				Measured			
		Sr	La	Mn	O	Sr	La	Mn	O
SMO	0	0.52	–	0.52	1.57	0.54±0.16	–	0.57±0.14	1.36±0.21
LSM25	0.25	0.37	0.121	0.49	1.48	0.38±0.11	0.12±0.02	0.42±0.17	1.65±0.27
LSM50	0.5	0.23	0.23	0.46	1.39	0.26±0.09	0.20±0.06	0.43±0.13	1.12±0.15
LMO	1	–	0.41	0.41	1.24	–	0.45±0.11	0.37±0.10	1.08±0.11

Electrospinning was performed at an accelerating voltage of 25 kV, with a needle-to-collector distance of 15 cm at a feed rate of 0.5 mL hr^{-1}. As-spun fibres were collected on a flat copper plate wrapped with aluminium foil. The samples were subsequently calcined in an air atmosphere at 1000°C, ramping with a rate of 3°C min^{-1} and held for 5 hr,

followed by a furnace cool. The sample fabrication process is schematically depicted in Figure 2.1.

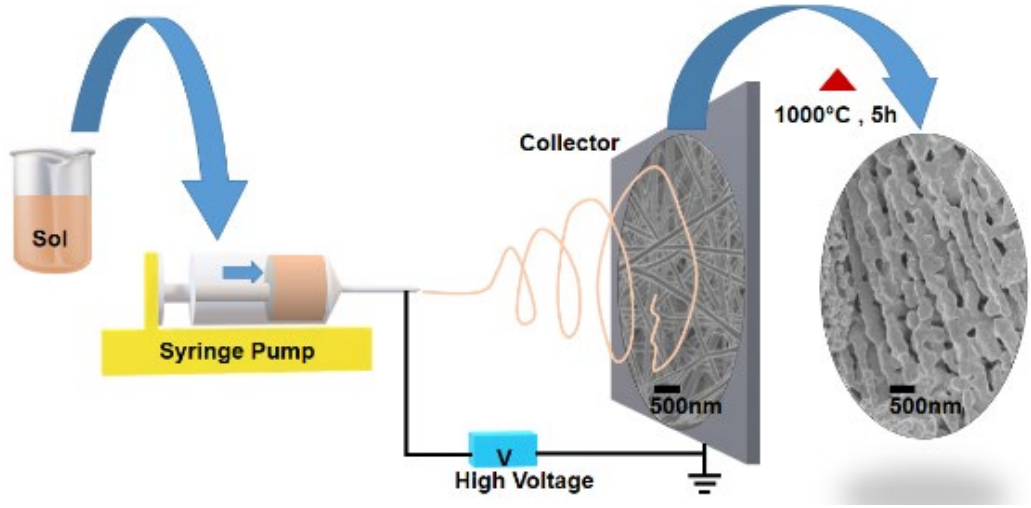

Figure 2.1. Fabrication of LSM samples via electrospinning method.

2.1.2 Cerium–vanadium mixed metal oxides

The Ce–V mixed metal oxygen carriers were synthesized via a liquid-phase precursor combustion method because the hygroscopic nature of the vanadium precursor was not suitable for the moisture sensitive electrospinning technique. Repeated experiments resulted in unspun vanadium and cerium hydroxides instead of well-structured fibers. In contrast, simultaneous transformation of metal cations into oxides and calcination, produced powders with nanocrystalline features and homogenous compositions via the liquid-phase precursor combustion method. In addition, this method offered an upscale production of nanoparticles with good control on the particle size and morphology.[242]

Ultra-fine, nano-structured xVCeO$_2$ (x = 0%; CeO$_2$, 1%; 1VCe, 3%; 3VCe, 5%; 5VCe, 7%; 7VCe, 25%; CV25, 50%; CV50, 75%; CV75, and 100%: V$_2$O$_5$) and xCeV$_2$O$_5$ (x = 1% ; 1CeV, 3% ; 3CeV, 5% ; 5CeV, and 7% ; 7CeV) powders were prepared for solar fuel synthesis, which will be thoroughly discussed in chapters 4, 5, and 6.

Briefly, the precursor solution for CeO$_2$ was prepared by dissolving cerium (III) nitrate hexahydrate (CeN$_3$O$_9$.6H$_2$O, Aldrich) in ethanol and stirred until its complete dissolution. For the synthesis of xVCeO$_2$ and xCeV$_2$O$_5$ metal oxides, separate solutions

of stoichiometric concentration of vanadium (V) oxytripropoxide ($C_9H_{21}O_4V$, Aldrich) and $CeN_3O_9.6H_2O$ in ethanol were mixed and stirred at room temperature until complete homogeneous solutions were achieved. The precursor solutions were dried at 80°C and then fired at 900°C for 2 hr. The ramp rate for drying and firing was kept constant at 3°C min^{-1}. The synthesis schematic for these oxygen carriers is shown in Figure 2.2.

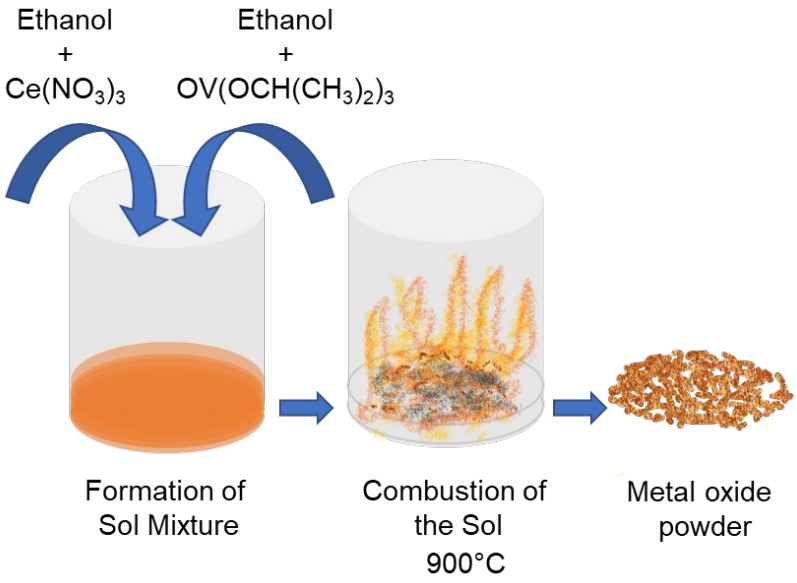

Figure 2.2. Fabrication of Ce–V mixed metal oxide powders via a liquid-phase precursor combustion method.

2.2 Characterization of metal oxides

Powder samples were characterized before and after the thermochemical cycles and chemical looping reforming of methane processes.

X-ray diffraction (XRD) analysis was carried out using a D2 phaser diffractometer (Bruker). The samples were scanned using a Cu kα (1.54 Å) radiation source with an operating voltage of 30 kV and a current of 10 mA. XRD patterns were recorded with a scanning rate of 0.75° min^{-1} in a 2θ range of 10–80° at an increment of 0.02°. Crystalline domain size was determined by applying the Scherrer equation on the most intense peaks obtained in the XRD patterns. Phase quantification was carried out by the Rietveld refinement technique utilizing Match 3 V. 3.8.1.143 (Crystal Impact) software.

X-ray photoelectron spectroscopy (XPS) analysis was performed using a Thermo Fisher ESCALAB 250Xi X-ray photoelectron spectrometer (XPS) microprobe equipped with a 180° double focusing hemispherical analyzer. A monochromatic Al K-Alpha source with a spot size of 200–900 μm was operated at a power of 180 W (15 kV×12 mA). The total pressure in the chamber was maintained at around 10^{-8} mbar. Two different spots on a 5×5 mm area of sample with an estimated depth of 4 mm were scanned with an energy of 160 eV. The pass energy was reduced to 40 eV for high resolution spectra. The data processing was performed using CasaXPS processing software version 2.3.18 (Casa Software Ltd., Teignmouth, UK). The aliphatic carbon peak C 1s at 284.8 eV was used as a reference for the binding energies of elements acquired in the survey spectra.

Structural analysis of the redox materials was carried out by utilizing a Raman imaging microscope (Renishaw Plc, model 2000) coupled to an Olympus BH2 microscope. The microscope is equipped with a motorized XYZ stage, air-cooled CCD detector and a CCD camera. The samples were excited by using a 785 nm NIR laser source and spectra were recorded in a Raman shift range of 100–1200 cm^{-1}. The samples were exposed for 20 s with an accumulation of 3 and the power was adjusted from 0.01%–0.5% (< 6 MW) according to the sample response.

Information about the Mn K, Ce L3 and V K edges was obtained from X-rays absorption spectroscopy (XAS) technique in X-ray absorption near edge structure (XANES) region. The spectra were obtained in transmission and florescence mode at BL5.2 of the Synchrotron Light Research Institute (SLRI), Thailand. Electron beam energy was 1.2 GeV and current ranged from 80 to 150 mA, while maximum photon flux was $1.1–1.7\times10^{11}$ photons.s^{-1}. Two germanium (220) single crystals were utilized as a monochromator for an X-ray beam size of 14 mm (width) and 1 mm (height) with a spatial

resolution of 0.2 eV. The normalized XANES spectra were processed and analyzed in Athena software.

A field emission scanning electron microscope (FESEM, Zeiss Ultraplus) was utilized to observe the morphology of nano-structured powders before and after thermochemical redox cycles. Particle size distribution and lattice plane spacing was determined by a high-resolution transmission electron microscope (HR-TEM, JEOL 2100F) with an operating voltage of 200 kV. The samples were deposited onto lacey carbon–coated 200 mesh copper grids. Primary particle size and lattice plane spacing were acquired *via* the ImageJ image processing software. Energy dispersive X-ray spectroscopy mapping (EDX) was performed *via* the scanning transmission electron microscopy (STEM) mode on the JEOL 2100F, to acquire information about the chemical composition of metal oxides before and after thermochemical processes. The area of interest was scanned by the STEM probe to obtain elemental mapping and EDX spectra.

Electron energy loss spectroscopy (EELS) was performed by utilizing a Hitachi HF500 Cs-STEM/TEM instrument equipped with a W (310) cold-cathode FEG electric field filament and a Cs probe STEM corrector. Accelerating voltage was set at 200 kV for the high-resolution imaging and EELS analysis.

Information about specific surface area and porosity of nano-structured powder samples was acquired *via* N_2 adsorption-desorption isotherms at 7K by utilizing TriStar II, Micromeritics. Powders were degassed at 523 K under vacuum (0.1 mBar) for 3 hr prior to the measurements.

2.3 Thermochemical testing

Thermogravimetric analysis (TGA) and differential thermal analysis (DTA) were carried out by using a (NETZSCH STA 449 F3 Jupiter). Mass change during consecutive redox cycles was recorded as an indicative of active redox reactions. Powder samples were reduced and then re-oxidized under a 10 mL min^{-1} flow of CH_4 and CO_2, respectively.

The total gas flow was kept constant at 125 mL min^{-1}, balanced with Ar carrier gas. Ar (125 mL min^{-1}) was used after every reduction and oxidation reaction to sweep any by-products and reacting gases from the system. Approximately 40 mg of powder was heated to 900 °C with a ramp rate of 20 °C min^{-1}. Isothermal reduction and oxidation reactions were carried out for 20 min and 10 min, respectively, while the Ar gas sweeping step was set for 5 min.

The cyclic thermochemical redox performance of metal oxides was evaluated in a vertical-tube reactor placed inside an infrared gold image furnace (P4C-VHT, Advance Riko). Powder samples weighing 250 ± 5 mg were placed between 2 ± 0.3 mm thick layers of highly porous and temperature resistant alumina-based fibrous wool (AlBF-1, 97% Al_2O_3 and 3% SiO_2, ZIRCAR). Powders and wool layers were centrally located in the alumina tube to ensure uniform heating, as shown in Figure 2.3. Powder mass was recorded before and after cycling to monitor the weight loss at the appropriate part of the process. Lower material activity was observed for sample masses greater than 300 mg because the small diameter of the alumina tube restricted the mass transfer in solid-gas reactions during redox cycling. Gas flow rates were regulated by flow rate controllers (F201CV, Bronkhorst), operated by an in-house developed LabVIEW (National InsrumentalTM) program code which was integrated with mass flow controllers and pneumatically actuated valves (1315R, Swagelok). The sample temperature was monitored by a B-type thermocouple sealed in an alumina sheath, located directly under the packed samples. The composition of the product gasses was recorded by a quadrupole mass spectrometer (OmniStar™ GSD 320, Pfeiffer Vacuum).

The tubular reactor was purged with argon (Ar grade 5.0) with a flow rate of 500 mL/min before every reduction and oxidation reaction, to remove any surface gas species (H_2, CO, CO_2) from the sample/tube/fitting surfaces, which may potentially affect the product gas composition. The reactor was heated in an inert atmosphere (Ar, 500 mL min^{-}

^{1}) from an ambient temperature to an optimized isothermal operating temperature of 900°C at a ramp of 100 °C min^{-1}. The powder samples were reduced in a gas flow of 20 mL min^{-1} CH_4 (grade 4.5), diluted with 230 mL min^{-1} Ar flow. CO_2 splitting by reduced metal oxide samples was carried out in the presence of 4%vol of CO_2 (grade 4.5) with a flow of 10 mL min^{-1} diluted with a 240 mL min^{-1} Ar flow. For water splitting, steam vapor was generated at 368 K in a bubbler filled with DI water. An Ar flow of 30 mL min^{-1} passed through the bubbler to carry the steam vapours and was further diluted by an Ar flow of 220 mL min^{-1} before delivering the vapours into the reactor tube. The total gas flow during the reduction and oxidation step was kept constant at 250 mL min^{-1}.

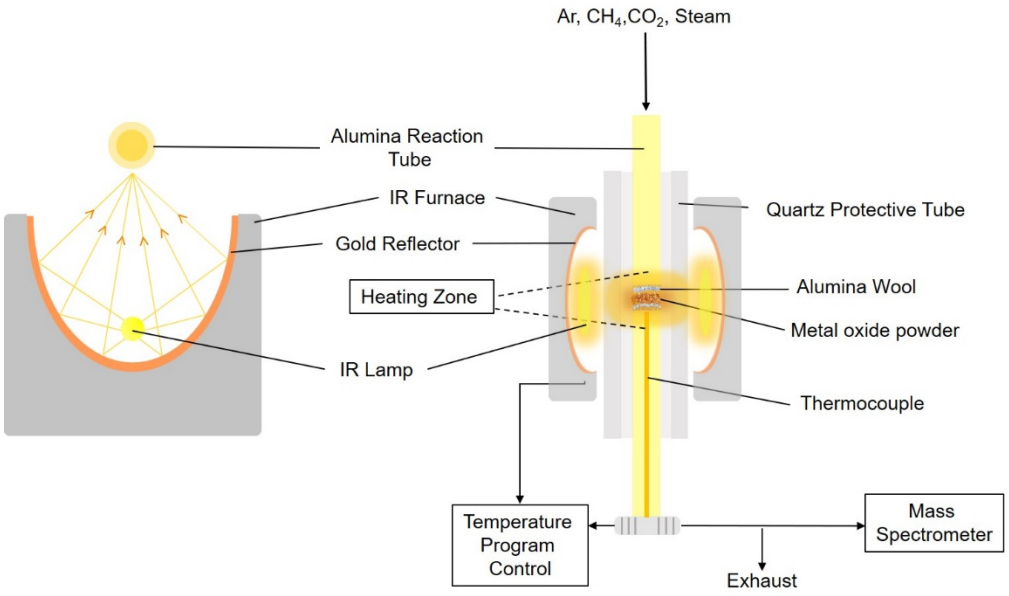

Figure 2.3. Schematic diagram indicating the tubular reactor set-up utilized for performing redox cycle experiments, mass-spectrometer used to analyze the reactant and product gases and the temperature program control.

Inert gas sweeping was done with argon at a flow rate of 500 mL min^{-1} before and after each reduction and oxidation step and repeated for each cycle. The sequence and duration of the gas flow during CO_2 and H_2O cycles was as follows:

MPO–CDS: Ar (5 min)/CH_4 (20 min)/Ar (5 min)/CO_2 (10 min)

MPO–WS: Ar (5 min)/CH_4 (20 min)/Ar (5 min)/ H_2O (10 min)

MPO–WS–CDS: Ar (5 min)/CH_4 (20 min)/Ar (5 min)/H_2O (7 min)/Ar (5 min)/CO_2 (7 min)

MPO–CDS–WS: Ar (5 min)/CH_4 (20 min)/Ar (5 min)/CO_2 (7 min)/Ar (5 min)/H_2O (7 min)

The redox performance of the nano-powders was tested over 10 preliminary cycles, followed by a stability test over 200 cycles. Changes in the structure and chemical nature of the oxide samples were studied after the 1st reduction, 10 cycles and 100 cycles during the CO_2 and H_2O splitting phases.

Chapter Three

$LaSrMnO_3$ Perovskites

Publications relevant to this chapter:

Asim Riaz, P. Kreider, F. Kremer, H. Tabassum, JS. Yeoh, W. Lipinski and A. Lowe, *Electrospun Manganese-Based Perovskites as Efficient Oxygen Exchange Redox Materials for Improved Solar Thermochemical CO_2 Splitting,* ACS Appl. Energy Mater. 2019, 2, 2494−2505.

Asim Riaz, Felipe Kermer, Suchinda Sattayaporn, Muhammad Umair Ali, Takuya Tsuzuki, Wojciech Lipinski, Adrian Lowe, *Structural re-arrangement in LSM perovskites for enhanced syngas production via solar thermochemical redox cycles.* ACS Catalysis, 2020, 10, 8263–8276.

3.1. Introduction

In this chapter, we investigate the reduction and oxidation behaviour of $La_xSr_{1-x}MnO_3$ (LSM, $x = 0…1$) nanoparticles during thermochemical CO_2 splitting cycles and chemical looping reforming of methane coupled to CO_2 and H_2O splitting reactions. Samples are synthesized *via* the electrospinning technique with compositional uniformity and morphological control.[243] Structural stability of these nano-powders is evaluated during the CO_2 splitting cycles at T_{red} = 1000–1400°C. Effect of temperature difference $\Delta T = T_{red} - T_{ox}$ from 0 K to 400 K is investigated on reduction extent of these materials. Effects of incorporation of soluble amount of La^{3+} in LSM on the theoretical oxygen exchange capacity of one mole of oxygen are studied. A detailed surface study of LSM samples is carried out and oxidation state of manganese ions is estimated with varying contents of La^{3+} present in the LSM lattice. Role of specific surface area of the LSM powders is investigated in terms of structural stability in the redox reactions.

Phase stability is a significant issue in perovskites for the partial oxidation of methane, as it determines the extent of solar fuel production efficiency. For example, Mn-based Perovskites show unstable behaviour and irreversibly transform to spinel and Ruddlesden-Popper structures during chemical reforming of methane.[230] However, such structural instability issues are not observed upon non-stoichiometric oxygen exchange during inert reduction of metal oxides.[244] It is still not understood how deteriorative such structural decomposition of Perovskite is towards the overall fuel production efficiencies and how structural stability can be achieved in perovskite during the cyclic redox reactions.

To address this research gap, the in-depth materials-based study is carried out in this work using $La_xSr_{1-x}MnO_3$ (LSM) perovskite. We investigate (1) the effect of La/Sr ratio on phase stability and fuel production efficiencies; (2) the effect of methane partial oxidation on the surface oxygen and cationic species of LSM and its relation with fuel

production efficiencies; (3) the effect of oxidation medium (CO_2 and H_2O) on the regeneration of Perovskites with detailed phase analysis, and (4) the morphological and chemical studies of LSM Perovskite before- and after redox cycles. $La_xSr_{1-x}MnO_3$ materials are synthesized using the electrospinning method. Their oxidation states, oxygen vacancies, phases, morphology and chemical composition before and after redox cycles are studied. Isothermal redox reactions are carried out at 900 °C for 10 consecutive cycles.

The findings of this chapter can inform studies of other families of perovskite oxides to overcome one of the key challenges for the efficient oxygen recovery during thermochemical redox cycles. In addition, it will enhance the in-depth investigation of the material's physiochemical properties before- and after the redox reactions before selection of a suitable oxygen carrier/catalyst.

3.2. Results

3.2.1 Characteristics of as-prepared LSM samples

SEM images of *as-spun* fibres reveal continuous fibre formation, shown in Figure 3.1. The addition of La with *x* varying from 0 to 1 changed the morphology of the fibres from continuous to branched. In addition, the diameter of the fibres increased with higher lanthanum content. This morphological change may explain the brittleness induced in *as-spun* LMO fibres.

The morphological investigations of as-prepared LSM perovskite powders revealed clusters of small particles in Sr-rich samples, while La-rich powders contain an ordered structure. As shown in Figures 3.2 a–c, increased amounts of La resulted in increased particle sizes. Figures 3.2 d–f show HR-TEM images of as-prepared LSM powders, also depicting the increase in particle size and lattice spacing by increasing La. Pure SMO has an average particle size of 115 ± 8 nm, which increased to 151 ± 18 nm with 50% addition of La, while pure LMO particles are the largest with an average size of 310 ± 25 nm. The

lattice spacing increased from 0.268 nm for pure SMO to 0.271 nm in LSM50 and 0.270 mm in pure LMO.

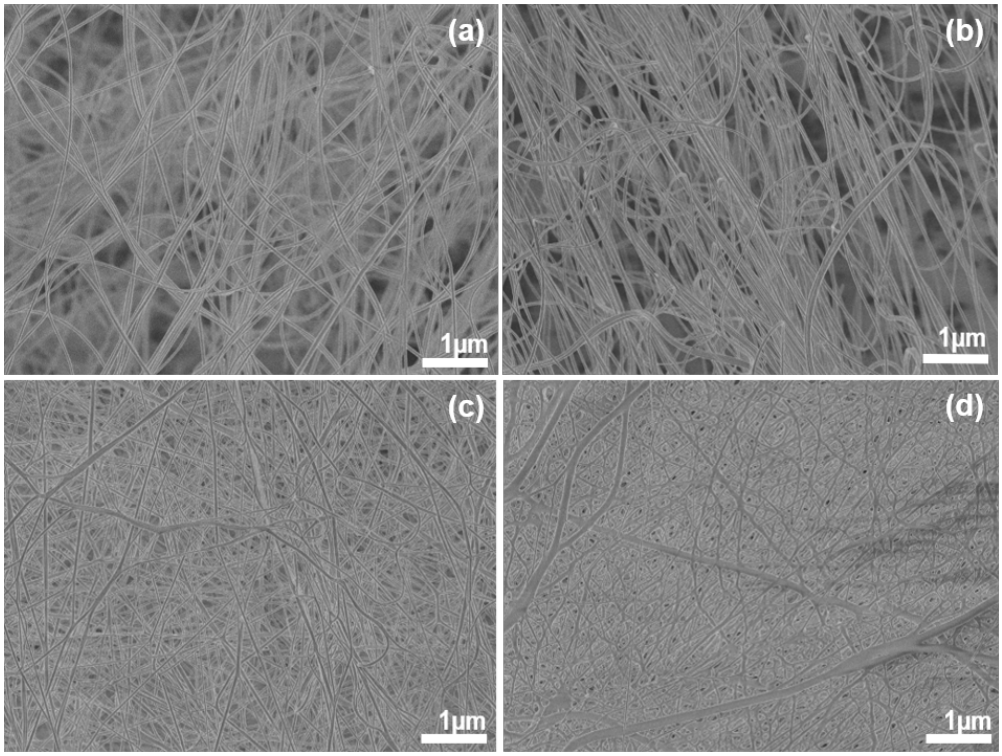

Figure 3.1. Scanning electron microscopy images of as-spun fibers of (a) SMO, (b) LSM25, (c) LSM50, and (d) LMO, representing change in the fibrous texture as a function of concentration of La^{3+} in LSM structure.

The XRD patterns of as-prepared samples are shown in Figure 3.3a. The peak profiles reveal the crystal symmetries of a typical perovskite structure, with some doublet peaks in samples with higher La^{3+} content, as reported elsewhere.[216,245,246] The splitting of XRD peaks in La rich LSM structures corresponds to the presence of cubic (Pm-3m (221)) phase due to the variable manganese valence. The space groups and basic lattice parameters of these four structures are presented in Table 3.1.

The addition of La in SMO induced a structural change. As the amount of La increases, the Mn-O (111) peak around 2θ 34° shifts to lower angles. High lanthanum contents induce strains in the Mn-O lattice which can be observed as diffraction peak splits in XRD patterns of LSM materials with 50% or more lanthanum (Figure 3.3b). For instance, the split of the Mn-O peak at around 34° is a result of diffraction from (110) and

(104) planes in pure LMO samples. Accordingly, the cell volume increased from 232 $Å^3$ for SMO to 346 $Å^3$ for LSM50. By the same token, inner lattice spacing increases with La addition (Figure 3.3c).

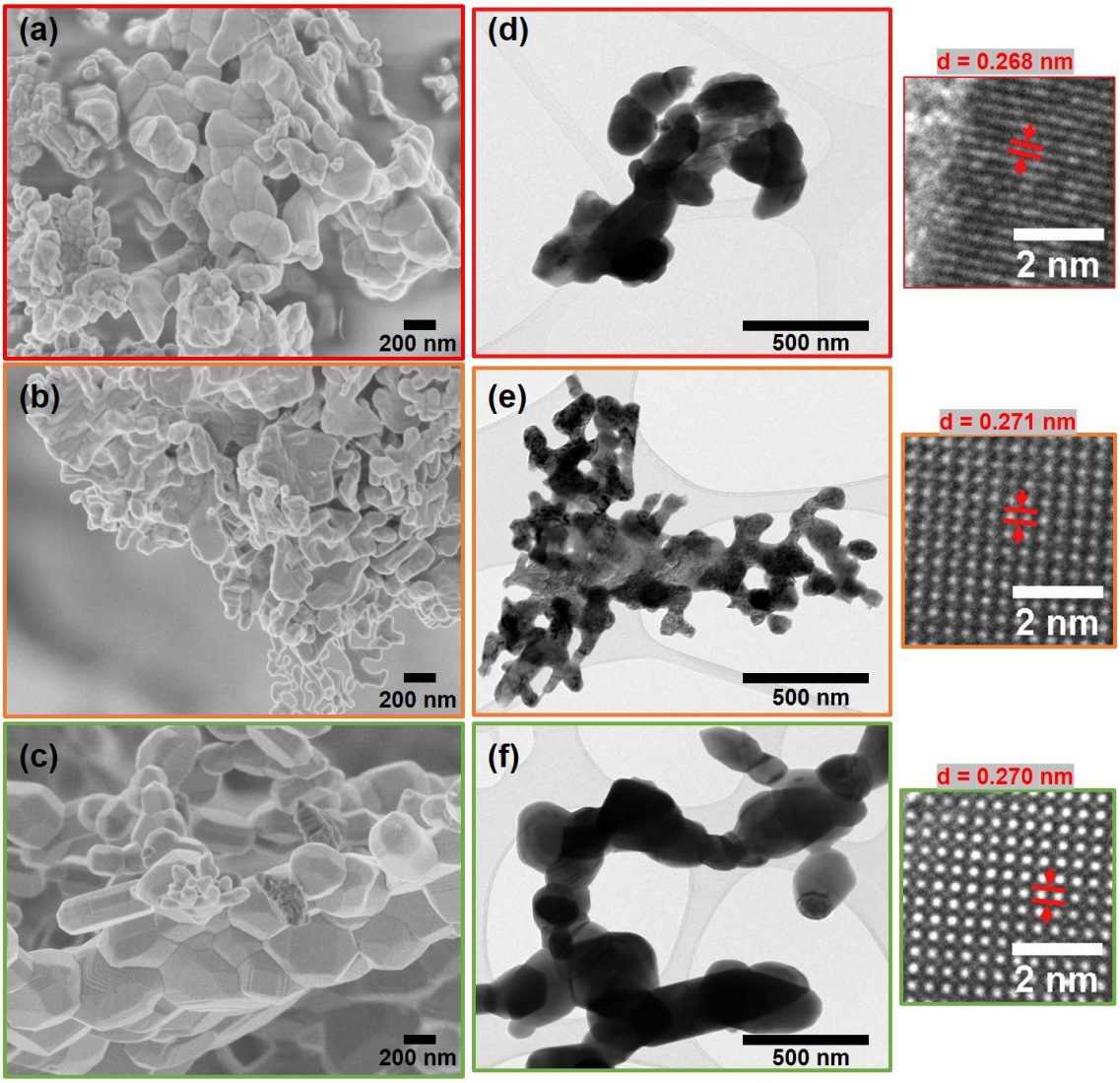

Figure 3.2. Morphological representation of as-prepared LSM Perovskite powders: FESEM micrographs of (a) SMO, (b) LSM50 and (c) LMO powders, TEM images of (d) SMO, (e) LSM50 and (f) LMO powders. HRTEM images show the inner planner spacing of respective SMO, LSM50 and LMO samples.

The Rietveld refinement on the XRD patterns (Table 3.2) revealed that the SMO powder contains 100% $SrMnO_3$ phase (COD # 96-152-9599), which decreased to13.8% with the addition of 25% La. On the other hand, 50% and 75% La addition result in 94.3% $La_{0.6}Sr_{0.4}MnO_3$ (COD # 96-153-3289) and 91.5% $La_{0.7}Sr_{0.3}MnO_3$ (COD # 96-152-1157)

phases, respectively. The remaining phase in LSM50 and LSM75 is $LaMnO_3$ (COD # 96-153-1527) phase. However, it can be inferred that Sr has a stronger tendency than La to form a tertiary oxide with Mn, while higher lanthanum content supports the development of $LaSrMnO_3$ structure.

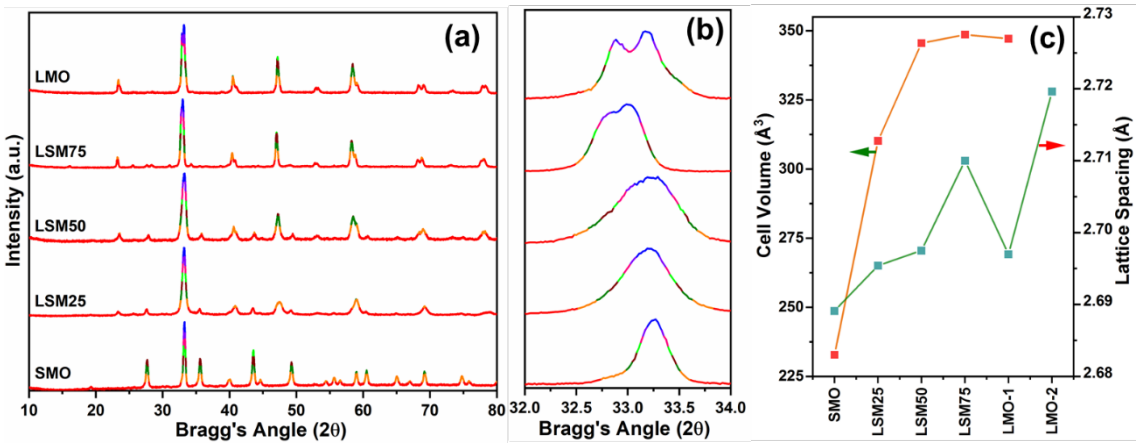

Figure 3.3. Structural and chemical analyses of as-prepared LSM Perovskites: (a) XRD patterns presenting the phase evolution with different La concentrations. (b) Shift and split of manganese oxide Bragg's angle peak with lanthanum incorporation from 0% to 100%. (c) Cell volume expansion and Bragg's angle peak shift in LSM structures due to large lanthanum cations.

Table 3.1. Basic lattice parameters and space groups of as-prepared LSM structures.

Material ID	Space group	Lattice Parameters (nm)		
		a	*b*	*c*
SMO	P63/mmc(194)	0.5443	0.5443	0.9070
LSM25	I4/mcm(140)	0.5442	0.5442	0.7766
LSM50	R-3c(167)	0.5505	0.5505	1.3354
LSM75	R-3c(167)	0.5492	0.5492	1.3333
LMO	R-3c(167)	0.5490	0.5490	1.3294

Elemental composition of the as-calcined samples is listed in Table 2.1. Figure 3.5a shows the elemental compositions determined from STEM-EDS spectra, where large La cations induced oxygen vacancies in La-rich LSM. The EDS elemental concentration data drift from the stoichiometric elemental calculations by only 9% ± 2. The STEM study revealed that Sr and Mn are homogenously distributed in SMO (Figure 3.4). However,

addition of La resulted in various Sr- and La- rich regions due to the formation of segregated phases, as discussed in the XRD analysis section of as-prepared LSM powders. As an example, Figure 3.5 d–g shows the elemental maps of as-prepared LSM25 powder, while Figure 3.5c shows the change in the La energy counts at different spots of the grey image shown in Figure 3.5b.

Table 3.2. Phases in pristine LSM powders, quantified by the Rietveld refinement method applied on XRD patterns.

	Phase (%)				
Sample ID	$SrMnO_3$	$La_{0.234}Sr_{0.76}Mn_{0.924}O_{2.79}$	$La_0.6Sr_{0.4}MnO3$	$La_{0.7}Sr_{0.3}MnO_3$	$LaMnO_3$
SMO	100	0	0	0	0
LSM25	13.8	86.2	0	0	0
LSM50	0	0	94.3	0	5.7
LSM75	0	0	0	91.5	8.5
LMO	0	0	0	0	100

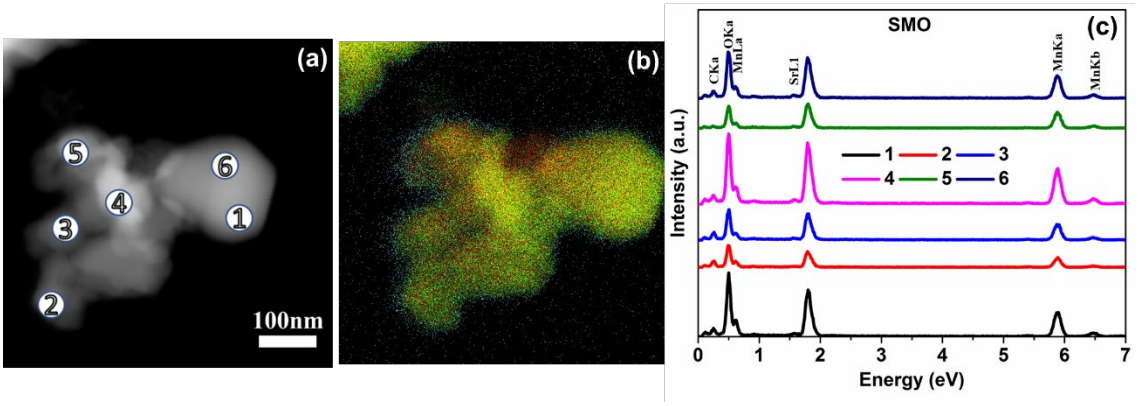

Figure 3.4. Chemical analysis of pristine SMO samples: (a) Greyscale and (b) colored overlay STEM-EDS map images of pristine SMO samples showing the distribution of Sr (red) and Mn (blue). (c) STEM-EDS spectra acquired on pristine SMO samples.

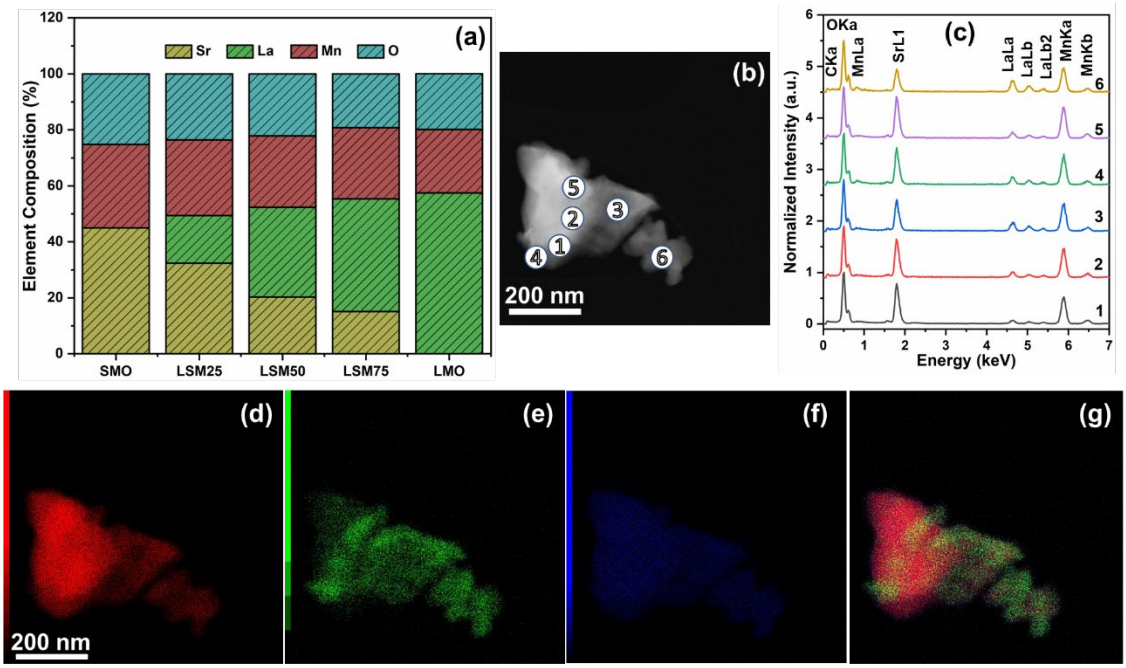

Figure 3.5. Structural and chemical analyses of as-prepared LSM Perovskites: (a) Effect of lanthanum addition on elemental distribution in LSM Perovskites. (b) Grey scale STEM image of pristine LSM25 sample corresponding to (c) EDS spectra measured at 6 different points. STEM–EDS color maps of (d) Sr, (e) La, (f) Mn and (g) overlay of pristine LSM25 powder samples.

XPS measurements were employed to investigate the oxidation states of the *as-prepared* LSM samples. The XPS results of as-synthesized LSM powders are shown in Figures 3.6. Three types of oxygen species were observed, referred to as OI, OII and OIII, which correspond to lattice oxygen, adsorbed oxygen O_2^{2-}/O^- and bulk oxygen, respectively, as shown in Figure 3.6a. A lattice peak is ascribed to the metal oxygen bond, which in the case of LSM is Mn-O. The O 1s peak of all LSM structures lies at around 529.3 eV with no significant energy shift with the amount of La (Figure 3.6a). The neighbouring shoulder at around 513.15 eV represents the presence of oxygen species due to possible surface oxidation, advantageous contaminants (CO_2, moisture etc.), SrO or the incomplete pyrolysis of PVP precursor material.[247]

The Mn 2p peak has significantly split spin-orbit components 2p 1/2 (~ 653 eV) and 2p 3/2 (~ 642 eV) as shown in Figure 3.6b. The energy difference of the split (ΔBE) is

11.58 eV in SMO and decreases to 11.37 eV in LMO. This occurs due to the shift of Mn2p 1/2 and Mn2p 3/2 peaks towards lower binding energies, representing a change in Mn oxidation states as a function of La concentration. The variation in the ratio between the intensities of Mn 2p 3/2 and 2p 1/2 peaks also indicates a change in the electronic configuration of Mn. Generally, Sr-rich LSM shows a higher 2p 3/2-to-2p 1/2 ratio than La-rich LSM powders.

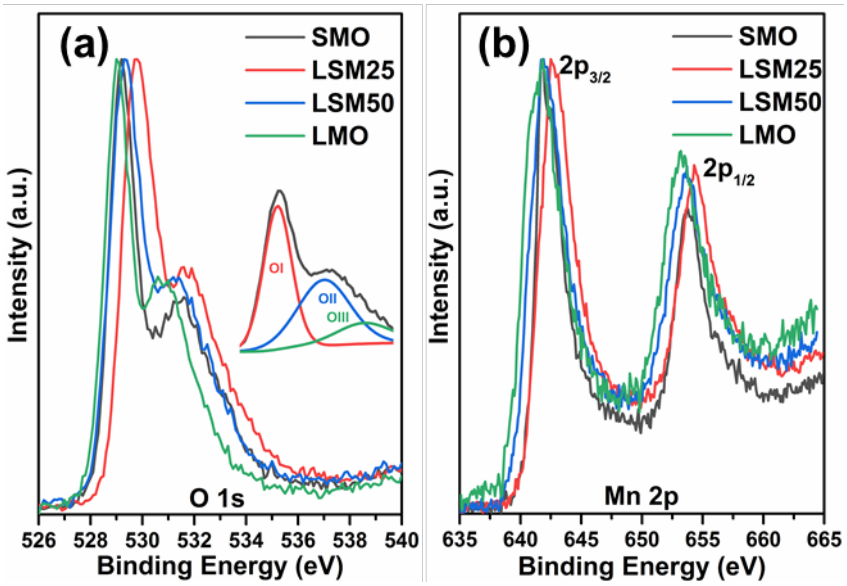

Figure 3.6. Surface and bulk chemical analysis of pristine LSM structures with variable La concentrations: XPS spectra representing (a) oxygen; O 1s, (b) manganese; Mn 2p, species. Shifts in binding energies and change in peak intensity describes the change in the chemical state of the LSM structure.

The increase in intensity of the 2p 1/2 peak is indicative of smaller cationic charge on the Mn in La-rich LSM structures.[244] The Mn 2p 3/2 peak at binding energies of > 642 eV represents the +4-oxidation state of Mn. Nevertheless, the exact oxidation state can be calculated from the splits in the Mn 3S peak.[248] The split in Mn 3s peaks increases from 3.9 eV to 5.32 eV with La addition and reaches a maximum in LSM75. The ionic charge on Mn is +4, which is seen in SMO and decreases to +3.7 in LMO.

XANES analysis provides useful information about the oxidation states and oxygen vacancies in LSM samples. Mn K-edge XANES spectra are presented in Figure 3.7a. The

Mn K-edge shifts monotonically to lower photon energies as a function of La concentration. The edge energy of SMO is 6555.3 eV which decreases to 6553.4 eV in LMO. Mn oxidation states can be calculated from the Mn K-edge spectra and by comparing to the Mn K-edge spectra of MnO, MnO_2 and Mn_2O_3 standard samples. As shown in Figure 3.7b, addition of La lowers the oxidation state from +4.8 for SMO to +4.3 for LMO. The charge shift on Mn greatly affects the oxygen vacancies present in the LSM structure with the higher Mn oxidation state representing a higher number of oxygen vacancies. The XPS and XANES studies indicate that oxygen vacancies can be controlled in the LSM structures by changing La concentration.

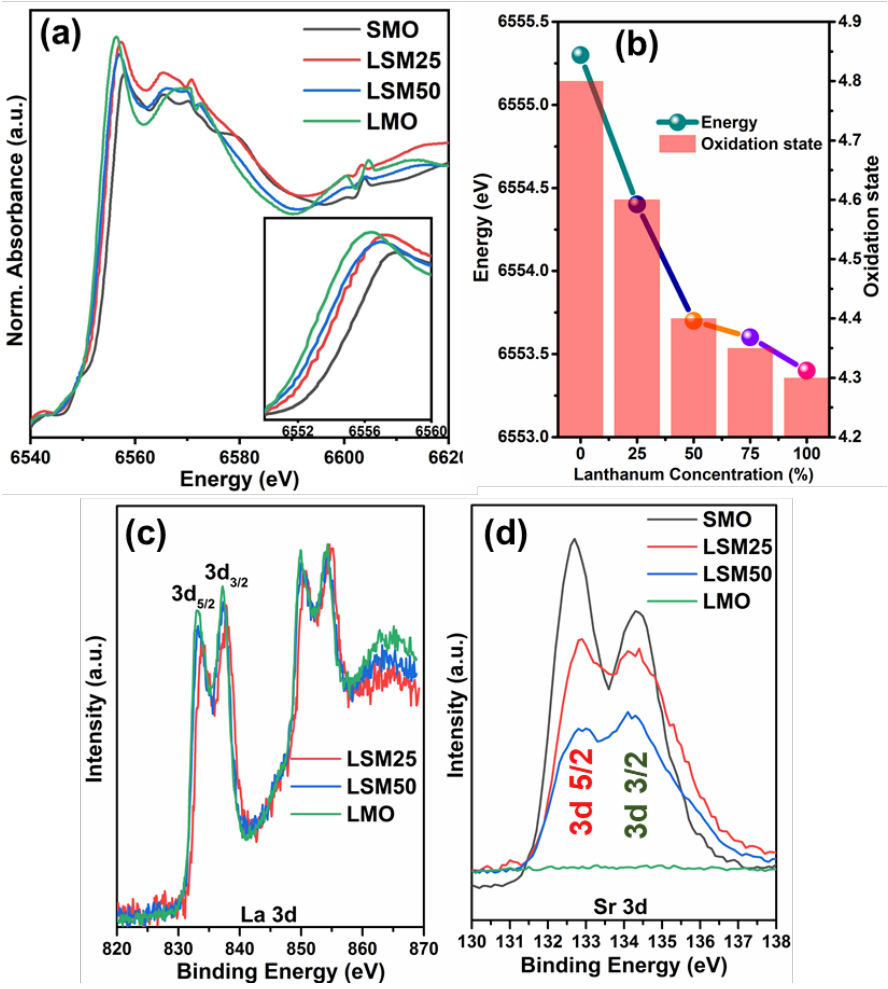

Figure 3.7. Surface and bulk chemical analysis of pristine LSM structures with variable La concentrations: (a) Mn K-edge XANES spectra of pristine LSM powders showing variation in the photon energies with lanthanum addition. (b) Photon energy shift and change in oxidation state as a function of lanthanum concentration. XPS spectra

representing (c) lanthanum; La 3d and (d) strontium; Sr 3d, species on pristine LSM powder surfaces. Shifts in binding energies and change in peak intensity describes the change in the chemical state of the LSM structure.

The energy difference in satellite (S) and main (M) XPS peaks of La $3d_{5/2}$ and La $3d_{3/2}$ (ΔBE) with La addition informs the change in the chemical state of surface La species. As shown in Figure 3.7c, a higher La content shifts the La 3d 5/2 peak to a higher binding energy; the ΔBE increased form 3.67 eV in LSM25 to 4.22 eV in LSM50. This indicates that the chemical bonds around La ions are stronger in La-rich samples, which would contribute to inhibiting the structural deterioration of LSM samples by methane and to facilitating a non-stoichiometric reduction, which will be discussed later. Figure 3.7d shows an orbital split of the Sr 3d peak into 3d 3/2 and 3d 5/2 peaks at around 134.4 eV and 132.5 eV, respectively. It is evident that the shape of this split is highly affected by La concentration. The change in the peak shape is attributed to the re-arrangement of Sr electronic configuration instead of a change in the oxidation state of Sr.[249]

3.2.2 Thermochemical performance 1: CO_2 splitting redox cycles

The CDS performance of the LMS powders was evaluated based on the relative mass change during multiple TC–CDS cycles for the three redox temperature schemes of Figure 3.8. The heating and cooling rate were set to 20 K min^{-1} with a holding time at each step of 10 min. The gas flow rate was kept varied from 50-100 mL min^{-1} for both N_2 (reduction) and CO_2/air (oxidation), to tune for better CO_2 splitting performance. After observing slow oxidation rates in low CO_2 flow rates, 100 mL min^{-1} flow rates are selected for the further experiments. For each combination of oxidation medium and temperature setting, experiments included baseline runs with a blank alumina crucible followed by actual thermochemical cycle runs with samples present in the sample holder.

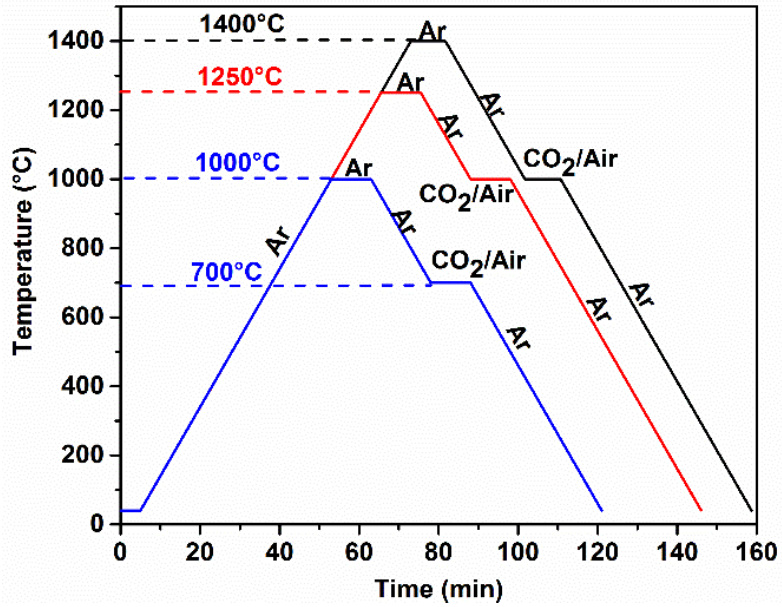

Figure 3.8. Temperature schemes designed for thermochemical cycling experiments with air and CO_2 as oxidizing media.

Increasing the reduction temperature from 1000°C to 1400°C resulted in an increase of the sample mass difference ($\Delta\%m$) between the oxidation and reduction steps, as shown in Figures 3.9a–c. The onset of reduction for SMO is observed at ~1000°C. The addition of larger lanthanum cations (La^{3+}) facilitates the oxygen exchange by creating lattice defects, which in result lowers the energy required to reduce the LSMO perovskites and lowers the reduction onset temperature to ~800°C, 765°C and 700°C for LSM25, LSM50 and LMO, respectively. Irreversible reduction of manganese in Mn_3O_4 from Mn^{3+} to Mn^{4+} is observed in Figure 3.10, which can be attributed to its inactivity in CO_2 splitting and possible diffusion of oxygen atoms into the structure or complete reduction of these oxides with structural deterioration.[216] However, the perovskite variants of manganates enable reversible redox capability within the structure.

The average mass difference ($\Delta\%m$) between the mass of LSM in oxidized state (m_{ox}) and reduced state (m_{red}) during TC–CDS cycles, is shown in Figure 3.9d. To remove the possible influence of organic impurities and possible presence of C from PVP, the results of the first cycle are excluded from the evaluation of initial material performance. LMO

showed the highest Δ%*m* of 0.56% at T_{red} = 1000°C, which slightly decreased at T_{red} to 1250°C and 1400°C by 0.12% and 0.05%, respectively. LSM50 demonstrated a higher Δ*m* (%) than other LSM compositions at a T_{red} = 1000°C. However, increasing the La^{3+} content resulted in a decrease in Δ*m* (%) at higher reduction temperatures compared to SMO which shows an increase of 2.25% in mass difference at T_{red} = 1400°C.

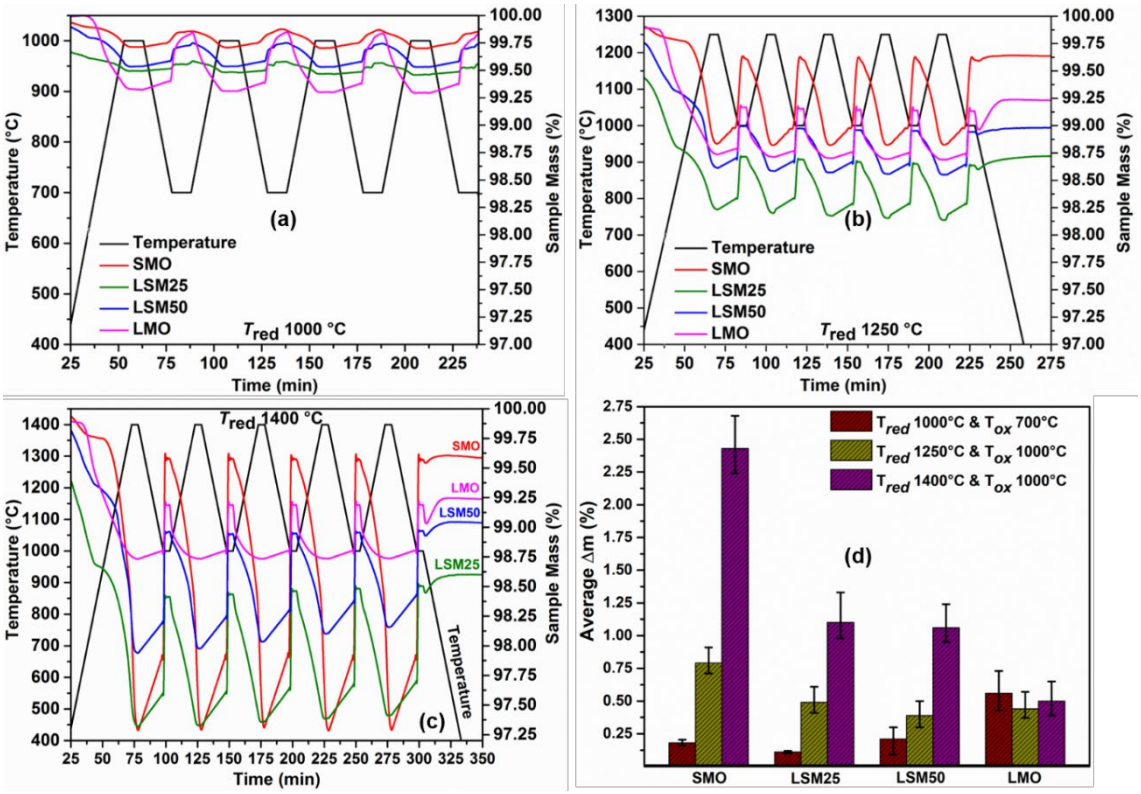

Figure 3.9. Temperature–time programs and mass loss(%) during thermochemical cycling for different reduction temperatures: (a–c) sample mass (%) change during TC–CDS cycles of SMO, LSM25, LSM50 and LMO in three different temperature schemes with (a) T_{red} = 1000°C and T_{ox} = 700°C (b) T_{red} = 1250°C and T_{ox} = 1000°C and (c) T_{red} = 1400°C and T_{ox} = 1000°C; (d) Average change in mass (%) during the redox reactions at three different temperature schemes, under the constant flow of CO_2 as the oxidizing medium.

Manganese ions in LSM structures play a key role in CO production as they act as a vacancy carrier and oxygen exchange medium. High La^{3+} amounts decrease the concentration of Mn^{4+} because the resulting stoichiometric balance of cations lowers the amount of manganese precursor due to the higher molar mass of lanthanum compared to

strontium. As a consequence, the cationic ratio B:A (Mn:Sr^{2+}/La^{3+}) decreases with increasing La^{3+} content from $x = 0$ to $x = 1$, as shown in Table 3.3. Hence, a decrease in the cationic ratio clearly relates to the lower-end performance of La^{3+} rich LSM compounds. In addition, high Sr^{2+} content creates a hole at Mn^{4+} sites which favours oxygen exchange in the LSM structure, whereas La^{3+} promotes oxygen deficiency in the LSM crystals.[95]

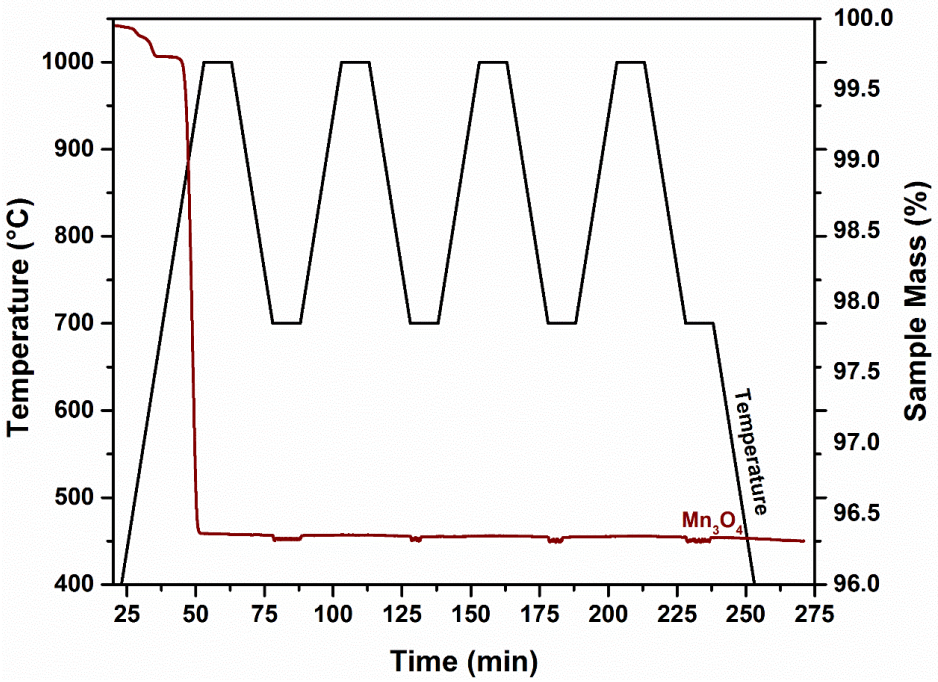

Figure 3.10. Weight loss (%) of Mn_3O_4 undergoing thermochemical cycling with T_{red} 1000°C and T_{ox} 700°C, over 4 cycles, representing irreversible reduction–oxidation of Mn_3O_4 with 3.5% of mass loss after the first reduction.

TGA data of the cycles were utilized to calculate the O_2 evolution rates per LSM mass during TC–CDS cycling, as shown in Figure 3.11a. A typical descending trend is observed after the first cycle, suggesting possible incomplete recovery of the oxidative state due to depletion of lattice oxygen ions after reduction. Possible densification of powder samples at elevated temperature also decreases the solid–gas transfer during cycling, which hinders re-oxidation and impacts the kinetics of the redox reactions over the number of cycles.[216] LMO powders demonstrated a high CO production rate of over

110 µmol min^{-1} g^{-1} at 700°C, which increased up to 200 µmol $min^{-1}g^{-1}$ at T_{ox} = 1000°C. However, SMO showed high rates of up to 400 µmol min^{-1} g^{-1} at T_{red} = 1400°C.

Table 3.3. Comparison of cationic ratios and oxygen content wt% (normalized from EDS data) in LSM samples before and after cycles with calculated stoichiometric values, with T-distribution of t95 (i.e. 95% uncertainty).

Sample ID	Process														
	Calculated			As-prepared			Cycled at T_{red} of								
							1000°C			1250°C			1400°C		
	A1/A2	B:A	O_2	A1/A2	B:A	O_2	A1/A2	B:A	O_2	A1/A2	B:A	O_2	A1/A2	B:A	O_2
SMO	-	0.63	25.19	-	0.66	21.7 ±3.6	-	0.71	23.4 ±3.5	-	0.65	25.4 ±3.5	-	0.62	31.2 ±7.5
LSM25	0.52	0.58	23.6	0.48	0.47	26.35 ±1.8	0.58	0.48	20.2 ±4.1	0.53	0.51	33.5 ±3.9	0.56	0.54	26.1 ±6.7
LSM50	1.58	0.48	22.2	1.22	0.47	17.9 ±2.3	1.29	0.46	24.2 ±5.7	1.34	0.42	20.5 ±3.8	1.32	0.46	29.7 ±1.1
LMO	-	0.4	19.82	-	0.32	17.2 ±2.3	-	0.36	24.1 ±6.1	-	0.49	25.7 ±4.8	-	0.31	20.2 ±3.7

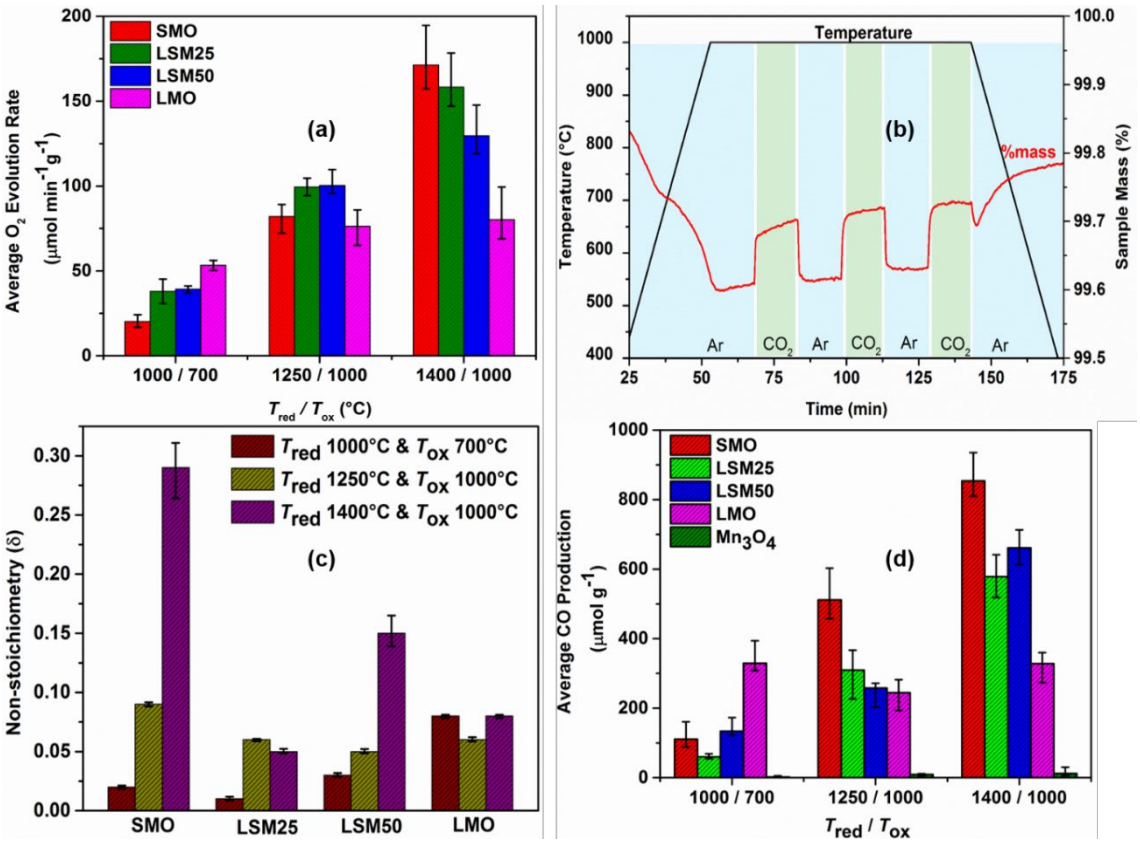

Figure 3.11. Graphical representation of the performance of LSM samples during TC–CDS cycles in terms of: (a) O_2 production rate per gram of LSM during multiple cycles at T_{red} = 1000°C and T_{ox} = 700°C, T_{red} = 1250°C and T_{ox} = 1000°C and T_{red} = 1400°C and T_{ox} = 1000°C; (b) sample mass (%) as a function of temperature during isothermal TC–CDS cycles carried out at 1000°C; (c) non-stoichiometry (δ) of LSM samples as a

function of different reduction-oxidation temperatures; and (d) Average CO yield of oxide samples during TC–CDS cycles.

Isothermal CDS curves for SMO are shown in Figure 3.11b. Interestingly, during the cooling step, the sample mass decreased suddenly after switching the gas from CO_2 to Ar. Subsequently, the sample mass increased to 99.79% of its initial value when the temperature was decreased to 950°C, which confirmed the reoxidation of reduced species during the decrease in temperature. A higher CO yield is observed in La^{3+}-rich LSM perovskites at lower reduction and oxidation temperatures, e.g. for isothermal CDS cycles the average CO of 223.94 μmol g^{-1} is produced by LMO samples, whereas 33.18 μmol g^{-1} of CO is produced with the addition of only 25% of La^{3+} in the LSM lattice. However, ~8–10% more oxygen is recovered during air cycling as compared to TC–CDS.

The amounts of substance for oxygen and CO evolved during reduction and air oxidation are calculated by the Reactions 3.1 and 3.2, respectively.[83]

$$n_{O_2} = \frac{\Delta m_{loss}}{2M_{O_2}M_{LSM}} \tag{3.1}$$

$$n_{CO} = \frac{\Delta m_{gain}}{2M_{O}M_{LSM}} \tag{3.2}$$

where Δm is the difference between the mass of oxidized (m_{ox}) and reduced (m_{red}) samples, and M_O is the molar mass of atomic oxygen. m_{red} was measured when reduction reached completion. Measurements of m_{ox} and m_{red} in equilibrium states allows for reduction of the drift effect.[83]

The oxygen exchange capacity of powder samples is calculated by Reaction 3.3.[100]

$$\delta = \frac{\Delta m \times M_{ABO_3}}{m_{ox} \times M_O} \tag{3.3}$$

where M_{ABO3} is the molar mass of the perovskite in an oxidized state. Non-stoichiometric behaviour of selected LSM samples at different reduction temperatures is

shown in Figure 3.11c. Deviation from average non-stoichiometry reaches a maximum for T_{red} = 1400°C. The results clearly indicate the high oxygen exchange capacity of SMO at T_{red} = 1400°C, which decreases with increasing the La^{3+} concentration from 0 to 1 in the LSM structure. This observation agrees with results of other studies,[100] in which an increase in fuel production by doping the A-site of perovskites with smaller ions such as yttrium was observed.

Figure 3.11d shows the average CO yield over multiple TC–CDS cycles. The reduction at T_{red} > 1000°C and re-oxidation at $T_{ox} \geq$ 700°C is thermodynamically favourable for high reduction extents, efficient oxygen recovery and CO production. This typical behaviour suggests a strong relation between reduction and oxidation temperatures with the CDS performance. However, hindrance in the solid-gas transfer due to the possible sintering of nanoparticles may result in a non-linear variation in CDS performance. The highest calculated CO of 921.37 μmol g^{-1} was recorded during the air oxidation of SMO nano powders at T_{red} = 1400°C and T_{ox} = 1000°C. However, LMO demonstrated the highest yields of around 364.25 μmol g^{-1} at T_{red} = 1000°C and T_{ox} = 700°C.

Depending on the capability of the material to react with CO_2, stoichiometric moles of CO are also determined from TGA data. An increase in CO yield is observed for LSM samples with x = 0, 0.25 and 0.50, at higher T_{red} and T_{ox}. At T_{red} = 1400°C and T_{ox} = 1000°C, SMO showed an average of 854.20 μmol g^{-1}, followed by LSM25 and LSM50 with 909 μmol g^{-1} and 661 μmol g^{-1} respectively. LMO showed the highest fuel production of 329 μmol g^{-1} at T_{red} = 1000°C and T_{ox} = 700°C. Table 3.4 represents the average CO and O_2 evolved during CDS cycles on various perovskites variant in this study and reported elsewhere. Clearly, the electrospun LSM nano-powders demonstrate a excellent redox capability for a range of reduction and oxidation temperatures during CDS cycling, as compared to ferrite and cobaltate-based perovskites.

Table 3.4. Performance comparison of different Perovskite variants used in this chapter and reported elsewhere, in terms of average CO and O_2 evolved determined from the TGA data obtained during TC–CDS cycling.

Material	T_{red} (°C)	O_2 evolved (μmol g^{-1})	T_{ox} (°C)	CO evolved (μmol g^{-1})	Reference
SMO	1400	532.52 ± 36.5	1000	854.2 ± 66.4	This work
SMO	1250	301.25 ± 24.8	1000	511.52 ± 41.2	This work
LSM25	1400	516.24 ± 19.55	1000	786.32 ± 41.6	This work
LSM50	1000	55.25 ± 3.55	1000	76.37 ± 15.2	This work
LSM50	1000	105.35 ± 6.9	700	134.65 ± 17.2	This work
LSM50	1400	512.55 ± 43.1	1000	701.91 ± 48.2	This work
LMO	1000	242.16 ± 36.2	700	329.32 ± 31.2	This work
LMO	1000	149.35 ± 11.2	1000	223.94 ± 19.5	This work
$Y_{0.5}Sr_{0.5}MnO_3$	1400	483	900	757	[99]
$La_{0.5}Ca_{0.5}MnO_3$	1400	315	1100	525	[99]
$La_{0.5}Sr_{0.5}MnO_3$	1400	201	1100	325	[250]
$La_{0.6}Sr_{0.4}Al_{0.6}Mn_{0.4}O_3$	1350	120	1000	247	[85]
$LaSrCoO_4$	1300	268	800	161	[251]
$La_{0.6}Sr_{0.4}MnO_3$	1350	348.8	1000	469.1	[234]
$La_{0.6}Sr_{0.4}Mn_{0.4}Fe_{0.6}O_3$	1350	333.2	1000	277.2	[234]
$La_{0.6}Sr_{0.4}FeO_3$	1350	427.3	1000	250.6	[234]
$La_{0.6}Sr_{0.4}FeO_3$	1200	337	1050	53	[233]
$Y_{0.5}Sr_{0.5}MnO_3$	1400	551	1050	112	[233]
$La_{0.5}Sr_{0.5}Mn_{0.5}Co_{0.5}O_3$	1300	538	1050	152	[233]

3.2.3 Thermochemical performance 2: MPO–CDS

Figure 3.12 shows thermochemical redox performance of LSM perovskites for oxidation-reduction cycling. All LSM powders demonstrate stable syngas production rates during reduction and oxidation reactions. Interestingly, all samples showed high CO rates peaks for the first reduction and oxidation cycle, which may be due to oxidation of the carbonaceous products adsorbed/absorbed in the powder sample. During methane partial oxidation (MPO) reactions, the syngas production rates of SMO were ~0.42 mmol g^{-1} min^{-1} H_2 and ~0.30 mmol g^{-1} min^{-1} CO (Figure 3.12a). La addition enhanced the production rates and a maximum of 0.60 mmol g^{-1} min^{-1} H_2 and 0.25 mmol g^{-1} min^{-1} was achieved with 50% La addition (Figure 3.12b). Further increases in La to 75% lowers the production rates and only 0.056 mmol g^{-1} min^{-1} H_2 and 0.023 mmol g^{-1} min^{-1} CO were

achieved. However, 100% substitution with La, LMO, produces H_2 and CO with a higher rate of 0.31 mmol g^{-1} min^{-1} and 0.21 mmol g^{-1} min^{-1}, respectively, compared to LSM75 (Figure 3.12c). The oxidation recovery in terms of CO production rates during CO_2 splitting (CDS) reaction also increased with La addition from 0.36 mmol g^{-1} min^{-1} for SMO to 0.84 mmol g^{-1} min^{-1} for LSM50.

TGA–DTA analysis is performed to replicate the MPO–CDS redox cycles in terms of mass change (Figure 3.12d). LSM25 showed the highest mass change of up to 11%, followed by SMO (9.5%) then LSM50 with 4.5%. LSM75 and LMO show only negligible mass changes. Structural rearrangement in LSM materials during redox cycles results in larger amounts of oxygen release when compared to non-stoichiometric oxygen exchange in La-rich LSM materials: which results in greater mass changes in Sr-rich LSM materials when compared to that of La-rich LSM.

Syngas production yields are calculated by taking the average of the H_2 and CO amounts produced during reduction and oxidation reactions of 10 consecutive cycles, as shown in Figure 3.12e. The syngas yield is the highest for LSM50 with an average value of 8.23 mmol g^{-1} H_2 and 3.61 mmol g^{-1} CO, followed by LSM25 with H_2 and CO yields of 7.07 mmol g^{-1} and 3.72 mmol g^{-1}, respectively. LMO produced the lowest; 3.33 mmol g^{-1} H_2 and 2.12 mmol g^{-1} CO.

Addition of La greatly influenced the reforming reaction in terms of H_2/CO ratios and CO selectivity; the H_2/CO ratio is increased from 1.18 for SMO to 2.36 for LSM50 (Figure 3.12f). CO selectivity increases with La addition and is highest (c.a. 91%) for LSM50 followed by LSM25, LMO and SMO. The high oxidation performance of LSM25 is the highest CO yield of 2.42 mmol g^{-1}, followed by LSM50 with 1.80 mmol g^{-1} of CO, during CO_2 splitting reaction.

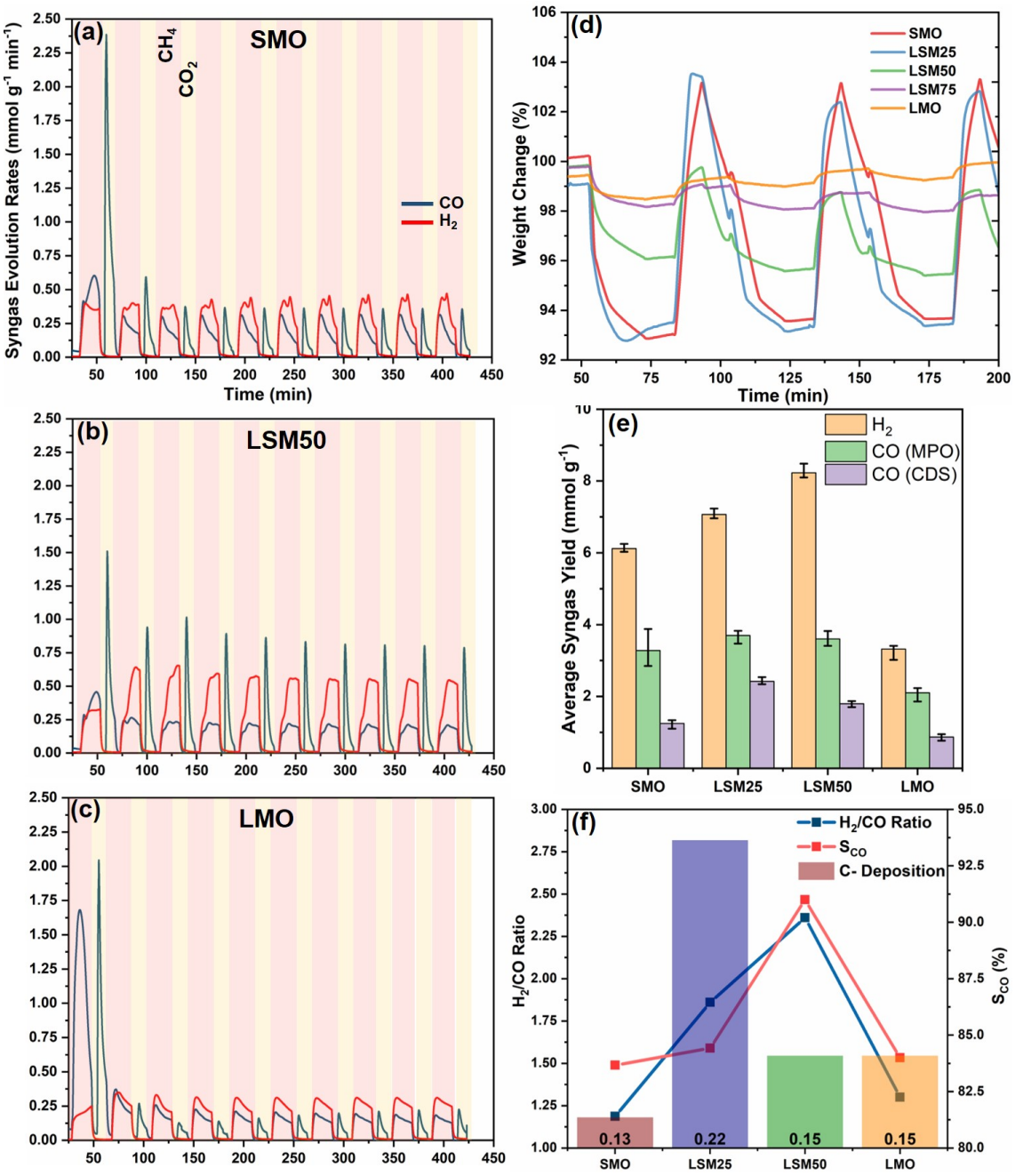

Figure 3.12. Thermochemical redox performance of LSM perovskites for MPO–CDS cycling: Syngas production rates by (a) SMO, (b) LSM50 and (c) LMO samples. (d) TGA–DTA analysis of LSM perovskites for MPO–CDS cycles in terms of mass change during redox reactions. (e) Average syngas yield in reduction and oxidation reactions during MPO–CDS cycles. (f) Carbon deposition, CO selectivity and H_2/CO ratios presented as a function of lanthanum concentration. MPO reaction rates data is utilized to calculate the mmol amounts of deposited carbon and H_2/CO ratios. Both reduction and oxidation reaction rates data are utilized to calculate CO selectivity.

The role of carbon deposition on the CO yield is studied to estimate the actual oxygen recovery in the LSM structures. Moles of calculated carbon are highest in LSM25, at

around 0.22 mmol, and lowest (0.13 mmol) in SMO. Despite the higher amount of deposited carbon, LSM25 can be considered as the best LSM Perovskite, where efficient carbon oxidation results in considerable CO and H_2 yields without affecting the H_2/CO ratio of 1.95.

3.2.4 Thermochemical performance 3: MPO–WS

Water splitting (WS) cycles were also performed to study the oxidation behaviour of the LSM structures with different La concentrations. In addition, the effect of La on H_2 purity and syngas yield were also studied. Syngas production rates from SMO samples are highest with a maximum value of 4.28 mmol g^{-1} min^{-1} H_2 and 1.16 mmol g^{-1} min^{-1} CO (Figure 3.13a). As shown in Figure 3.13b, LSM25 is the only LSM system with high H_2 and CO rates of 3.13 mmol g^{-1} min^{-1} and 0.85 mmol g^{-1} min^{-1}, respectively, while LSM50, LSM75 and LMO have negligible production rates. The results indicate that the oxide species that are formed after reduction reactions are incompatible with steam to cause the re-oxidation reaction. The reasons will be discussed in detail in the following sections around the structural study of LSM samples after redox cycles.

The syngas yields for MPO–WS cycles are estimated in the same manner as for MOP–CDS cycles and are shown in Figure 3.13e. H_2 and CO yields are highest for SMO (32.6 mmol g^{-1} and 11.48 mmol g^{-1} respectively). Considering the H_2/CO ratios and CO selectivity, SMO appears to be the best among LSM samples. Nonetheless, LSM25 also promoted considerable CO_2 production with a maximum rate of 0.21 mmol g^{-1} min^{-1} (Figure 3.13c). Despite this, the H_2/CO ratios for SMO and LSM25 are greater than 2, which indicates the formation of solid carbon (resulted from methane cracking) in addition to the H_2 and CO products during the methane partial oxidation reaction. However, LSM25 produced the H_2 yields of 12.41 mmol g^{-1} (Figure 3.13e). The purity of H_2 produced with LSM25 is also higher than that with SMO, where only 9.1% of CO is observed during the WS reaction, as shown in Figure 3.13f.

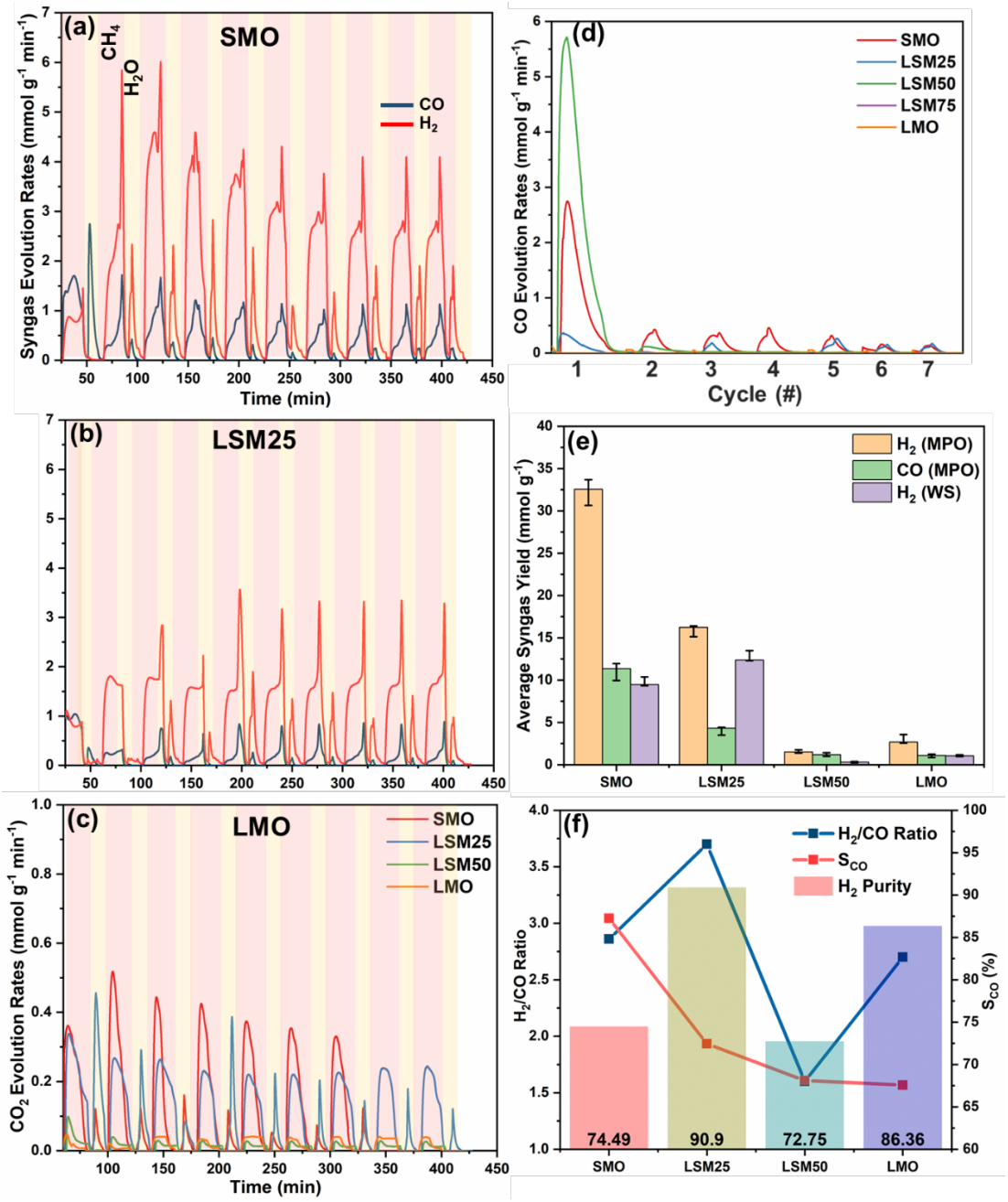

Figure 3.13. Thermochemical redox performance of LSM samples during MPO–WS cycles: Syngas production rates from (a) SMO, (b) LSM25, and (c) rates of CO_2 produced by LSM materials, during reduction and oxidation reaction of MPO–WS cycles. (d) CO evolution rates during WS reaction by LSM powders with different lanthanum concentrations. (e) Average syngas yields from LSM powders during redox cycles. (f) H_2/CO ratios, CO selectivity and H_2 purity achieved by different LSM powders. H_2 purity is calculated by the CO and H_2 rates data acquired during WS reaction.

The purity of H_2 produced from LSM25 is also higher than that from SMO, where only 9.1% of CO is observed during the WS reaction with LSM25 (Figure 3.13f).

However, high production rates of CO are observed with SMO sample (Figure 3.13d), resulting is only 74.54% pure H_2. Overall, LSM25 shows controlled methane partial oxidation with lower CO_2 rate, while producing high H_2 yields and purity.

3.2.5 LSM perovskites after cycling: Inert reduction

Figure 3.14a–d shows the TEM images of SMO, LSM25, LSM50 and LMO powders after CDS cycling at T_{red} = 1400°C. SMO underwent distinct restructuring during thermochemical carbon dioxide splitting (TC–CDS), resulting an increase in the particle size from 18.12 ± 6.1 nm to 256.12 ± 25 nm with an 89% decrease in specific surface area. However, SMO still had the highest pore volume of 0.16 cm^3g^{-1} (Table 3.5) among all LSM powders. This high pore volume increases the surface available to the redox reactions, which contributes to enhanced oxygen transport during CDS cycling.

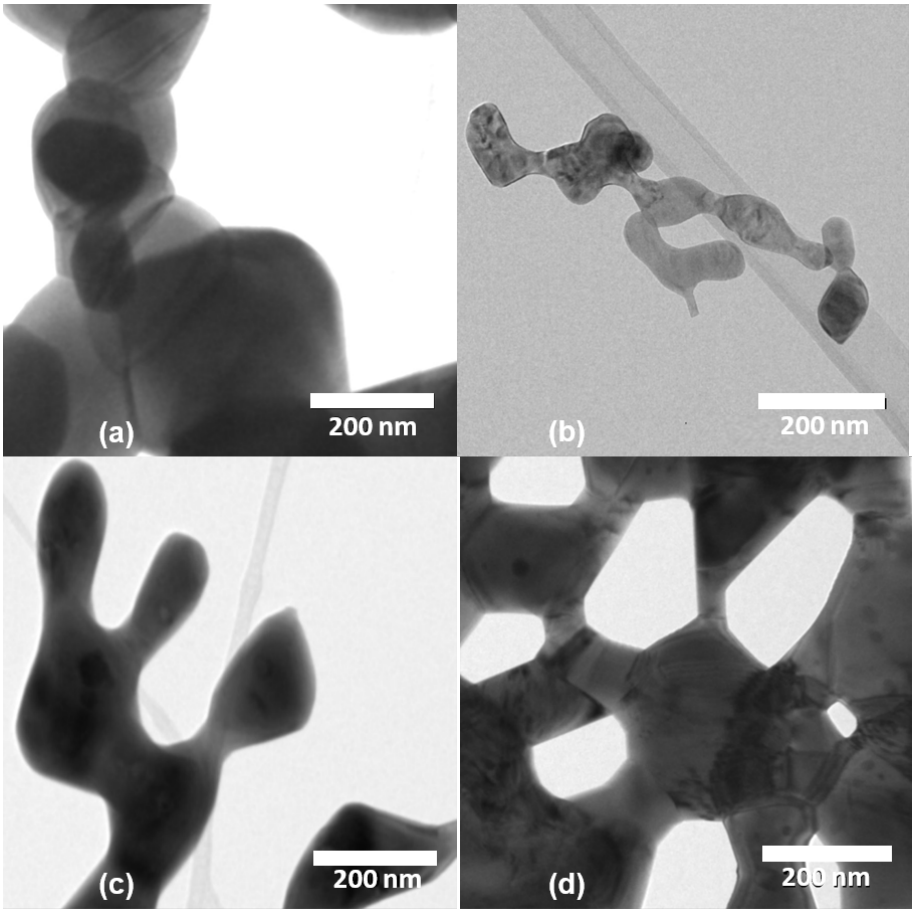

Figure 3.14. Transmission electron microscope images depicting the morphological changes in the samples of (a) SMO, (b) LSM25, (c) LSM50, and (d) LMO after cycling at T_{red} = 1400°C.

The most intense restructuring was observed in the cycled LMO morphology, as shown in Figure 3.14d, where the nano-sized LMO particles underwent substantial grain growth, resulting in highly sintered sub-micron particles of *ca*. 320.2 ± 81.24 nm. Table 3.5 summarises the specific surface area (SSA) and average particle diameter, determined by nitrogen adsorption and desorption isotherms. LMO particles had a specific surface area of 2.256 m^2 g^{-1} (Table 3.5) after 5 TC-CDS cycles, which is significantly lower than the original value of 76.29 m^2 g^{-1}. Crystal growth from 24 nm to 61 nm is also observed in LMO powders after CDS cycling.

Table 3.5. Comparison of structure properties of LSM samples before and after thermochemical cycling with T_{red} = 1400°C. The error data represent 95%-confidence intervals about the mean.[a]

Material	*d*-spacing (Å)	*SSA* (m^2g^{-1})		d_{TEM} (nm)		d_{XRD} (nm)		d_{BET} (nm)		V_{BJH} (cm^3 g^{-1})	
		Initial	Cycled	Initial	Cycled	Initial	Cycled	Initial	Cycled	Initial	Cycled
SMO	2.705	145.5 ±10	14.637 ±2.5	18.12 ±6.1	256.12 ± 25	25.14 ±2.5	45.98 ±4.8	35.21 ±4.5	176.61 ±5.6	0.561 ±0.08	0.16 ±0.01
LSM25	2.7191	135.2 ±8	10.821 ±1.4	23.35 ± 11.2	289.84 ± 51	13.75 ±1.8	37.22 ±6.5	17.35 ±2.4	79.83 ±5.6	0.695 ±0.1	0.13 ±0.02
LSM50	2.7445	97.21 ±5	6.273 ±1.1	35.22 ± 4.2	224.5 ± 13.5	18.21 ±2.3	50.21 ±4.8	25.45 ±3.4	133.45 ±12.5	0.527 ±0.05	0.089 ±0.01
LMO	2.6939	76.29 ±7	4.256 ±0.8	25.15 ± 4.5	320.2 ± 81	24.31 ±2.8	61.75 ±9.7	57.89 ±3.4	378.39 ±15.5	0.35 ±0.07	0.017 ±0.007

[a] Specific surface area (SSA), Sauter mean diameter (d_{BET}), crystal size (d_{XRD}), particle size determined by TEM micrographs (d_{TEM}) and V_{BJH} adsorption pore volume (V_{BJH}).

This sintering effect resulted in a 92% decrease in the specific surface area and a 98% loss of pore volume, which reduced the available surface for redox reactions and lowered the reduction extents of LMO at T_{red} > 1000°C. In addition, an increase in particle size led to slower reaction kinetics in LMO. LSM25 and LSM50 underwent moderate structural changes during CDS cycling as observed in Table 3.5. For LSM25, the specific surface area and the pore volume decreased by 92% and 81.3%, respectively. For LSM50, the specific surface area the pore volume decreased by 93.6% and 83.2%, respectively.

XRD patterns of Mn_3O_4 and LSM samples *before* and *after* thermochemical cycling are shown in Figure 3.15. Additional peaks in the range 25–30° in LSM50 and SMO were observed after 5 thermochemical cycles with T_{red} = 1000°C and T_{ox} = 700°C. These peaks correspond to strontium manganite (JCPDF: 28-1233) phase after re-oxidation of LSM at low temperatures. However, complete re-oxidation is observed at 1000°C, retaining the stoichiometric balance with high concentration of lanthanum in LSM structures.

A shift in Bragg characteristics was observed towards higher angles in the XRD spectra with substitution of La^{3+} with Sr^{2+}, creating a charge balance for the ABO_3-type perovskite structure.[252] In Sr^{2+}-rich LSM compounds, a vacancy is created at the B-site i.e. Mn^{3+} to Mn^{4+}. In case of La^{3+} doping, Mn^{4+} is replaced by Mn^{3+}, which is responsible for lower oxygen exchange capacity of La^{3+}-rich LSM compounds, resulting in a low overall redox performance in TC–CDS cycles.[216]

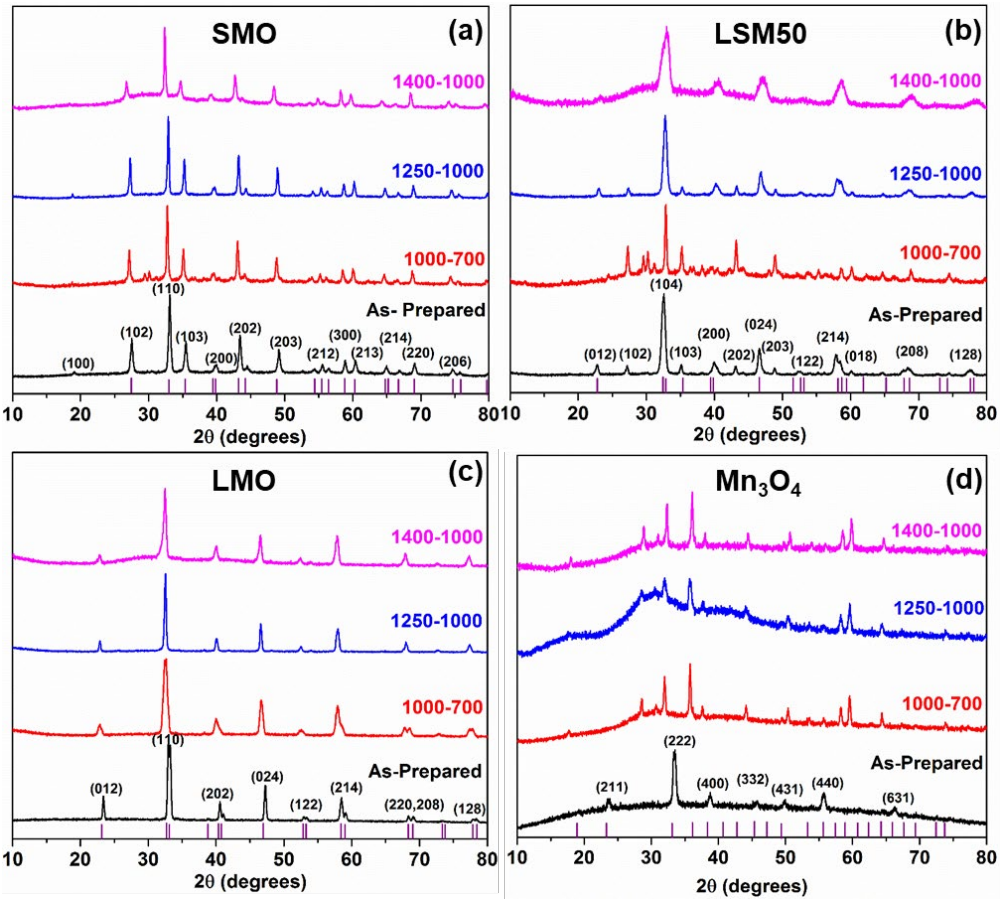

Figure 3.15. X-ray diffraction patterns: (a) SMO, (b) LSM25, (c) LSM50, (d) LMO, and (e) Mn3O4, before (black) and after thermochemical cycling at Tred – Tox = 1000°C –

700°C (red), 1250°C – 1000°C (blue) and 1400°C – 1000°C (magenta). Irreversible phase change from Mn_3O_4 to $Mn2O_3/MnO_2$ due to thermochemical cycling can be observed in the Mn_3O_4 profiles.

Figure 3.15d shows the presence of MnO_2 (JCPDS # 24-0734) and Mn_2O_3 (JCPDS # 81-1947) phases in XRD spectra of *cycled* Mn_3O_4, which corresponds to the non-cyclic re-oxidation.[253] In addition, cubic-to-tetragonal transition of Mn_3O_4 is observed for the *cycled* samples. The increase in the *d*-spacing suggests lattice expansion in LSM structures with up to 50% of added lanthanum, which is not only responsible for the increase in the defect concentration but also tends to increase the particle size (Table 3.5).[252,254]

3.2.6 LSM perovskites after cycling: Methane partial oxidation

Thermochemical performance is understood by investigating the structural changes occurring in LSM structures during MPO, MPO–CDS and MPO–WS reactions. Methane partial oxidation is the first step for all MPO–CDS and MPO–WS reactions, which explains the initial structural changes occurring in LSM structure upon reduction. Also, the regeneration of the LSM structure upon reoxidation during CO_2 and H_2O splitting reaction determines the cyclability and durability of LSM oxygen carriers during the redox cycles. XRD is utilized to study the LSM structures after the reduction and reoxidation reactions. XRD patterns of reduced LSMs with various La concentrations are presented in Figure 3.16a. The LSM structures go through a range of structural destructions during the MPO reaction. A prime product of LSM structural breakage is MnO which is high in Sr-rich LSM structures and decreases with La addition. Table 3.6 presents the products formed after the redox reactions. SMO contains 7.7% Mn_2O_3, which is not observed in other LSM structures. In addition, $SrMnO_3$ transforms to Sr_2MnO_4, which is observed in reduced SMO and LSM25 samples. With 50% La, a higher fraction of $LSMO_{2.5}$ is obtained than with Sr_2MnO_4 and MnO. No MnO or $SrMnO_3/Sr_2MnO_4$ are

observed in LSM75 and LMO after reduction. This clearly indicates non-stoichiometric reduction of LSM75 and LMO, where La prevents structural deterioration. In contrast, the reduction of Sr-rich LSM structures leads to breakage and results various segregated phases.

Elemental segregation was visualized by analysing reduced LSM samples with STEM-EDS mapping. Figure 3.17 a–e represents the STEM maps of Sr, Mn and La elements in reduced LSM25 samples. Regions with high concentrations of Mn, La and Sr can be observed in the overlay image of individual elemental maps, consistent with the results of the XRD study.

The re-oxidation behaviour of reduced LSM species via CO_2 and H_2O splitting reactions was studied in terms of structural changes and was correlated to syngas production performance. Figure 3.16a shows the XRD patterns of LSM samples obtained after 10 consecutive MPO–CDS and MPO–WS cycles. The recovery of the $SrMnO_3$ phase is observed along with an increase in the MnO phase by 8% in SMO. The MnO phase is highest in SMO after MPO–CDS cycles. Increase in the MnO phase suggests continuous breakage of LSM structures after successive reduction-oxidation reactions, resulting in the irreversible formation of MnO phase. This also indicates that the MnO phase does not play any role in the fuel production step of CDS and WS cycles. The formation of the MnO phase drastically decreases by 17% with 50% of La addition, while no MnO phase is observed in LSM75 and LMO after 10 MPO-CDS cycles (Figure 3.16b). This also explains the higher extent of recovery of the LSM phase and inhibition of structural breakage during MPO reaction in La-rich LSM structures.

XRD analysis of re-oxidized LSM samples reveals interesting information and answers the low-end fuel production performance of some LSM perovskites during MPO–WS cycles. As anticipated, structural breakdown was prominent in strontium-rich LSM structures, resulting in a highest yield of 37.9% of MnO phase in LSM25, followed

by 23.2% in SMO. However, MnO is not present in LSM50, LSM75 and LMO after WS reactions.

Perovskite regeneration percentages can be calculated from the phase quantification of XRD patterns (Table 3.6), as shown in Figure 3.16d. LSM50 and LMO showed 100% regeneration of the perovskite structures after oxidation by steam. However, Sr-rich LSMs have only around 60% of Perovskite phase and the rest is MnO phase after MPO–WS cycles. The recovery of original perovskite phases is increased in all LSM structures by 16–25% during MPO–WS cycles when compared to that of MPO–CDS cycles. This is possible due to suppressed LSM breakage and formation of MnO phase during MPO–WS cycles.

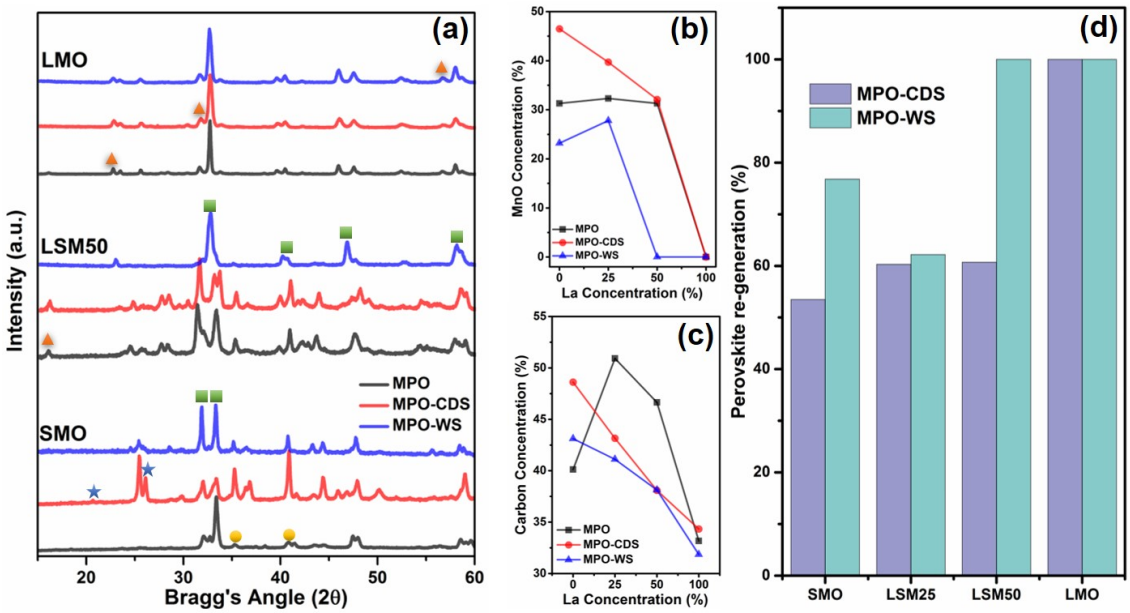

Figure 3.16. Bulk and surface chemical analysis of LSM Perovskites after thermochemical redox cycles: (a) XRD patterns of SMO, LSM50 and LMO powders after MPO, MPO–CDS and MPO–WS cycles representing re-generation of the LSM structure. Green squares represent the (La/Sr) MnO_x, Yellow circles correspond to the MnO phase, while blue stars and orange triangles depict the presence of Sr and La, respectively. (b) Concentration of MnO phase formed after reduction and re-oxidation reactions in LSM structures with different lanthanum concentrations. XRD data is utilized to calculate the MnO phase by Rietveld refinement methods. (c) Carbon deposition on LSM powder surfaces as a function of lanthanum concentration. Carbon concentration is calculated from XPS data obtained on C 1s region. (d) Perovskite regeneration in LSM structures

during MPO–CDS and MPO–WS cycles. The regeneration is quantified from the concentration of LSM structure formed after re-oxidation reaction by CO_2 and H_2O.

This also indicates that CDS reactions cause disintegration of the LSM structure by CO_2 poisoning and C deposition. Surface carbon concentration (%) on the LSM samples during reduction, CO_2 and H_2O splitting reactions is shown in Figure 3.16c. Evidently, carbon deposition is lower during MPO–WS cycles when compared to MPO and MPO–CDS reactions. In addition, surface carbon content decreased with La addition, which suggests that La contributes to impeding methane cracking and CO_2 poisoning. Interestingly, surface carbon contents on reduced SMO are lower than on LSM25 and LSM50. Possible formation of $SrCO_3$ may be a reason for the lower carbon concentration on reduced SMO.[98]

Table 3.6. Phases quantified after MPO, MPO–CDS and MPO–WS cycled SMO, LSM25, LSM50 and LMO samples. Phase quantification is carried out by applying Rietveld refinement methods on XRD patterns.

	Phase (%)							
Sample ID (Reduced)	**$SrMnO_3$**	**$La_{0.234}Sr_{0.76}Mn_{0.924}O_{2.79}$**	**$LaMnO_3$**	**Sr_2MnO_4**	**MnO**	**Mn_2O_3**	**SrO_2**	**$La_{0.6}Sr_{0.4}MnO_{2.5}$**
SMO	0	0	0	47.7	31.3	7.7	0	0
LSM25	0	14.7	0	41.9	32.3	0	8.7	0
LSM50	21	0	0	0	31.3	0	0	47.7
LMO	0	0	100	0	0	0	0	0

	Phase (%)					
Sample ID (MPO-CDS)	**$LA_{0.6}Sr_{0.4}MnO_3$**	**$LaMnO_3$**	**$LaMnO_3$**	**$Sr2MnO_4$**	**MnO**	**$La_{0.5}Sr_{0.75}MnO_2$**
SMO	0	0	0	60.3	39.7	0
LSM25	0	0	6.7	28.5	46.9	17.9
LSM50	60.6	0	0	0	39.2	0
LMO	0	100	0	0	0	0

	Phase (%)				
Sample ID (MPO-WS)	**$LaMnO_3$**	**Sr_2MnO_4**	**MnO**	**$La_{0.5}Sr_{0.75}MnO_2$**	**$La_{0.6}Sr_{0.4}MnO_3$**
SMO	0	76.8	23.2	0	0
LSM25	3.9	27.5	37.8	30.8	0
LSM50	0	11.7	0	0	88.3
LMO	100	0	0	0	0

A visual description of phase segregation in LSM samples after 10 consecutive MPO-CDS cycles is presented in Figures 3.18 a, c, and e. MnO particle is detected on strontium oxide in SMO. Similarly, rod-like SrO particles are observed on the particle aggregates. $SrMnO_x$, $LaSrMnO_x$ and SrO are found in the overlay image of the STEM map of LSM50 after 10 MPO-CDS cycles. Variable elemental peak intensities in EDS spectra also confirm the different concentrations of Sr, Mn and La at various points of the samples (Figure 3.18 b, d and f).

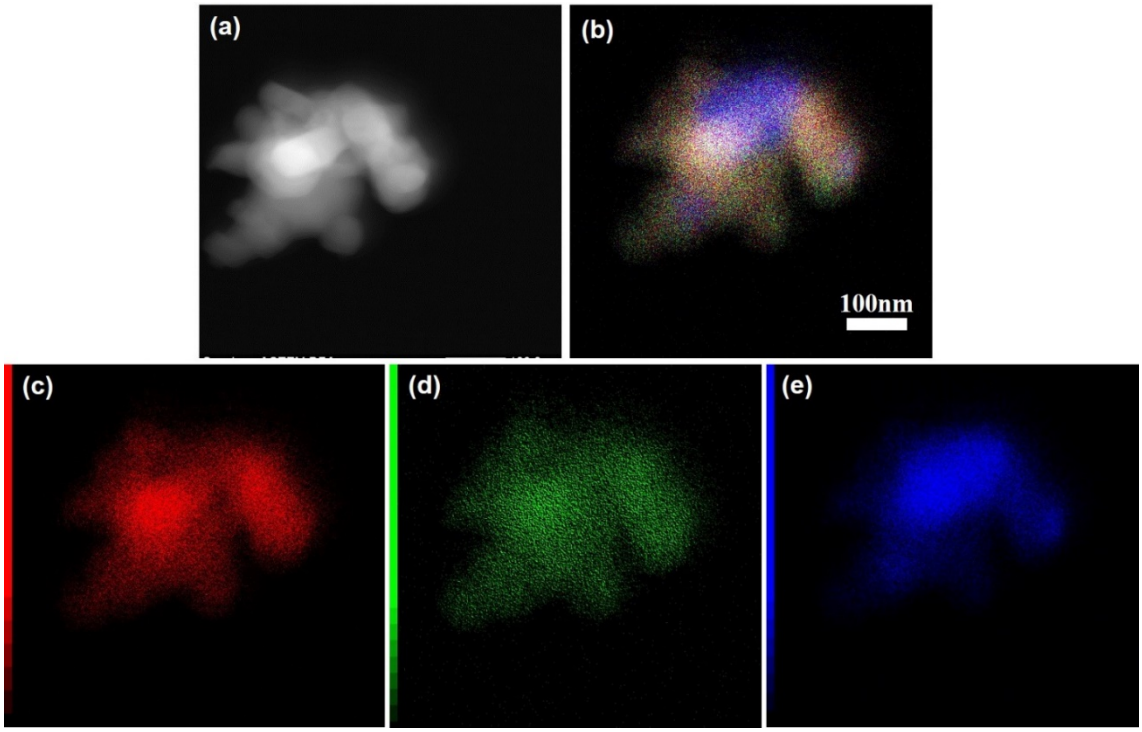

Figure 3.17. Chemical analysis of reduced LSM25 sample: (a) Greyscale, (b) colored overlay, (c) Sr, (d) La and (e) Mn STEM-EDS maps of LSM25 sample after methane partial oxidation reaction.

Similar STEM maps are obtained on LSM samples after MPO–WS cycles. MnO particles are observed in SMO and LSM25, while high concentrations of LSM phase refers to the perovskite structure recovery upon re-oxidation by H_2O, Figures 3.18 g, i and k. EDS spectra of SMO and LSM25 after WS cycles show different elemental concentrations at different regions of a sample (Figure 3.18 h, j and l). The STEM maps

of samples after MPO–CDS and MPO–WS cycles are in good agreement with the XRD results.

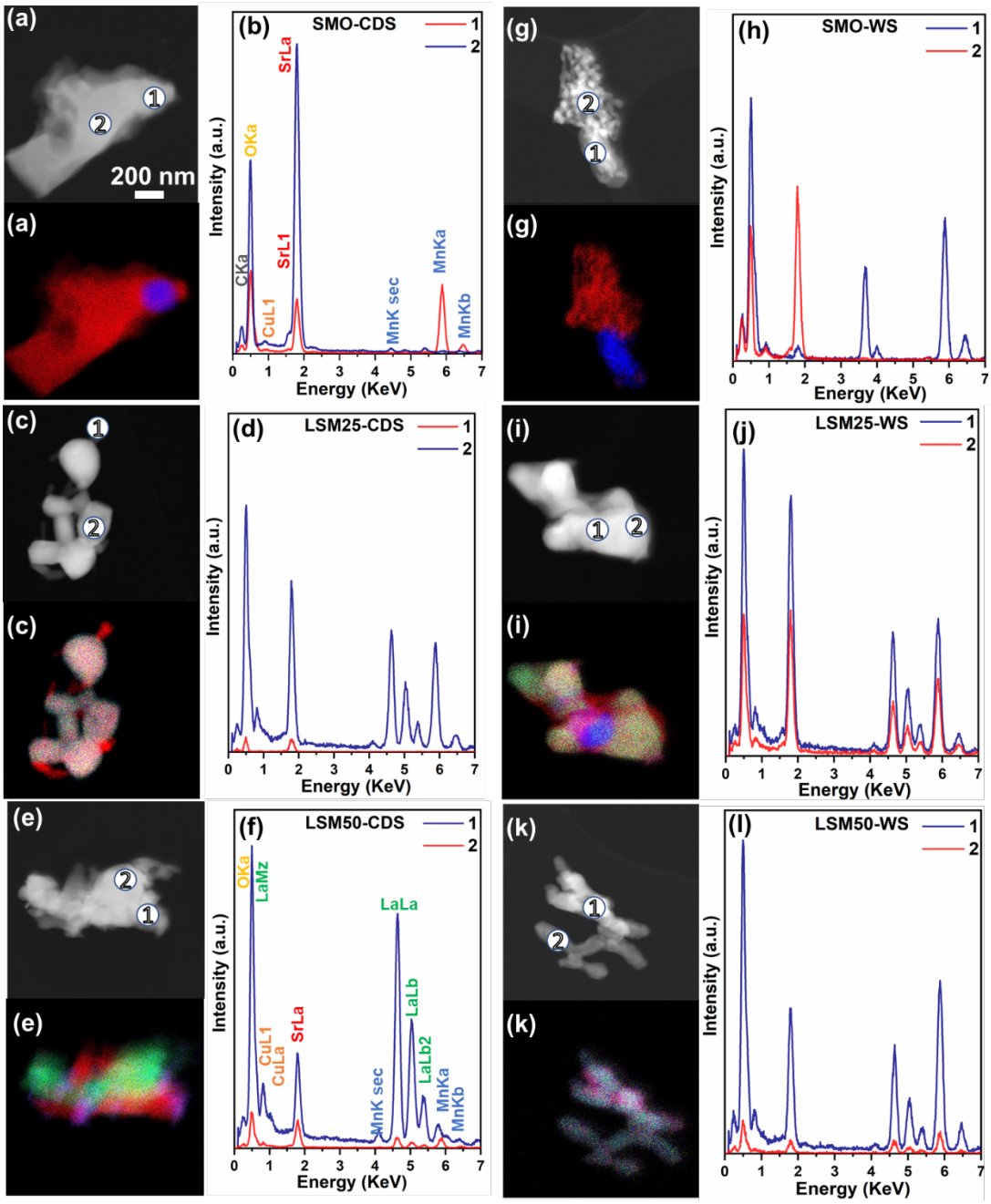

Figure 3.18. Chemical analysis of SMO, LSM25 and LSM50 samples after MPO–CDS and MPO–WS cycling carried out by STEM–EDS analysis: Grey scale and overlay color maps of (a) SMO, (c) LSM25 and (e) LSM50 samples after MPO–CDS and (g) SMO, (i) LSM25 and (k) LSM50 samples after MPO–WS cycling. STEM–EDS spectra of (b) SMO, (d) LSM25 and (f) LSM50 correspond to MPO–CDS and (h) SMO, (j) LSM25 and (l) LSM50 refers to MPO–WS cycling.

XPS and XANES analysis on reduced and re-oxidized LSM powders provide critical insights on the electronic changes occurring on surface and bulk levels. Figure 3.19 a–b represents the O 1s region of the XPS spectra obtained on SMO, LSM50 and LMO powder surfaces after reduction and re-oxidation reactions. Clearly, addition of La results in a broader lattice oxygen (OI) peak when compared to pure SMO and LMO samples.

An increase in surface-adsorbed oxygen species (OIII) in reduced LMO powder surfaces is observed, which relates to surface oxygen exchange activities. Re-oxidation of LMO results in a decline in lattice oxygen species and an intense peak for surface adsorbed oxygen is observed. This may be due to lower oxygen exchange between LMO particles and CO_2, which results in lower CO production yields, as discussed in the thermochemical performance section. In addition, Sr concentration also plays a critical role in the surface oxygen concentration. XPS data is utilized to estimate the oxygen concentration on LSM powder surfaces, as shown in Figure 3.19c. Evidently, an increase in Sr content results in a higher concentration of surface oxygen species when compared to La-rich LSM structures. SMO powders possess the highest concentration of surface oxygen species during reduction and oxidation reactions followed by LSM50 and LMO. This explains the low lattice oxygen peak in LMO after cycling. It is also observed that Sr concentration is increased after CO_2 splitting reactions and is higher than that in H_2O splitting reactions. This refers to higher redox activity by Sr at SMO surface during CO_2 splitting reactions compared to H_2O splitting reactions.

Deconvoluted XPS spectra of Mn 2p for SMO, LSM50 and LMO Perovskite structures are shown in Figure 3.19d. Clearly, a satellite peak for MnO is observed in SMO and LSM50 samples, which confirms the XRD findings about structural disintegration after reduction and oxidation reactions. A shift towards lower binding energies is observed in the SMO sample after re-oxidation reaction, which also refers to oxygen depletion and lower oxidation states for manganese. In contrast, LMO showed a

higher energy shift after the re-oxidation reaction, while no considerable intensities for satellite MnO peak are observed after cycling.

Changes in Mn oxidation state are also investigated by XANES and EXAFS analysis after reduction and re-oxidation reactions. The XANES spectra for the Mn K-edge are shown in Figure 3.19e and changes in oxidation states along with energy shifts for the Mn K-edge are presented in Table 3.7. The Mn K-edge shifts to lower energies i.e. 6544.6 eV in pure SMO and 6552.5 eV in LMO, after MPO reaction, which corresponds to the creation of oxygen vacancies in the lattice.

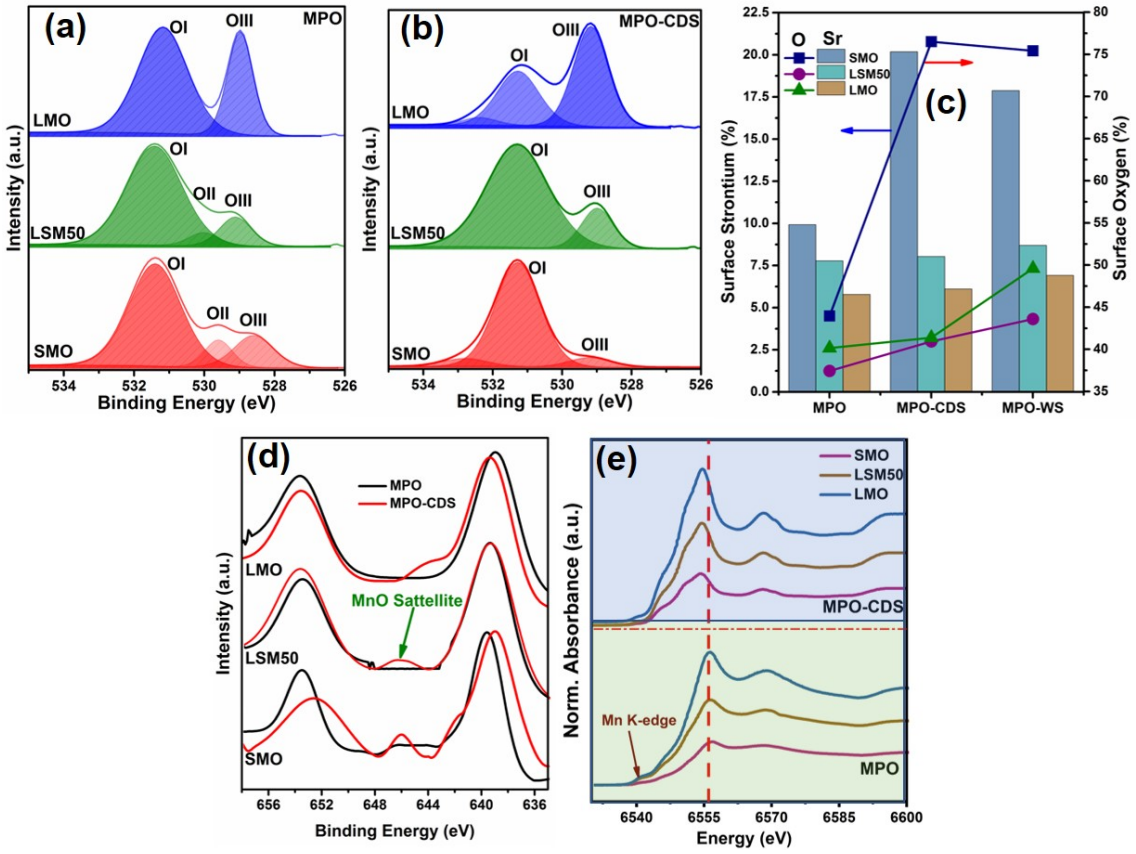

Figure 3.19. Surface and bulk chemical analysis after redox cycling: XPS O 1s spectra of (a) reduced and (b) MPO–CDS cycled SMO, LSM50 and LMO samples. (c) Correlation of surface strontium with surface oxygen species on MPO, MPO–CDS and MPO–WS cycled SMO, LSM50 and LMO powder surfaces. (d) XPS Mn 2p and (e) Ex-situ XANES Mn K-edge spectra acquired on reduced and re-oxidized (CDS) SMO, LSM50 and LMO powder.

Oxidation states of LSM samples were calculated by comparing the experimental energy data with standard data of Mn metal, MnO, Mn_2O_3, MnO_2 and Mn_3O_4 (Figure 3.20 and Table 3.7). The oxidation states of SMO and LSM25 drastically decreased to 1.7 and 1.5, respectively, while only 0.3 cationic charge is removed from LMO after reduction. This confirms the high concentration of MnO phase in pure SMO and LSM25 compared in LMO.

Table 3.7. Ex-situ XANES analysis on pristine, reduced, and re-oxidized LSM Perovskites: Information about photon energy and calculated oxidation states in standard manganese oxide samples. While oxidation state is calculated from the linear equation curve plotted on the XANES data acquired on standard manganese oxide samples.

Sample	E_0 (eV)	Oxidation state
Mn foil	6538.9	0.0
MnO	6544.4	2.0
Mn_3O_4	6547.8	2.7
Mn_2O_3	6548.6	3.0
MnO_2	6552.1	4.0
Pristine SMO	6555.3	4.0
MPO SMO	6544.6	2.8
Pristine LSM25	6554.4	3.9
MPO LSM25	6544.2	2.8
Pristine LSM50	6553.7	3.7
Pristine LMO	6553.4	3.6
MPO LMO	6552.5	3.4

LSM samples underwent a certain degree of sintering during MPO–CDS and MPO–WS cycles. Fusion of small particles into agglomerates is observed in SMO, while an organized layer of individual particles can be seen in La-rich LSM structures, as shown in Figure 3.21a–i. The particle size of SMO powders increased up to 400 nm ± 26 and 1 µm ± 200 nm during MPO-CDS and MPO-WS cycles, respectively. Addition of La showed a suppressed particle size growth during the cycling. With 25% La, particles sintered to a size up to 289 nm ± 19 and 320 nm ± 15 during CDS and WS cycles,

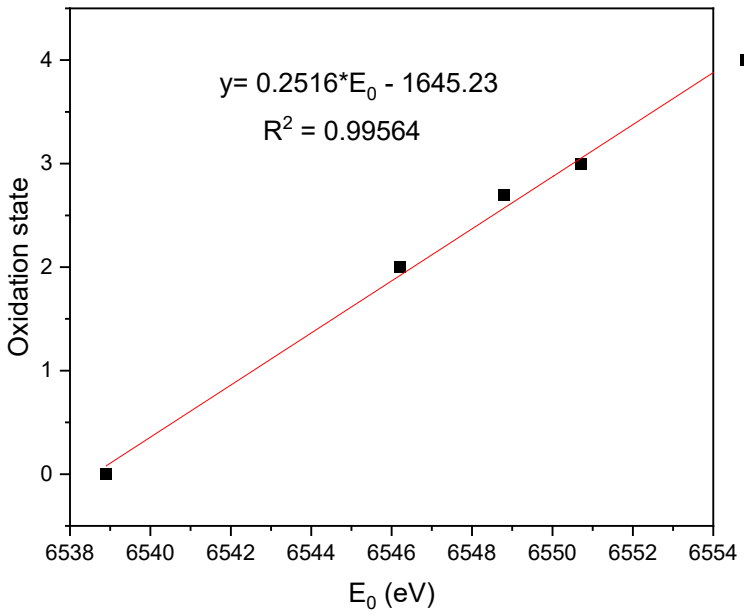

Figure 3.20. Linear equation plot between photon energies and respective oxidation states of standard manganese oxide samples Mn, MnO, Mn_3O_4, Mn_2O_3 and MnO_2 with cationic charge 0, +2, +2.7, +3 and +4, respectively.

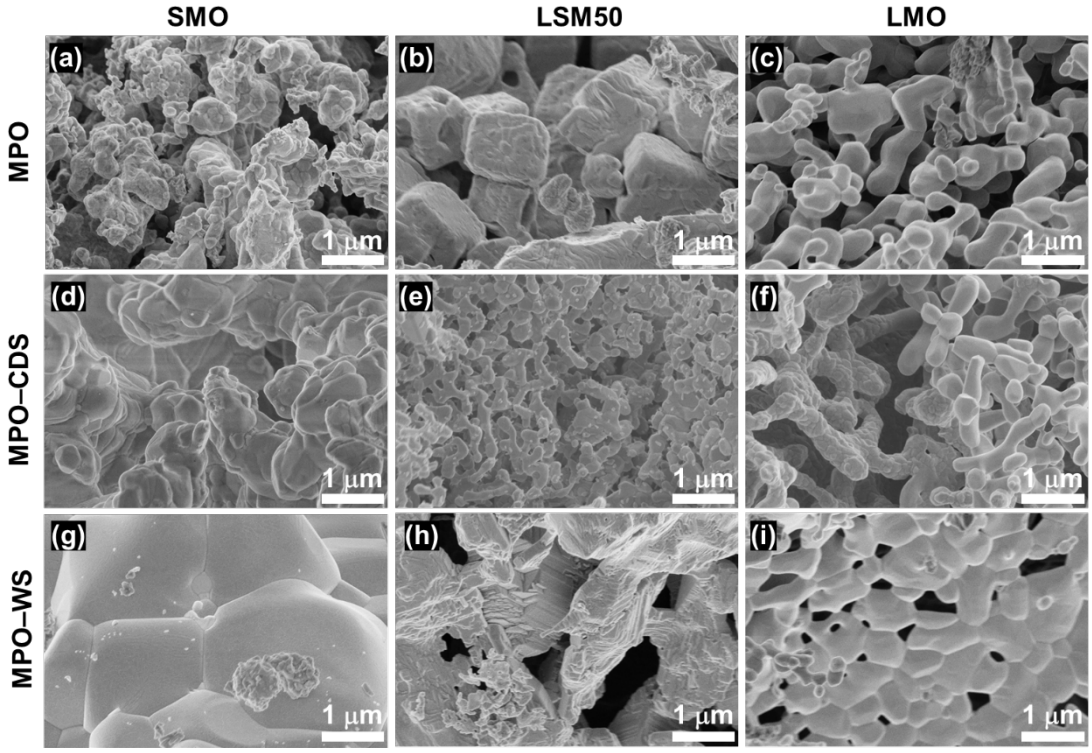

Figure 3.21. Morphological analysis of LSM powders after redox cycling: FESEM micrographs of after cycling (a), (d) and (g) SMO, (b), (e) and (h) LSM50 and (c), (f) and (i) LMO samples. Particle growth and sintering is dominant in Sr-rich samples, while ordered individual particles are observed in pure LMO powders.

respectively. LMO samples consist of a particle network with an average particle size of 269 nm ± 17 and 342 nm ± 11 after MPO–CDS and MPO–WS cycling, respectively. As the powder structure plays a key role in the solid-to-gas transfer, suppressed sintering in powders is crucial and can be achieved by La addition in SMO.

3.3. Discussion

Manganese mono-oxide (MnO) is the by-product of structural disintegration of LSM during redox cycling and does not contribute to either reduction or oxidation reactions. Figure 3.22a represents the reaction products of different oxide species of manganese with CH_4. Evidently, MPO reaction by MnO does not result in any syngas product except for H_2, which is produced due to the thermal cracking of methane after 900°C. In contrast, MnO_2 and Mn_2O_3 actively reform methane at temperatures as low as 650°C, producing considerable amounts of CO and H_2. The enthalpy of the reaction is higher for MnO_2 and Mn_2O_3 than that of MnO, which is in line with the published findings about the redox activity of pure manganese oxides (Figure 3.22 b and 3.23c).[168] However, the structural configuration of Perovskites enhances the redox activity by improving the oxygen exchange capacity of manganese oxides, as Mn (B-site cation) is the active cation in oxygen exchange. This can only be achieved if structural stability is achieved to avoid the formation of MnO phase, where La addition plays a key role to protect the LSM structure from breakage.

TGA/DTA analysis for up to 30 consecutive cycles is performed on LSM25 to study the energy and mass loss during MPO–CDS redox cycles. Stable mass change profiles are observed during reduction and oxidation reactions (Figure 3.22d). A maximum of 10.5% mass change is achieved during the redox cycles. The enthalpy of reaction increases after 3 cycles to 10 cycles, which decreases and stabilizes afterwards. Changes in enthalpy may be due to the formation of MnO phase in the LSM structure, which stabilized when MnO saturation level is achieved. The schematic illustration in Figure

3.22e explains the effect of La on the formation of MnO phase and how it protects the Sr/La-Mn bond to be broken. Large concentrations of oxygen vacancies in La-rich LSM result in strong La-Mn/La-Sr-Mn bonds and weakens the Mn-O bond, which is opposite in Sr-rich LSM materials. This results in an easy oxygen removal during the methane partial oxidation reaction. In contrast, the strong reducing power of CH_4 easily weakens the Sr-Mn bond and cause structural breakage.

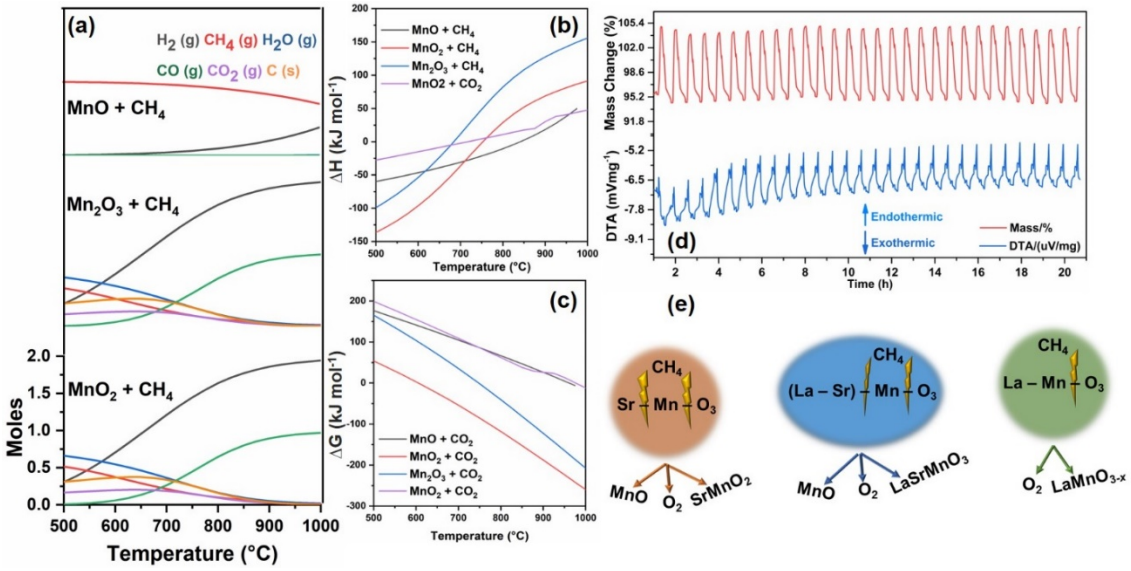

Figure 3.22. Mechanistic analysis of redox cycles: (a) Products of methane partial oxidation reaction by MnO, Mn_2O_3 and MnO_2. No activity for CO production is indicative of MnO participation in the MPO reaction. (b) Enthalpy and (c) Gibbs free energy of MPO and CDS reactions by different oxides of manganese. (d) TGA–DTA analysis for mass change and DTA measurements during 30 consecutive MPO–CDS redox cycles on LSM25 sample. (e) Proposed mechanism of methane action on M-Mn and Mn-O bonds with- and without lanthanum and its effect on resulting products.

The results of XANES and XPS studies relating to the change in Mn oxidation states are the key indicators of the involvement of Mn in redox activities. However, formation of MnO appears to be unavoidable in stoichiometric reductions of the LSM structure. Addition of La to the lattice lowers the overall oxidation state of Mn, which results in a stronger Mn-O-(La/Sr) bond. This protects the LSM structure from breaking under the harsh reducing atmospheres of CH_4 and promotes non-stoichiometric reduction. The

results of syngas production rates support this argument; the addition of La beyond 50% results in lower syngas rates and yields when compared to Sr-rich LSM samples. However, LMO produced considerable yields of syngas, while LSM25 and LSM50 are the best LSM structures for producing the highest syngas yields. In addition, 25 and 50% La addition also significantly lower MnO formation and a considerable improvement in LSM structural regeneration is observed after reoxidation.

3.4. Conclusions

Strontium manganite perovskites with variable lanthanum concentrations (0%, 25%, 50%, 75% and 100%) are studied for dry and steam chemical looping reforming of methane. The effects of specific surface area, oxidizing medium (air/CO_2), reduction–oxidation temperatures and concentration of La^{3+} on the redox performance of the materials with different La^{3+} and Sr^{2+} concentrations were elucidated. The electrospinning technique produced faceted and uniform nano-sized particles, with diameters ranging from 18.12 ± 6.1 nm to 35.22 ± 4.2 nm, high specific surface area of up to 145.55 m^2g^{-1} and a pore volume of 0.561 cm^3 g^{-1}. These structural properties seen in LSM allowed for high CO yields, up to 854.20 μmol g^{-1}, with fast kinetics of ~400 μmol $g^{-1}min^{-1}$ at T_{red} = 1400°C in case of SMO. The highest redox capacity was observed in SMO (δ = 0.29) at T_{red} = 1400°C during thermochemical cycling with CO_2 splitting, whereas high La^{3+} fractions increased the redox capacity to δ = 0.08 at relatively low reduction temperatures (1000°C) with CO production rate up to ~200 μmol $g^{-1}min^{-1}$. In addition, Sr^{2+}-rich LSM compounds retained the grain morphology with definite grain boundaries, which demonstrates their high suitability for thermochemical redox cycling at reduction temperatures up to 1400°C. The combination of La^{3+} and Sr^{2+} in manganite systems can be useful for performance improvement at moderately high temperatures (1250°C). The effect of manganese oxidation state in LSM systems on the CO_2 splitting performance was critically examined. SMO demonstrated the highest CO yield with fast rates, showing

a high oxygen exchange capacity at high reduction temperatures. In sum, this study resulted in nano-structured LSM materials with a set of robust structural properties such as specific surface area and high pore volume, which can in turn serve as a roadmap towards engineering of premium quality redox materials by electrospinning technique for enhanced solar fuel production via high-temperature thermochemical redox cycling.

The role of lanthanum on structural and phase stability in terms of phase disintegration and regeneration was the focus of this study. In addition, the effect of MnO formation on synthesis gas production rates and yields was also investigated. Incorporation of lanthanum resulted in lower manganese oxidation states in as-prepared LSM structures when compared to pure SMO. Lanthanum addition also prevented the structural disintegration and promoted the nonstoichiometric redox reaction mechanisms. Stoichiometric reduction of LSM structures results in structural breakage, which is unavoidable with high strontium concentrations. Syngas production yields are improved by 57% and 35% with 25 and 50% lanthanum, respectively when compared to that of pure $SrMnO_3$ and $LaMnO_3$ perovskites. However, more than 50% lanthanum content shifts the redox behavior from stoichiometric to non-stoichiometric and lowers the overall syngas yields. In conclusion, this structural study gives insights into the redox behavior with respect to the structural changes in LSM perovskite oxides with the help of advanced characterization techniques.

Chapter Four

V-doped Ceria Metal Oxides

Publications relevant to this chapter:

Asim Riaz, Felipe Kermer, Suchinda Sattayaporn, Takuya Tsuzuki, Wojciech Lipinski, Adrian Lowe, *an experimental demonstration of Vanadium doped nanostructured ceria for enhanced solar thermochemical syngas production*, Nano Energy, (81) 2021, 105639.

4.1 Introduction

In previous chapter, LSM perovskites were explored for syngas production via thermochemical redox cycling and chemical looping reforming of methane. The delegate nature of the structural stability of perovskites in methane atmospheres and high temperature reduction in inert atmospheres, lead to the search for more structurally stable materials.

Based on the findings in previous chapter, a facile method for incorporation of vanadium into the ceria lattice is explored in this chapter. Methane partial oxidation (MPO) under continuous heating up to 1000°C is performed to find the lowest possible temperature for the peak syngas production rates and yields. Short (S) and long (L) cycles of CO_2 (MPO–CDS) and H_2O (MPO–WS) splitting reactions are performed to investigate the effects of vanadium doping on the syngas production performance of ceria. We observed that vanadium doping lowers the reduction temperature and enhances the syngas production rates and yields for up to 200 continuous cycles. Structural studies revealed that beyond the saturation level (i.e. 5% V), excess vanadium forms V_2O_5, which reacts with CeO_2 and results in a $CeVO_4$ phase. The vanadium present inside the ceria lattice and $CeVO_4$ presents a variety of redox mechanisms which significantly affects the thermochemical performances of V-doped ceria with vanadium content before and after the saturation levels. These findings are used to design and synthesize new materials with high thermochemical redox performance.

4.2 Results

4.2.1. *x*$VCeO_2$ materials before redox cycles

FESEM analysis revealed initial morphological information about the pristine x$VCeO_2$ nanostructures. The average particle size increased from 18 ± 5 nm in pure nano-ceria to 38 ± 6 nm after 7% of vanadium addition, and a porous network of nanoparticles was observed with vanadium addition (Figure 4.1). Figure 4.2a shows particle distribution in

the ceria nanopowders doped with 3% vanadium, where estimated average particle size of 20 ± 5 nm is observed. The vanadium incorporation also caused lattice distortion in the ceria structures and the lattice spacing increased from 0.125 nm in pure nanoceria to 0.145 nm in 5VCeO2 nano powders. However, vanadium contents greater than 5% lowered the lattice spacing, due to the possible vanadium saturation in the CeO_2 lattice and segregation of the CeVO4 phase (Reaction 1).

$$2CeO_2 + V_2O_5 = 2CeVO_4 + \frac{1}{2} O_2 \quad (4.1)$$

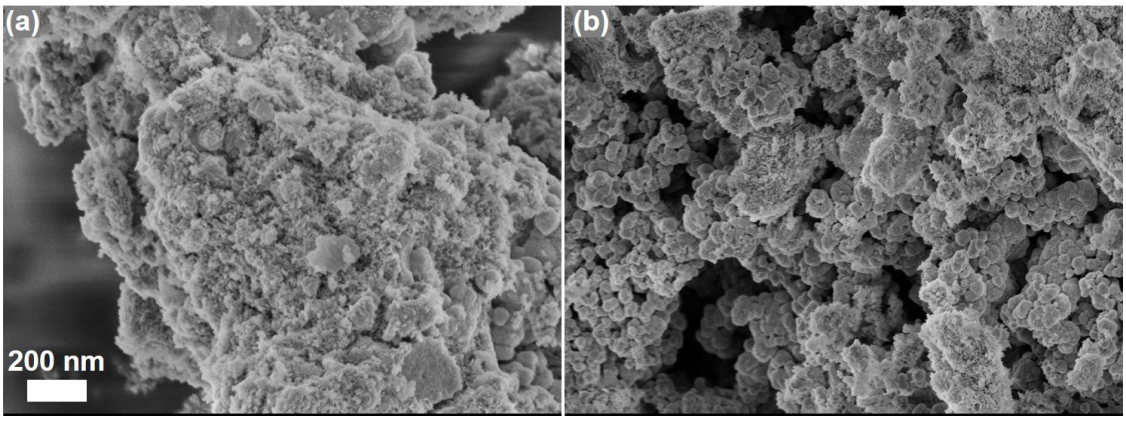

Figure 4.1. Morphological study of the pristine materials: SEM micrographs of pristine (a) pure ceria and (b) 7% V doped ceria powders.

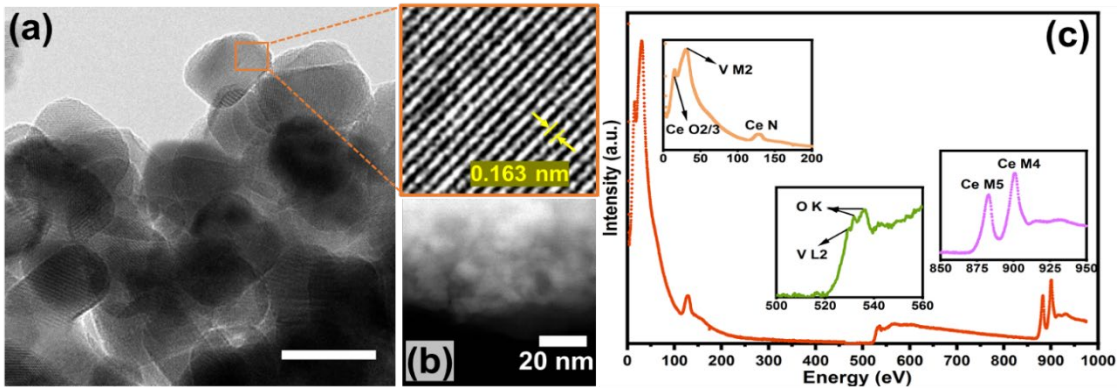

Figure 4.2. Morphological and structural analysis of pristine xVCeO2 materials: (a) HR-TEM micrograph showing the particle size distribution in the 3VCeO2 sample. An expanded section from the image shows the inner lattice spacing. (b) HAADF image of the 3VCeO2 sample. (c) EELS spectra containing information about CeO 2,3, Ce M4, Ce M5, O K, V L2 and V M2 edges in the 3VCeO2 sample.

EELS spectra measured from the respective high-angle annular dark-field (HAADF) image (Figure 4.2b), showed the major edges of vanadium, cerium and oxygen elements (Figure 4.2c). The major edges of cerium Ce O2 at 15 eV, Ce N at 120 eV, Ce M5 at 883 eV and Ce M4 at 901 eV indicated high cerium (IV) concentrations in the CeO_2 lattice. Major edges of vanadium, V L2 at 529 eV and V M2 at 38 eV confirmed the presence of V^{5+} in the CeO_2 lattice, (Figure 4.2c).[255]

Figures 4.3b and 4.3c present the elemental distribution of vanadium in the pristine $3VCeO_2$ nano powders. The EDS spectra acquired at different spots on the grey scale image (Figure 4.3a) of $3VCeO_2$ powders are shown in Figure 4.3d. Distinct elemental energy peaks of Ce and V in the EDS spectra confirmed the vanadium presence along with the cerium and oxygen elements.

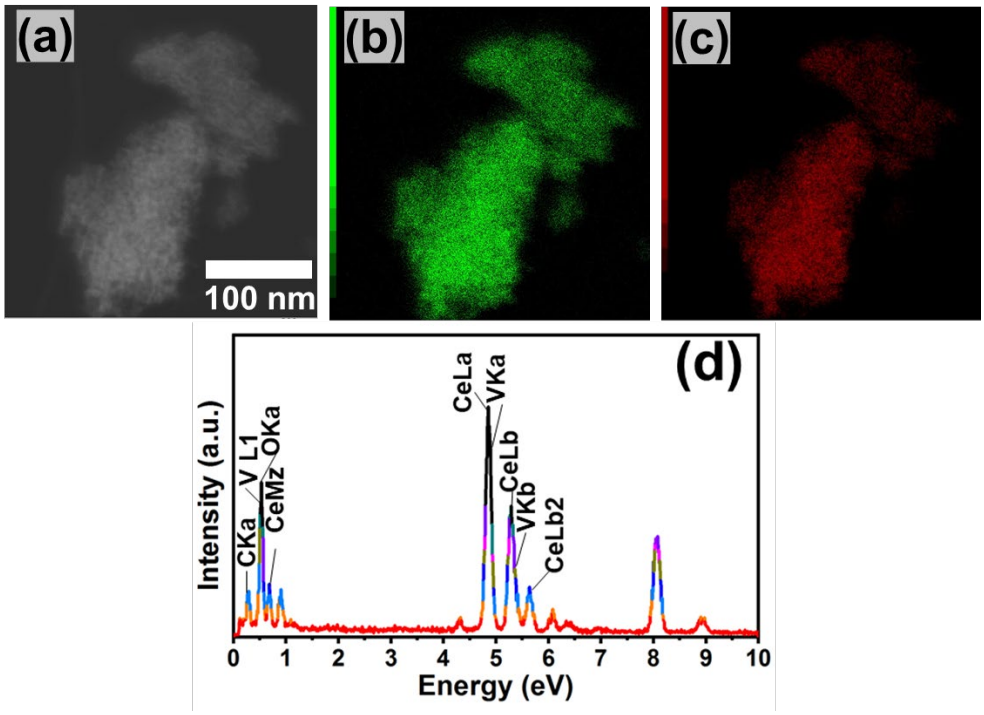

Figure 4.3. Chemical analysis of pristine materials: STEM-EDS maps of (a) Ce (red) and (b) vanadium (green) elements corresponding to the 1d grey scale image of $3VCeO_2$ sample. (c) EDS spectra measured from the grey scale image shown in part 1a.

XRD analysis provided information about changes in the ceria structure such as Bragg's angle shift, lattice spacing and phase segregation. Figure 4.4a shows the XRD patterns for pristine xVCeO$_2$ nano powders. A triclinic CeO$_2$ crystal structure was confirmed from the pure ceria XRD pattern.[256] Vanadium doping below 5% showed a slight 2θ shift and phase quantification revealed a 100% CeO$_2$ phase. However, further addition exceeded the saturation limit of vanadium in the CeO$_2$ lattice and promoted the formation of CeVO$_4$ phase, as described in Reaction 4.1.[257] Figure 4.4b shows the evolving CeVO$_4$ phase, as the XRD peak intensity at ~25° increased in 7VCeO$_2$ powders. Figure 4.4c presents changes in the lattice spacing and CeVO$_4$ phase concentration in CeO$_2$ nano powders with vanadium addition. Considerable amounts of approximately 8.2% of CeVO$_4$ phase were observed after 7%V addition to the CeO$_2$ nano structures.

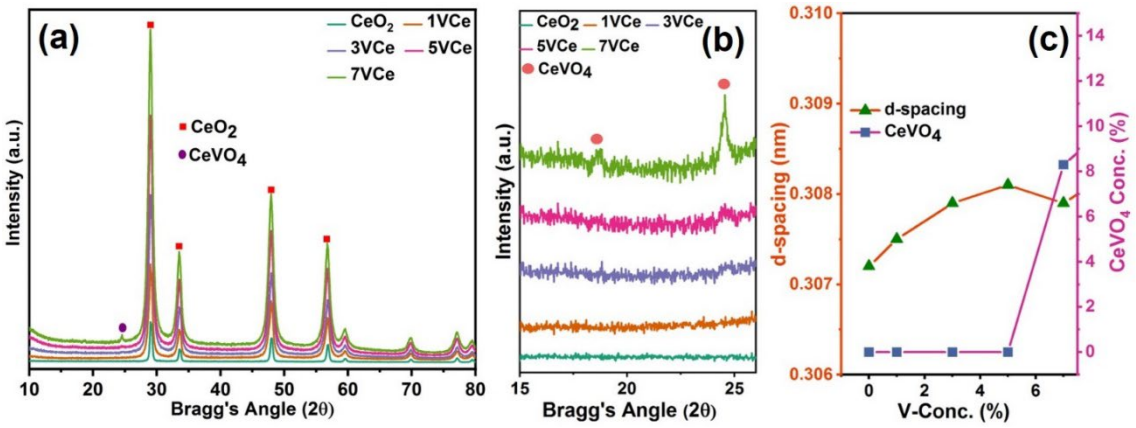

Figure 4.4. Structural analysis of pristine materials: (a) XRD patterns of pristine xVCeO$_2$ materials. (b) Evolution of CeVO$_4$ phase with the addition of vanadium in ceria. (c) Variations in d spacing and CeVO$_4$ concentrations as a function of vanadium content.

Further analysis performed using the Raman technique evaluated the structural changes induced by vanadium doping into the CeO$_2$ nano structures. Figure 4.5 compares the Raman spectra of V-doped ceria powders with the pure CeO$_2$ and V$_2$O$_5$ used as reference. Vanadium doping slightly shifted the CeO$_2$ peak at 461.87 cm^{-1} towards low Raman frequencies.[258,259] Raman shift peaks at 861.25, 799.21, 787.84, 379.54, and

259.19 cm^{-1} confirmed the formation of $CeVO_4$ phase in the V-doped ceria powders with vanadium content greater than 5%.[257,259,260]

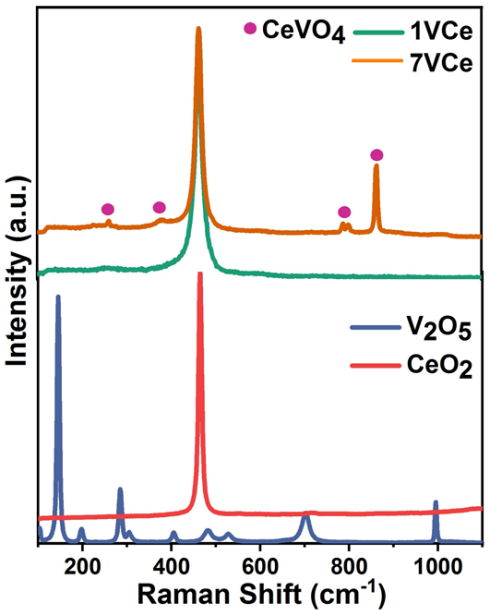

Figure 4.5. Structural analysis of pristine materials: Raman spectra with information about the evolution of the $CeVO_4$ phase with V addition in CeO_2 structures along with the spectra of reference CeO_2 and V_2O_5 samples.

To gain insights into the effects of vanadium doping on the surface chemical composition, the V-doped ceria nano powders were investigated by XPS analysis. Figures 4.6a–4.6c present the photoemission spectra of O 1s, Ce 3d and V 2p measured on pristine 1, 3, and 9% V-doped ceria powder surfaces. The oxygen O 1s spectra were fitted into three different components: The first peak (OI) situated at 529.3 eV is associated with the lattice oxygen; the second peak (OII) at ~530.1–531.2 eV corresponds to the oxygen atoms situated near the vacancy-rich regions; the third peak (OIII) at 532.6 eV is ascribed to the physiosorbed H_2O or –OH species. The lattice oxygen O1 peak shifted towards higher binding energies, depicting stronger M–O bonds due vanadium incorporation in the CeO_2 lattice, as compared to that in the pure CeO_2 structures.[261] The oxygen leaching in Reaction 4.1 resulted in higher concentrations of the OII species in the 7VCe sample compared to that of xVCeO_2 with x = 1–5 %. The Ce 3d spin-orbital split multiplets of

CeO_2 mostly remained unchanged after vanadium doping (Figure 4.6b). However, the intensity of the 3d 3/2 peak at 917 eV decreased in the 7VCe sample due to the presence of Ce^{3+} in the growing $CeVO_4$ phase. In addition, strong V 2P 3/2 and 5/2 peaks in the 7VCe sample characterizes vanadium onto the surface of ceria nanopowders (Figure 4.6c).

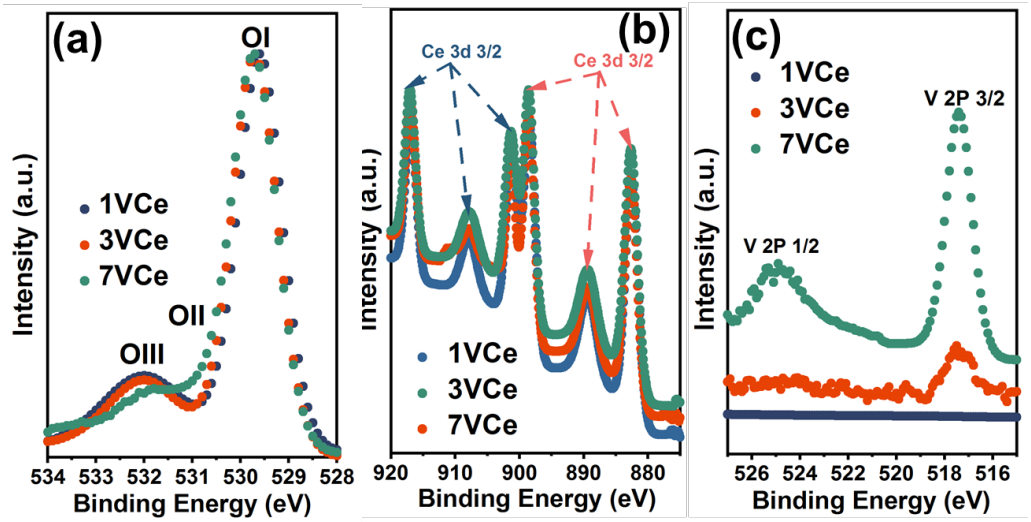

Figure 4.6. Structural analysis of pristine materials: XPS spectra measured from (a) O 1s, (b) Ce 3d and (c) V 2P spin orbitals in $xVCeO_2$ materials with variable vanadium concentrations.

Photon energy spectra of Ce L3 and V K edges were obtained from ex-situ XANES analysis of V-doped CeO_2 powder samples (Figure 4.7). The oxidation states of Ce and V were calculated by comparing the acquired photon energy data with cerium and vanadium oxide standards (Figure 4.8). The Ce L3-edge energy for pure and V-doped CeO_2 was recorded at 5727 eV and the calculated cerium oxidation state (+4) also remained unchanged due to the dominating CeO_2 phase (Figure 4.7a). The $CeVO_4$ phase growth in the 7VCe sample results in a slight shift of the vanadium K-edge to higher energies (5483.0 eV) and the calculated positive charge on vanadium was also increased to +5.1 (Figure 4.7b Table 4.1). Low intensities of the pre-edge absorption feature at 5469.79 eV confirmed the XPS findings on high oxygen concentrations near vacancy-

rich regions in the 7VCe sample.[262] This also refers to the formation of V–O bonds cluster in $CeVO_4$ phase.

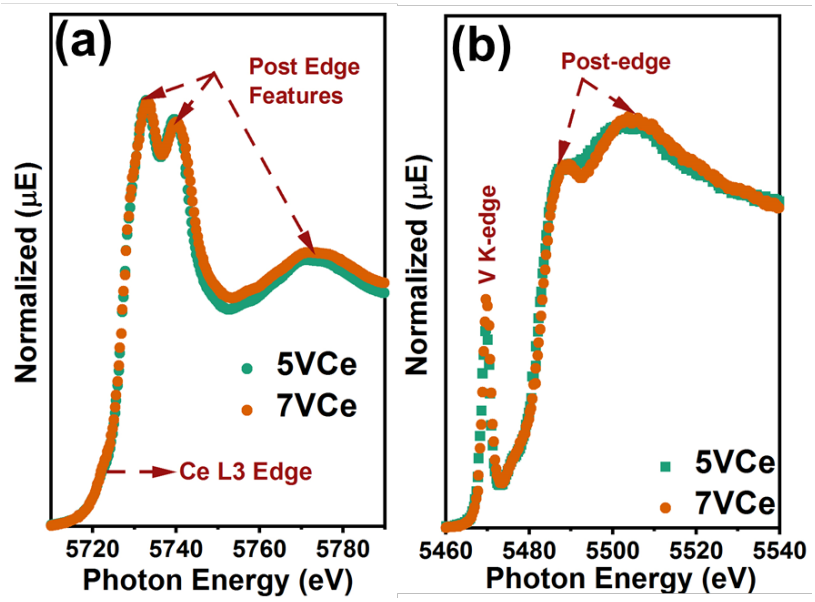

Figure 4.7. Structural study of pristine materials: XANES spectra of (a) Ce L3 and (b) V K edges in 5VCe and 7VCe samples.

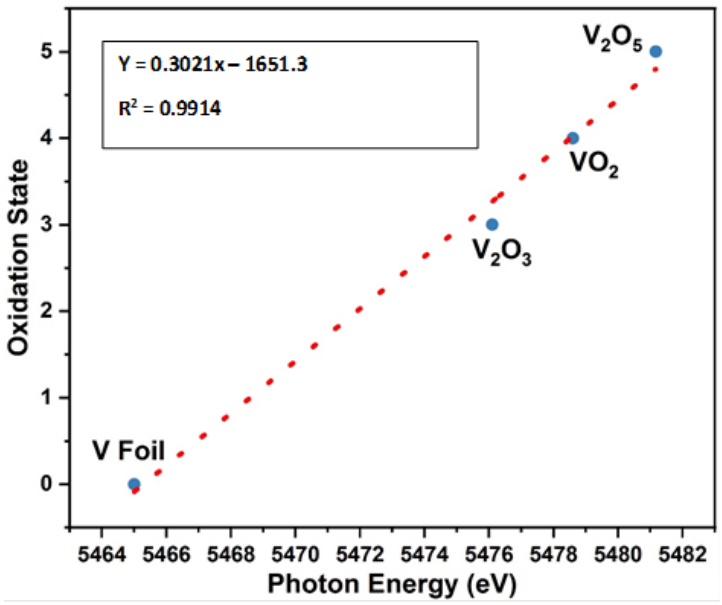

Figure 4.8. Linear fit for the oxidation states of V foil, V_2O_3, VO_2 and V_2O_5 standard samples, measured by XANES analysis.

Table 4.1. Oxidation states and photon energies of the V K edge of the standard and experimental samples, measured by the XANES technique.

Sample	E_0 (eV)	Oxidation state
V foil	5465.0	0.0
V_2O_3	5476.1	3.0
VO_2	5478.6	4.0
V_2O_5	5481.2	5.0
$5VCeO_2$	5482.7	5.0
$9VCeO_2$	5483.0	5.1
Reduced 5VCe	5476.6	3.2
Oxidized 5VCe	5480.9	4.5
Reduced 9VCe	5479.3	4.0
Oxidized 9VCe	5480.6	4.4

4.2.2. Thermochemical performance 1: MPO activation temperature

Multiple aspects of the thermochemical performance of pristine xVCeO$_2$ including MPO activation temperature, fuel production rates and yields were evaluated. The MPO activation temperature experiment was performed by heating the powder samples from ambient temperature to 1000°C with a ramp rate of 3°C min^{-1} in a CH_4 atmosphere. Figure 4.9a shows the spontaneous H_2 production rates produced by xVCeO$_2$ powders during reduction. The recorded temperature for the peak H_2 rates (0.33 mmol min^{-1} g^{-1}) produced by pure ceria was 964.36 °C. Vanadium addition significantly reduced the temperature for its peak syngas production rates (Figure 4.9b) where only 1%V resulted in the peak production rates of H_2 (0.57 mmol min^{-1} g^{-1}) and CO (0.23 mmol min^{-1} g^{-1}), at 883.69 °C. Highest rates of H_2 (0.6 mmol min^{-1} g^{-1}) and CO (0.17 mmol min^{-1} g^{-1}) were achieved at the lowest temperature of 785.35 °C with 5%V doping. The kinetics of methane reforming were significantly slower than the thermal cracking of methane. Thus, the recorded instantaneous H_2 rates were much higher than that of CO.

Activation of the MPO reaction was further investigated by TGA/DTA analysis. Samples were heated from ambient temperature to 1000 °C at a ramp rate of 3° min^{-1},

while the methane flow was kept constant at 10 mL min^{-1} with 115 mL min^{-1} Ar as carrier gas. The spontaneous mass change was recorded as a function of temperature (Figure 4.9c), simulating the gas production rates shown in Figure 4.9a.

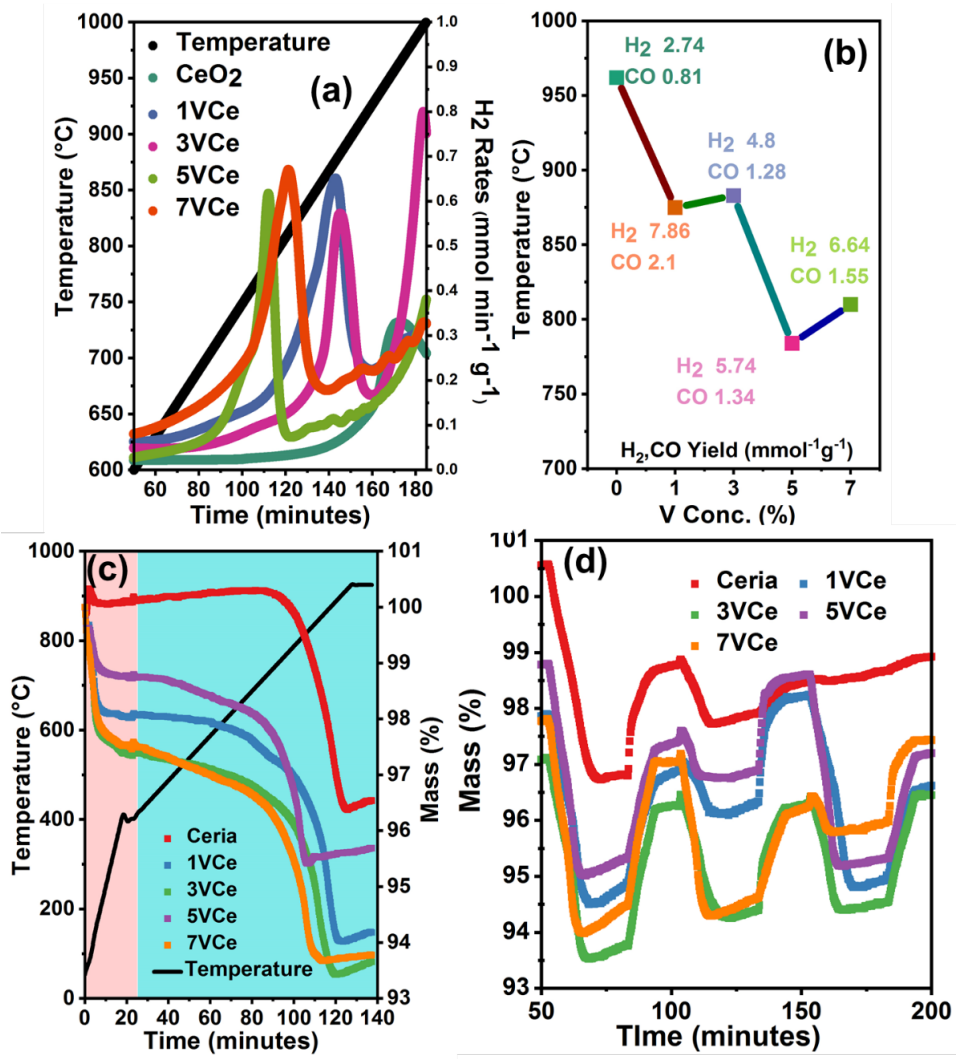

Figure 4.9. Thermodynamic effects of vanadium doping in ceria: (a) H_2 evolution profiles of $xVCeO_2$ samples during constant heating from RT to 1000°C in CH_4 atmosphere. (b) Peak H_2 and CO rates at temperatures achieved by pure and V-doped ceria powders. (c) TG mass variance in $xVCeO_2$ samples during the continuous heating from RT to 400°C in Ar and from 400°C to 1000°C in CH_4 atmosphere. (d) TG mass change (%) in $xVCeO_2$ powders during three consecutive MPO–CDS redox cycles.

Evidently, the mass loss started at higher temperatures in pure ceria when compared to that of V-doped ceria samples. The mass loss in 5VCe powder was maximum with the lowest recorded temperature, which is in line with the results obtained in Figure 4.9a and

4.9b. Considering the temperature variance, an optimized temperature (i.e. 900°C) was set to further investigate pure and V-doped ceria powders for MPO–CDS and MPO–WS redox cycles.

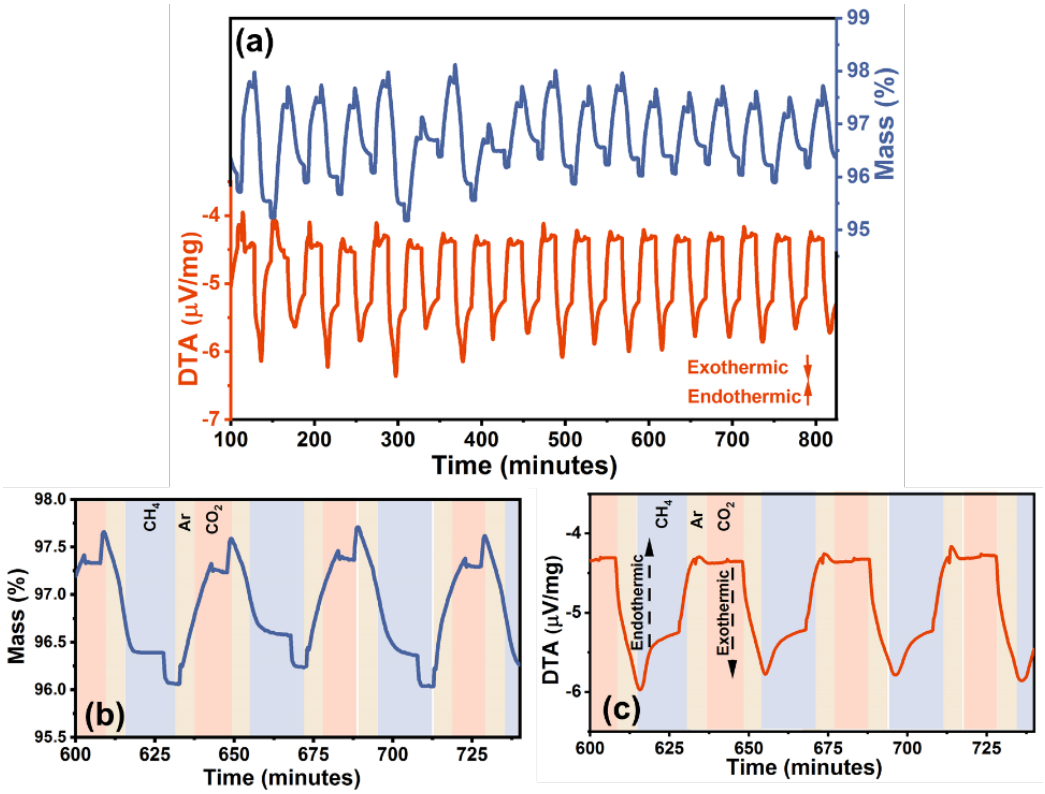

Figure 4.10. Thermogravimetric analysis of V-doped ceria materials: (a) TGA and DTA analysis of 3VCeO$_2$ samples for 20 consecutive MPO–CDS redox cycles. Expanded view of (b) TGA and (c) corresponding DTA signals for cycles 14 to 16.

The mass change (Δm%) during three preliminary MPO–CDS redox cycles is presented in Figure 4.9d. The Δm (%) in pure ceria powders decreased to half after the first cycle, while doping of vanadium significantly enhanced and stabilized the mass change. The recorded mass change and enthalpy of reactions for 3VCe samples during 20 consecutive MPO–CDS cycles are presented in Figure 4.10a. Clearly, stable mass change and enthalpies are observed without significant changes after the first few cycles. The expanded view of TGA and DTA graph for cycles 14th to16th presents a clear image of mass change and enthalpy during the MPO–CDS redox cycles (Figure 4.10b and 4.10c).

4.2.3. Thermochemical performance 2: MPO–CDS

The syngas production performance was evaluated during short and long reduction and oxidation cycles. The duration of reduction and oxidation reactions was 20 min and 10 min, respectively, which is increased to 90 min for reduction and 70 min for the oxidation reaction. In the following figures and discussions in the text, the short redox cycles will be referred to as S/MPO–CDS and S/MPO–WS, while the L/MPO–CDS and L/MPO–WS will be used to refer to the long redox cycles.

The syngas production rates improved with vanadium doping in ceria. The highest production rates for H_2 2.8 mmol min^{-1} g^{-1} and CO 1.32 mmol min^{-1} g^{-1} were achieved by 1VCe powders during the S/MPO reaction, which was 4 times higher than that of pure ceria and 3 times higher than pure $CeVO_4$ (Figures 4.11and 4.12a).

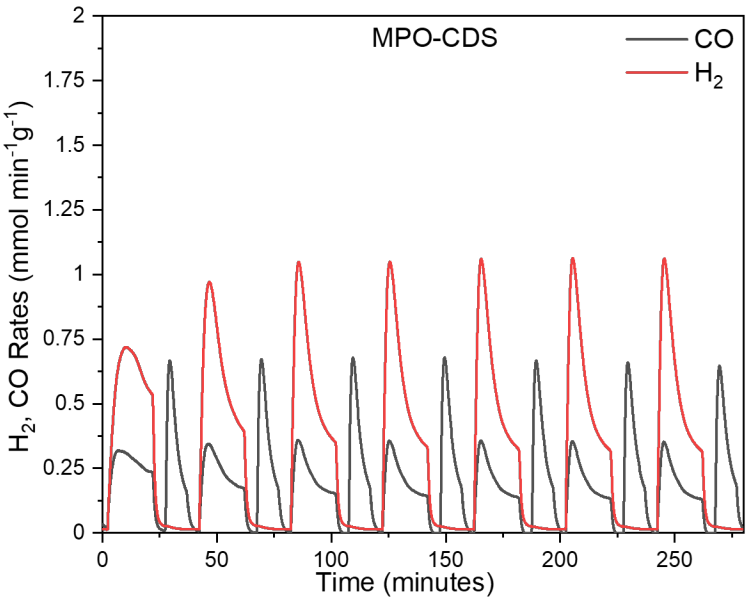

Figure 4.11. Syngas production rates by pure $CeVO_4$ during MPO–CDS cycles.

Further increase in the vanadium content showed up to a 200% increase in syngas production rates compared to pure ceria. The 1VCe sample produced the highest rates of CO up to 1.25 mmol $min^{-1}g^{-1}$, during the CO_2 splitting reaction. Overall, all the *x*$VCeO_2$ materials showed enhanced syngas production performance compared to pure ceria and $CeVO_4$, during the S/MPO–CDS redox cycles.

Syngas yields produced by the *x*VCeO$_2$ powders during S/MPO–CDS cycles are presented in Figure 4.12b. The highest yields of H$_2$ (18.5 mmol g^{-1}) and CO (8.1 mmol g^{-1}) were achieved with the 1VCe sample upon reduction, while 6.8 mmol g^{-1} of CO were produced during the CO$_2$ splitting reaction. A decline in the syngas yields was observed in the 3VCe and 5VCe samples. This may be due to the saturated vanadium atoms impeding the oxygen exchange in the ceria lattice, which was overcame by prolonging the redox reactions. The 1VCe sample demonstrated a high CO selectivity (SCO) of 96.58% and H$_2$/CO ratio of 2.1 with only 0.1153 mmol/g of deposited carbon, during the S/MPO–CDS redox cycles, (Figure 4.12c). However, despite high oxygen ion conductivity, ceria produced the largest amounts of deposited carbon due to its low cycle capacity.

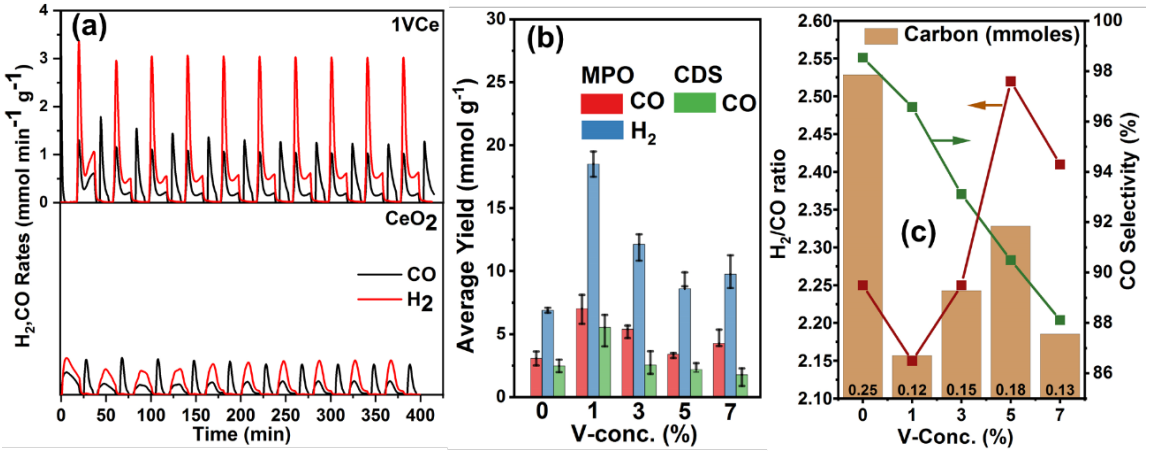

Figure 4.12. Thermochemical syngas production performance of V-doped ceria materials during S/MPO–CDS redox cycles: (a) Syngas production rates comparison between pure ceria and the 1VCe sample, (b) average syngas yields and (c) H$_2$/CO ratios, CO selectivity and deposited carbon moles as a function of vanadium concentration in CeO$_2$ powders.

The 7VCeO$_2$ powders produced the highest average rates of H$_2$ (11 mmol min^{-1} g^{-1}) and CO (2.5 mmol min^{-1} g^{-1}) during the L/MPO reaction while CO yields of up to 2.5 mmol min^{-1}g^{-1} were recorded during the L/CDS reaction (Figure 4.13a). Long reductions enhanced the oxygen exchange, possibly due to the migration of saturated vanadium

atoms from the lattice to the surface of the 4ceria particles. High $CeVO_4$ contents in the xVCeO$_2$ powders after the L/MPO–CDS cycles supported this suggestion.

Prolonged reduction and oxidation reactions significantly affected the syngas yields during the L/MPO–CDS redox cycles (Figure 4.13b). The 7VCe sample produced the highest yields of H_2 (117 mmol g^{-1}) and CO (35 mmol g^{-1}) during the L/MPO reaction, while the re-oxidation resulted in 57 mmol g^{-1} of CO (Figure 4.4e). This contrasts with the data recorded during the S/MPO–CDS redox cycle and will be discussed in the post cycling structural study and the discussion section. Pure ceria produced a substantial amount (0.41 mmol/g) of deposited carbon, which decreased significantly with vanadium content. In addition, the H_2/CO ratio also decreased from 4.25 in pure ceria to 2.52 in the 1VCe sample (Figure 4.13c).

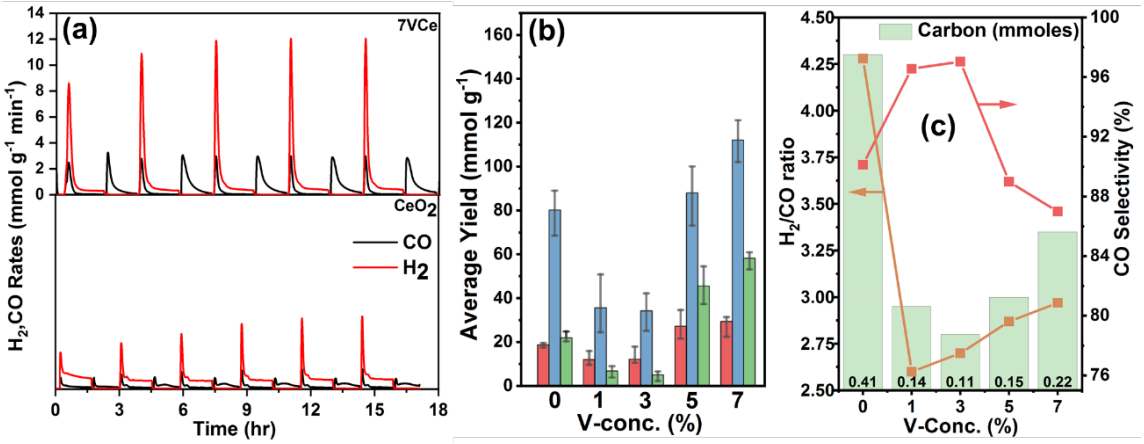

Figure 4.13. Thermochemical syngas production performance of V-doped ceria materials during L/MPO–CDS: Comparison of syngas production (a) rates and (b) yields by pure ceria and V-doped ceria powders. (c) Change in H_2/CO ratios, CO selectivity and deposited carbon moles with various vanadium concentrations.

4.2.4. Thermochemical performance 3: MPO–WS

The reoxidation potential of xVCeO$_2$ materials was evaluated during S/MPO–WS and L/MPO–WS redox cycles. Water splitting reactions significantly affected the MPO

reaction rate profiles where the rates of methane reforming reaction rose exponentially, after a period of slow reaction kinetics (Figure 4.14a).

Syngas production rates and yields drastically increased with V-doped ceria, during the S/MPO–WS and L/MPO–WS redox cycles. Figure 4.14a shows higher and more stable syngas rates produced by the V-doped ceria sample when compared to that of pure ceria. In addition to the V-doped ceria nanostructures, pure $CeVO_4$ powders also showed significantly improved and stable syngas production rates than that of pure CeO_2 powders, yet not the highest.

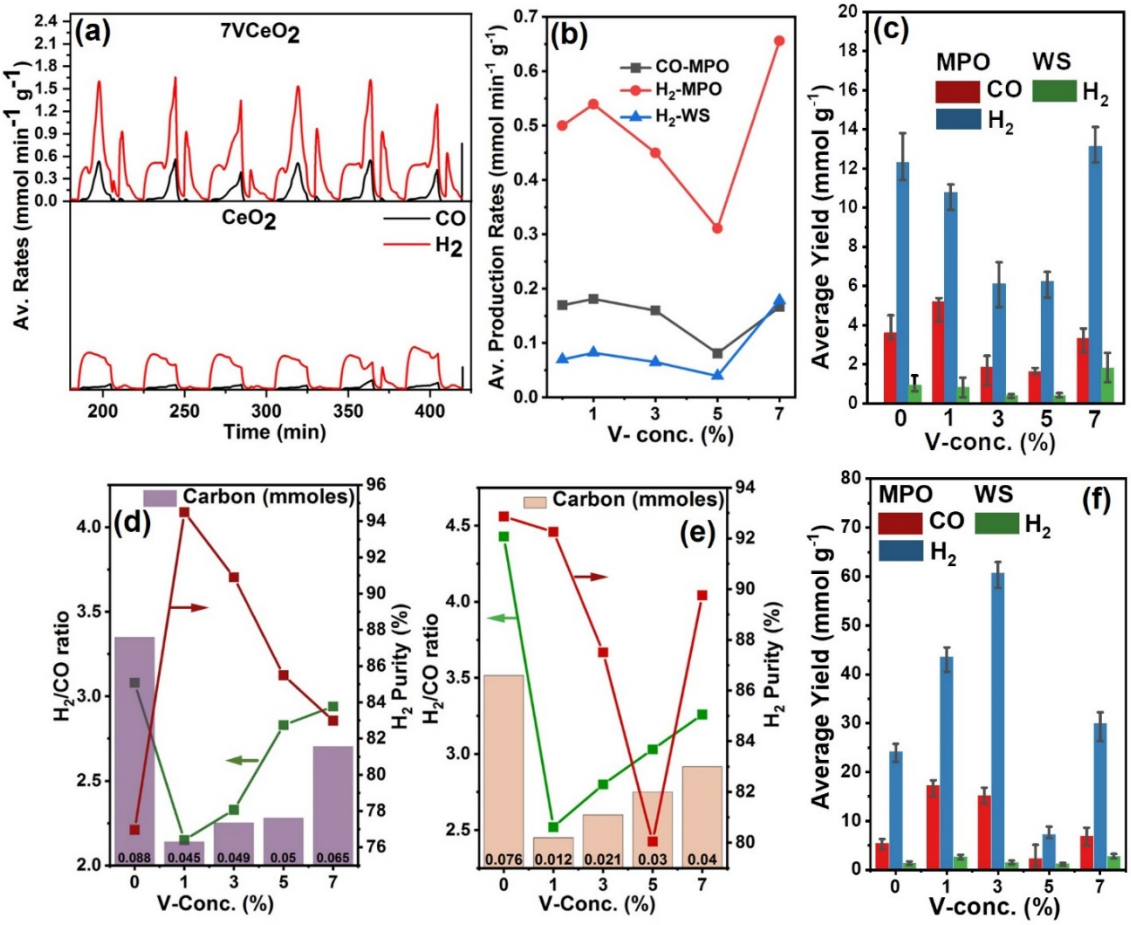

Figure 4.14. Thermochemical syngas production performance during S/MPO–WS and L/MPO–WS redox cycles: (a) Comparison of the average syngas production rates between pure ceria and the 7VCe sample during 6 consecutive S/MPO–WS redox cycles. (b) Average syngas rates produced by $xVCeO_2$ samples. (c) Average yields of syngas and (d) H_2/CO ratios, purity of H_2 and carbon contents recorded during S/MPO–WS redox

cycles. (e) H_2/CO ratios, purity of H_2 and carbon contents and (f) average syngas yields, recorded during the L/MPO–WS redox cycles.

The average syngas production rates from the 7VCe sample were the highest with 0.67 mmol min^{-1} g^{-1} of H_2 and 0.29 mmol min^{-1} g^{-1} during the S/MPO reaction while reoxidation by the water splitting reaction resulted in 0.22 mmol min^{-1} g^{-1} of H_2 (Figure 4.14b). The yields of H_2 and CO produced by 7VCe samples were 12.8 mmol g^{-1} and 5.85 mmol g^{-1}, respectively, during the S/MPO reaction. The amount of H_2 (1.9 mmol g^{-1}) produced during the H_2O splitting reaction was twice that produced by pure ceria (Figure 4.14c). Significant improvements in the purity of the H_2 and H_2/CO ratio were observed after vanadium doping of ceria. The purity of H_2 varied from 76% in pure ceria to 95% after V-doping (Figure 4.14d). The oxidation of carbon species by H_2O significantly slowed down the powder's reoxidation and resulted in low H_2 yields and low H_2 purity. Pure ceria showed high H_2/CO ratios and elevated amounts of carbon content, which is significantly improved by up to 200% after vanadium doping and the oxidation of surface carbon was prominent in the L/MPO–WS redox cycles (Figure 4.14e). However, this also resulted in relatively lower H_2 yields from the H_2O splitting reactions compared to that from S/MPO–WS cycling (Figure 4.14f).

4.2.5. Post cycling material study

Cyclic redox reactions carried out at high temperatures resulted in the sintering of nano powders, which indirectly affected the thermochemical redox performance by hindering the solid-gas transfer. The durations and temperatures of cycles greatly influenced the extent of sintering. For instance, large particles are observed after high temperature reduction and long redox cycles as compared to those in short duration cycles being carried out at 900°C (Figure 4.15).

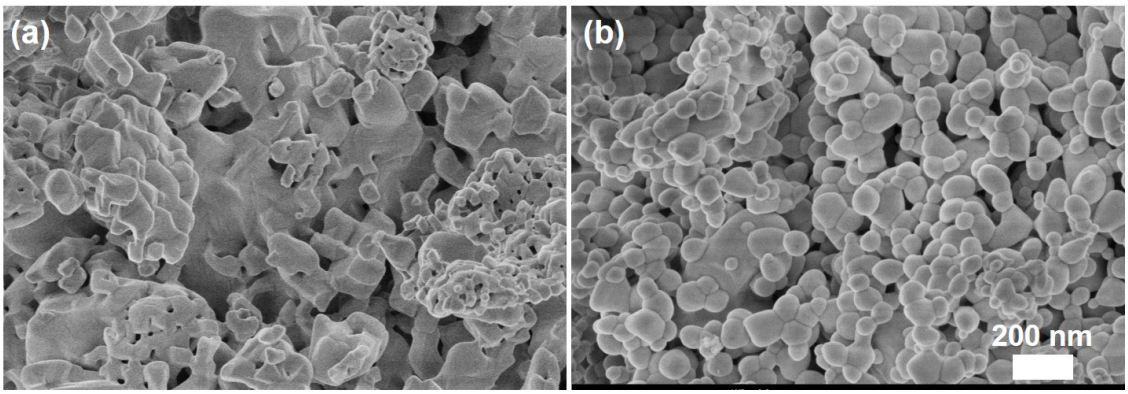

Figure 4.15. SEM micrographs of the 5VCeO$_2$ sample after (a) L/MPO–CDS and (b) S/MPO–CDS redox cycles.

The X-Ray diffraction technique was utilized to study the structural and phase changes in the pure nano ceria and V-doped ceria nanostructures after redox cycling. Reduction of *x*VCeO$_2$ nanostructures resulted in a simple non-stoichiometric oxygen exchange in ceria (Figure 4.16a). The diffraction peaks of the CeVO$_4$ phase disappeared after its reduction to the CeVO$_3$ phase (Reaction 4.2), which was recovered upon the reoxidation reactions.[263,264] Higher concentrations of CeVO$_4$ phase were observed after the L/ MPO–CDS cycles when compared to that of S/MPO–CDS cycles. The deposited carbon during the prolonged exposure to the carbonaceous atmosphere caused slow oxygen exchange to the ceria lattice. Instead, the surface vanadium and cerium species were reoxidized and formed the CeVO$_4$ compound, after the removal of surface carbon. Another possible reason for the high CeVO$_4$ phase may be the prolonged oxidation of surface carbon, which eased up the oxygen exchange for the reoxidation reactions. The considerable amounts *c.a.* 13.9% of CeVO$_3$ along with the 7.6% CeVO$_4$ phase in 7VCeO$_2$ powders showed the partial reoxidation of CeVO$_3$ phase during the L/MPO–CDS cycles.

$$CeVO_4 \underset{\text{Oxidation}}{\overset{\text{Reduction}}{\rightleftharpoons}} CeVO_3 + \frac{1}{2} O_2 \qquad (4.2)$$

The water splitting reactions facilitated the cyclic CeVO$_4$ concentrations due to the low deposited carbon contents, as compared to that of S/MPO–CDS and L/MPO–CDS

redox cycles. Small amounts (5%) of $CeVO_4$ were also observed in the $5VCeO_2$ powders after the MPO–WS cycles, which indicates the escape of vanadium from the ceria lattice to the surface of ceria nanoparticles. This depicts faster kinetics for Reaction 4.2 on the surface compared to that of non-stoichiometric reoxidation of reduced pure ceria nanostructures. However, the unsaturated vanadium content improved the kinetics and cycle capacity of ceria by inducing lattice distortions due to variable cationic radius and the V^{+5} cations draw more oxygen species into the ceria lattice.

The deposited carbon was investigated by the EDS technique and compared to the reduction and reoxidation reactions. A green color STEM-EDS map shows well-dispersed carbon content on the reduced $5VCeO_2$ powders (Figure 4.16b and 4.16c). The EDS spectra show the higher intensity counts of the C Ka peak in reduced samples, when compared to those from the oxidized samples. In addition, the powder surfaces covered with carbon also lowered the intensities of other elements present in the reduced $5VCeO_2$ powders (Figure 4.16d).

Figures 4.16e and 4.16f show the changes in the surface oxygen species induced by cyclic oxygen exchange during the reduction and re-oxidation reactions. Low OI to OII intensity ratios pointed to oxygen removal and increased numbers of oxygen vacancies in the reduced sample compared to that of the reoxidized sample. The counts of lattice oxygen OI were significantly lower in the 5VCe sample than that in the 1VCe sample, which suggests a high extent of oxygen removal in the V-saturated ceria lattice. However, the high OII and OIII areas were related to poor oxygen recovery in the 5VCe sample after reoxidation. It can be inferred that the saturated vanadium atoms impede oxygen transport into the ceria lattice. However, longer oxidation cycles helped in improving the oxygen exchange and cycle capacity.

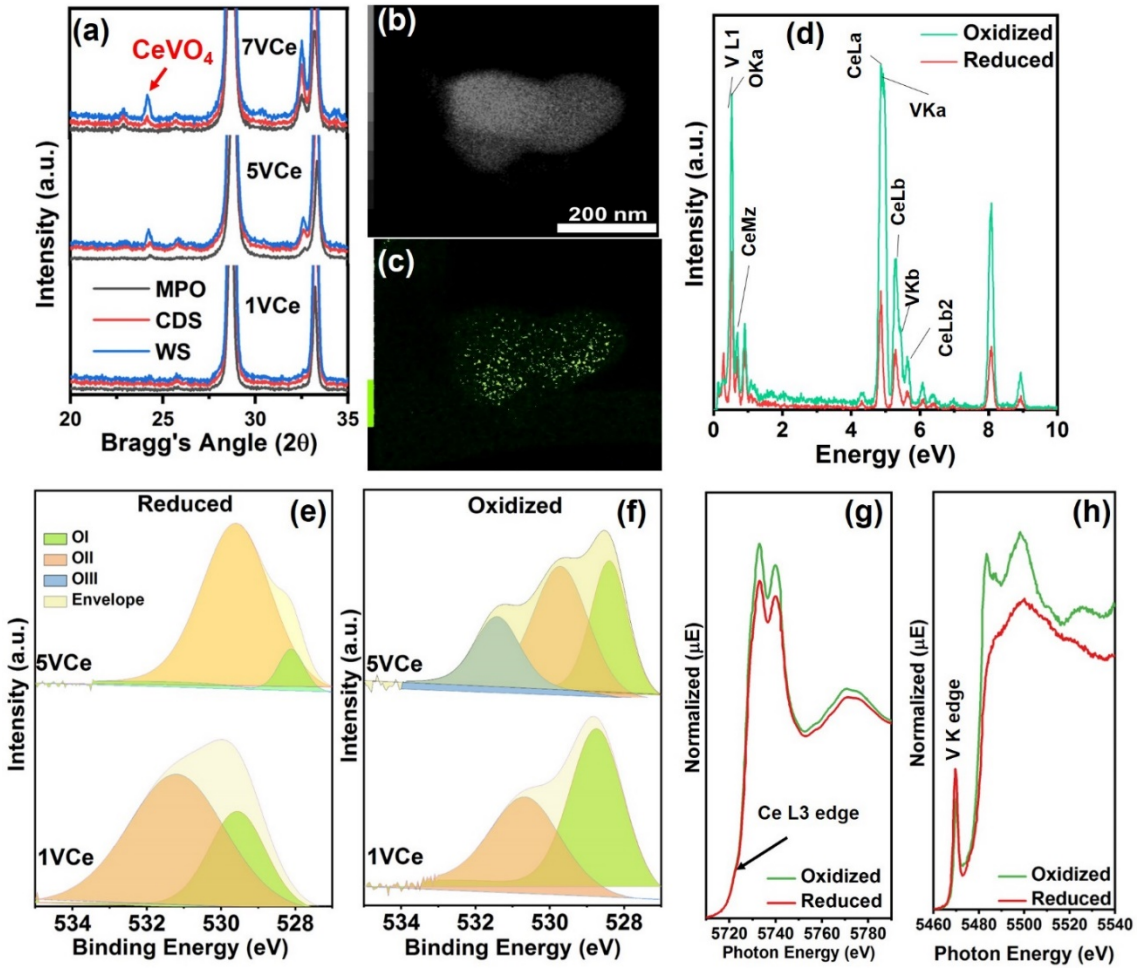

Figure 4.16. Structural study of cycled $xVCeO_2$ samples: (a) XRD patterns of cycled $xVCeO_2$ with 1, 5 and 7% vanadium. Information about the $CeVO_4$ phase evaluation after reduction, CO_2 splitting and water splitting reaction is shown from 20°–35°. (b) Grey scale and (c) green (carbon) STEM-EDS maps and (d) EDS spectra of $5VCeO_2$ powders after the redox reactions. XPS O 1s spectra of $xVCeO_2$ samples after (e) reduction and (f) re-oxidation reactions with different areas of OI, OII and OIII peaks. XANES spectra of (g) Ce L3 and (h) V K edges of $5VCeO_2$ samples after reduction and re-oxidation reactions.

Ex-situ XANES analysis revealed the chemical states of Ce and V elements after the redox reactions (Figure 4.16g and 4.16h). The photon energy of the Ce L3-edge remained unchanged at 5727eV. The post-edge features of the Ce L3 and V K edges showed lower intensity counts due to the oxygen vacancy created after reduction. In addition, absorption of the V K-edge shifted to lower photon energies in the reduced samples when compared to that of the oxidized sample.

Stability of the V-doped ceria sample is demonstrated by performing 200 continuous S/MPO–CDS redox cycles. An expected initial decline in the syngas production rates was observed, which may be due to incomplete oxygen recovery (Figure 4.17a). On average, H_2 and CO are produced at a rate of 1.94 mmol min^{-1} g^{-1} and 0.91 mmol min^{-1} g^{-1}, respectively, during the MPO reaction. The CO production rates by CO_2 splitting were nearly equal to those produced during the MPO reaction.

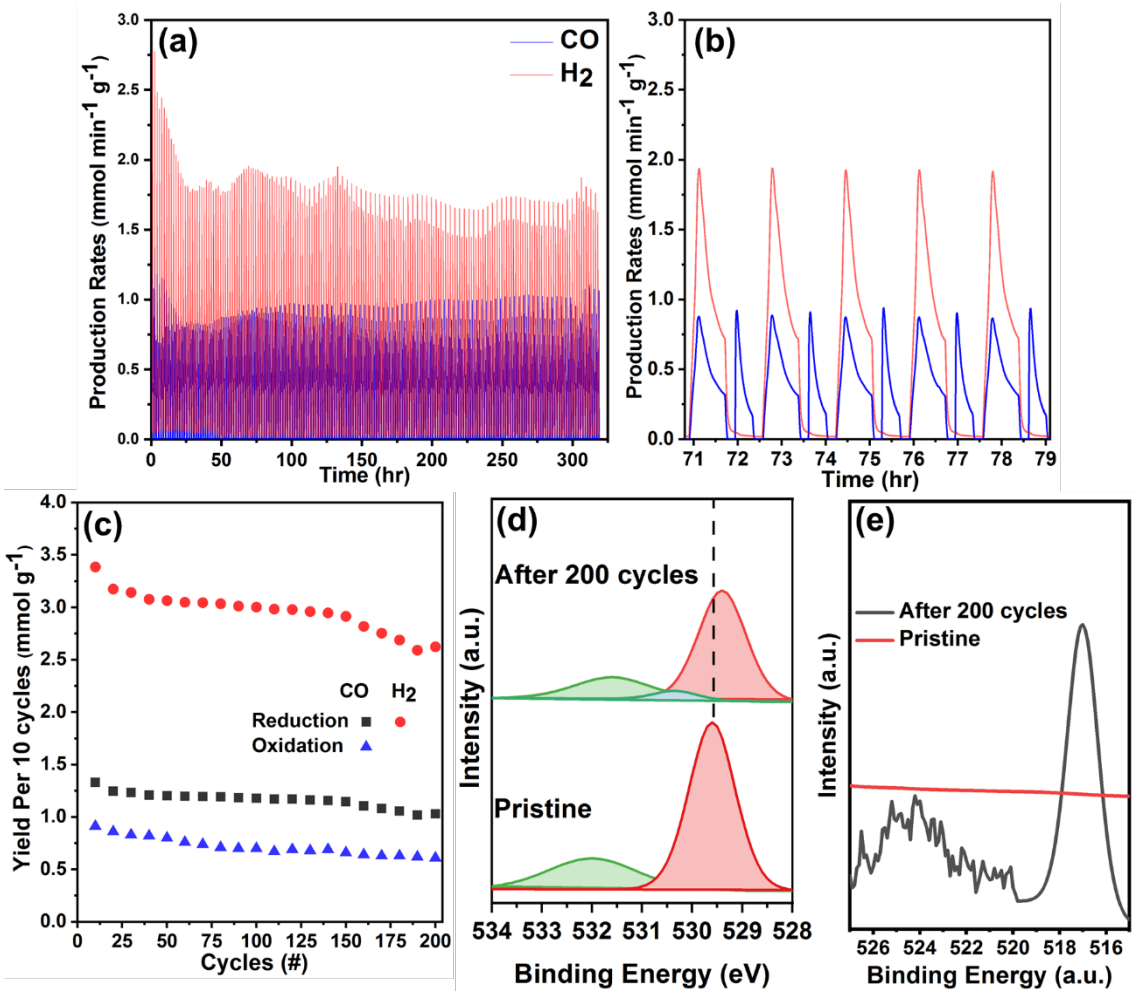

Figure 4.17. Thermochemical redox stability test of $1VCeO_2$ powders and mechanism: (a) syngas production rates, (b) expanded view of production rates for 5 cycles and (c) syngas yields produced during 200 S/MPO–CDS redox cycles. XPS (d) O1s and (e) V 2P spectra of pristine and after cycled $1VCeO_2$ powders.

Figure 4.17b shows an expanded view of the syngas production rates from the 30th to the 35th cycle of the stability test. Average yields of H_2 and CO produced in the reduction

step were 3.1 mmol g^{-1} and 1.37 mmol g^{-1}, respectively and the oxidation of the samples produced up to 0.89 mmol g^{-1} of CO on average (Figure 4.17c). The surface analysis revealed with counts of OI on after-cycled 1VCeO_2 powder surfaces were lower than that on the pristine sample, which also relates to the incomplete oxygen recovery by the lattice (Figure 4.17d). However, surface carbon species may also be the reason for the low oxygen signal. Repeated oxygen exchange pulls the vanadium atoms from the ceria lattice to the surface during the 200-cycle test, which can be observed in the V 2P spectrum measured on after-cycled powder surfaces (Figure 4.17e).

4.3 Discussion

The structural data acquired by XRD, XPS, TEM and XANES suggests three stages of vanadium incorporation into the ceria lattice: (1) pre saturation (1–3%V), (2) saturation (5%V), and (3) post saturation (>5%V), as shown in Figure 4.18. The lattice spacing increases in stage 1 due to the lattice distortions caused by the mismatch in cationic radii. The expanded lattice along with the +5-oxidation state of vanadium create more oxygen vacancies and facilitate the oxygen transport and results in an efficient reforming of methane. According to the phase quantification data, high concentrations of vanadium promote the formation of $CeVO_4$ by impeding the oxygen flow in the ceria lattice. The syngas rates and yield data acquired during the thermochemical performance testing also confirms low oxygen exchange in 5VCe samples during the reduction and oxidation cycles while lattice oxygen in 1VCe is almost double that of vacancy oxygen, which points to an efficient oxygen recovery due to easy oxygen flow. The segregation of $CeVO_4$ on CeO_2 particles is achieved in the post-saturation stage of vanadium doping, which greatly influences the redox performance of ceria.

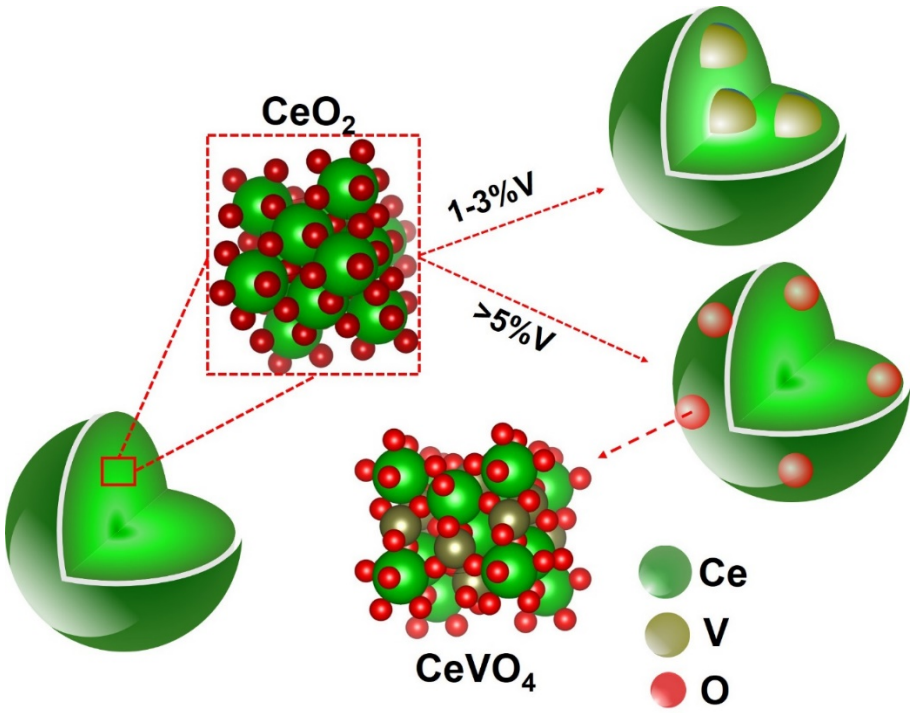

Figure 4.18. Proposed mechanism of vanadium doping in ceria powders.

Cyclic $CeVO_4$ formation with high V-contents pushes the vanadium ions onto the powder surface and cause methane cracking and CO_2 poisoning. High H_2/CO ratios and deposited carbon verify this statement in V-rich *x*VCe samples during MPO–CDS cycles, when compared to that of MPO–WS redox cycles. Pure $CeVO_4$ powders show similar result, where considerable amounts of CO during the H_2O splitting reaction indicate the oxidation of carbon deposited onto the powder surface. This indicates that existence of the separate CeO_2 phase contributes to impeding the methane cracking via its high ionic conductivities, whereas the vanadium ions present onto the powder surface promote the catalytic reduction of methane and produce solid carbon. Here, the doping concentration of vanadium must be controlled to avoid the formation of $CeVO_4$ in the V-doped CeO_2 nanostructures. However, the role of $CeVO_4$ is entirely different in the CeO_2-$CeVO_4$ "mixed-phase" systems, as reported in our previous study.[256] Based on the before and after cycling XPS analysis and the syngas yields data, we hypothesize that vanadium situated in the lattice improves the cycle capacity of ceria with no direct interactions with

the reactant atmosphere, whereas surface vanadium actively participates in the redox reactions and results in high carbon contents and low fuel purity.

The duration of the redox reactions also plays a significant role in the rates of methane partial oxidation and CO_2/H_2O splitting cycles. The after-cycling XPS analysis of V-doped CeO_2 nanopowders confirms the migration of saturated vanadium atoms from the lattice to the surface of ceria particles during long reductions. Whereas, short reduction reactions produce less carbon content, and the H_2/CO ratios are controlled, which is not the case in long redox cycles. The oxygen exchange in the V-saturated xVCeO$_2$ powders also improves during the L/MPO–CDS redox cycles due to long reduction durations at high temperatures.

The nature of oxidation atmospheres displays a critical effect on material behavior and the chemistry of redox reactions. The carbonaceous atmosphere drastically increases the H_2/CO ratios and produces more carbon deposits compared to that from the H_2O splitting reactions, which can be verified from figures 4 and 5. The oxidation of surface carbon species greatly influences the regeneration of $CeVO_4$ phase by suppressing the oxygen transfer, which can be avoided by optimizing the CH_4 and CO_2 flow rates.

4.4 Conclusions

This chapter demonstrates for doping of vanadium into the ceria structures to produce syngas via solar-driven thermochemical redox cycles. Different doping concentrations were strategically incorporated to investigate the saturation limit of vanadium into the ceria structures. This helped to evaluate the role of vanadium in the enhancement of syngas production rates and yields when it is present in the lattice and on the surface of ceria. The vanadium atoms situated inside the ceria lattice simply increased the cycle capacity of ceria by facilitating the oxygen exchange in the expanded lattice and the surface vanadium reacted with CeO_2 and form a separate $CeVO_4$ phase. This segregated

phase took part in the catalytic partial oxidation of methane by exchanging ½ of its O_2 molecule. The activation temperature for an efficient methane partial oxidation reaction decreased from 962°C in pure ceria to 784°C in V-doped ceria. The syngas production yields also increased by 200–400% with stable rates, after the vanadium doping. A long-term stability test produced up to 90 mmol g^{-1} of total syngas during 200 cycles of CO_2 splitting reactions. During these consecutive cycles, V-doped ceria exhibits continuous release of oxygen during the reduction reactions and efficiently draws oxygen from CO_2 upon reoxidation. The XPS study reveals that some vanadium escapes the lattice and accumulates on the surface of ceria powders due to the repetitive exchange of oxygen. However, low vanadium contents (below the saturation levels) on the surface do not react with ceria. X-ray diffraction reveals that the carbonaceous environments promote the vanadium and ceria reactions when compared to H_2O. This first demonstration of V-doped ceria in thermochemical redox cycles, leaves significant room for improvement and may lead to the design of new oxygen carriers and catalysts, which will result in the desired thermochemical performance.

Chapter Five

Ce-Doped V_2O_5 Metal Oxides

Publications relevant to this chapter:

Asim Riaz, Wojciech Lipinski, Adrian Lowe, *Cyclic oxygen exchange capacity of Ce-doped V_2O_5 materials for syngas production via high temperature chemical looping reforming of methane*. Under Review in ACS Catalysis

5.1 Introduction

Significant improvements observed in the syngas production rates and yields by doping CeO_2 lattice with V^{5+} lead to investigate the effects of Ce^{4+} doping into the V_2O_5 lattice. Provided the considerably different redox mechanism, thermochemical performances of V-doped CeO_2 and Ce-doped V_2O_5 materials are presented in separate chapters 4 and 5.

In this chapter, an effective way of unlocking the catalytic properties of vanadia (V_2O_5) for syngas production via thermochemical chemical looping reforming of methane is presented. A fractional amount of cerium was incorporated into the V_2O_5 lattice via a facile liquid phase precursor combustion method. The structural analysis revealed critical information about the phase changes occurring in the vanadia structures after the doping of cerium cations. Pure and Ce-doped vanadia powders were tested for the syngas production via thermochemical looping reforming of methane coupled to H_2O and CO_2 splitting reactions. Chemical nature of powder surfaces was analysed via the XPS technique before and after the cycling. A mechanism for the redox activity of Ce-doped vanadia structures was proposed and correlated with the syngas production performance.

5.2 Results

5.2.1. Pre-cycling materials characterization

Structural, chemical, and morphological studies were carried out to investigate the effects of doping into the V_2O_5 lattice. The FESEM analysis showed a clear decline in the particle size of V_2O_5 powders after cerium incorporation. Furthermore, the highly faceted and crystalline features were approaching a needle like morphology, as shown in Figure 5.1a–5.1c. HRTEM micrographs confirmed the findings of the FESEM analysis, where formation of small and spherical particles can be observed in Figure 5.2a and 5.2b. The insets in the HRTEM images revealed an increased lattice spacing from 0.237 nm in pure V_2O_5 to 0.307 nm in 1CeV powders, which shows distortions in the V_2O_5 lattice caused by the incorporation of larger cerium cations.

X-ray diffraction analysis showed the structural changes induced in the V_2O_5 lattice after cerium doping (Figure 5.3a). Rietveld refinement method is applied on the XRD patterns to quantify phases in the pure and Ce-doped V_2O_5 powders. Lattice expansion caused by the large cerium cations reduced the V^{5+} species to V^{3+} and up to 77.1 % of V_2O_3 phase is observed after 9 % of cerium incorporation. In addition, cerium cations migrated to the surface of Ce-rich V_2O_5 powders and form up to 10.3 % of $CeVO_4$ phase in 9CeV sample. The evolving V_2O_3 and $CeVO_4$ phases with the increasing Ce concentration can be observed in the XRD patterns of pure and Ce-doped V_2O_5 powders (Table 5.1).

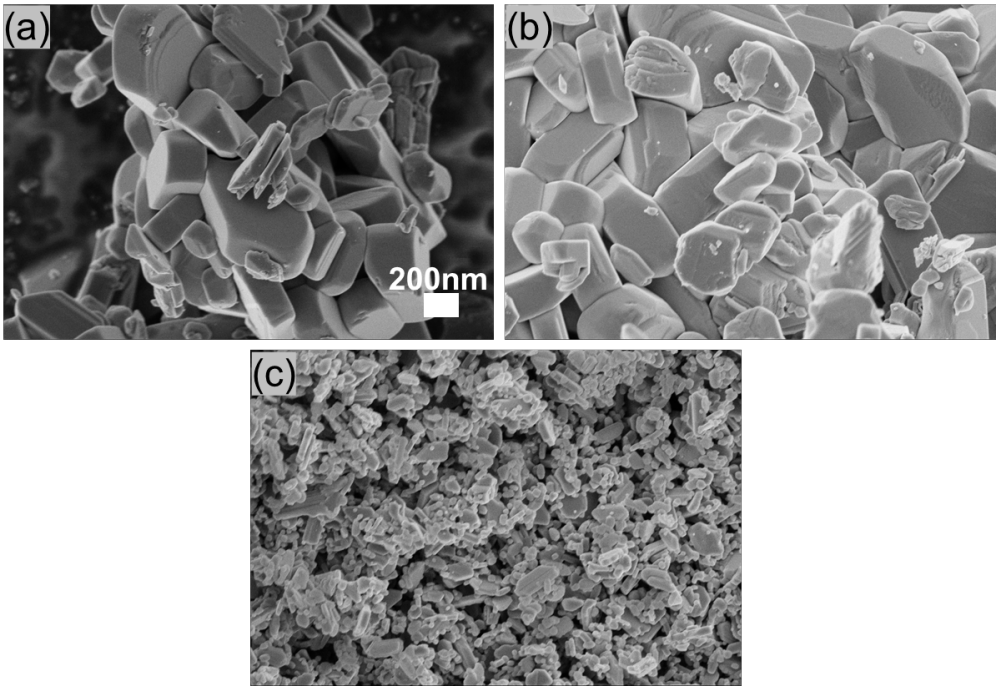

Figure 5.1. Morphological analysis of as-prepared pure and Ce-doped V_2O_5 powders: FESEM micrographs of (a) pure V_2O_5, (b) 3CeV and (c) 9CeV powders.

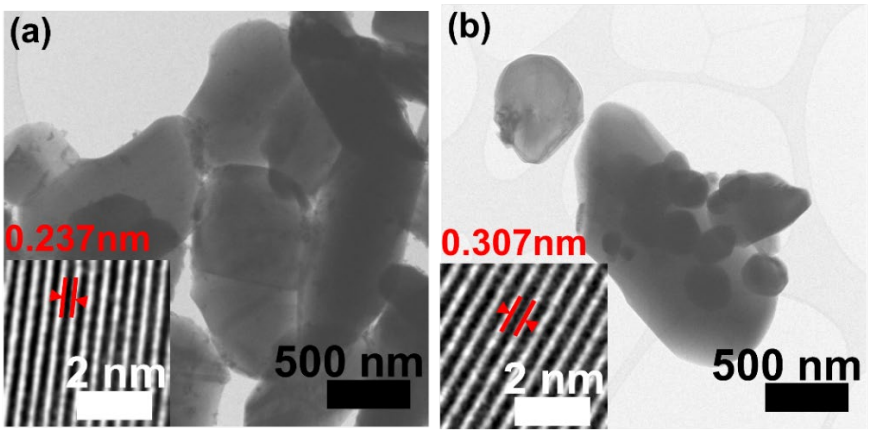

Figure 5.2. Morphological analysis of as-prepared pure and Ce-doped V_2O_5 powders: HRTEM micrographs of (a) pure V_2O_5 and (b) 1CeV powders with insets showing the inner lattice spacing.

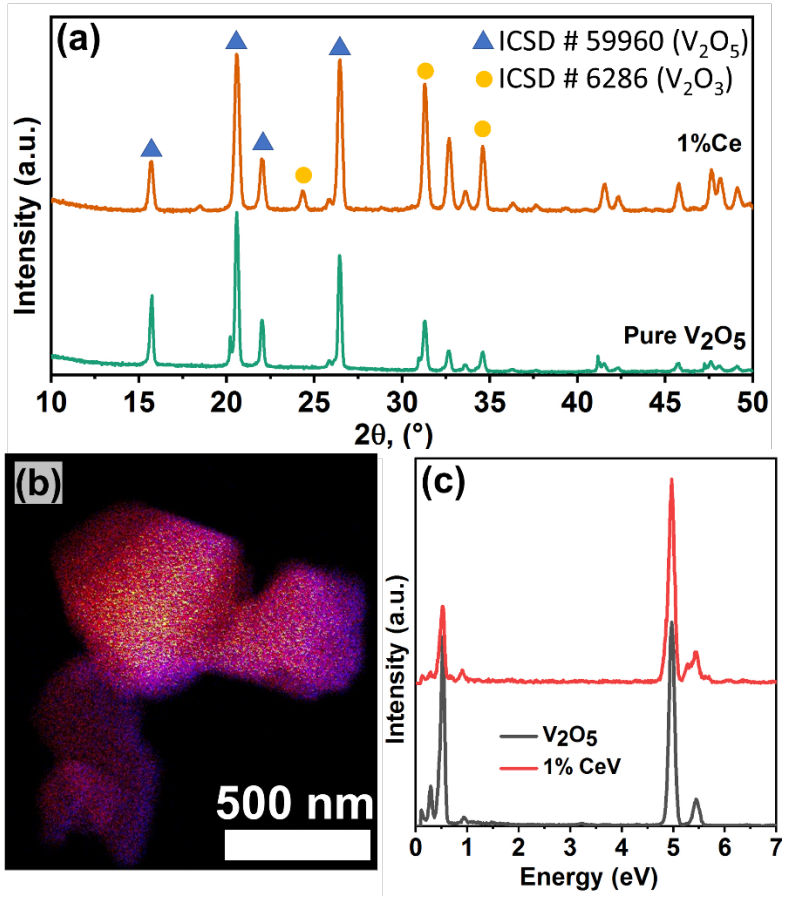

Figure 5.3. Structural and Chemical analysis of as-prepared pure and Ce-doped V_2O_5 powders: (a) XRD patterns of pure V_2O_5 and 1CeV powders, showing evolving V_2O_3 and $CeVO_4$ phase after doping. (b) Overlay image of STEM-EDS maps of 1CeV powders and (c) EDS spectra of pure V_2O_5 and 1CeV powders, showing presence of cerium in the V_2O_5 powders after doping.

Table 5.1. Distribution of phases in as-prepared pure and Ce-doped V_2O_5 powders quantified by applying the Rietveld refinement method on the XRD data.

Material	CeO_2	V_2O_5	V_2O_3	V_2O_4	$CeVO_4$	VC	VO
V_2O_5	0	100	0	0	0	0	0
1CeV	0	94.1	4.9	0	1	0	0
3CeV	0	41.3	55.7	0	3	0	0
5CeV	0	36	59.1	0	4.9	0	0
7CeV	0	25.1	66	0	8.9	0	0
9CeV	0	12.5	77.1	0	10.3	0	0

STEM-EDS technique is used to carry out chemical analysis on pure and Ce-doped V_2O_5 samples. Figure 5.3b shows the overlay image of STEM-EDS elemental mapping of 1CeV sample, where the yellow colour represents cerium. The EDS spectra of pure V_2O_5 and 1CeV samples is shown in Figure 5.3c, where the shoulder peak at 5.23 eV is associated with Ce Lb energy levels.[265] The presence of cerium in doped V_2O_5 was further confirmed by the electron energy loss spectroscopy (EELS) technique, (Figure 5.4a and 5.4b). The Ce O2, Ce CN, Ce M5 and Ce M4 peaks at 15 eV, 120 eV, 883 eV and 801 eV showed the fingerprint EELS signals of cerium, which aligns with the reported EELS features of Ce.[266] EELS features of vanadium are confirmed from the V M2, V L2 and V L3 peaks situated at 38 eV, 519 eV and 525 eV, respectively.

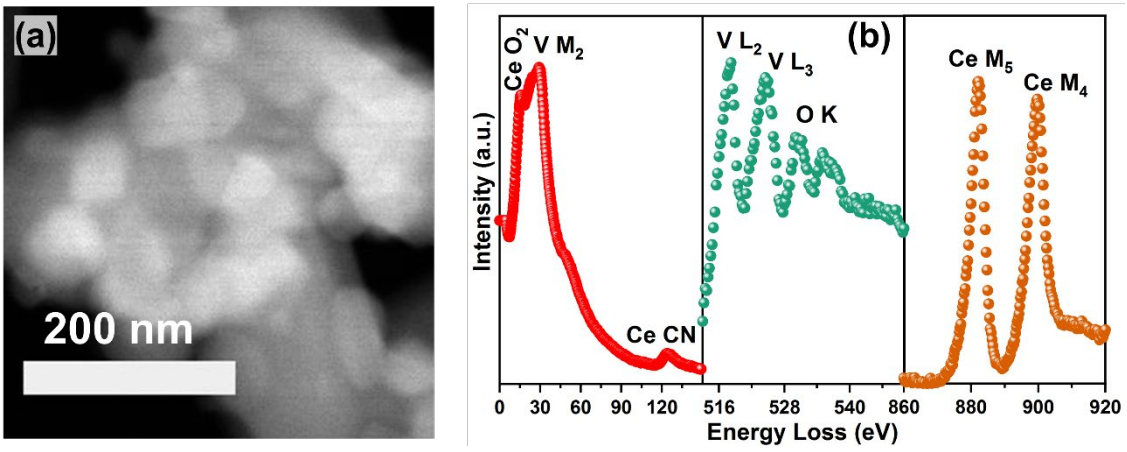

Figure 5.4. Structural analysis of as-prepared pure and Ce-doped V_2O_5 powders: (a) HAADF image and (b) EELS spectra of 1CeV powders.

Formation of V_2O_3 is further confirmed from the Raman spectroscopy technique. Figure 5.5a shows the growing peak of V_2O_3 at Raman shift of 538 cm^{-1}, while distinct peaks of $CeVO_4$ at 860 cm^{-1} and 798 cm^{-1} in the Ce-doped V_2O_5 powders are also observed in the Ce-doped V_2O_5 powders. (Figure 5.5a).[267]

The XPS analysis was carried out to investigate the presence of cerium on the surface of as-prepared V_2O_5 powders. Evidently, the concentration of cerium ions onto the V_2O_5 surfaces increased with higher doping content, Figure 5.5b. Furthermore, the absence of a peak at 917 eV confirms the presence of Ce^{3+} ions in $CeVO_4$, instead of Ce^{4+} ions in the independent oxides of cerium (i.e. CeO_2).

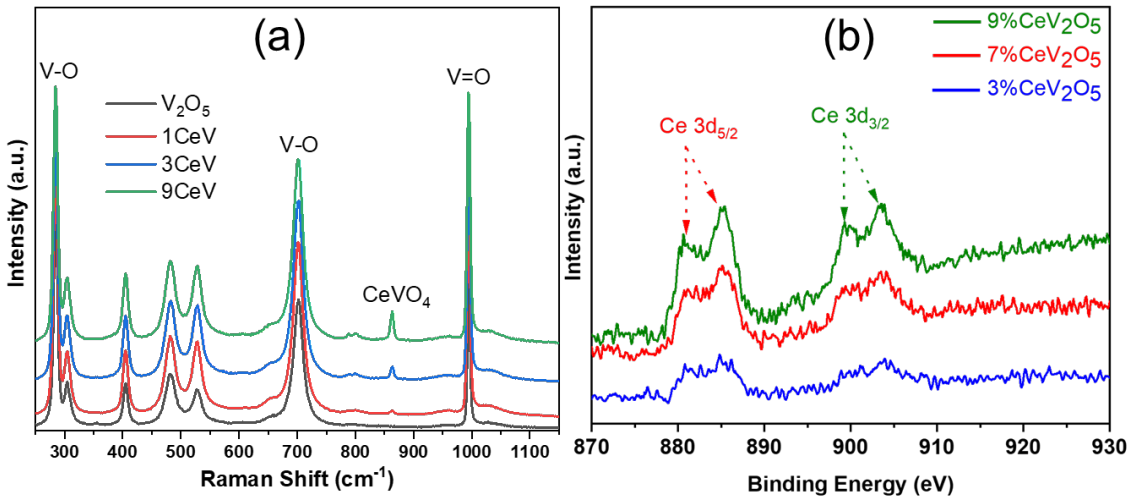

Figure 5.5. Structural and Surface analysis of as-prepared pure and Ce-doped V_2O_5 powders: (a) Raman spectra of pure and Ce-doped V_2O_5 powders depicting the evolution of $CeVO_4$ phase with cerium doping. (b) XPS spectra of pure and Ce-doped V_2O_5 powders showing high Ce^{3+} content onto the powder surfaces with the increasing doping concentrations.

5.2.2. Thermochemical syngas production performance

Different aspects of thermochemical performance of the Ce-doped V_2O_5 powders are compared with the pure V_2O_5 powder samples. These aspects include the activation temperature for methane partial oxidation, preliminary CO_2/H_2O splitting cycles and long-term stability test for up to 100 consecutive cycles.

The activation of pure and Ce-doped V_2O_5 for the methane reforming reaction was investigated by heating the powder samples under a CH_4 flow (20 mL min^{-1}) from 400°C to 1000°C with a heating rate of 3°C. Evolutions of H_2 and CO were monitored by mass spectrometry as described in section 2.3. Figures 5.6a and 5.6b show the instantaneous rates of CO and H_2 produced during the activation test, respectively. It is evident that the CO and H_2 production rates significantly increased after Ce doping.

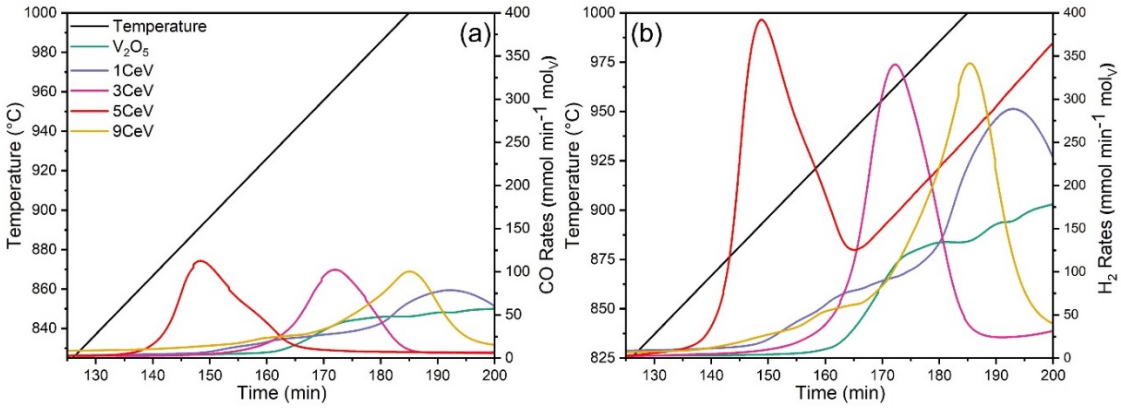

Figure 5.6. Instantaneous (a) CO and (b) H_2 production rates achieved by pure and Ce-doped V_2O_5 powders during a continuous heating from ambient temperature to 1000°C under methane atmosphere.

Ten preliminary WS and CDS cycles were performed to investigate the syngas production performance of pure and Ce-doped V_2O_5 powders. A Blank test is carried out to investigate the amounts of CO and H_2 produced due to possible thermal decomposition of reactant gases. Figure 5.7a compares the syngas produced during MPO–CDS cycles with a blank reactor and with 1CeV sample. Negligible amount of syngas is observed during the blank run, which clearly highlights the role of the redox materials toward achieving efficient and stable syngas production rates. Figures 5.8a, 5.7b and 5.8b compare the syngas production rates of the pure V_2O_5, V_2O_3 with 1CeV powders during MPO–CDS redox cycles. Clearly, pure V_2O_3 and V_2O_5 powders showed inferior and unstable syngas production rates when compared to that of the Ce-doped vanadia samples, where the rates of H_2 and CO produced by 1CeV are up to 500% higher than the

pure V_2O_5 powders. Here, the initial slow rates are due to the slow activation of Ce-doped vanadia powders, which increase and stabilize at 450 $mmol_{H2}$ mol_V min^{-1} and 120 $mmol_{CO}$ mol_V min^{-1} during the MPO reaction, while the average rates of 400 $mmol_{CO}$ mol_V min^{-1} are achieved during the CO_2 splitting step of MPO–CDS cycles. Notably, the syngas production rates achieved during the long-duration reduction-oxidation reactions are up to 80% higher than that of shorter MPO–CDS cycles, Figure 5.8c.

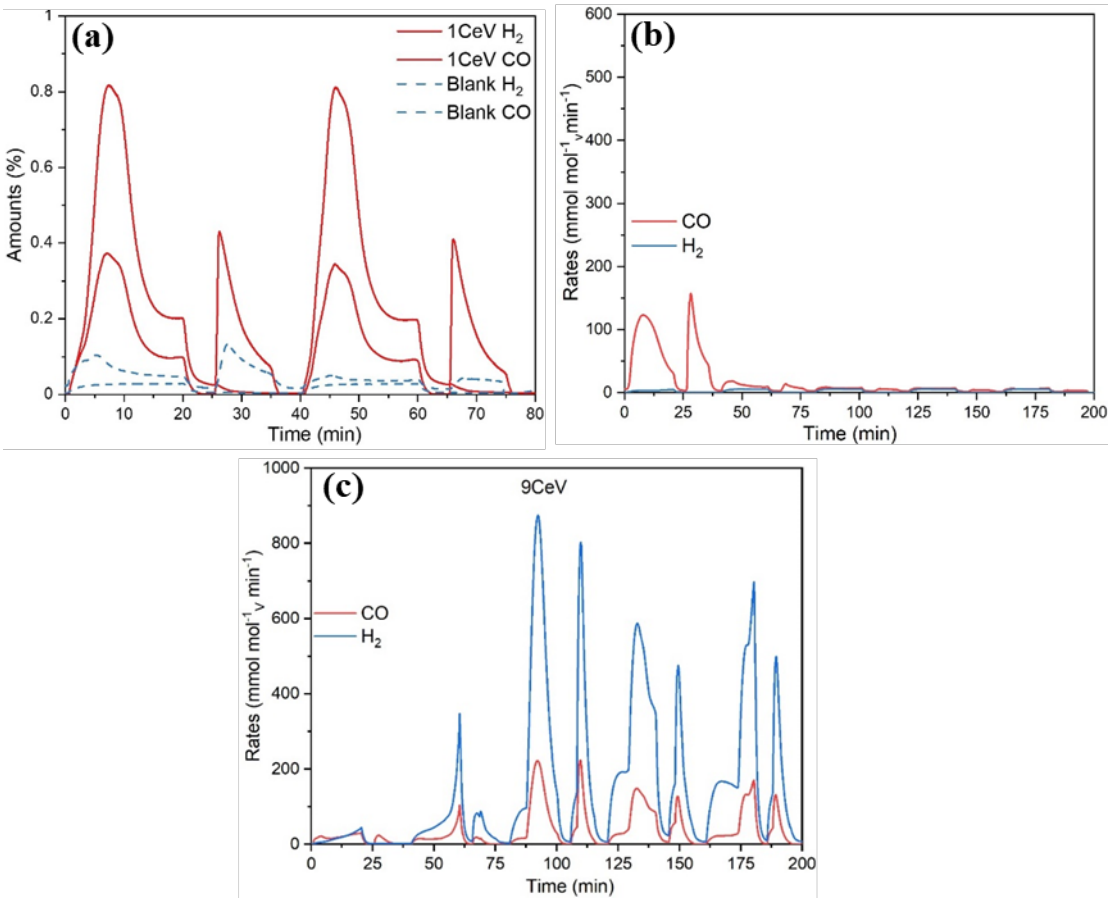

Figure 5.7. Mass-Spectrometer signals for H_2 and CO recorded during MPO-CDS redox cycles for blank and 1CeV samples. (b) Syngas production rates produced by pure V_2O_3 powders during 5 continuous MPO-CDS redox cycles. (c) Syngas production rates produced by 9CeV powders during MPO–WS cycles.

The activation of the pure and Ce-doped V_2O_5 powders is slower during the H_2O splitting reactions as compared to that of CO_2 splitting, as shown in Figure 5.8d. This may be due to a low affinity of these reduced oxygen carriers towards steam compared to CO_2. The highest rates of 180 $mmol_{H2}$ mol_V min^{-1} and 45 $mmol_{CO}$ mol_V min^{-1} during MPO and

210 $mmol_{H2}$ mol_V min^{-1} upon H_2O splitting are achieved by the 1CeV powder samples, while these rates increased by up to 300% with 9 % of cerium incorporation, as shown in Figure 5.7c. However, considerable amounts of CO are observed in the H_2O splitting step, which depicts the oxidation of carbon deposited on the powder surface.

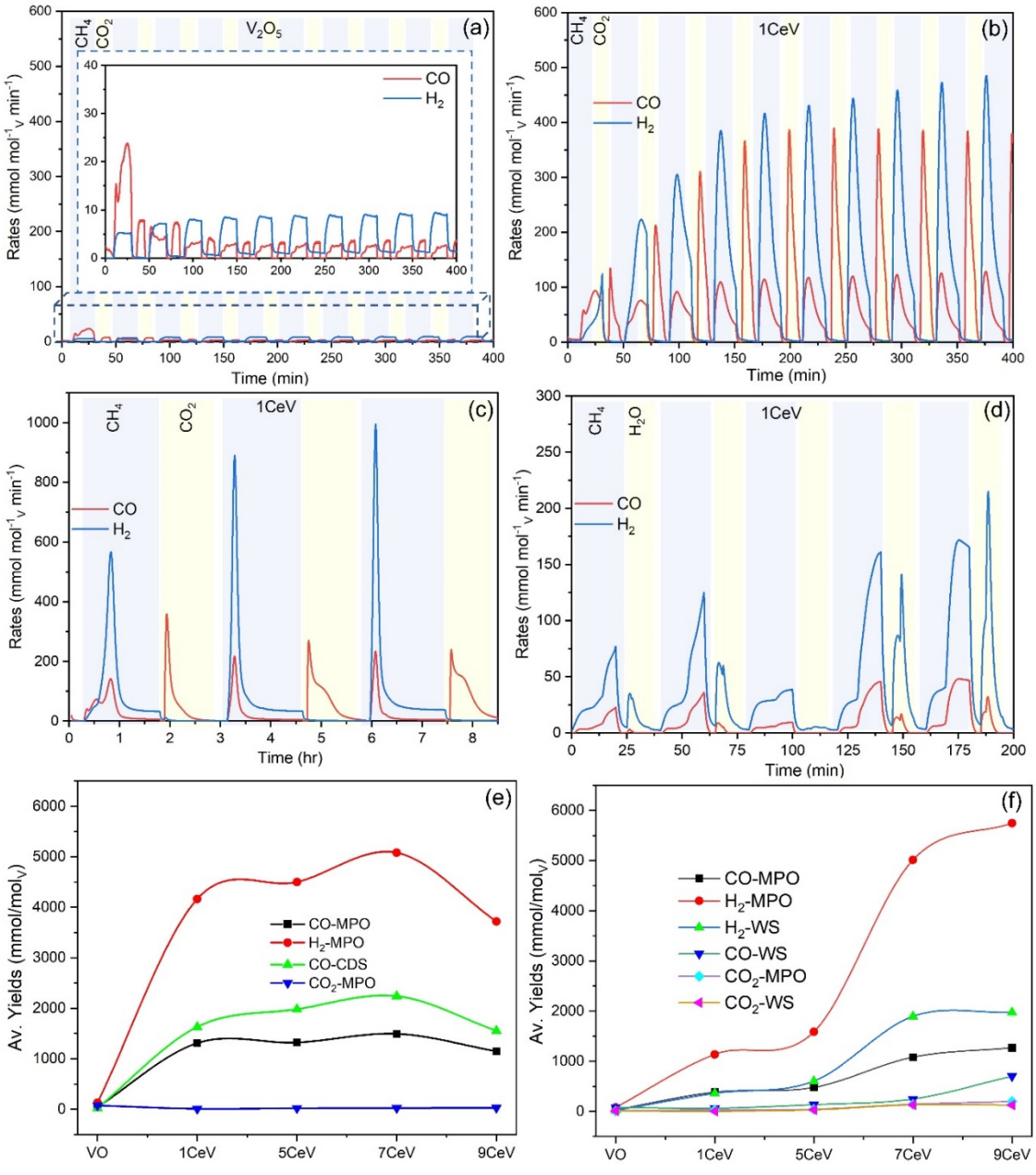

Figure 5.8. Thermochemical fuel production performance: Syngas production rates achieved by (a) pure V_2O_5 and (b) 1CeV powders during 10 MPO–CDS cycles. (c) Syngas production rates achieved by 1CeV powders during (c) MPO–CDS and (d) MPO–WS cycles. Syngas production yields produced by pure and Ce-doped V_2O_5 samples during (e) MPO–CDS and (f) MPO–WS cycling.

The average syngas yields produced during the MPO–CDS and MPO–WS cycling are presented in Figures 5.8e and 5.8f, respectively. High CO yields up to 1.5 mol/mol$_V$ are achieved during the methane partial oxidation reaction of MPO–CDS cycling as compared to that of MPO–WS cycling with maximum CO yields up to 1.02 mol/mol$_V$. Similarly, a higher (*c.*a 0.6) methane conversion is achieved for the MPO–CDS cycling when compared to that of 0.41 during the MPO–WS cycling. The recorded CO_2 to CO conversion ranged from 74% for 1CeV sample to 83% for the 7CeV sample. However, the purity of H_2 is lower for the Ce-rich vanadia materials due to considerable amounts of CO produced upon the oxidation of solid carbon during the H_2O splitting reaction. High solid carbon deposited onto the powder surfaces with high cerium concentration *c.a.* 0.31 mmol support these findings. Notably, negligible amounts of CO_2 are produced during the methane partial oxidation reaction, which leads to high fuel selectivity achieved by the Ce-doped vanadia materials. The maximum CO selectivity achieved for 1CeV powders is 99.3% and 92.7% during the MPO–CDS and MPO–WS cycling, respectively, which is decreased with high cerium contents. In addition, trivial amounts of CO_2 and CO resulted in high purity of H_2 up to 94% during the WS reactions.

5.2.3. Post-cycling materials characterization

The structural and surface analysis of the pure and Ce-doped V_2O_5 powders is carried out after redox cycling. XRD analysis revealed no phase change in the pure and Ce-doped V_2O_5 powders after Ar reduction, while the V_2O_5, V_2O_3 and $CeVO_4$ phases in these powders are mainly reduced into V_2O_4, VO and $CeVO_3$, respectively, when reduced by methane, as shown in Figure 5.9a. Pure V_2O_5 is mainly reduced into V_2O_4 along with the fractions of vanadium carbide (VC) and VO, while the reduced Ce-rich V_2O_5 powders mainly consisted of VO phase. The repeated reduction and oxidation resulted in the V_2O_3 phase as the main constituent in Ce-V_2O_5 powders, while considerable amounts of VO

and VC of up to 20% are also observed possibly due to the incomplete oxidation of the reduced species, as shown in Figure 5.9b and 5.9c.

The inferior syngas production performance of the pure V_2O_3 powders is inconsistent with the former efficient redox behaviour of Ce-doped vanadia powders, where V_2O_3 is the major constituent. Here, cerium plays a crucial role in facilitating the ion mobility and ensuring cyclic and efficient oxygen exchange due to lattice distortions caused by its large cationic radii. In addition, the after cycled pure V_2O_3 powder revealed the presence of V_2O_5 and melting of powder (V_2O_5) is also observed onto the alumina wool, which largely contributes towards the poor syngas rates of pure vanadia samples. So, cerium addition enhances the structural stability of vanadia powders as well.

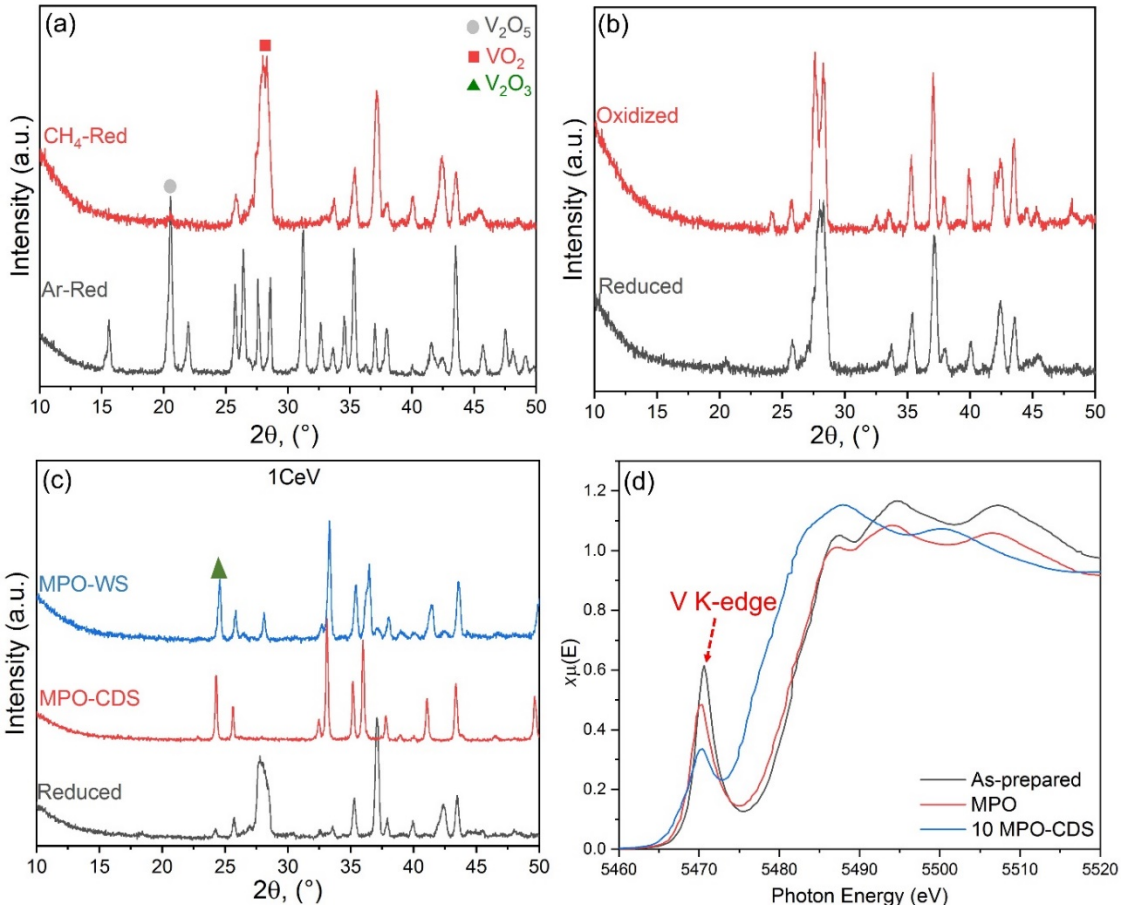

Figure 5.9. Post cycling structural study of 1CeV powders: XRD patterns acquired after (a) reduction under CH_4 and Ar atmospheres, and redox reactions during (b) MPO–CDS

and (c) MPO–WS cycles. (d) Comparison of XANES V^{5+} K-edge spectrum of as prepared, reduced and after MPO–CDS cycling.

The XANES analysis revealed a growing V_2O_3 phase in the Ce-doped V_2O_5 powders after cycling, where intensity of the V^{5+} K-edge peak decreased by up to 50% after 10 MPO–CDS cycles, as shown in Figure 5.9d. The surface interactions during the repeated redox reactions, promoted the formation of $CeVO_4$ phase on the powder surfaces, which corresponds to the residual V^{5+} K-edge peak in the XANES spectra, Figure 5d. This can be further confirmed from the backscattered and FESEM analysis of the Ce-doped V_2O_5 powders after cycling.

The distribution of phases in the Ce-doped V_2O_5 powders is significantly affected by the duration of redox reactions, oxidation atmosphere and concentration of cerium ions. For instance, high cerium content promoted the formation of V_2O_3 phase after reduction and oxidation reactions. The formation of VC phase is prominent in the Ce-rich powders after CDS cycling as compared to the WS, Figure 5.9c. Furthermore, the concentration of $CeVO_3$ phase is higher after CDS cycling when compared to the WS cycling, which indicates to formation of a cyclic $CeVO_4$/$CeVO_3$ redox pair during the WS cycling, while the carbonaceous atmosphere (CO_2) suppresses the oxidation of reduced powders.

XPS analysis revealed the nature of oxygen species present onto the powder surfaces before and after cycling. The reduction of 5CeV powders in methane and Ar atmosphere presented distinct changes in the oxygen species OI, OII and OIII, termed as lattice oxygen, near vacancy region and surface adsorbed, respectively. Large area of OII peak depicts high extents of oxygen exchange in samples during the MPO reaction as compared to the reduction in Atmosphere. Whereas, the formation of CO caused higher surface adsorbed species during the MPO reaction, as shown in Figure 5.10a. The XPS spectra of reduced and reoxidized 5CeV powders are presented in Figure 5.10b, where changes in OI and OII species are associated with the exchange of oxygen during the reduction and

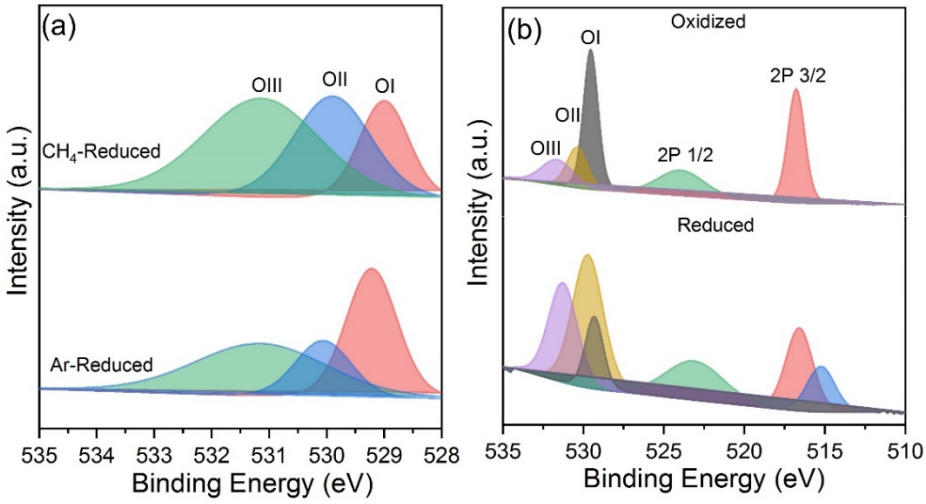

Figure 5. 10. Surface analysis of oxygen carriers after cycling: (a) XPS spectra of reduced 3CeV powders in CH_4 and Ar atmosphere. (b) XPS spectra of 3CeV powders, acquired after the reduction and oxidation reactions during MPO–CDS cycles.

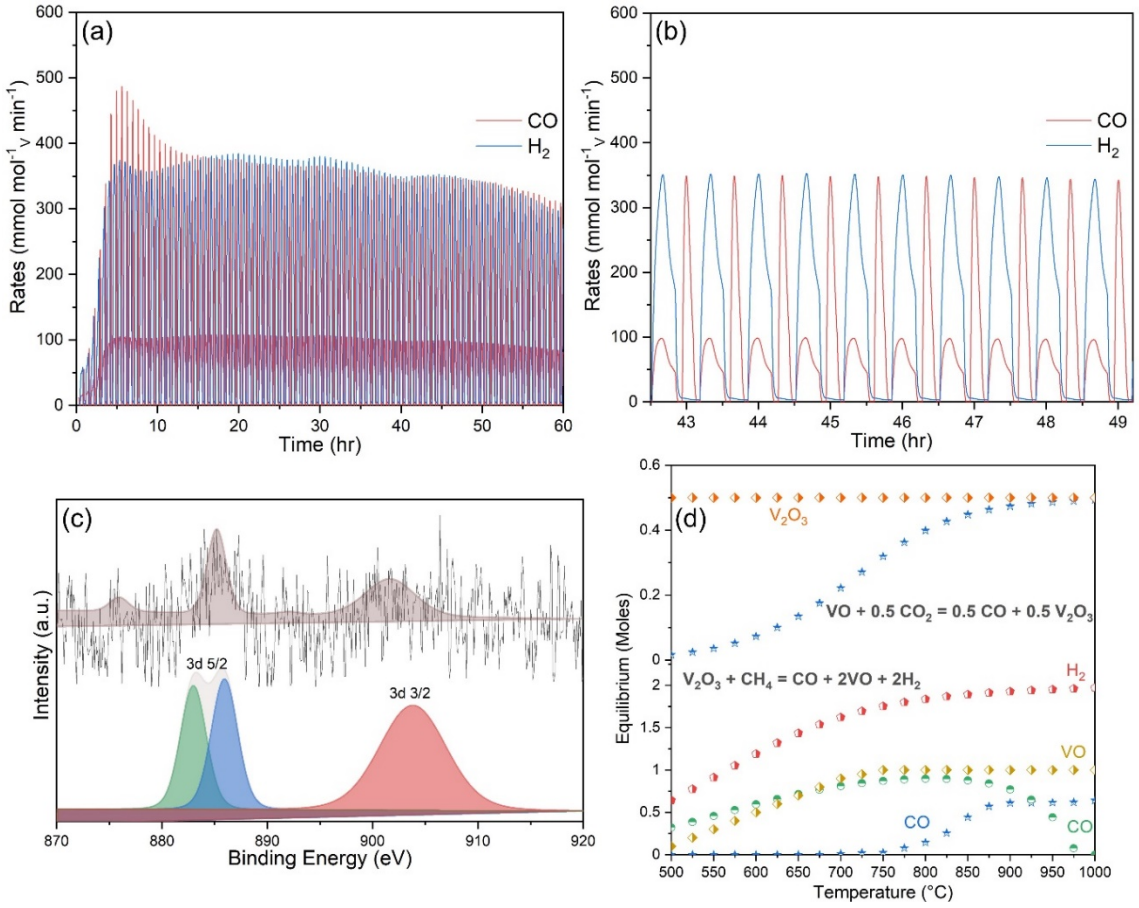

Figure 5.11. (a) Syngas production rates achieved by 1CeV powders during 200 continuous MPO–CDS cycles. (b) The expanded view of part (a) from 63rd to 72th cycle. (c) XPS spectra of 1CeV sample, acquired after the 100 MPO–CDS cycles. (d) Equilibrium distribution of products formed during the MPO and CDS reactions,

produced by the V_2O_3/VO redox pair. The reactions have been balanced and equilibrium products were calculated by Factsage.

oxidation reactions. A split in the V 2P 3/2 is observed after reduction, which may correspond to the multiple valance states of vanadium formed during the MPO reaction.

A long-term stability test of up to 100 MPO–CDS cycles is performed on the Ce-doped V_2O_5 powders. The syngas production rates increased and stabilized after the initial slow rates, Figure 5.11a. The average rates of up to 360 $mmol_{H2}$ g^{-1} min^{-1} and 150 $mmol_{CO}$ g^{-1} min^{-1} are achieved during the methane partial oxidation reaction, while the splitting of CO_2 resulted in 180 $mmol_{CO}$ g^{-1} min^{-1}, Figure 5.11b. The repeated reduction and oxidation reactions promoted the cerium ions to interact with the reactant gases at the powder surfaces. The presence of cerium onto the powder surface can be confirmed from the XPS analysis, as shown in Figure 5.11c.

5.3 Discussion

Structural study revealed that fractional incorporation of cerium into the V_2O_5 lattice shifts the oxidation state from +5 to +3. Surface analysis showed cerium onto the surface of powders with cerium doping concentrations greater than 5%, which is further confirmed by the presence of $CeVO_4$ phase observed in the XRD analysis. Repeated reduction and oxidation reactions resulted in a V_2O_3/VO redox pair. The equilibrium phases calculated by Factsage equilibrium module in the V_2O_3/VO cycle during the reduction and oxidation reactions are presented in Figure 5.11d, where the V_2O_3 phase is reduced to VO during methane reforming and reoxidised by CO_2 into V_2O_3. Here, the stability of V_2O_3/VO cycle is greatly influenced by the concentration of cerium ions which are responsible of a complete conversion of V_2O_5 to V_2O_3 phase and result in a reversible redox pair (V_2O_3/VO) without the issue of powder melting and produce considerable rates of syngas during the thermochemical redox reactions. However, cerium ions present inside lattice and onto the surface of vanadia structure, may have

entirely different characteristics for the redox reactions, depending on the cerium concentration. For instance, lattice cerium ions enhance the structural stability and ion conductivity of the vanadia powders, while surface cerium ions lower the methane cracking. Whereas a segregated phase "$CeVO_4$" is formed on the surface of Ce-rich vanadia powders, which has adverse effects on the syngas production performance. For instance, formation of a $CeVO_4/CeVO_3$ redox pair is cyclic when surrounded by cerium cations, as reported in our previous study.[268] whereas the reoxidation of the $CeVO_3$ is slow on vanadia powders and impedes the oxygen flow into the vanadia structure, which results in inferior syngas production performance. In addition, carbonaceous atmospheres further slowdown the reoxidation of $CeVO_3$ phase, which in result lowers the overall syngas yields and fuel selectivity. Hence, Ce-doped vanadia powders are independent of the $CeVO_4$, in fact formation of the $CeVO_4$ phase leaves few cerium cations, required to achieve high oxygen exchange capacity in vanadia structure. Non-cyclic and unstable redox behaviour of pure V_2O_5 and V_2O_3 materials also highlight the role of cerium incorporation for repeated and efficient oxygen exchange capacity during the methane partial oxidation and CO_2/H_2O splitting reactions.

5.4 Conclusion

In this study, a way to utilize vanadium-based oxygen carriers for syngas production via high temperature chemical looping reforming of methane is demonstrated. Fractional amounts of large cerium cations are incorporated into the V_2O_5 lattice, which resulted in a V_2O_5 to V_2O_3 phase transition and formed a segregated $CeVO_4$ phase on the surface. Compared to the pure V_2O_3 phase, combination of cerium and V_2O_3 showed excellent redox capability and chemical stability at high temperatures. The structural and phase analysis revealed a VO/V_2O_3 redox pair formed during the repeated reduction and oxidation reactions for up to 200 cycles. Formation of this redox pair is resulted after the initial slow syngas production. Cerium cations tend to move between the surface and lattice of the vanadia powders, which significantly affected the syngas production performance, depending on the doping concentration. For instance, low concentrations of cerium improve the rates and yields of syngas produced by the vanadia powders. Whereas large quantity of the $CeVO_4$ phase is formed in the cerium rich vanadia powders, which slowed down the reoxidation rates and result in high carbon contents and low syngas yields. These findings promote a comprehensive research on the materials aspect of oxygen carriers while developing new metal oxides for syngas production via thermochemical routes.

Chapter Six

CeO_2–V_2O_5 Mixed Metal Oxides

Publications relevant to this chapter:

Asim Riaz, MU. ALI, W. Lipinski and A. Lowe, (2019), *Enhanced oxygen exchange capacity in nanostructured ceria–vanadia multi-phase oxygen carriers for solar thermal fuel production*, Journal of Materials Chemistry A, 7, 27349-27360

Asim Riaz, MU. Ali, TG. Enge, T. Tsuzuki, A. Lowe and W. Lipinski, *Concentration-Dependent Solar Thermochemical CO_2/H_2O Splitting Performance by Vanadia-Ceria Multi-Phase Metal Oxide Systems,* Research, 3049534

6.1 Introduction

After successful demonstration of doped cerium and vanadium oxides systems in chapter 4 and 5, this chapter presents a method for stabilizing the reaction rates and structural parameters of ceria by utilizing the vanadia−ceria binary phase system. The materials are synthesized by a facile liquid phase precursor combustion method. Compared to the conventional impregnation method, liquid phase precursor combustion methods deliver better control of particle size, morphology, and dispersion of vanadia particles on the ceria. V-to-Ce atomic ratios of 0 to 100% are investigated. Structural studies of Ce–V–O systems revealed that surface vanadia species on ceria play an important role around stable reaction rates over 100 cycles during H_2O and CO_2 splitting at 900°C. Oxidation of Ce–V–O during CDS, WS, WS–CDS and WS–CDS after MPO also reveals interesting facts about metal–CO_2 and metal–H_2O interactions. We observed that sequential WS and CDS cycles enhanced the hydrogen purity and production yield during the WS step. This resulted in higher and stable MPO rates because addition of a CDS step after WS reaction oxidized the remaining reduced Ce–V–O species and there is more stoichiometric oxygen present to partially oxidize the methane, while introducing a WS step after the CDS reaction oxidized the deposited carbon on the oxygen carriers. We also observed that combination of vanadia and ceria greatly stabilized the microstructure and specific surface area of pure nano-structured ceria. We believe that this study may be useful in the development of new, efficient oxygen carriers for upscale production of solar fuel *via* thermochemical redox reactions. Specifically, the sequential WS and CDS cycling can be utilized on the wide range of oxygen carriers reported earlier e.g., recently developed Ce-doped Mn_3O_4 [206] and La-doped strontium manganates.[244]

6.2 Results

6.2.1. Materials characterization

Figure 6.1 shows transmission electron microscopy (TEM) images of as-prepared vanadia–ceria systems, representing a similar nanoscale morphology consisting of agglomerated semi-spherical particles. The particle size increased with increasing V concentration. The average particle size of pure CeO_2 is 12 ± 3 nm, which increased to 55 ± 5 nm with the addition of 75% V, while pure V_2O_5 has the highest average particle size of 89 ± 3 nm.

Structural comparison of as-prepared pure nano-structured ceria and CV25 nanoparticles is shown in Figures 6.2a and 6.2b. High-resolution transmission electron microscope (HRTEM) analysis of samples revealed similar semi-spherical nanoparticles exposing two distinct lattice spacings of 0.437 nm and 0.307 nm corresponding to the (010) and (111) planes of vanadia and ceria, respectively (Figure 6.2b). These findings confirm the two distinct phases of ceria and cerium vanadate, observed in the XRD patterns with crystallite sizes of 12 ± 2.5 nm and 13 ± 3.2 nm for pure nano-structured ceria and CeO_2–V_2O_5 binary phase systems, respectively.

Energy dispersive X-ray spectroscopy (EDX) analysis revealed distinct emission energy peaks of Ce, V and carbon content before and after methane partial oxidation of CV25, as shown in Figure 6.2b and 6.2c. The STEM-EDS mapping of reduced CV25 sample represents the elemental distribution of vanadium, cerium and carbon after the methane partial oxidation reaction, as shown in Figure 6.2e and 6.2f. The intensity of the carbon peak was higher in the reduced CV25 sample than in the as-prepared CV25 sample, which indicates possible carbon deposition on the metal oxide.

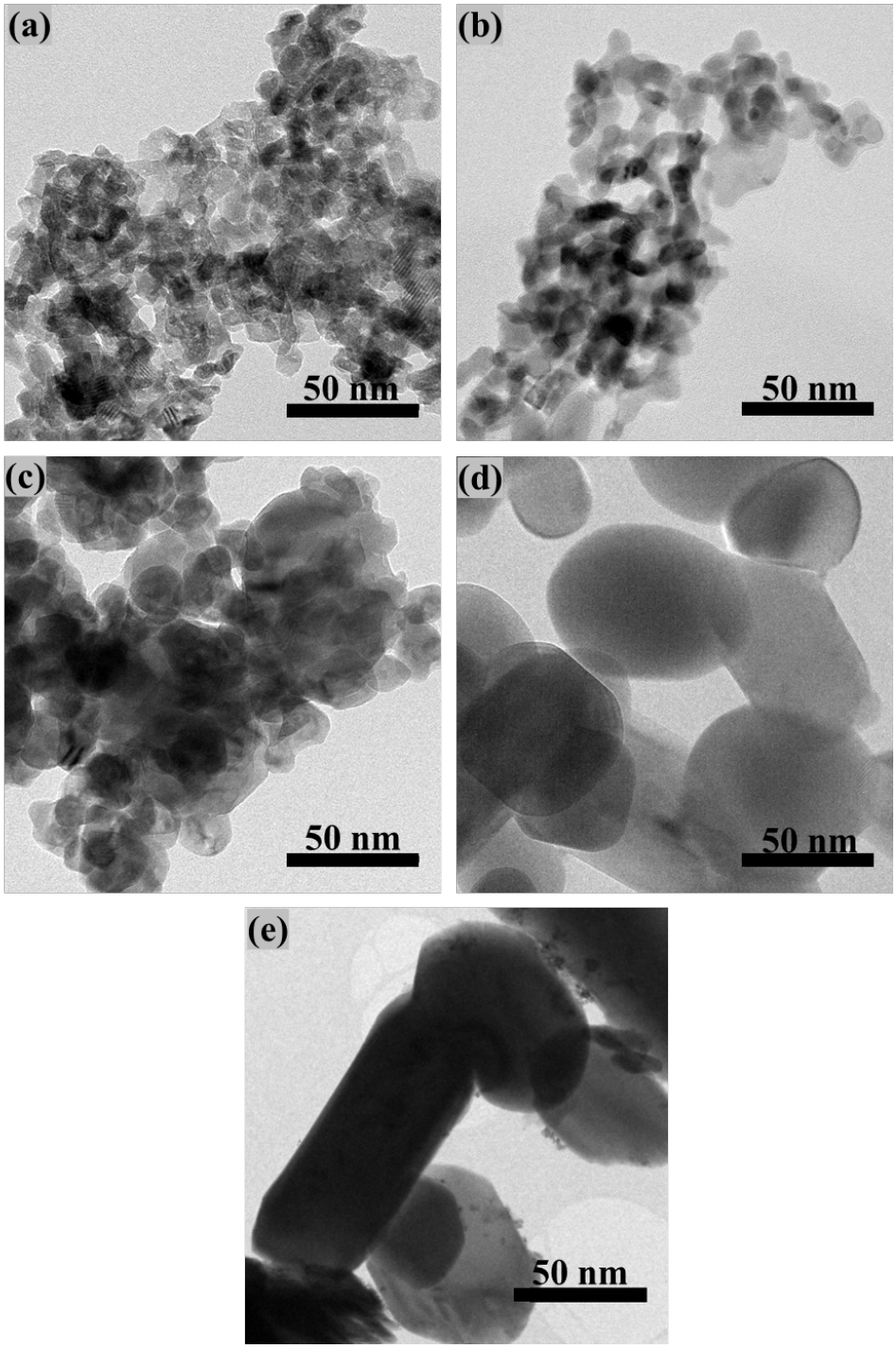

Figure 6.1. Morphology and size estimation: Transmission electron microscopy images of as-prepared (a) pure CeO_2, (b) CV25, (c) CV50, (d) CV75, and (e) pure V_2O_5. The inserts in each image shows the lattice spacing and crystal planes of the vanadia–ceria system.

The morphological study of vanadia–ceria systems after MPO–CDS cycles was carried out using FESEM. It revealed extensive sintering in pure V_2O_5 and CeO_2 samples,

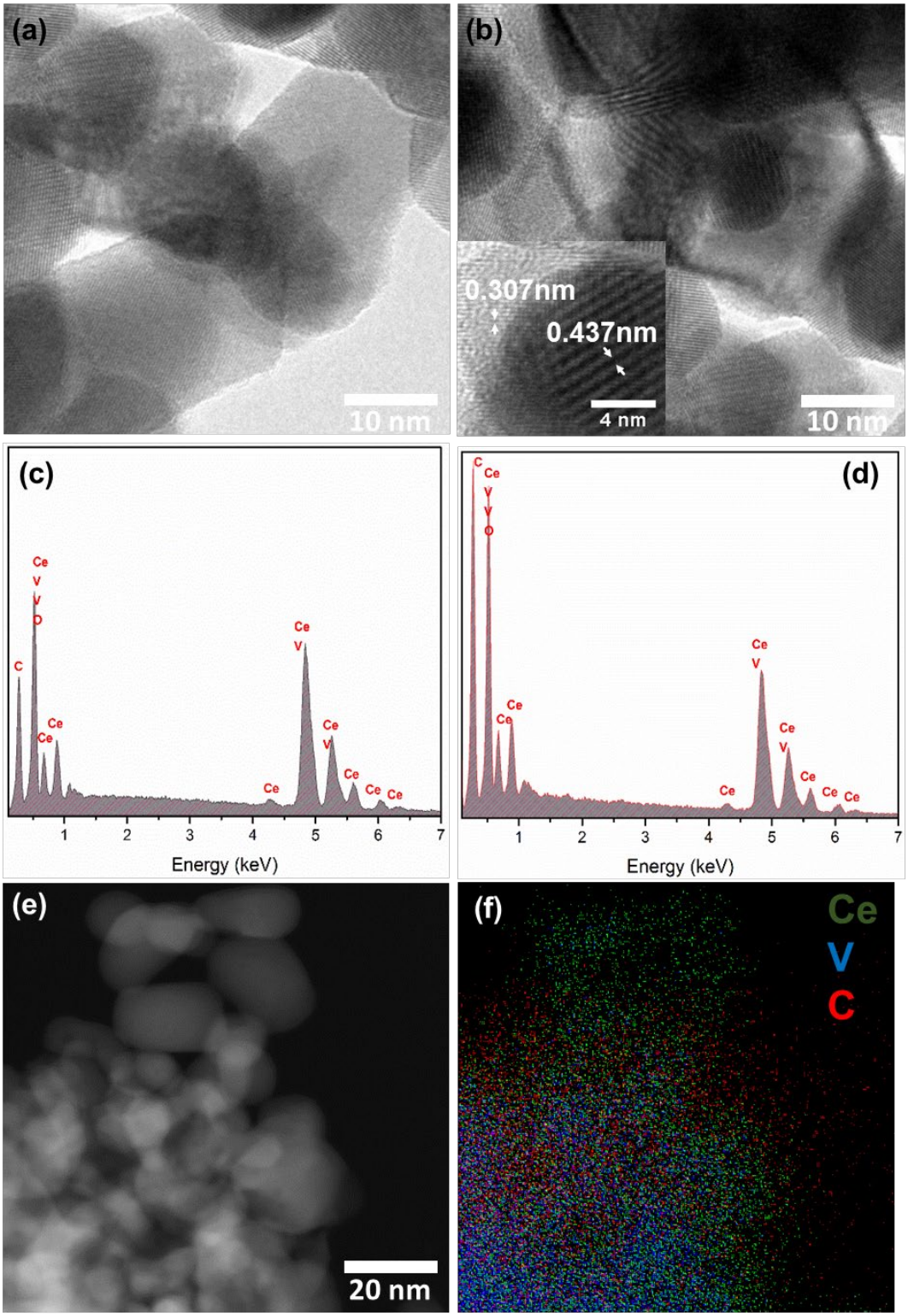

Figure 6.2. Chemical and morphological characterization of pure nano-ceria and CV25: HRTEM images representing the size and morphology of as-prepared (a) pure ceria and (b) CV25, nanoparticles. Inset shows d-spacings of vanadium and cerium present in CV25. EDS spectra of (c) as prepared and (d) reduced CV25 nanoparticles. STEM EDS (e) grey scan and (f) overlay mapping of reduced CV25 showing the distribution of Ce (green), V (blue) and C (red) in samples after methane partial oxidation.

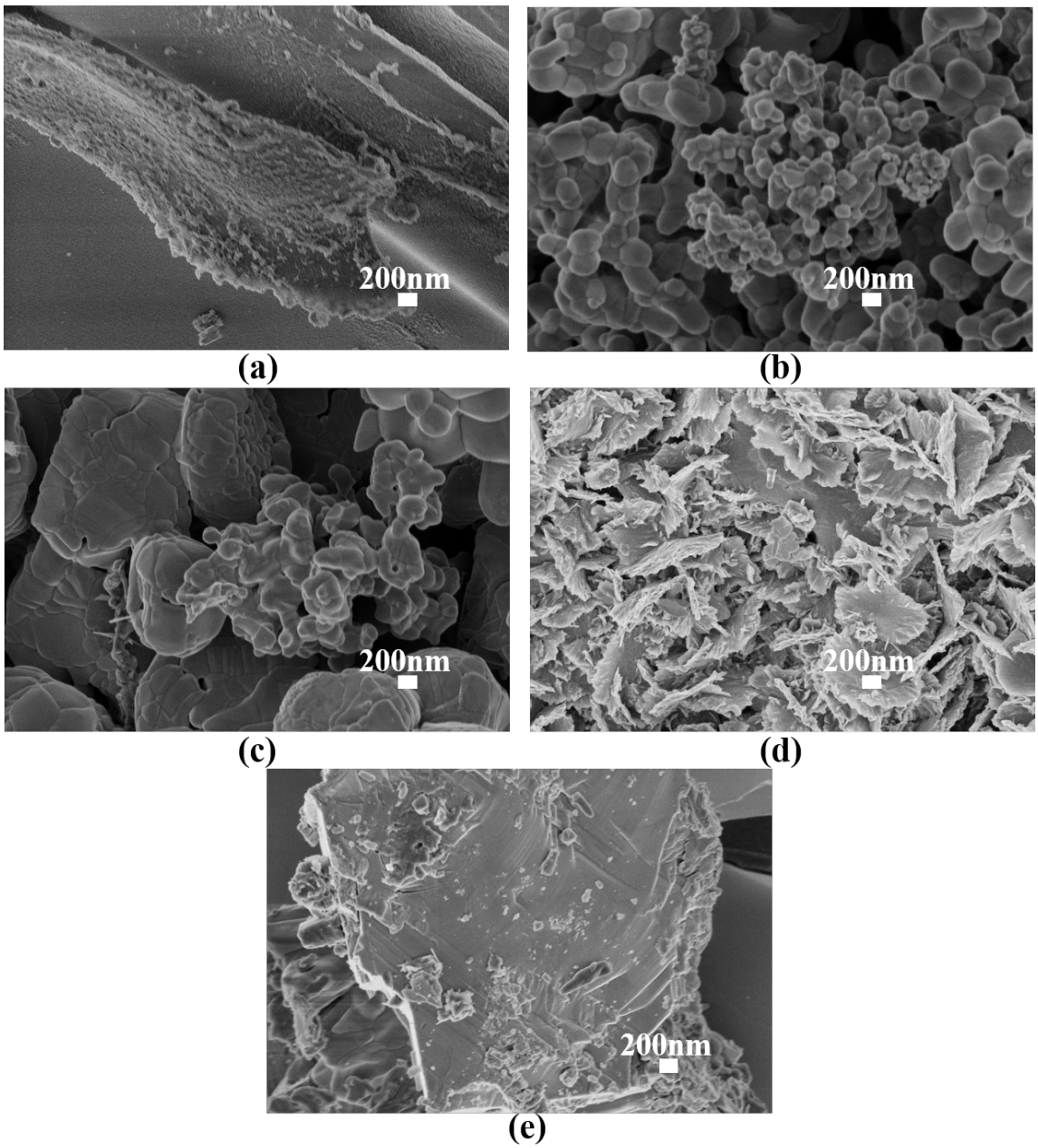

Figure 6.3. Morphological investigation of cycled V_2O_5–CeO_2 systems after MPO–CDS redox cycles: Scanning electron microscopy images of after MPO–CDS cycled (a) Pure CeO_2, (b) CV25, (c) CV50, (d) CV75 and (e) V_2O_5, showing the change in morphology of the metal oxides due to high temperature sintering and chemical reactions occurring on surface and bulk of powders.

showing individual particles fused into large microparticles. The sintering was most prominent in V-rich vanadia–ceria mixed-metal-oxides particles (Figure 6.3a–e).

The TEM image of a reduced CV75 sample before MPO–CDS cycles showed sintering of small particles forming a sheet-like morphology, while individual particles were also

observed. The CV75 sample after MPO–CDS cycles showed extensive sintering which resulted in a particle size of > 500 nm.

XRD spectra of as-prepared CeO_2, V_2O_5 and vanadia–ceria ultrafine particles are presented in Figure 6.4a. Pure ceria consisted of a dominant peak of triclinic crystal structure with a low-angle shoulder of cubic CeO_2. As-prepared nano-structured ceria was calcined at 600°C and 900°C to further investigate this behaviour. Low temperature calcination resulted in amorphous-like triclinic structures, while at the higher calcination temperature, a more defined crystalline triclinic ceria was seen with shoulder peaks of cubic ceria. A comparison of XRD patterns obtained from calcined, commercial, reference triclinic and cubic ceria structures is presented in Figure 6.5a.

Addition of V in CeO_2 promoted the formation of cerium vanadate ($CeVO_4$, JCPDS # 72-0282) as seen in Reaction 5.1, accompanied by a change in the valence of Ce from Ce^{+4} to Ce^{+3}, while the valence of V remains V^{5+}.

Evolution of the $CeVO_4$ phase was observed from the growth of shoulder peaks at 2θ 48.2° and doublets at 2θ 32.87° with the increase in vanadium content greater than 25%. Controlled conversion of CeO_2 and V_2O_5 into $CeVO_4$ was observed up to 25%V loading, where a mixture of CeO_2 and $CeVO_4$ with a ratio of CeO_2:$CeVO_4$ (~3) was achieved. However, a further increase in vanadium concentration resulted in a drastic decline in the CeO_2 concentration by 96% with 75%V addition. This was visualized by the ratio of CeO_2 to $CeVO_4$ intensities (I_{CeO2}/I_{CeVO4}) evaluated from XRD patterns of as- prepared vanadia–ceria systems, presented in Figure 6.5b. Large quantities of V_2O_3 up to 46.1% were also observed along with only 17% $CeVO_4$ with 75%V addition.

XRD patterns of reduced vanadia–ceria systems are presented in Figure 6.4b. Reduced pure CeO_2 did not undergo any structural change except shifting of diffraction peaks to lower angles, possibly caused by oxygen depletion. However, reduction of pure V_2O_5

resulted in the conversion of V^{5+} to V^{4+}, which can be seen as the presence of a VO_2 phase in the XRD pattern of reduced V_2O_5 and CV75.[269] The presence of vanadium carbide (JCPDS#89-1096) and metallic V indicated the catalytic interaction of pure V_2O_5 with methane to produce carbon during the methane partial oxidation reaction.[134,270,271] A decline in the peak intensities of the $CeVO_4$ phase was observed for CV25, which indicated the conversion of V^{5+} to V^{3+} due to the formation of a $CeVO_3$ phase.

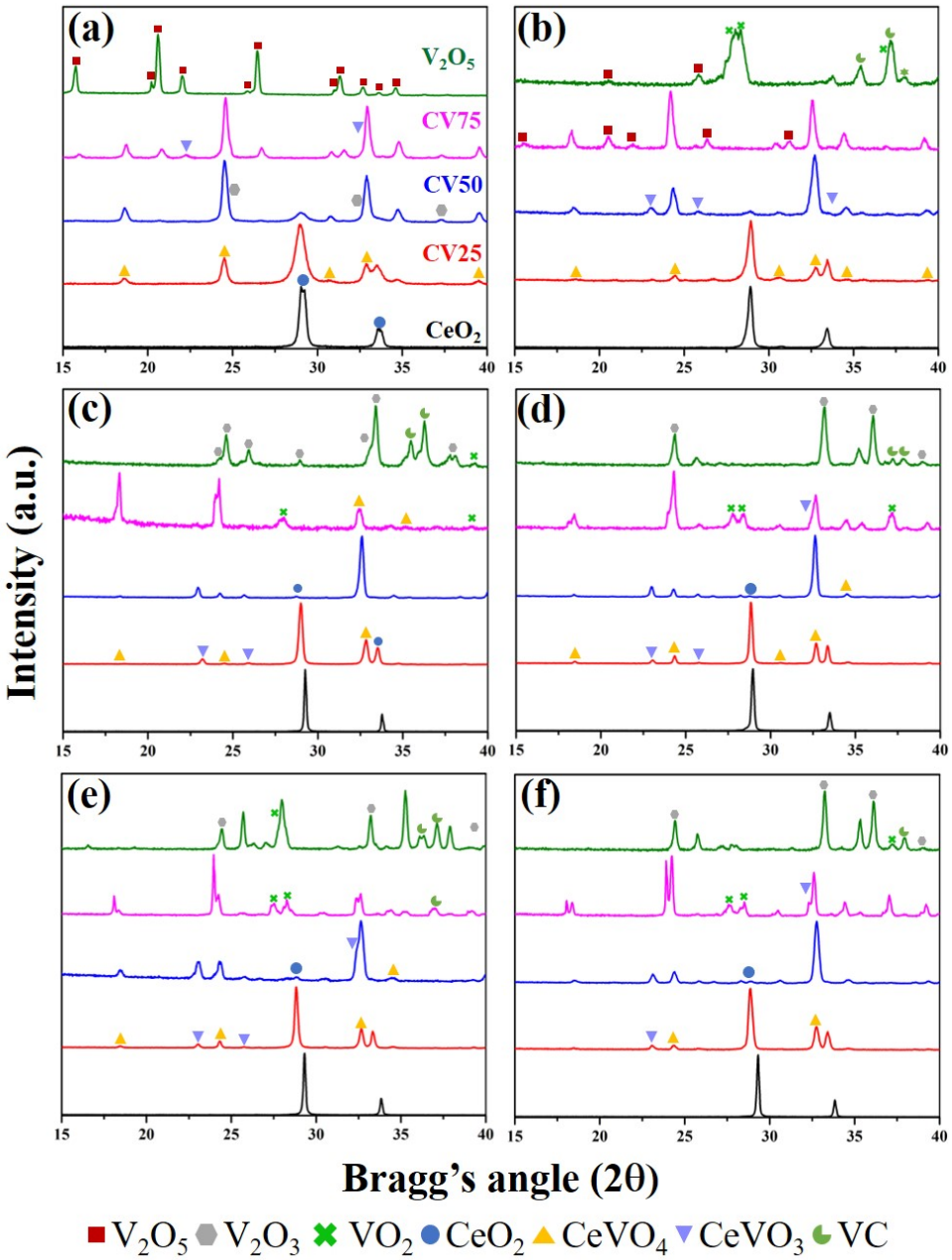

Figure 6.4. Structural analysis of vanadia–ceria systems: XRD patterns of (a) as-prepared and after cycled (b) reduced, (c) MPO–CDS, (d) MPO–WS, (e) MPO–WS–CDS, and (f) MPO–CDS–WS, pure ceria, CV25, CV50, CV75, and pure V_2O_5 representing the

evolution of $CeVO_4$ as a function of vanadium content and structural changes in after-cycling. Spheres, upward cones, hexagons, downward cones, squares, crosses, and crescents represent CeO_2, $CeVO_4$, V_2O_3, $CeVO_3$, V_2O_5, VO_2, and VC phase, respectively.

The XRD patterns of pure V_2O_5, CV25, CV50 and CV75 samples after 10 consecutive cycles of MPO–CDS, MPO–WS, MPO–WS–CDS and MPO–CDS–WS are presented in Figures 6.4c–6.4f. In CV25, the diffraction angles of $CeVO_4$ shifted to lower angles after 10 MPO–CDS cycles. The presence of peaks associated with $CeVO_3$ indicates the partial oxidation of $CeVO_3$ to $CeVO_4$ due possibly to incomplete recovery of oxygen. This phenomenon can be related to the carbon deposition on oxygen carriers which hinders the re-oxidation of reduced species, resulting in few oxygen species in the material being available for an efficient methane reforming reaction. Consequently, it results in further methane cracking with high H_2 products and low CO emission, resulting in a high H_2/CO ratio.

Segregated phases of $CeVO_3$, $CeVO_4$ and VO_2 were observed in the XRD patterns of CV75. However, oxidation of reduced V_2O_5 resulted in the oxidation of vanadium carbide and metallic V to V_2O_3 and VO_2. The XRD analysis of V_2O_5–CeO_2 systems after the redox cycles revealed that formation of the $CeVO_4$ phase increases with increasing V content, reflecting the contribution of V in the redox reactions. Ce^{3+} sites were stabilized by the valance change (Ce^{4+} to Ce^{3+}) during the formation of $CeVO_3$/$CeVO_4$.[260,263] However, addition of a CDS step after WS oxidizes carbon from the surface of the oxygen carrier which reduces methane cracking during the MPO step. This was verified by comparing the H_2/CO ratios of CV25 during MPO–WS, MPO–WS–CDS and MPO–CDS–WS. High fuel production yields during MPO–CDS and MPO–WS–CDS cycles with high fuel selectivity were achieved when compared to that of the MPO–WS and MPO–CDS–WS cycles, which will be explained later.

The surface analysis of as-prepared samples complemented the findings of the XRD analysis. A typical XPS spectrum of pure CeO_2 was composed of two multiplets of 3d 3/2 at 900 and 898 eV, 3d 5/2 at 888 and 882 eV, and neighbouring 2 peaks at 907 and 916 eV, as presented in Figure 6.6a.

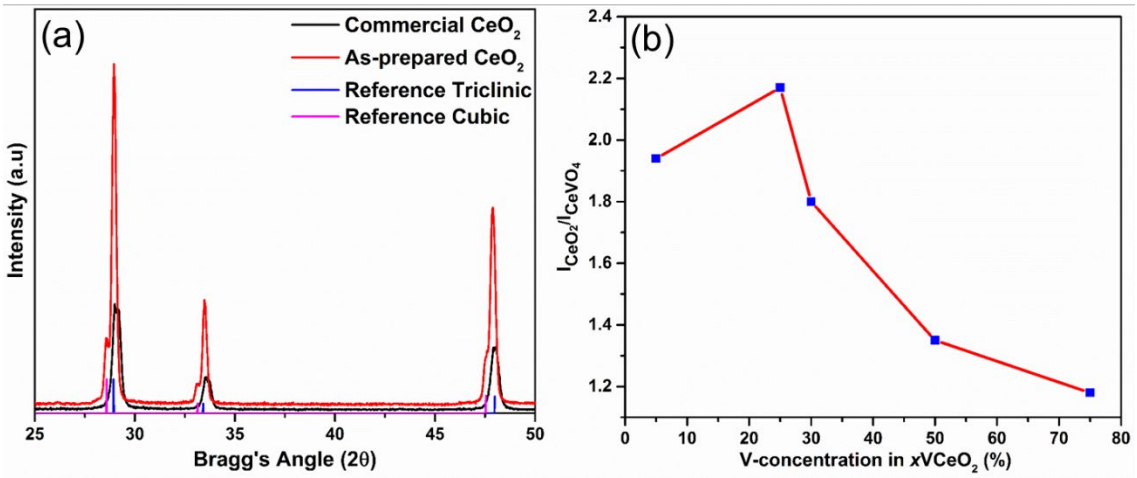

Figure 6.5. Structural comparison of different CeO_2 structures: (a) XRD pattern of as-prepared CeO_2 representing a triclinic (COD ID: 96-721-7888) with a low angle shoulder cubic (COD ID: 96-434-3162); XRD pattern of commercial CeO_2 powder purchased from Sigma. Reference patterns are obtained from the crystallographic open database (COD). (b) XRD peak Intensity ratios of $CeO_2/CeVO_4$ representing the phase segregation of CeO_2 and $CeVO_4$ in $xVCeO_2$ (x=5–75%).

The locations of these six peaks corresponding to the spin-orbit doublets of 3d 3/2 and 5/2 were in good agreement with the reported XPS analysis of Ce^{4+}/Ce^{3+}. The binding energy of O 1s is 529.02 eV, corroborating the presence of lattice oxygen species, while the neighbouring peak at 531.46 eV refers to the presence of adsorbed oxygen molecules. The binding energy of Ce 3d3/2 peaks changed from 888.5 eV to 885.2 eV with increasing V contents, due to increase in the $CeVO_4$ content. In addition, the disappearance of Ce^{4+} peak at ~916 eV confirmed the change of Ce valence from +4 to +3 due to increasing concentrations of $CeVO_4$ in the CV75 sample.

The binding energies of 516.9 eV and 524.66 eV shown in Figure 6.6b correspond to V 2p 3/2 and V 2p 1/2 spin-orbits in *x*$VCeO_2$ powder samples, respectively, depicting the

+5 valence state of vanadium.[261] In addition, the Ce 3d 3/2- to -3d 5/2 ratio decreased with increasing V content in vanadia–ceria systems. An increase in the binding energies of O 1s with V addition also indicates the presence of Ce (III) states and Ce–O–V interactions.

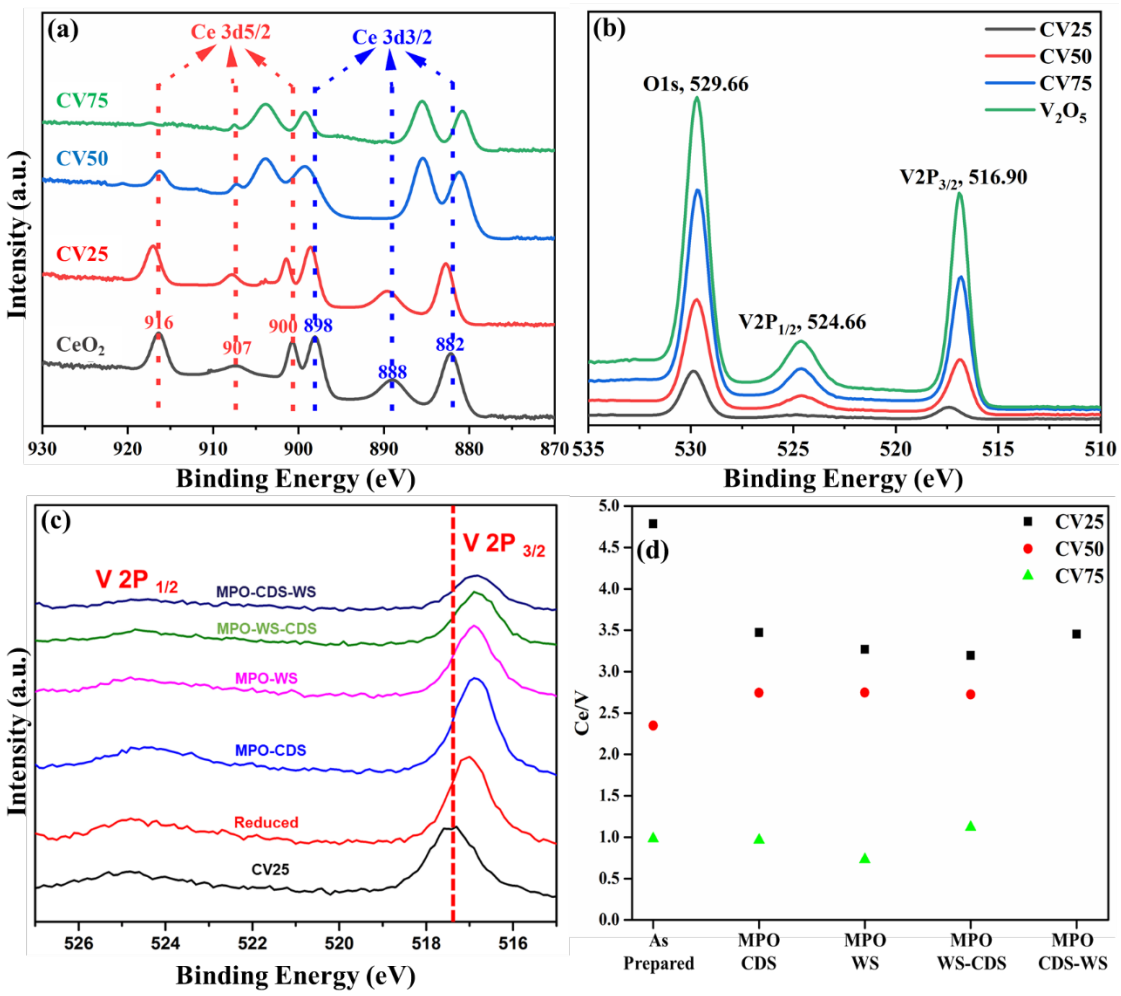

Figure 6.6. Chemical analysis of vanadia–ceria systems: XPS spectra of as-prepared vanadia–ceria metal oxide systems in the (a) Ce 3d and (b) V 2P and O 1s regions. (c) XPS spectra of the CV25 sample after MPO, MPO–CDS, MPO–WS, MPO–WS–CDS and MPO–CDS–WS redox cycles representing change in V 2P signature peaks. (d) Ce/V ratios in as-prepared and cycled CV25, CV50, and CV75 samples, obtained by ICP-OES analysis.

XPS spectra of reduced V_2O_5, CV25 and CV75 are shown in Figure 6.7. Higher V^{5+} content can be confirmed from the increasing intensities of V 2P1/2 and V 2P3/2 in Ce–V systems with increasing V content (CV25 → CV75 → pure V_2O_5). The O 1s peaks

shifted to high binding energies with higher V content, due to a higher $CeVO_4$ content.[272] An additional shoulder peak of V 2P3/2 was observed in reduced V_2O_5 due to the presence of VO_2. An additional O 1s peak was also observed at 531.89 eV for reduced V_2O_5. After the first MPO–CDS cycle, the additional O 1s peak merged into the main O 1s peak. This may be due to neighbouring vanadium species with multiple oxygen states. High concentrations of surface-adsorbed oxygen molecules may also contribute to the presence of the additional O 1s peak. A shift in the V $2P_{3/2}$ peak towards low binding energy was observed in CV25 samples after reduction and all other redox cycles (Figure 6.6c). This shift corresponds to the presence of V^{3+} species along with V^{+5} due to the co-existence of $CeVO_4$ and $CeVO_3$ phases, as discussed in the XRD section.

The information obtained from the XPS spectra provides an insight into the phenomenon of possible V volatilization. By obtaining Ce/V and V/O ratios, the loss of V can be quantified. In as-prepared powders, the V/O ratio increased, and Ce/V ratio decreases with increasing the V content. After the methane partial oxidation reaction, an increase in the V/O and Ce/V ratios was observed due to oxygen and V loss. However, after 10 consecutive cycles, a further decrease of the V/O ratio was observed, which suggests the loss of V and incomplete oxygen recovery. Ce/V segregation is also a possible reason for variable V concentrations at the surface. This can be further investigated by quantifying Ce and V concentrations in the bulk *via* the ICP-OES technique with a precision of up to parts per billion (ppb) level. The Ce/V ratios before and after thermochemical redox cycles are presented in Figure 6.6d.

An expected decline in the Ce/V ratio is observed in as-prepared Ce–V oxide samples due to higher V content. However, an irregular trend was observed after redox cycling, which suggests that segregation of Ce/V and V loss both contribute to the variable concentrations of V.

The nature of the interactions between ceria and vanadia was further investigated from the information obtained by Raman spectroscopy, as shown in Figure 6.8. A Raman spectrum of as-prepared pure vanadia nanoparticles was used as a reference. Pure CeO_2 has a Raman shift at 461 cm^{-1} corresponding to the F_{2g} symmetry of the cubic structure,[266,273] while pure V_2O_5 shows multiple signature peaks at 122, 144, 197, 229, 257, 284, 303, 376, 405, 463, 528, 703, 788, 801 and 863 cm^{-1} (Figure 6.8a).[274,275]

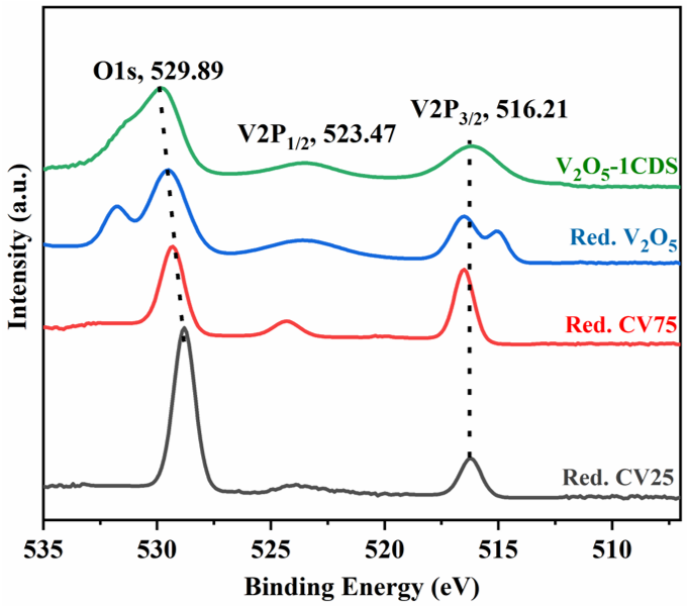

Figure 6.7. Surface chemical analysis of after-cycled samples: X-Ray photoelectron spectra of reduced CV25, CV75 and V_2O_5 and MPO–CDS-cycled V_2O_5 samples, depicting the binding energy shift and change in intensities.

The Raman bands at 279.14 and 711.14 cm^{-1} validated the formation of crystalline V_2O_5 nanoparticles along with the surface vanadia species (V=O) at 122.25 and 970–1030 cm^{-1}, in the pure nano-vanadia samples.[274,275] Two Raman bands related to the V–O–Ce and V–O–V bridging modes of $CeVO_4$ at 787.84 cm^{-1} and 799.21 cm^{-1}, along with the bands at 861.25, 379.54 and 259.19 cm^{-1} confirmed the formation of $CeVO_4$. The disappearance of the V=O band at 970–1030 cm^{-1} and a decline in the intensity of the CeO_2 band at 461.87 cm^{-1} was also related to conversion of CeO_2 and V_2O_5 into $CeVO_4$ (Reaction 6.1).

A decrease in the ratios of the signature peaks of $CeVO_4$ at 861 cm^{-1} to CeO_2 at 461 cm^{-1} was observed after the redox cycles, which indicates a decrease in $CeVO_4$ concentration and formation of $CeVO_3$ (Figure 6.8b). This ratio in CV25 was the lowest after MPO–WS and highest after MPO–CDS cycling. The XPS findings on possible vanadium loss and oxygen depletion in CV25 samples after MPO–WS and MPO–CDS–WS redox samples can be verified by the decline in the signature peak of the V=O species at 122.25 cm^{-1}. In contrast, this peak was most intense after reduction and MPO–CDS, followed by MPO–WS–CDS redox cycling, indicating high concentrations of available surface vanadia species for methane partial oxidation reaction. This finding supports the better reforming performance during MPO–CDS and MPO–WS–CDS redox cycling as compared to that of MPO–WS and MPO–CDS–WS redox cycling.

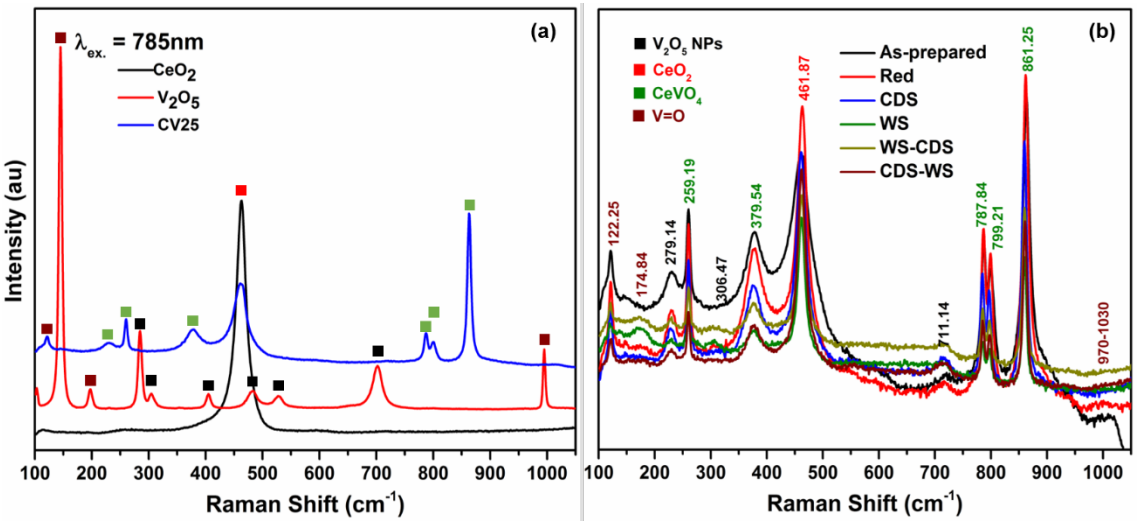

Figure 6.8. Structural characterization of oxygen carriers: (a) Raman spectra of as-prepared pure nano-ceria, pure vanadia and CV25 nanoparticles, representing the presence of fingerprint peaks of CeO_2, V_2O_5 and $CeVO_4$, (b) Raman spectra of CV25 nanoparticles as-prepared and after MPO, MPO–CDS, MPO–WS, MPO–WS–CDS and MPO–CDS–WS redox cycles.

6.2.2. Thermochemical performance

The performance of vanadia–ceria systems was evaluated based on the oxygen exchange capacity and the yield of syngas per mole of V during 10 consecutive thermochemical

redox reaction cycles. Moles of Ce ions were considered for the calculation of rates and yields of syngas production for pure CeO_2 sample. Figure 6.9 shows the oxygen evolution rates during the reduction and oxidation steps of MPO–CDS, MPO–WS, MPO–WS–CDS and MPO–CDS–WS cycles. In the following discussion, the oxygen rates calculated from CO/CO_2 evolution rates are referred to as "O1 rates", while oxygen rates deduced directly from the oxygen signal obtained during gas analysis are referred to as "O2 rates". This set of data provides an insight into material's ability to react with reducing and oxidizing atmospheres.

During MPO–CDS cycles, pure CeO_2 showed stable average O1 evolution rates of around 0.08 mol mol^{-1}_{Ce} min^{-1} with a peak of 0.107 mol mol^{-1}_{Ce} min^{-1}. In contrast, pure V_2O_5 exhibited the highest rates of 0.5 mol mol^{-1}_{V} min^{-1}. An increase in O1 rates from 0.27 mol mol^{-1}_{V} min^{-1} to 0.43 mol mol^{-1}_{V} min^{-1} was observed with the addition of V from 25% to 75%. In addition, vanadia–ceria multi-phase systems demonstrated high and stable oxygen evolution rates during the CO_2 splitting reactions with the highest rate of 0.35 mol mol^{-1}_{V} min^{-1} for 75%V.

During MPO–WS redox cycling, a similar trend of increasing O1 rates with the addition of V (25–75%) content was observed. Pure V_2O_5 showed the highest oxygen evolution rates up to 0.45 mol mol^{-1}_{V} min^{-1}, followed by CV75 with rates of up to 0.38 mol mol^{-1}_{V} min^{-1}, during the reduction step of MPO–WS redox cycles. Interestingly, pure V_2O_5 showed considerable O1 rates in water splitting reactions, which relate to oxidation of the carbon species formed during methane partial oxidation reaction. This phenomenon supports the findings from the XRD analysis of reduced and oxidized pure V_2O_5.

Following this result, in order to investigate the effect of oxidation atmosphere on the reactivity of reduced oxygen carriers with steam and CO_2, a combination of WS and CDS reactions following the methane partial oxidation step, i.e. MPO–WS–CDS, was performed. During the methane partial oxidation step of MPO–WS–CDS cycles, pure

V_2O_5 and CV75 demonstrated the highest O1 rates of 3.75 mol mol^{-1}_V min^{-1}, closely followed by CV50 at 3.69 mol mol^{-1}_V min^{-1} and CV25 at 2.85 mol mol^{-1}_V min^{-1}.

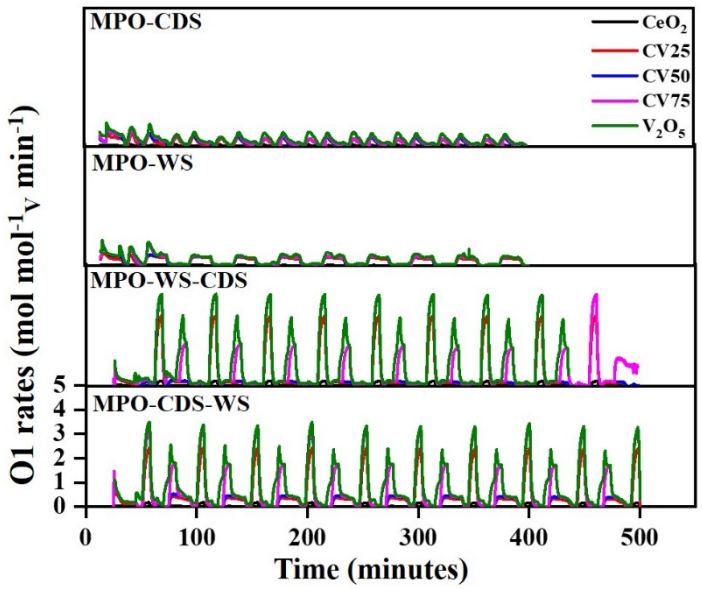

Figure 6.9. Oxygen exchange performance of vanadia–ceria metal oxide systems: oxygen evolution rates (O1) calculated from the amounts of CO and CO_2.

During the WS step, the O1 rates were highest for pure V_2O_5 followed by the rates for CV75, which confirms a vanadium carbide presence in pure V_2O_5 and CV75. Lowering the V content minimizes this carbide formation, resulting in a pure H_2 release during water splitting reaction. Consequently, CV25 and CV50 showed moderate to high O1 rates with pure H_2 production during MPO–WS–CDS cycles.

A similar trend was observed during the MPO–CDS–WS cycles. During the methane partial oxidation reaction, pure V_2O_5 showed the highest O1 rates at 3.35 mol mol^{-1}_V min^{-1}, closely followed by CV75 and CV50 at 3.25 mol mol^{-1}_V min^{-1}. However, the O1 rates significantly increased during the oxidation step, with a more than fivefold increase in CO production when compared to MPO–CDS cycling. The high VO_2 content observed in the XRD spectra also confirms a higher oxygen recovery in re-oxidized pure V_2O_5 and CV75 samples during MPO–CDS–WS cycles as compared to V_2O_5 and CV75 re-oxidized to V_2O_3 during MPO–CDS cycles. An increase in the $CeVO_4$ phase also supports efficient re-oxidation of CV25 and CV50 during MPO–CDS–WS cycles.

The rates of "O2" during all four types of redox cycles are presented in Figure 6.10. The "O2" rates increased with V content (25–100%) during the methane partial oxidation step of the MPO–CDS cycles, while the highest O2 rate of 20 mmol mol^{-1}_{V} min^{-1} is observed for pure V_2O_5. The evolution rates tend to decrease over multiple cycles due to the oxidation of the deposited carbon and the carbide formation. Interestingly, no considerable O2 rates were observed after the first MPO–WS cycle, while these rates are high in sequential WS and CDS cycles. In addition, O2 rates are higher for high-Ce systems than high-V systems. This agrees with the results of XRD study, where V^{4+} (in VO_2) is observed in CV75 and pure V_2O_5 samples, representing better re-oxidation capacity of these samples. In contrast, V^{3+} of $CeVO_3$ was observed in CV25 and CV50 samples, demonstrating an incomplete re-oxidation during WS reactions in these samples.

Oxygen exchange capacity and redox rates of pure nano-structured ceria and CV25 were evaluated *via* 10 consecutive two-step thermochemical redox cycles. The reduction and oxidation behaviour and performance in terms of fuel production rates and yields were evaluated during MPO–CDS, MPO–WS, MPO–WS–CDS and MPO–CDS–WS redox cycling. Methane conversion was calculated by Reaction 1.10, to investigate the material's behavior during the methane partial oxidation reaction. Table 6.1 shows the methane conversion by pure ceria and CV25 samples during the MPO–CDS, MPO–WS, MPO–WS–CDS and MPO–CDS–WS redox cycle tests performed in this chapter. CV25 clearly shows a higher methane conversion when compared to that of pure ceria in all four-cycle tests. Comparing the methane conversion seen in the four types of cycle tests, it was highest during MPO–CDS followed by the MPO–WS–CDS redox cycles and lowest in the MPO–WS cycles, indicating inferior methane reforming during MPO–WS cycling.

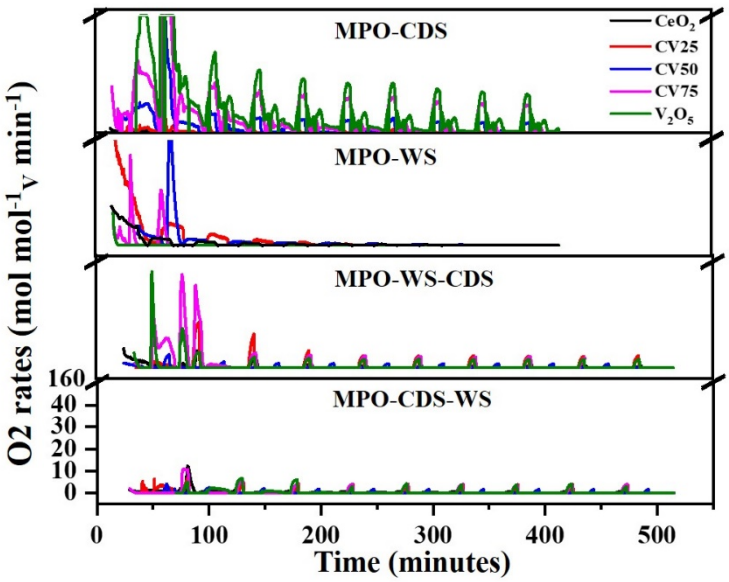

Figure 6.10. Oxygen exchange performance of vanadia–ceria metal oxide systems: Oxygen signal from a mass spectrometer (referred in the text as O2) during the reduction and oxidation steps of MPO–CDS, MPO–WS, MPO–WS–CDS, and MPO–CDS–WS redox cycles. The vertical-scale break denoted by the dash is from 50 to 150 mmol mol^{-1}_V min^{-1}.

Table 6.1. Methane conversion by pure ceria and CV25 samples during dry/steam chemical looping reforming of methane.

Process	Materials	
	Ceria	**CV25**
MPO–CDS	0.1158	0.12
MPO–WS	0.034	0.072
MPO–WS–CDS	0.059	0.09
MPO–CDS–WS	0.0323	0.077

High rates of syngas production during the reduction step of MPO–CDS by CV25 were observed with an average rate of 12.96 mL $min^{-1}g^{-1}$ and 4.88 mL $min^{-1}g^{-1}$ for H_2 and CO respectively, as shown in Figures 6.11a and 6.11c. The calculated H_2/CO ratio was close to 2 with an average value of around 2.15, indicating controlled methane partial oxidation (Table 6.2). In contrast, the average production rates for H_2 and CO produced by pure

nano-structured ceria were only 7.12 mL $min^{-1}g^{-1}$ and 2.47 mL $min^{-1}g^{-1}$, respectively. However, methane cracking is observed after the first cycle of the MPO–WS process, resulting in significant increases in the H_2/CO ratio reaching up to a value of around 4.59 and 3.38 in pure nano-structured ceria and CV25 respectively.

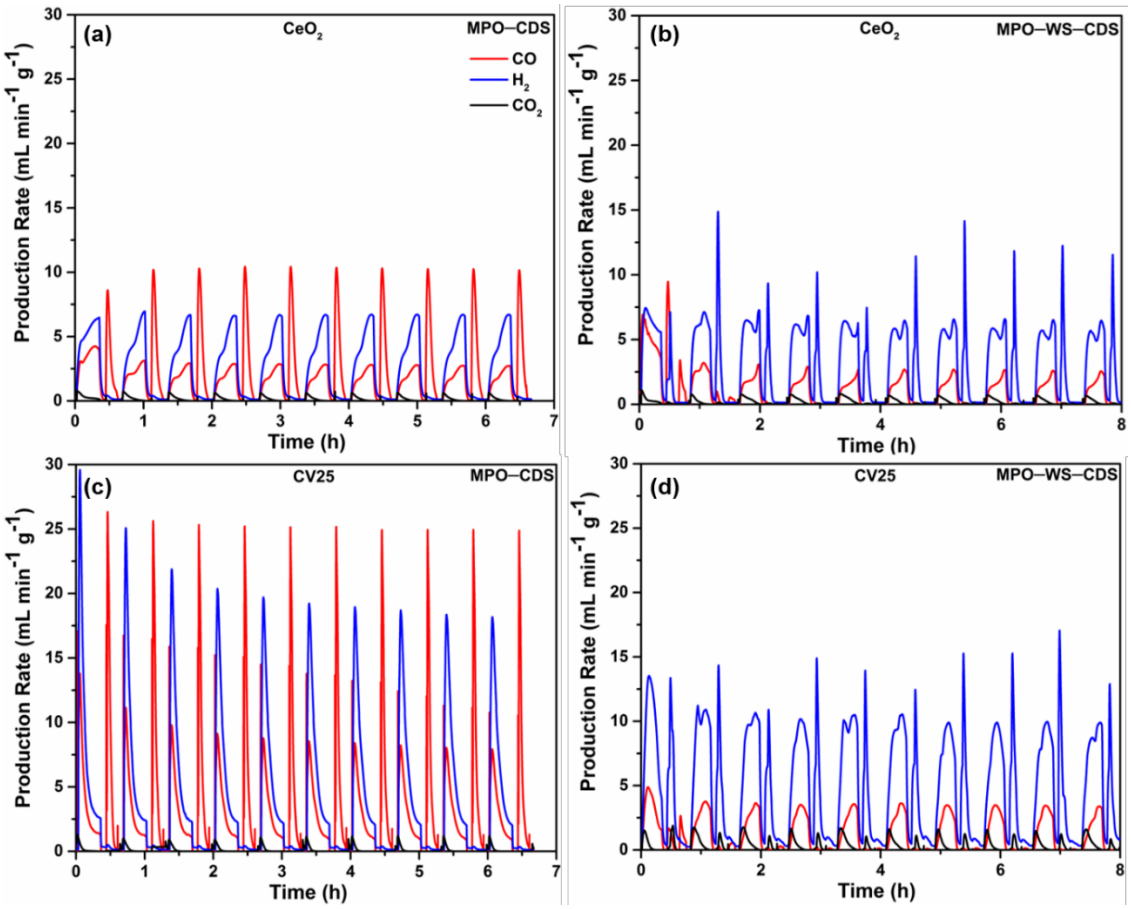

Figure 6.11. Thermochemical redox cycle performance evolution in terms of production rates of H_2, CO and CO_2 during MPO–CDS and MPO–WS–CDS cycles on: (a) and (b) pure nano-structured ceria; (c) and (d) CV25.

The water splitting rate was close to 10 mLmin^{-1} g^{-1} - more than double the pure nano-ceria ca. 4.25 mL $min^{-1}g^{-1}$, as shown in Figures 6.12a and 6.12c. The CO selectivity S(CO) was determined from the cycle data, by utilizing Reaction 1.11. A higher value of S(CO) is obtained by CV25 during the MPO–WS–CDS cycles when compared to that of pure nano-structured ceria. Elevated production rates of CO_2 in the MPO step of MPO–WS cycling result in a lower CO selectivity. Carbon deposition on the oxygen carriers can be

associated with this, which may possibly promote methane cracking instead of reforming of methane, resulting in high H_2/CO ratios being obtained during MPO–WS cycling.

Reaction kinetics play a critical role in the H_2 and CO redox rates profiles, which are greatly affected by the amount of reactant gasses reaching the oxygen carrier. In a fixed bed reactor design, the homogenous concentration of reactant gases reaching the oxygen carriers is limited by the gas flow through solid materials, which greatly influences the CH_4-to-O_2 ratios. It is observed that in the beginning of the MPO reaction, small amounts of CO_2 are produced due to low CH_4 concentrations, as shown in real time gas profiles obtained from mass spectrometer readings (Figure 6.13). As the required concentration of CH_4 is achieved and stabilized, no CO_2 is observed, and reaction rates of H_2 and CO are increased.

Sequential WS and CDS reaction tests after the MPO step were performed to investigate the oxidation behaviour of these nano-structured oxygen carriers in CO_2 and H_2O as oxidizing mediums, (Figures 6.11b and 6.11d). In the first attempt, WS–CDS cycles were performed after the MPO reduction of oxygen carriers, while flushing with Ar for 5 min at 500 ml min^{-1} before each oxidation step. The reduction rate profile for both the oxygen carriers changed after the first cycle, where an increase in the H_2 production rate was observed after 4 mins of reduction and reached its maximum value after the maximum rate of CO was achieved. A significant improvement in the H_2/CO ratio is achieved in the MPO step of the MPO–WS–CDS redox cycle when compared to simple MPO–WS cycles. The highest calculated H_2/CO ratio from CV25 was 3.1 at the 5^{th} cycle, subsequently decreasing and becoming stable at around 2.21. However, in the case of pure nano-structured ceria, the ratio appeared to be unstable and fluctuated from 3.4 to 2.8. The H_2 production rates of pure nano-structured ceria were observed to be unstable during the WS step of the MPO–WS–CDS cycles, despite achieving rates as high as 10.21 mL min^{-1} g^{-1} for a few cycles. In contrast, CV25 exhibited high and stable

rates of water splitting reactions up to 15.12 mL min^{-1} g^{-1}, with considerable stability throughout the 10 cycles. This finding indicates possible structural stability in pure nano-structured ceria induced by the surface vanadia particles, which additionally improve the ion mobility in the structure.

The counter-effect of steam on methane reforming is studied by performing MPO–CDS–WS cycling (Figures 6.12b and 6.12d). After the first cycle, the H_2 production rate increased significantly with a H_2/CO ratio reaching 6.3 and 4.8 for pure nano-structured ceria and CV25, respectively. The CO production rate during the MPO step did not undergo a substantial increase for CV25 and a considerable amount of CO_2 was observed.

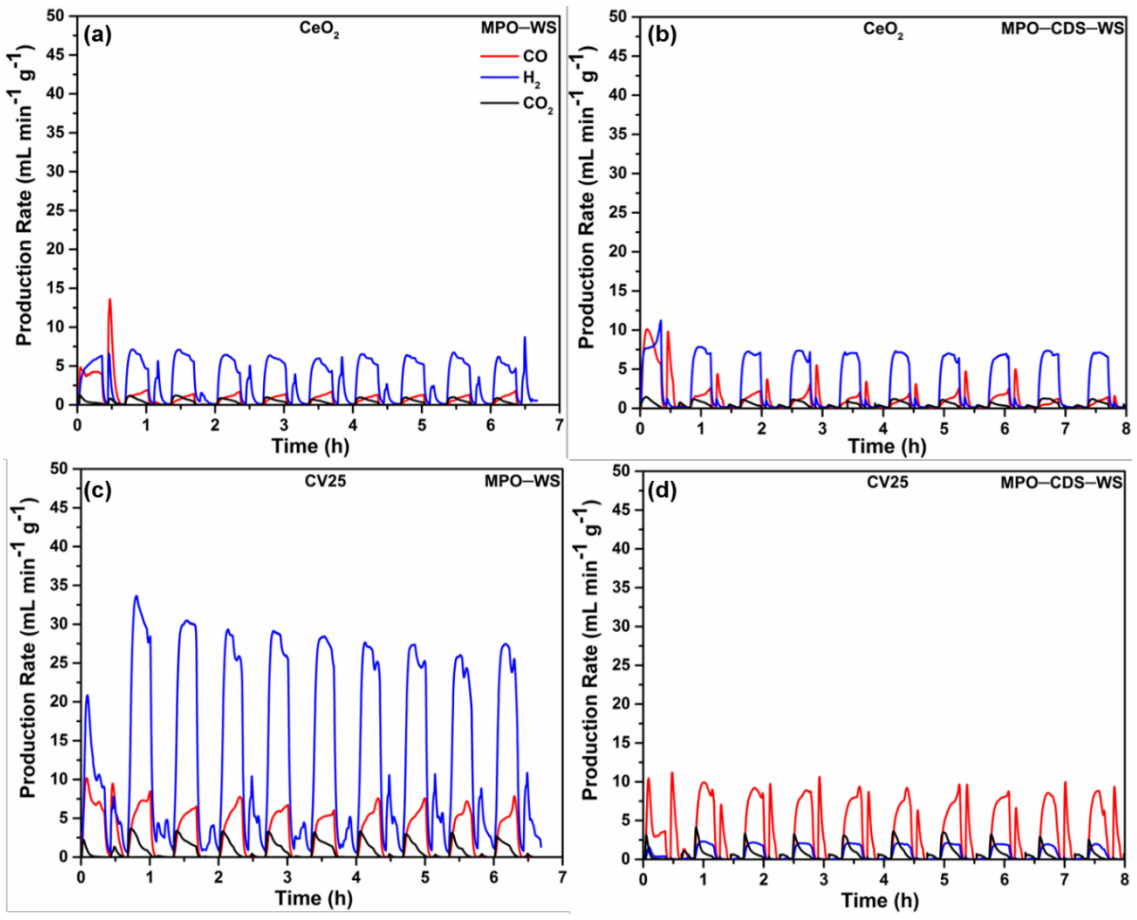

Figure 6.12. Production rates of H_2 (blue), CO (red) and CO_2 (black) during: (a) MPO–WS and (b) MPO–CDS–WS on pure nanostructured ceria; (c) MPO–WS and (d) MPO–CDS–WS on CV25. High CO_2 production rates relative to the CO rates are presented in MPO–WS cycles. MPO–CDS–WS represents incomplete oxidation of methane, resulting high H_2 rates.

However, deterioration in the CO production rates was observed in pure nano-structured ceria. The presence of H_2 in the CDS oxidation step indicates the presence of residual methane in the system. It is worth noting that the H_2 during the second oxidation (i.e. WS), clearly reveals the presence of oxygen vacancies in the structure of the oxygen carriers due to an incomplete re-oxidation during the CDS cycle. Moreover, the presence of a small amount of CO_2 also indicates the possible carbon deposition on the surface of the oxygen carriers during MPO and CDS reactions.

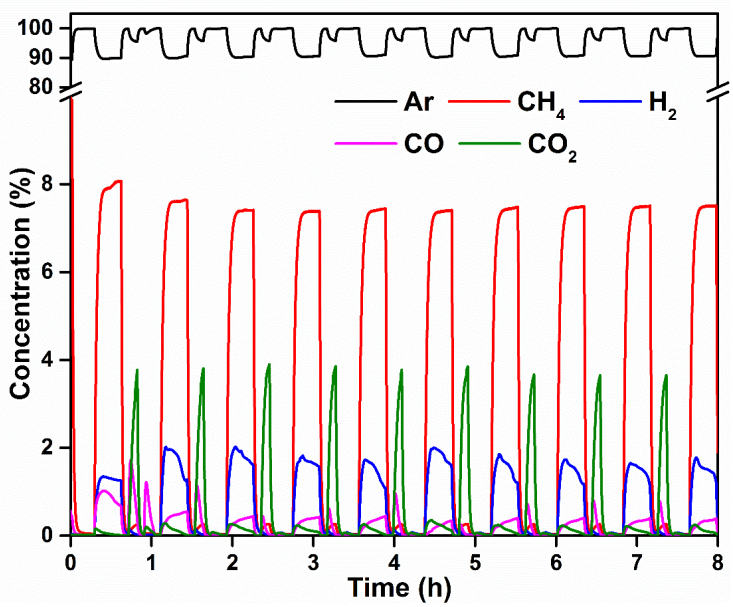

Figure 6.13. Real-time reactant and product gas production profiles measured by mass-spectrometer during MPO–WS–CDS redox cycles.

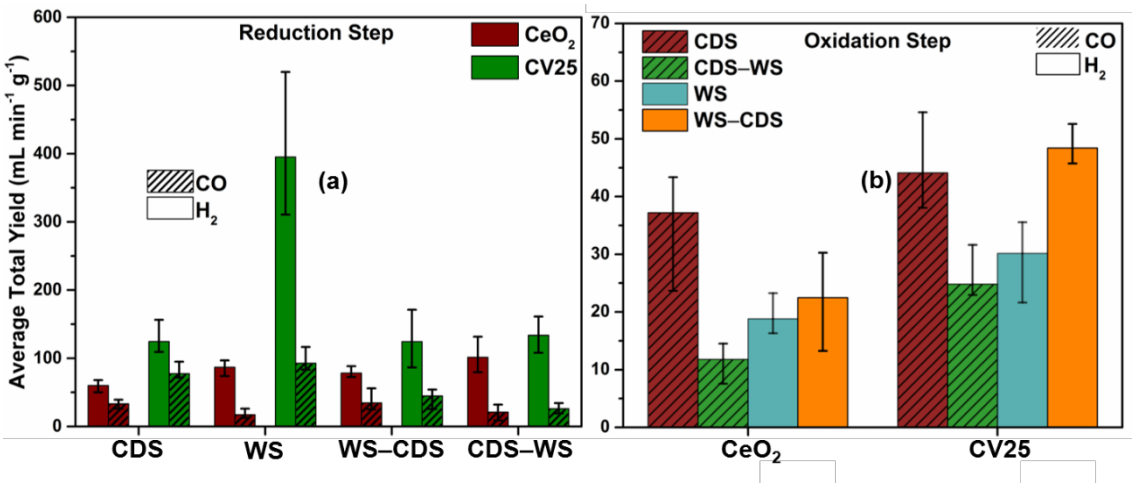

Figure 6.14. Thermochemical redox cycles performance evaluation in terms of average of total H_2 and CO yield during the period of: (a) Reduction and (b) oxidation steps of 10

MPO–CDS, MPO–WS, MPO–WS–CDS & MPO–CDS–WS cycles on pure nano-ceria and CV25. Error bars represent the deviation of maximum and minimum yield from the average yield value.

The total fuel production data along with information about H_2/CO ratios and CO selectivity S(CO), recorded during the whole duration of the reduction and oxidation steps is presented in Table 6.2 and 6.3. Evidently, CV25 produced nearly double the yield of H_2 and CO when compared to pure nano-structured ceria, with a near ideal H_2/CO ratio of 2.12 and CO selectivity up to 90.14%, during MPO–CDS redox cycles. Despite the high H_2 (78.2 mL g^{-1}) and CO (19.9 mL g^{-1}) yields produced by pure ceria, the H_2 yield during oxidation is still lower than CV25. This is possible because of less oxygen vacancies produced during the methane partial oxidation step of the MPO–WS redox cycles, which results in low H_2 yields in the H_2O splitting reaction.

Introducing a CDS step after the WS reaction improves the overall methane reforming process and lowers the H_2/CO ratio. In addition, the H_2 yield during the WS step is higher and more stable in MPO–WS–CDS cycling than in the simple MPO–WS redox cycles. However, utilizing WS as a complementary step for CDS in MPO–CDS–WS cycling exhibits inefficient reduction of oxygen carriers in the MPO step, as observed in the MPO–WS cycles. A considerable amount of H_2 up to 3.4 mL g^{-1} is produced by CV25 in the WS step along with a small amount of CO_2 (around 1.1 mL g^{-1}). However, a drop in the CO yield during the MPO and CDS step of the MPO–CDS–WS cycle is observed in pure nano-structured ceria when compared to the simple MPO–CDS.

The average total CO yield calculated for pure nano-structured ceria and CV25 during the reduction and oxidation reactions is shown in Figure 6.14. Methane partial oxidation by CV25resulted in H_2 and CO yields of up to 130.12 mL g^{-1} & 87.34 mL g^{-1}, respectively, which is more than double of that produced by pure ceria during MPO–CDS redox cycles. A decline in CO yields by 300% in CV25 and 170% in pure ceria was observed after the addition of the WS step after CDS during MPO–CDS–WS cycling. The H_2 products

showed a considerable increase, suggesting an inefficient reforming of methane. Similar to rate-based information, yields of H_2 produced during the methane partial oxidation showed a drastic increase during MPO–WS redox cycles. Addition of the CDS step after the WS step i.e., MPO–WS–CDS, not only improved the H_2/CO ratio but also increased the H_2 yields resulting from splitting of H_2O. The reasons for this phenomenon have been discussed in previous sections.

The stability test for pure nano-structured ceria and CV25 was performed through 100 cycles of the MPO–CDS and MPO–WS–CDS reactions. The fuel production rates yield per cycle and 5 cycles post 100 cycles are presented in Figures 6.15 and 6.16**.** A typical decline in the production rates and yields are observed in both oxygen carriers indicating possible sintering and incomplete oxygen recovery, (Figures 6.15a, 6.15b, 6.16a and 6.16b). The fuel yield is calculated by taking the average yield over 5 cycles during the run of 100 cycles. A 47% and 63% increase in the fuel yield is observed in CV25 over pure nano-structured ceria during MPO–CDS and MPO–WS–CDS redox cycles, respectively, as shown in Figures 6.15c, 6.15d, 6.16c and 6.16d. The long-term stability test of the pure nano-structured ceria and CV25 was further investigated by measuring the oxygen exchange capacity by performing 5 cycles of MPO–CDS and MPO–WS–CDS reactions after the 100 redox cycles. Notably, the H_2 and CO production rates of pure nano-structured ceria and CV25 were largely unchanged and maintained a high performance, like the as-prepared material, as shown in Figures 6.15e, 6.15f, 6.16e and 6.16f.

Table 6.2. Performance evaluation of pure ceria and CV25 samples in terms of H_2/CO ratio, CO selectivity and fuel yield during oxidation and reduction steps of MPO–CDS and MPO–WS cycles.

		MPO–CDS					MPO–WS				
		Reduction				Oxidation	Reduction				Oxidation
Material	**Cycle (#)**	**H_2 yield (mL g^{-1}_{MO})**	**CO yield (mL g^{-1}_{MO})**	**SCO (%)**	**H_2/CO**	**CO yield (mL g^{-1}_{MO})**	**H_2 yield (mL g^{-1}_{MO}**	**CO yield (mL g^{-1}_{MO})**	**SCO (%)**	**H_2/CO**	**H_2 yield (mL g^{-1}_{MO})**
CeO_2	2	78.27	39.12	66.52	2.01	42.47	107.1	26.11	89.59	4.1	21.62
	4	68.4	37.4	59.06	1.83	43.2	93.8	19.1	87.1	4.92	20.1
	6	59.9	33.8	50.55	1.77	38.8	78.2	19.9	59.26	3.93	23.2
	8	51.58	29.14	76.8	1.78	34.49	78.62	14.52	36.74	5.87	19.15
	10	43.9	26.2	49.6	1.73	23.7	65.8	15.7	24.15	4.17	23.3
CV25	2	157	94.9	86.03	1.95	82.6	520	117	84.96	4.46	32.4
	4	128.34	74.51	85.35	2.12	65.39	477.92	112.45	77.92	4.25	51.522
	6	120.8	71.72	78.29	2.15	56.82	417.57	132.98	74.5	3.14	26.45
	8	114	65.91	83.75	2.22	43.75	389.2	152	67.69	2.56	67.04
	10	109.19	62.39	90.14	2.18	39.85	344.02	131.06	63.25	2.52	71.69

Table 6.3. Performance evaluation of pure ceria and CV25 samples in terms of H_2/CO ratio, CO selectivity and fuel yield during oxidation and reduction steps of MPO–WS–CDS and MPO–CDS–WS cycles.

		MPO–WS–CDS					MPO–CDS–WS				
		Reduction				Oxidation	Reduction				Oxidation
Material	**Cycle (#)**	**H_2 yield ($mL\ g^{-1}_{MO}$)**	**CO yield ($mL\ g^{-1}_{MO}$)**	**SCO (%)**	**H_2/CO**	**H2 yield ($mL\ g^{-1}_{MO}$)**	**H_2 yield ($mL\ g^{-1}_{MO}$)**	**CO yield ($mL\ g^{-1}_{MO}$)**	**SCO (%)**	**H_2/CO**	**CO yield ($mL\ g^{-1}_{MO}$)**
CeO_2	2	112.27	56.01	88.38	2.01	50.26	131.62	32.05	87.73	4.1	17.91
	4	84.8	46.42	88.4	1.82	16.66	112.3	22.49	85.7	4.99	19.49
	6	70.34	33.13	88	2.23	14.23	102.5	16.27	71.4	6.29	9.48
	8	58.14	32.17	84.95	1.75	20.36	82.82	27.54	42.16	3	7.92
	10	54.68	27.6	84.8	1.98	29.09	79.5	13.07	27.8	6.08	6.85
CV25	2	171.2	65.38	92.8	3.16	54.5	161.25	34.28	94.2	4.7	27.41
	4	153.48	54.19	92.2	2.32	42.78	142.87	29.33	88.49	4.87	30.35
	6	138.26	51.84	90.29	2.29	36.52	116.51	25.81	55.1	4.38	17.7
	8	125.78	48.66	90.13	2.41	36.52	121.39	27.98	37.43	4.45	31.14
	10	109.16	46.12	89.89	2.37	34.15	138.81	31.47	26.3	4.41	18.72

The structural reorganization of the materials under investigation was evaluated by the determination of specific surface area and pore volume *via* BET analysis, before and after 100 cycles. The as-prepared nano-structured ceria possessed a higher specific surface area of 81.77 $m^2 g^{-1}$ compared to that of CV25 with a surface area of 65.2 $m^2 g^{-1}$. Despite a 79% decline in surface area, CV25 exhibited a high and consistent oxygen exchange capacity during and after the 100 cycles. On the other hand, a 92% decrease in the surface area in pure nano-structured ceria is observed after the 100-cycle test. This shows that vanadia–ceria multi-phase systems not only support the redox capability for fuel production, but also avoid drastic deterioration through structural re-organization.

Overall, the vanadia−ceria binary phase redox oxide performed better than pure nano-structured ceria by achieving 53% higher H_2 and 51% higher CO yields during the methane partial oxidation and a 47% higher CO yield in the CO_2 splitting step in MPO–CDS reactions over 100 cycles. High yields of H_2 and CO are achieved in CV25 during sequential WS and CDS reactions (MPO–WS–CDS), with a 48% and 45% increase respectively, when compared to pure nano-structured ceria. The H_2 and CO yields during the reduction and oxidation reactions of MPO–WS–CDS and IGS-WS–CDS cycles are tabulated in Table 6.4 and compared to the current benchmark material (ceria) and other redox oxides reported recently, where MPO-driven reduction of oxygen carriers results higher reduction extents with efficient syngas yields, a controlled H_2/CO ratio (~2) is another important aspect of an effective syngas production process.

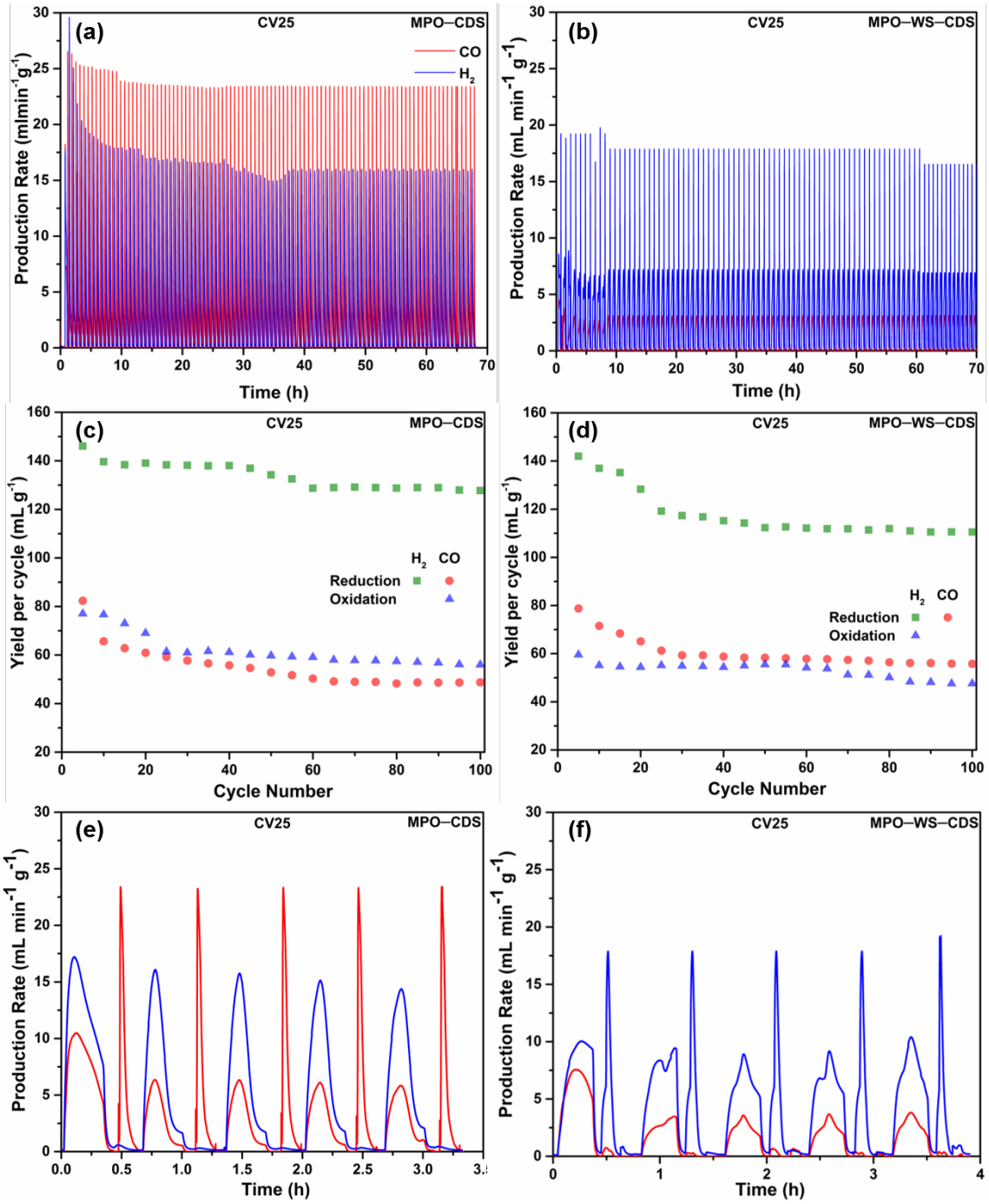

Figure 6.15. Performance evaluation of CV25 during MPO–CDS and MPO–WS–CDS cycles: (a) and (b) H_2 and CO production rates during 100 cycles; (c) and (d) Average yield calculated after each step of 5 cycles; (e) and (f) syngas production rates during 5 redox cycles performed after the 100 cycles stability test.

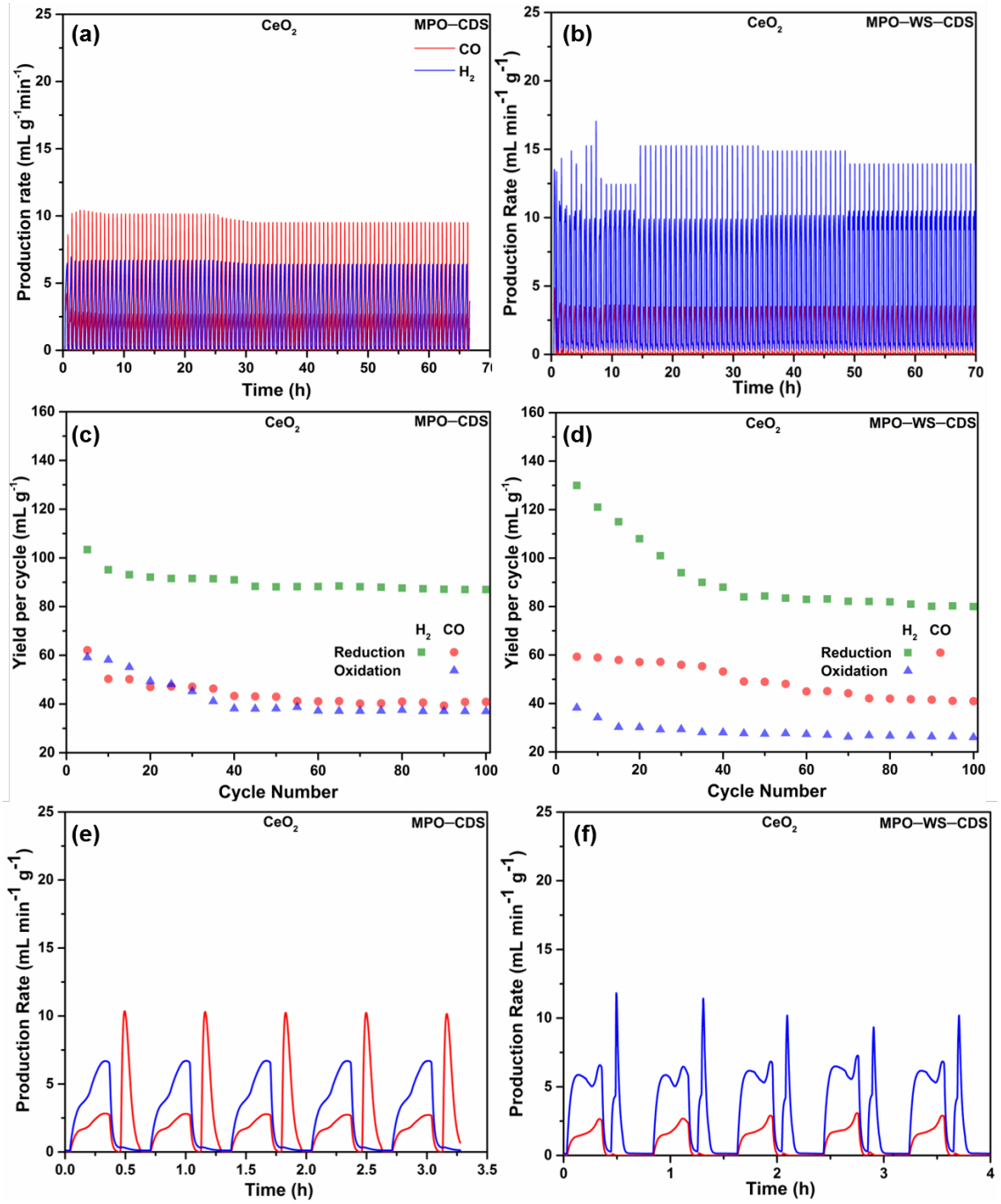

Figure 6.16. Thermochemical performance evaluation of nano-ceria during MPO–CDS and MPO–WS–CDS redox cycles: (a) and (b) H_2 and CO production rates; (c) and (d) average yield per 5 cycles; (e) and (f) 5 post 100 cycles.

Notably, a mass-specific CO yield of 91 mL g^{-1} is achieved with CV25 samples during CO_2 splitting (e.g. 70% higher than the recently reported CO yield on $La_{0.6}Ca_{0.4}MnO_3$ during reverse water gas shift reactions),[114] which is attributed to the extraordinary oxygen exchange capacity of CV25. Gao et. al. reported a high CO yield of 397 mLg^{-1} during the CO_2 splitting step carried out for over 70min^{-1}.

However, the long reduction durations resulted in a high H_2/CO ratio of 4.47, which deviates significantly from the H_2/CO ratio (i.e., 2) required for an ideal methane partial oxidation reaction. Pure nano-structured ceria in this chapter depicted a higher H_2 and CO yield of 122 mL g^{-1} and 58 mL g^{-1}, while retaining the H_2/CO ratio close to 2, as compared to other reported ceria structures.[168] However, the multi-phase vanadia−ceria system outperformed the pure nano-structured ceria by producing H_2 (261 mLg^{-1}) and CO (118 mL g^{-1}) with a H_2/CO ratio of 2.18 during the MPO reaction and 91 mLg^{-1} of CO in oxidation step of 100 cycles of MPO–CDS reactions. Improved water splitting yields were observed with combined WS–CDS reaction on CV25 over the 100 cycles with a maximum H_2/CO ratio of 2.21 when compared to MPO–WS with a H_2/CO ratio of 2.89 in pure nano-structured ceria.

6.3 Discussion

Ceria possesses a high bulk oxygen mobility in its non-stoichiometric cubic structure and is efficient in creating oxygen vacancies upon reduction. Matta et al. have reported poor ethane oxidation on ceria-supported vanadia at 550°C.[264] Addition of vanadia up to 5wt% loading in ceria results in a deterioration in the catalytic activity of ceria. The high density of surface vanadia readily reacts with ceria and forms $CeVO_4$, which may not be a fully reversible reaction due to oxygen leaching. Ceria exists in both 3^+ ($CeVO_4$) and 4^+ (CeO_2) oxidation states in ceria–vanadia multi-phase systems due to segregated phases of $CeVO_4$ and CeO_2.

The formation reaction of $CeVO_4$ also gives a ½ oxygen molecule towards the methane oxidation and results in the $CeVO_3$ phase consisting of Ce^{4+} and V^{3+}, where re-oxidation of $CeVO_3$ consumes oxygen from oxidation medium and forms $CeVO_4$ and re-oxidized ceria. Consequently, co-existence of CeO_2 and $CeVO_4$ results in more oxygen species for reduction and oxidation reactions compared to pure ceria. The high density of surface vanadia species contributes the most in the formation of $CeVO_4$ because of its

high extent of reduction,[263] whilst the V^{5+} species interact with the ceria and promote its reduction from Ce^{4+} to Ce^{3+}, depending upon the reducing power of hydrocarbon and V^{5+} loading. The re-oxidation of cerium vanadate occurs *via* oxygen buffering by cerium, where cerium assists the re-oxidation of the reduced metal oxide system.[259,263,275–278]

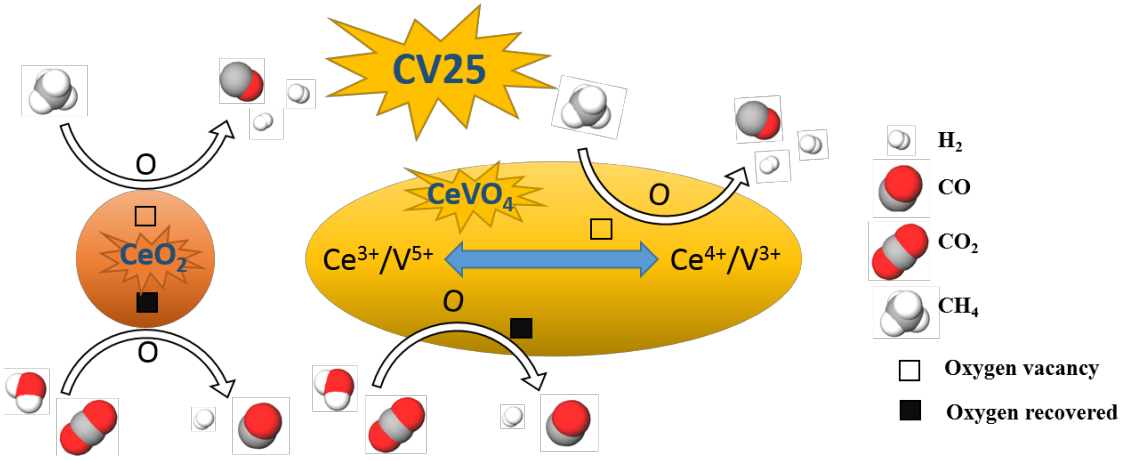

Figure 6.17. Proposed mechanism for the contribution of CeO_2 and $CeVO_4$ towards cyclic reduction and oxidation reactions for syngas production. Vanadium increases sites available for reduction, while cerium ions increase the charge transfer.

Moreover, the interaction of surface vanadia with ceria stabilizes the surface Ce^{3+} by modulating the valance change in C^{4+}/Ce^{3+} due to cyclic formation of $CeVO_4$ to $CeVO_3$, which potentially can suppress the combustion of hydrocarbons during the redox cycles.[260] Hence, the co-existence of CeO_2 and $CeVO_4$ phases demonstrates a synergic effect in the redox reactions resulting better syngas yields as compared to pure ceria, as shown in Figure 6.17.

Table 6.4. Performance comparisons of solar fuel production by oxygen carriers evaluated in this study and other benchmark materials reported recently. t_c: operating time; N_c: number of cycles; T_{red}: reduction temperature; T_{ox}: oxidation temperature; Y_{H_2}: hydrogen yield; Y_{CO}: CO yield; WS: water splitting; CDS: CO_2 splitting; MPO: methane partial oxidation; IGS: inert gas sweeping; RWGS: reverse water gas shift; FBAR: fixed bed alumina reactor; PCTSR: porous ceria tube solar reactor; CRSR: cavity receiver solar reactor; FBQR: fixed bed quartz reactor; FBR: fixed bed reactor; SD-TGA: solar driven thermo-gravimetric analysis; MRS: micro-reactor system; FBR[a]: fluidized bed reactor; SFR: stagnation flow reactor; QUTR: quartz U-tube reactor.

Material	**Process**	t_c **(h)**	N_c **(#)**	**Reduction**			**Oxidation**			**H_2:CO**	**Reactor type**	**Ref.**
				T_{red} (K)	Y_{H_2} mLg^{-1}	Y_{CO} mLg^{-1}	T_{ox} (K)	Y_{H_2} mLg^{-1}	Y_{CO} mLg^{-1}			
CeO_2	MPO–CDS	66.7	100	1173	122	58	1173	-	49	2.09	FBAR	This work
CeO_2	MPO–WS–CDS	66.7	100	1173	168	79	1173	71	-	2.14	FBAR	This work
25% V CeO_2	MPO–CDS	66.7	100	1173	261	118	1173	-	91	2.18	FBAR	This work
25% V CeO_2	MPO–WS	6.7	10	1173	665	230	1173	160	5	2.89	FBAR	This work
25% V CeO_2	MPO–WS–CDS	66.7	100	1173	320	145	1173	220	2	2.21	FBAR	This work
CeO_2	IGS-WS	167	500	1773	-	-	1073	14	-	-	PCTSR	[192]
CeO_2	IGS-WS–CDS	>8	10	1700	-	-	1100	2	0.9	-	CRSR	[27]
CeO_2	MPO–CDS	12	10	1173	81	39	1173	-	55	2.09	FBAR	[22]
CeO_2	MPO–CDS	46.7	100	1173	44	16	1173	-	35	2.74	FBAR	[168]
3% Ce Mn_3O_4	MPO–CDS	46.7	100	1173	77	20	1173	-	29	3.47	FBAR	[22]
3% Ce Mn_3O_4	MPO–CDS	11.7	4	1173	640	143	1173	-	397	4.47	FBAR	[22]
3% Ce Mn_3O_4	MPO–WS	2	2	1173	846	253	1173	254	81	3.34	FBAR	[22]
$Ce_{0.8}Zr_{0.2}O_2$	MPO–WS	>2.7	1	973	29	14	773	19	-	2.08	FBQR	[35]
$Ce_{0.7}Fe_{0.3}O_3$	MPO–WS	>6.3	10	1123	27	14	973	23	-	1.89	FBR	[150]
CeO_2/SiC	MPO–WS	0.7	3	1273	17	10	1273	27	-	1.72	SD-TGA	[160]
Fe_3O_4	MPO–WS	15.5	6	1223	159	79	1123	117	-	2.00	FBR	[279]
$LaFeO_3/CeO_2$	MPO–WS	> 27	30	1073	45	6	1073	5	-	7.40	MRS	[160]
$LaFe_{0.9}Ni_{0.1}O_3$	MPO–WS		10	1123	-	-	1123	150	-	-	FBR[a]	[247]
$CoFe_2O_4/Al_2O_3$	IGS-WS	4.6	3	1623	-	-	1623	2	-	-	SFR	[25]
$Sr_{0.6}La_{0.4}Mn_{0.6}Al_{0.4}O_3$	IGS-CDS	40	80	1623	-	-	1273	-	3	-	SFR	[85]
$La_{0.6}Ca_{0.4}MnO_3$	RWGS	3.3	5	823	-	-	823	-	28	-	QUTR	[114]

6.4Conclusions

This chapter is the first demonstration of the vanadia–ceria multiphase system for thermochemical fuel production via methane partial oxidation followed by CO_2, H_2O, CO_2–H_2O and H_2O–CO_2 splitting. The materials were synthesized using a facile method involving combustion of liquid phase Ce and V precursors with V concentrations in the range 0–100%. Improved structural stability was achieved in mixed vanadia–ceria systems as compared to pure CeO_2 and pure V_2O_5. Enough vanadium in CeO_2 result in a multiphase system consisting of CeO_2 and $CeVO_4$, which increases syngas production rates by 68% during H_2O splitting and 47% CO_2 splitting reactions, when compared to pure nanostructured ceria. Efficient re-oxidation of $CeVO_3$ to $CeVO_4$ plays a critical role to obtain high syngas yields, which is achieved by coupling H_2O and CO_2 splitting reactions. The long-term cycling performance of these redox oxide pairs demonstrates that the oxygen exchange in the vanadia–ceria system during the redox reactions is highly reversible and can be performed up to hundred cycles, while maintaining high redox rates. In conclusion, these findings provide evidence that these binary phase systems can be used for the large-scale fuel production via improved thermochemical redox cycles.

Chapter Seven

Conclusions and Future Work

7.1 Conclusions

Since the importance of renewable fuels is well-known, efforts for replacing fossil fuels with carbon-neutral fuels have been intensified. However, this transition is still hindered by the high cost and low efficiency of large-scale production by utilizing sustainable resources. Solar thermochemical redox cycles and chemical looping reforming of methane have been considered economical and efficient techniques for bulk renewable fuel production. In addition, thermochemical processes can store and transport solar energy at ambient conditions and utilize outside daylight hours. However, finding efficient redox materials with suitable thermochemical properties remains a major challenge for the research community.

In this thesis, recent research in the area of solar fuel production via thermochemical routes was summarized. Following this, thermochemical, material, and thermodynamic aspects of fuel production performance via redox cycles and chemical looping reforming were compared. Thereafter, the latest progress and major achievements in the field of material research for the redox cycles and chemical looping reforming were briefly reviewed. The critical assessment of cycle chemistry and thermochemical characteristics of the state-of-the-art redox materials paved vital foundations for the aim of this thesis, which is to achieve the benchmark standards for solar thermochemical syngas production performance via structural engineering of mixed-metal oxides.

Firstly, structural effects of lanthanum addition to the $La_xSr_{1-x}MnO_3$ Perovskite oxides were explored for syngas production via redox cycles and chemical looping reforming of methane (Chapter 3). The oxygen exchange capacity of these Perovskites was evaluated at different reduction and oxidation temperatures. Various structural features such as morphology and surface area were studied as a function of thermochemical performance. Later, the $La_xSr_{1-x}MnO_3$ Perovskites were tested for up to

20 cycles of CO_2 and H_2O splitting reactions coupled to the methane partial oxidation reaction. Phase stability as a crucial factor in determining the suitability for these materials for chemical looping reforming of methane was critically discussed. It was found that addition of lanthanum plays a key role in the phase stabilization and fuel selectivity of the $La_xSr_{1-x}MnO_3$ Perovskites during the chemical looping reforming of methane. However, despite structural disintegration, manganese plays an active role in redox activities and its oxidation state is greatly influenced by lanthanum concentration and oxidation medium. These findings provide a set of benchmark standards for engineering efficient redox materials for bulk renewable fuel production.

Secondly, vanadium was considered in the form of vanadium oxides. Vanadium is the 20th most abundant element in the earth's crust, with excellent catalytic properties but mostly undermined for high temperature syngas production applications due to the intrinsically constraining thermodynamics for cyclic transition among different oxidation states. As an alternative, the concept of vanadium and CeO_2 mixed-metal oxides was introduced for the first time for efficient solar fuel production via chemical looping reforming of methane.

In Chapter 4, structural and thermochemical aspects of vanadium doping of CeO_2 nanostructures were critically assessed for efficient syngas production. The primary objective of vanadium doping was to enhance and optimize the cycle capacity of ceria at low isothermal temperatures. Optimized doping of ceria nanostructures was carried out after carefully following the structural characterization findings, where the maximum intake capacity of the ceria lattice for V^{5+} ions was revealed. As a result, the V-doped ceria oxides achieved record-high syngas yields and CO_2/H_2O splitting capacities with benchmark kinetics for over 200 continuous chemical looping dry/steam reforming of methane cycles. After the high-end performance of V-doped ceria materials, a facile method to utilize V_2O_5 structures for the chemical looping reforming of methane coupled

to the H_2O and CO_2 splitting reactions was investigated in Chapter 5. By incorporating fractional amounts of large cerium cations, the V_2O_5 lattice expanded and created oxygen vacancies, which led to a V^{5+}-to-V^{3+} transition and formed a segregated $CeVO_4$ phase. After a subsequent number of redox cycles, a VO/V_2O_3 redox pair was formed which showed extraordinary reversible oxygen exchange capacity with fast and stable redox kinetics for over 200 continuous cycles. The surface analysis revealed migration of the cerium cations to the surface of V_2O_5 powders after repeated reduction and oxidation reactions, which helped in optimizing the H_2/CO ratios close to 2. The robust structural enhancement achieved in the V/Ce doped metal oxides, the oxygen exchange capacity and ion mobility in the vanadia–ceria binary phase system were explored in Chapter 6. Critical structural analysis revealed that vanadia provided more reducing states for the hydrocarbon oxidation, while ceria acted as an oxygen buffer for the re-oxidation of reduced vanadia. A carbon dioxide splitting step was introduced between the methane partial oxidation and H2O splitting steps which activated the oxygen carrier by creating sufficient oxygen vacancies for efficient oxidation of methane and resisted methane cracking for over 100 cycles. The CeO_2–$CeVO_4$ multiphase system with 25% vanadium exhibited extraordinarily high oxygen exchange capacity and produced high and pure H_2 yields of 220 mL g^{-1} during the water splitting step of sequential water and carbon dioxide splitting, while maintaining a H_2/CO ratio close to 2. These findings suggest that the optimized combination of vanadium and cerium with a range of physiochemical properties promise for upscale synthesis of solar fuels via chemical looping reforming and prompts the researchers to explore the method of lattice cationic substitution in the redox materials to improve solar fuel production via thermochemical routes.

7.2 Future Work

This work here demonstrated the structural engineering of manganese-based Perovskites and Ce-V based metal oxides for syngas production via solar thermochemical redox

cycles and chemical looping reforming of methane reactions. Regardless of the research advancements presented in this thesis, considerable work remains to be accomplished in this field. For instance, the mechanism proposed in this study for the structural disintegration of the Perovskite oxides during chemical looping reforming of methane needs to be evaluated for other Perovskite oxides for performance optimization. The proposed mechanism of V-Ce doped metal oxides needs to be validated by, for instance, Density Functional Theory (DFT) studies for better understanding of electronic properties of co-existing cerium and vanadium ions. In addition, the interaction between Ce and V ions during the redox processes needs to be simulated by the molecular dynamics study to understand the contribution of these ions towards enhancement in syngas production. In-situ characterization could be applied to capture insightful information about the structural evolution of these materials during the redox processes.

Structural stability could be improved by fabricating reticulated porous structures of these redox materials for high temperature applications. Utilization of vanadium as a potential cationic substitution into the other state-of-the-art binary or ternary metal oxides may exhibit enhanced cycle capacity for improved syngas yields. It would be interesting to evaluate such systems with high ion mobilities and catalytic properties for other research fields such as electrochemical catalysis/energy storage and fuel cells.

References

1 US Energy Information Administration (EIA), *Forecast. Anal.*, 2007, **2008**, Energy Information Administration.

2 L. Xiao, S. Y. Wu and Y. R. Li, *Renew. Energy*, 2012, **41**, 1–12.

3 P. T. Krenzke, J. R. Fosheim and J. H. Davidson, *Sol. Energy*, 2017, **156**, 48–72.

4 M. Luo, Y. Yi, S. Wang, Z. Wang, M. Du, J. Pan and Q. Wang, *Renew. Sustain. Energy Rev.*, 2018, **81**, 3186–3214.

5 J. R. Scheffe and A. Steinfeld, *Mater. Today*, 2014, **17**, 341–348.

6 C. Agrafiotis, M. Roeb and C. Sattler, *Renew. Sustain. Energy Rev.*, 2015, **42**, 254–285.

7 M. E. Dry, *J. Chem. Technol. Biotechnol.*, 2002, **77**, 43–50.

8 A. Steinfeld, *Sol. Energy*, 2005, **78**, 603–615.

9 R. Bader and W. Lipiński, eds. M. J. Blanco and L. R. Santigosa, woodhead publishing, Amsterdam, 2017, pp. 403–459.

10 M. Romero and A. Steinfeld, *Energy Environ. Sci.*, 2012, **5**, 9234–9245.

11 E. A. Fletcher and R. L. Moen, *Science*, 1977, **197**, 1050–1056.

12 A. Kogan, *Int. J. Hydrogen Energy*, 1998, **23**, 89–98.

13 E. A. Fletcher, *Ind. Eng. Chem. Res.*, 1999, **38**, 2275–2282.

14 A. J. Traynor and R. J. Jensen, *Ind. Eng. Chem. Res.*, 2002, **41**, 1935–1939.

15 S. Abanades, P. Charvin, G. Flamant And P. Neveu, *Energy*, 2006, **31**, 2805–2822.

16 T. Kodama, *Prog. Energy Combust. Sci.*, 2003, **29**, 567–597.

17 T. Kodama and N. Gokon, *Chem. Rev.*, 2007, **107**, 4048–4077.

18 R. F. Service, *Science*, 2009, **326**, 1472–1475.

19 Y. Lu, L. Zhu, C. Agrafiotis, J. Vieten, M. Roeb and C. Sattler, *Prog. Energy Combust. Sci.*, 2019, **75**, 100785.

20 M. Roeb, M. Neises, N. Monnerie, F. Call, H. Simon, C. Sattler, M. Schmücker and R. Pitz-Paal, *Materials (Basel).*, 2012, **5**, 2015–2054.

21 J. Kim, T. A. Johnson, J. E. Miller, E. B. Stechel and C. T. Maravelias, *Energy Environ. Sci.*, 2012, **5**, 8417–8429.

22 X. Gao, A. Vidal, A. Bayon, R. Bader, J. Hinkley, W. Lipiński and A. Tricoli, *J. Mater. Chem. A*, 2016, **4**, 9614–9624.

23 P. T. Krenzke and J. H. Davidson, *Energy and Fuels*, 2014, **28**, 4088–4095.

24 J. Lapp, J. H. Davidson and W. Lipiński, *Energy*, 2012, **37**, 591–600.

25 C. L. Muhich, B. W. Evanko, K. C. Weston, P. Lichty, X. Liang, J. Martinek, C. B. Musgrave and A. W. Weimer, *Science*, 2013, **341**, 540–542.

26 R. Bader, L. J. Venstrom, J. H. Davidson and W. Lipiński, *Energy and Fuels*, 2013, **27**, 5533–5544.

27 P. Furler, J. R. Scheffe and A. Steinfeld, *Energy Environ. Sci.*, 2012, **5**, 6098–6103.

28 I. Ermanoski, N. P. Siegel and E. B. Stechel, *J. Sol. Energy Eng. Trans. ASME*, , DOI:10.1115/1.4023356.

29 I. Ermanoski, J. E. Miller and M. D. Allendorf, *Phys. Chem. Chem. Phys.*, 2014, **16**, 8418–8427.

30 B. Bulfin, F. Call, M. Lange, O. Lübben, C. Sattler, R. Pitz-Paal and I. V Shvets,

Energy and Fuels, 2015, **29**, 1001–1009.

31 S. Brendelberger, M. Roeb, M. Lange and C. Sattler, *Sol. Energy*, 2015, **122**, 1011–1022.

32 B. D. Ehrhart, C. L. Muhich, I. Al-Shankiti and A. W. Weimer, *Int. J. Hydrogen Energy*, 2016, **41**, 19904–19914.

33 W. T. Gibbons, L. J. Venstrom, R. M. De Smith, J. H. Davidson and G. S. Jackson, *Phys. Chem. Chem. Phys.*, 2014, **16**, 14271–14280.

34 K. Otsuka, Y. Wang, E. Sunada and I. Yamanaka, *J. Catal.*, 1998, **175**, 152–160.

35 K. Otsuka, Y. Wang and M. Nakamura, *Appl. Catal. A Gen.*, 1999, **183**, 317–324.

36 K. Otsuka, T. Ushiyama and I. Yamanaka, *Chem. Lett.*, 1993, **22**, 1517–1520.

37 K. S. Kang, C. H. Kim, W. C. Cho, K. K. Bae, S. W. Woo and C. S. Park, *Int. J. Hydrogen Energy*, 2008, **33**, 4560–4568.

38 W. C. Chueh and S. M. Haile, *ChemSusChem*, 2009, **2**, 735–739.

39 L. Li, Y. Song, B. Jiang, K. Wang and Q. Zhang, *Energy*, 2017, **131**, 58–66.

40 C. Huang, J. Wu, Y. T. Chen, M. Tian, A. I. Rykov, B. Hou, J. Lin, C. R. Chang, X. Pan, J. Wang, A. Wang and X. Wang, *Commun. Chem.*, 2018, **1**, 2–11.

41 H. H. Jeong, J. H. Kwak, G. Y. Han and K. J. Yoon, *Int. J. Hydrogen Energy*, 2011, **36**, 15221–15230.

42 P. T. Krenzke, J. R. Fosheim, J. Zheng and J. H. Davidson, *Int. J. Hydrogen Energy*, 2016, **41**, 12799–12811.

43 A. Steinfeld, S. Sanders and R. Palumbo, *Sol. Energy*, 1999, **65**, 43–53.

44 M. Forster, *Energy*, 2004, **29**, 789–799.

45 K. J. Warren, J. Reim, K. Randhir, B. Greek, R. Carrillo, D. W. Hahn and J. R. Scheffe, *Energy Technol.*, 2017, **5**, 2138–2149.

46 L. O. Schunk, W. Lipiński and A. Steinfeld, *Chem. Eng. J.*, 2009, **150**, 502–508.

47 K. Z. House, A. C. Baclig, M. Ranjan, E. A. Van Nierop, J. Wilcox and H. J. Herzog, *Proc. Natl. Acad. Sci. U. S. A.*, 2011, **108**, 20428–20433.

48 Y. Zheng, K. Li, H. Wang, D. Tian, Y. Wang, X. Zhu, Y. Wei, M. Zheng and Y. Luo, *Appl. Catal. B Environ.*, 2017, **202**, 51–63.

49 M. Fathi, E. Bjorgum, T. Viig and O. A. Rokstad, *Catal. Today*, 2000, **63**, 489–497.

50 J. Kim, C. A. Henao, T. A. Johnson, D. E. Dedrick, J. E. Miller, E. B. Stechel and C. T. Maravelias, *Energy Environ. Sci.*, 2011, **4**, 3122–3132.

51 F. Cheng, J. Shen, B. Peng, Y. Pan, Z. Tao and J. Chen, *Nat. Chem.*, 2011, **3**, 79–84.

52 W. C. Chueh and S. M. Haile, *Philos. Trans. R. Soc. A Math. Phys. Eng. Sci.*, 2010, **368**, 3269–3294.

53 L. J. Venstrom, N. Petkovich, S. Rudisill, A. Stein and J. H. Davidson, *J. Sol. Energy Eng.*, 2012, **134**, 011005–011012.

54 S. Ackermann, J. R. Scheffe and A. Steinfeld, *J. Phys. Chem. C*, 2014, **118**, 5216–5225.

55 B. Bulfin, L. Hoffmann, L. De Oliveira, N. Knoblauch, F. Call, M. Roeb, C. Sattler and M. Schmücker, *Phys. Chem. Chem. Phys.*, 2016, **18**, 23147–23154.

56 A. H. McDaniel, A. Ambrosini, E. N. Coker, J. E. Miller, W. C. Chueh, R. O'Hayre and J. Tong, *Energy Procedia*, 2014, **49**, 2009–2018.

57 S. Dey and C. N. R. R. Rao, *ACS Energy Lett.*, 2016, **1**, 237–243.

58 G. A. Ozin, *Joule*, 2017, **1**, 19–23.

59 H. Kaneko, T. Miura, H. Ishihara, S. Taku, T. Yokoyama, H. Nakajima and Y. Tamaura, *Energy*, 2007, **32**, 656–663.

60 P. Furler, J. Scheffe, M. Gorbar, L. Moes, U. Vogt and A. Steinfeld, *Energy and Fuels*, 2012, **26**, 7051–7059.

61 A. C. Gladen and J. H. Davidson, *Sol. Energy*, 2016, **139**, 524–532.

62 S. Agarwal, X. Zhu, E. J. M. Hensen, B. L. Mojet and L. Lefferts, *J. Phys. Chem. C*, 2015, **119**, 12423–12433.

63 D. R. Barcellos, F. G. Coury, A. Emery, M. Sanders, J. Tong, A. McDaniel, C. Wolverton, M. Kaufman and R. O'Hayre, *Inorg. Chem.*, 2019, **58**, 7705–7714.

64 Z. Zhao, M. Uddi, N. Tsvetkov, B. Yildiz and A. F. Ghoniem, *J. Phys. Chem. C*, 2017, **121**, 11055–11068.

65 I. Ilgaz Soykal, H. Sohn, J. T. Miller and U. S. Ozkan, *Top. Catal.*, 2014, **57**, 785–795.

66 L. J. Ma, L. S. Chen and S. Y. Chen, *Solid State Sci.*, 2009, **11**, 176–181.

67 C. L. Hanselman, D. N. Tafen, D. R. Alfonso, J. W. Lekse, C. Matranga, D. C. Miller and C. E. Gounaris, *Comput. Chem. Eng.*, 2019, **126**, 168–177.

68 N. P. Siegel, J. E. Miller, I. Ermanoski, R. B. Diver and E. B. Stechel, *Ind. Eng. Chem. Res.*, 2013, **52**, 3276–3286.

69 Y. Wang, Y. Zheng, Y. Wang, H. Wang, X. Zhu, Y. Wei, Y. Wang, L. Jiang, Z. Yang and K. Li, *J. Power Sources*, 2020, **449**, 227505.

70 P. Charvin, S. Abanades, G. Flamant and F. Lemort, *Energy*, 2007, **32**, 1124–1133.

71 J. Zhu, W. Wang, S. Lian, X. Hua and Z. Xia, *J. Mater. Cycles Waste Manag.*, 2017, **19**, 453–462.

72 S. Abanades and I. Villafan-Vidales, *Int. J. Energy Res.*, 2013, **37**, 598–608.

73 R. R. Bhosale, A. Kumar, L. J. P. Van Den Broeke, S. Gharbia, D. Dardor, M. Jilani, J. Folady, M. S. Al-Fakih and M. A. Tarsad, *Int. J. Hydrogen Energy*, 2015, **40**, 1639–1650.

74 D. Cebrucean, V. Cebrucean, I. Ionel and H. Spliethoff, *Clean Technol. Environ. Policy*, 2017, **19**, 451–470.

75 S. Abanades and H. I. Villafan-Vidales, *Chem. Eng. J.*, 2011, **175**, 368–375.

76 A. K. Singh, N. J. Auyeung, K. Randhir, R. Mishra, K. M. Allen, J. Petrasch and J. F. Klausner, *Ind. Eng. Chem. Res.*, 2015, **54**, 6793–6803.

77 D. Sanfilippo, *Catal. Today*, 2016, **272**, 58–68.

78 T. Kodama, Y. Nakamuro and T. Mizuno, *J. Sol. Energy Eng. Trans. ASME*, 2006, **128**, 3–7.

79 G. Voitic, S. Nestl, K. Malli, J. Wagner, B. Bitschnau, F. A. Mautner and V. Hacker, *RSC Adv.*, 2016, **6**, 53533–53541.

80 M. Kojima, T. Sano, Y. Wada, T. Yamamoto, M. Tsuji and Y. Tamaura, *J. Phys. Chem. Solids*, 1996, **57**, 1757–1763.

81 E. N. Coker, A. Ambrosini, M. A. Rodriguez and J. E. Miller, *J. Mater. Chem.*, 2011, **21**, 10767–10776.

82 F. Fresno, R. Fernández-Saavedra, M. Belén Gómez-Mancebo, A. Vidal, M. Sánchez, M. Isabel Rucandio, A. J. Quejido and M. Romero, *Int. J. Hydrogen*

Energy, 2009, **34**, 2918–2924.

83 T. Cooper, J. R. Scheffe, M. E. Galvez, R. Jacot, G. Patzke and A. Steinfeld, *Energy Technol.*, 2015, **3**, 1130–1142.

84 Q. Jiang, G. Zhou, Z. Jiang and C. Li, *Sol. Energy*, 2014, **99**, 55–66.

85 A. H. McDaniel, E. C. Miller, D. Arifin, A. Ambrosini, E. N. Coker, R. O'Hayre, W. C. Chueh and J. Tong, *Energy Environ. Sci.*, 2013, **6**, 2424–2428.

86 M. E. Gálvez, R. Jacot, J. Scheffe, T. Cooper, G. Patzke and A. Steinfeld, *Phys. Chem. Chem. Phys.*, 2015, **17**, 6629–6634.

87 S. M. Babiniec, E. N. Coker, J. E. Miller and A. Ambrosini, *Sol. Energy*, 2015, **118**, 451–459.

88 A. Evdou, V. Zaspalis and L. Nalbandian, *Int. J. Hydrogen Energy*, 2008, **33**, 5554–5562.

89 A. Evdou, V. Zaspalis and L. Nalbandian, *Fuel*, 2010, **89**, 1265–1273.

90 L. Nalbandian, A. Evdou and V. Zaspalis, *Int. J. Hydrogen Energy*, 2011, **36**, 6657–6670.

91 D. Sastre, A. J. Carrillo, D. P. Serrano, P. Pizarro and J. M. Coronado, *Top. Catal.*, 2017, **60**, 1108–1118.

92 R. J. Carrillo and J. R. Scheffe, *Energy and Fuels*, 2019, **33**, 12871–12884.

93 M. Ezbiri, M. Takacs, D. Theiler, R. Michalsky and A. Steinfeld, *J. Mater. Chem. A*, 2017, **5**, 4172–4182.

94 A. J. Carrillo, A. H. Bork, T. Moser, E. Sediva, Z. D. Hood and J. L. M. Rupp, *Adv. Energy Mater.*, 2019, **9**, 1–13.

95 J. R. Scheffe, D. Weibel and A. Steinfeld, *Energy and Fuels*, 2013, **27**, 4250–4257.

96 C. K. Yang, Y. Yamazaki, A. Aydin and S. M. Haile, *J. Mater. Chem. A*, 2014, **2**, 13612–13623.

97 M. Orfila, M. Linares, R. Molina, J. Á. Botas, R. Sanz and J. Marugán, *Int. J. Hydrogen Energy*, 2016, **41**, 19329–19338.

98 E. hyeok Yang, Y. S. Noh, G. H. Hong, D. J. Moon, E. hyeok Yang, Y. S. Noh, G. H. Hong, D. J. Moon, E. hyeok Yang, Y. S. Noh, G. H. Hong and D. J. Moon, *Catal. Today*, 2018, **299**, 242–250.

99 S. Dey, B. S. Naidu and C. N. R. Rao, *Chem. - A Eur. J.*, 2015, **21**, 7077–7081.

100 C. N. R. Rao and S. Dey, *J. Solid State Chem.*, 2016, **242**, 107–115.

101 K. Randhir, N. R. Rhodes, L. Li, N. AuYeung, D. W. Hahn, R. Mei and J. F. Klausner, *Sol. Energy*, 2018, **163**, 1–15.

102 R. R. Bhosale, R. V Shende and J. A. Puszynski, *Int. J. Hydrogen Energy*, 2012, **37**, 2924–2934.

103 M. S. C. Chan, W. Liu, M. Ismail, Y. Yang, S. A. Scott and J. S. Dennis, *Chem. Eng. J.*, 2016, **296**, 406–411.

104 P. Zhang, H. Lu, Y. Zhou, L. Zhang, Z. Wu, S. Yang, H. Shi, Q. Zhu, Y. Chen and S. Dai, *Nat. Commun.*, 2015, **6**, 8446.

105 C. Alvani, G. Ennas, A. La Barbera, G. Marongiu, F. Padella and F. Varsano, *Int. J. Hydrogen Energy*, 2005, **30**, 1407–1411.

106 X. Tang, Y. Li, X. Huang, Y. Xu, H. Zhu, J. Wang and W. Shen, *Appl. Catal. B Environ.*, 2006, **62**, 265–273.

107 P. B. Kreider, H. H. Funke, K. Cuche, M. Schmidt, A. Steinfeld and A. W. Weimer,

Int. J. Hydrogen Energy, 2011, **36**, 7028–7037.

108 T. M. Francis, P. R. Lichty and A. W. Weimer, *Chem. Eng. Sci.*, 2010, **65**, 3709–3717.

109 M. Wiechen, M. M. Najafpour, S. I. Allakhverdiev and L. Spiccia, *Energy Environ. Sci.*, 2014, **7**, 2203–2212.

110 A. Bayón, V. A. De La Peña O'Shea, D. P. Serrano and J. M. Coronado, *Int. J. Hydrogen Energy*, 2013, **38**, 13143–13152.

111 S. Lorentzou, G. Karagiannakis, C. Pagkoura, A. Zygogianni and A. G. Konstandopoulos, *Energy Procedia*, 2014, **49**, 1999–2008.

112 L. J. MA, L. S. Chen and S. Y. Chen, *Mater. Chem. Phys.*, 2007, **105**, 122–126.

113 P. Singh and M. S. Hegde, *Chem. Mater.*, 2010, **22**, 762–768.

114 D. Maiti, B. J. Hare, Y. A. Daza, A. E. Ramos, J. N. Kuhn and V. R. Bhethanabotla, *Energy Environ. Sci.*, 2018, **11**, 648–659.

115 M. Portarapillo, A. Aronne, A. Di Benedetto, C. Imparato, G. Landi and G. Luciani, *Chem. Eng. Trans.*, 2019, **74**, 43–48.

116 R. Michalsky, V. Botu, C. M. Hargus, A. A. Peterson and A. Steinfeld, *Adv. Energy Mater.*, 2015, **5**, 1–10.

117 A. Le Gal and S. Abanades, *J. Phys. Chem. C*, 2012, **116**, 13516–13523.

118 M. Pavone, A. B. Muñoz-García, A. M. Ritzmann and E. A. Carter, *J. Phys. Chem. C*, 2014, **118**, 13346–13356.

119 M. Inoue, N. Hasegawa, R. Uehara, N. Gokon, H. Kaneko and Y. Tamaura, *Sol. Energy*, 2004, **76**, 309–315.

120 A. Stamatiou, P. G. Loutzenhiser and A. Steinfeld, *Energy and Fuels*, 2010, **24**, 2716–2722.

121 M. E. Gálvez, P. G. Loutzenhiser, I. Hischier and A. Steinfeld, *Energy and Fuels*, 2008, **22**, 3544–3550.

122 A. Steinfeld, *Int. J. Hydrogen Energy*, 2002, **27**, 611–619.

123 T. Kodama, Y. Kondoh, R. Yamamoto, H. Andou and N. Satou, *Sol. Energy*, 2005, **78**, 623–631.

124 L. J. Venstrom, R. M. De Smith, Y. Hao, S. M. Haile and J. H. Davidson, *Energy and Fuels*, 2014, **28**, 2732–2742.

125 T. Kodama, N. Gokon and R. Yamamoto, *Sol. Energy*, 2008, **82**, 73–79.

126 M. Tou, R. Michalsky and A. Steinfeld, *Joule*, 2017, **1**, 146–154.

127 A. Steinfeld, C. Larson, R. Palumbo and M. Foley, *Energy*, 1996, **21**, 205–222.

128 A. Steinfeld, A. Frei, P. Kuhn and D. Wuillemin, *Int. J. Hydrogen Energy*, 1995, **20**, 793–804.

129 A. Steinfeld, P. Kuhn and J. Karni, *Energy*, 1993, **18**, 239–249.

130 A. Steinfeld and I. Spiewak, *Energy Convers. Manag.*, 1998, **39**, 1513–1518.

131 A. Steinfeld, *Energy*, 1997, **22**, 311–316.

132 K. S. Go, S. R. Son, S. D. Kim, K. S. Kang and C. S. Park, *Int. J. Hydrogen Energy*, 2009, **34**, 1301–1309.

133 S. Kräupl and A. Steinfeld, *J. Sol. Energy Eng. Trans. ASME*, 2001, **123**, 133–137.

134 T. Kodama, H. Ohtake, S. Matsumoto, A. Aoki, T. Shimizu and Y. Kitayama, *Energy*, 2000, **25**, 411–425.

135 T. Shimizu, K. Shimizu, Y. Kitayama and T. Kodama, *Sol. Energy*, 2001, **71**, 315–324.

136 A. Sim, N. W. Cant and D. L. Trimm, *Int. J. Hydrogen Energy*, 2010, **35**, 8953–8961.

137 J. T. Jang, J. H. Kwak, G. Y. Han, J. W. Bae, C. Il Ahn and K. J. Yoon, *Int. J. Hydrogen Energy*, 2015, **40**, 2518–2528.

138 E. R. Stobbe, B. A. De Boer and J. W. Geus, *Catal. Today*, 1999, **47**, 161–167.

139 L. F. de Diego, M. Ortiz, J. Adánez, F. García-Labiano, A. Abad and P. Gayán, *Chem. Eng. J.*, 2008, **144**, 289–298.

140 S. Takenaka, N. Hanaizumi, V. T. D. Son and K. Otsuka, *J. Catal.*, 2004, **228**, 405–416.

141 S. Takenaka, K. Nomura, N. Hanaizumi and K. Otsuka, *Appl. Catal. A Gen.*, , DOI:10.1016/j.apcata.2004.12.028.

142 K.-S. S. Kang, C.-H. H. Kim, K.-K. K. Bae, W.-C. C. Cho, W.-J. J. Kim, Y.-H. H. Kim, S.-H. H. Kim and C.-S. S. Park, *Int. J. Hydrogen Energy*, 2010, **35**, 568–576.

143 K.-S. S. Cha, H.-S. S. Kim, B.-K. K. Yoo, Y.-S. S. Lee, K.-S. S. Kang, C.-S. S. Park and Y.-H. H. Kim, *Int. J. Hydrogen Energy*, 2009, **34**, 1801–1808.

144 K.-S. S. Cha, B.-K. K. Yoo, H.-S. S. Kim, T.-G. G. Ryu, K.-S. S. Kang, C.-S. S. Park and Y.-H. H. Kim, *Int. J. Energy Res.*, 2010, **34**, 422–430.

145 K. S. Go, S. R. Son and S. D. Kim, *Int. J. Hydrogen Energy*, 2008, **33**, 5986–5995.

146 M. Rydén, A. Lyngfelt, T. Mattisson, D. Chen, A. Holmen and E. Bjørgum, *Int. J. Greenh. Gas Control*, 2008, **2**, 21–36.

147 L. Protasova and F. Snijkers, *Fuel*, 2016, **181**, 75–93.

148 X. L. Sang, K. Z. Li, H. Wang and Y. G. Wei, *Rare Met.*, 2014, **33**, 230–238.

149 H. J. Wei, Y. Cao, W. J. Ji and C. T. Au, *Catal. Commun.*, 2008, **9**, 2509–2514.

150 X. Zhu, H. Wang, Y. Wei, K. Li and X. Cheng, *J. Rare Earths*, 2010, **28**, 907–913.

151 Z. Gu, K. Li, H. Wang, Y. Wei, D. Yan and T. Qiao, *Kinet. Catal.*, 2013, **54**, 326–333.

152 Z. Gu, K. Li, S. Qing, X. Zhu, Y. Wei, Y. Li and H. Wang, *RSC Adv.*, 2014, **4**, 47191–47199.

153 Z. Gu, K. Li, H. Wang, S. Qing, X. Zhu, Y. Wei, X. Cheng, H. Yu and Y. Cao, *Appl. Energy*, 2016, **163**, 19–31.

154 H. S. Kim, K. S. Cha, B. K. Yoo, T. G. Ryu, Y. S. Lee, C. S. Park and Y. H. Kim, *J. Ind. Eng. Chem.*, 2010, **16**, 81–86.

155 A. Jha, D. W. Jeong, W. J. Jang, Y. L. Lee and H. S. Roh, *Int. J. Hydrogen Energy*, 2015, **40**, 9209–9216.

156 X. Zhu, H. Wang, Y. Wei, K. Li and X. Cheng, *J. Nat. Gas Chem.*, 2011, **20**, 281–286.

157 X. Zhu, H. Wang, Y. Wei, K. Li and X. Cheng, *Mendeleev Commun.*, 2011, **21**, 221–223.

158 X. Zhu, K. Li, Y. Wei, H. Wang and L. Sun, *Energy and Fuels*, 2014, **28**, 754–760.

159 X. Zhu, Y. Wei, H. Wang and K. Li, *Int. J. Hydrogen Energy*, 2013, **38**, 4492–4501.

160 M. M. Nair and S. Abanades, *Energy Fuels*, 2016, **30**, 6050–6058.

161 J. R. González-Velasco, M. A. Gutiérrez-Ortiz, J. L. Marc, J. A. Botas, M. P. González-Marcos and G. Blanchard, *Appl. Catal. B Environ.*, 1999, **22**, 167–178.

162 S. P. Jiang, *J. Mater. Sci.*, 2008, **43**, 6799–6833.

163 C. L. Muhich, B. D. Ehrhart, I. Al-Shankiti, B. J. Ward, C. B. Musgrave and A. W. Weimer, *Wiley Interdiscip. Rev. Energy Environ.*, 2016, **5**, 261–287.

164 C. Agrafiotis, H. Von Storch, M. Roeb, C. Sattler, C. Agra, H. Von Storch, M. Roeb, C. Sattler, C. Agrafiotis, H. Von Storch, M. Roeb and C. Sattler, *Renew. Sustain. Energy Rev.*, 2014, **29**, 656–682.

165 M. Tang, L. Xu and M. Fan, *Appl. Energy*, 2015, **151**, 143–156.

166 S. A. M. M. Said, M. Waseeuddin and D. S. A. A. Simakov, *Renew. Sustain. Energy Rev.*, 2016, **59**, 149–159.

167 A. Steinfeld, P. Kuhn, A. Reller, R. Palumbo, J. Murray and Y. Tamaura, *Int. J. Hydrogen Energy*, 1998, **23**, 767–774.

168 X. Gao, G. Liu, Y. Zhu, P. Kreider, A. Bayon, T. Gengenbach, T. Lu, Y. Liu, J. Hinkley, W. Lipiński and A. Tricoli, *Nano Energy*, 2018, **50**, 347–358.

169 T. Rager and J. Golczewski, *Zeitschrift fur Phys. Chemie*, 2005, **219**, 235–246.

170 R. Palumbo, J. Léde, O. Boutin, E. Elorza Ricart, A. Steinfeld, S. Möller, A. Weidenkaff, E. A. Fletcher and J. Bielicki, *Chem. Eng. Sci.*, 1998, **53**, 2503–2517.

171 C. Perkins, P. R. Lichty and A. W. Weimer, *Int. J. Hydrogen Energy*, 2008, **33**, 499–510.

172 P. G. Loutzenhiser, A. Meier and A. Steinfeld, *Materials (Basel).*, 2010, **3**, 4922–4938.

173 S. Abanades, P. Charvin, F. Lemont and G. Flamant, *Int. J. Hydrogen Energy*,

2008, **33**, 6021–6030.

174 G. Levêque, R. Bader, W. Lipiński and S. Haussener, *Sol. Energy*, 2017, **156**, 133–148.

175 I. Vishnevetsky and M. Epstein, *J. Sol. Energy Eng. Trans. ASME*, 2009, **131**, 210071–210078.

176 J. E. Miller, A. H. McDaniel and M. D. Allendorf, *Adv. Energy Mater.*, 2014, **4**, 1300469.

177 P. Pantu, K. Kim and G. R. Gavalas, *Appl. Catal. A Gen.*, 2000, **193**, 203–214.

178 K. Li, H. Wang, Y. Wei and D. Yan, *Int. J. Hydrogen Energy*, 2011, **36**, 3471–3482.

179 T. Nakamura, *Sol. Energy*, 1977, **19**, 467–475.

180 N. Gokon, H. Murayama, J. Umeda, T. Hatamachi and T. Kodama, *Int. J. Hydrogen Energy*, 2009, **34**, 1208–1217.

181 J. R. Scheffe, M. D. Allendorf, E. N. Coker, B. W. Jacobs, A. H. McDaniel and A. W. Weimer, *Chem. Mater.*, 2011, **23**, 2030–2038.

182 M. D. Allendorf, R. B. Diver, N. P. Siegel and J. E. Miller, *Energy and Fuels*, 2008, **22**, 4115–4124.

183 M. Roeb, M. Neises, J. P. Säck, P. Rietbrock, N. Monnerie, J. Dersch, M. Schmitz and C. Sattler, *Int. J. Hydrogen Energy*, 2009, **34**, 4537–4545.

184 H. Ishihara, H. Kaneko, N. Hasegawa and Y. Tamaura, *Energy*, 2008, **33**, 1788–1793.

185 C. C. Agrafiotis, C. Pagkoura, A. Zygogianni, G. Karagiannakis, M. Kostoglou and A. G. Konstandopoulos, *Int. J. Hydrogen Energy*, 2012, **37**, 8964–8980.

186 J. R. Scheffe, A. Francés, D. M. King, X. Liang, B. A. Branch, A. S. Cavanagh, S. M. George and A. W. Weimer, *Thin Solid Films*, 2009, **517**, 1874–1879.

187 H. Kaneko, T. Kodama, N. Gokon, Y. Tamaura, K. Lovegrove and A. Luzzi, *Sol. Energy*, 2004, **76**, 317–322.

188 K. Ehrensberger, A. Frei, P. Kuhn, H. R. Oswald and P. Hug, *Solid State Ionics*, 1995, **78**, 151–160.

189 J. R. Scheffe, J. Li and A. W. Weimer, *Int. J. Hydrogen Energy*, 2010, **35**, 3333–3340.

190 D. Arifin, V. J. Aston, X. Liang, A. H. McDaniel and A. W. Weimer, *Energy Environ. Sci.*, 2012, **5**, 9438.

191 D. Yadav and R. Banerjee, *Renew. Sustain. Energy Rev.*, 2016, **54**, 497–532.

192 W. C. Chueh, C. Falter, M. Abbott, D. Scipio, P. Furler, S. M. Haile and A. Steinfeld, *Science*, 2010, **330**, 1797–801.

193 S. Abanades and G. Flamant, *Sol. Energy*, 2006, **80**, 1611–1623.

194 Y. Hao, C.-K. K. Yang and S. M. Haile, *Phys. Chem. Chem. Phys.*, 2013, **15**, 17084–17092.

195 S. Abanades, A. Legal, A. Cordier, G. Peraudeau, G. Flamant and A. Julbe, *J. Mater. Sci.*, 2010, **45**, 4163–4173.

196 A. Le Gal, S. Abanades, N. Bion, T. Le Mercier and V. Harlé, *Energy and Fuels*, 2013, **27**, 6068–6078.

197 Q. L. Meng, C. Il Lee, T. Ishihara, H. Kaneko and Y. Tamaura, *Int. J. Hydrogen Energy*, 2011, **36**, 13435–13441.

198 H. L. Zhang, J. Baeyens, J. Degrève and G. Cacères, *Renew. Sustain. Energy Rev.*,

2013, **22**, 466–481.

199 R. J. Panlener, R. N. Blumenthal and J. E. Garnier, *J. Phys. Chem. Solids*, 1975, **36**, 1213–1222.

200 T. Otake, H. Yugami, K. Yashiro, Y. Nigara, T. Kawada and J. Mizusaki, *Solid State Ionics*, 2003, **161**, 181–186.

201 P. Furler, J. Scheffe, D. Marxer, M. Gorbar, A. Bonk, U. Vogt and A. Steinfeld, *Phys. Chem. Chem. Phys.*, 2014, **16**, 10503–10511.

202 S. Ackermann, M. Takacs, J. Scheffe and A. Steinfeld, *Int. J. Heat Mass Transf.*, 2017, **107**, 439–449.

203 M. Takacs, S. Ackermann, A. Bonk, M. Neises-von Puttkamer, P. Haueter, J. R. Scheffe, U. F. Vogt and A. Steinfeld, *AIChE J.*, 2017, **63**, 1263–1271.

204 D. Marxer, P. Furler, M. Takacs and A. Steinfeld, *Energy Environ. Sci.*, 2017, **10**, 1142–1149.

205 J. R. Scheffe and A. Steinfeld, *Energy and Fuels*, 2012, **26**, 1928–1936.

206 X. Gao, I. Di Bernardo, P. Kreider, T. Tran-Phu, X. Cai, N. Wang, Y. Zhu, M. B. Venkataraman, J. Lipton-Duffin, A. Bayon, W. Lipiński and A. Tricoli, *ACS Catal.*, 2019, **9**, 9880–9890.

207 S. Li, V. M. Wheeler, P. B. Kreider, R. Bader and W. Lipiński, *Energy and Fuels*, 2018, **32**, 10848–10863.

208 R. J. Carrillo and J. R. Scheffe, *Sol. Energy*, 2017, **156**, 3–20.

209 S. Mulmi, H. Chen, A. Hassan, J. F. Marco, F. J. Berry, F. Sharif, P. R. Slater, E. P. L. Roberts, S. Adams and V. Thangadurai, *J. Mater. Chem. A*, 2017, **5**, 6874–6883.

210 T. R. Sahoo, M. Armandi, R. Arletti, M. Piumetti, S. Bensaid, M. Manzoli, S. R. Panda and B. Bonelli, *Appl. Catal. B Environ.*, 2017, **211**, 31–45.

211 A. Le Gal, S. Abanades and G. Flamant, *Energy and Fuels*, 2011, **25**, 4836–4845.

212 F. He, Y. Wei, H. Li and H. Wang, *Energy and Fuels*, 2009, **23**, 2095–2102.

213 X. DAI, C. YU, R. LI, Q. WU and Z. HAO, *J. Rare Earths*, 2008, **26**, 76–80.

214 K. Li, M. Haneda, Z. Gu, H. Wang and M. Ozawa, *Mater. Lett.*, 2013, **93**, 129–132.

215 K. Li, H. Wang, Y. Wei and D. Yan, *Appl. Catal. B Environ.*, 2010, **97**, 361–372.

216 A. Demont and St´ephane Abanades, *RSC Adv.*, 2014, **2**, 54885–54891.

217 K. Zhao, F. He, Z. Huang, G. Wei, A. Zheng, H. Li and Z. Zhao, *Appl. Energy*, 2016, **168**, 193–203.

218 F. He, X. Li, K. Zhao, Z. Huang, G. Wei and H. Li, *Fuel*, 2013, **108**, 465–473.

219 A. Evdou, L. Nalbandian and V. T. Zaspalis, *J. Memb. Sci.*, 2008, **325**, 704–711.

220 X. Dai, C. Yu and Q. Wu, *J. Nat. Gas Chem.*, 2008, **17**, 415–418.

221 X. Dai, J. Cheng, Z. Li, M. Liu, Y. Ma and X. Zhang, *Chem. Eng. Sci.*, 2016, **153**, 236–245.

222 X. P. Dai, R. J. Li, C. C. Yu and Z. P. Hao, *J. Phys. Chem. B*, 2006, **110**, 22525–22531.

223 K. Zhao, F. He, Z. Huang, A. Zheng, H. Li and Z. Zhao, *Int. J. Hydrogen Energy*, 2014, **39**, 3243–3252.

224 O. Mihai, D. Chen and A. Holmen, *J. Catal.*, 2012, **293**, 175–185.

225 F. Mudu, U. Olsbye, B. Arstad, S. Diplas, Y. Li and H. Fjellvåg, *Appl. Catal. A*

Gen., 2016, **523**, 171–181.

226 A. Mishra, N. Galinsky, F. He, E. E. Santiso and F. Li, *Catal. Sci. Technol.*, 2016, **6**, 4535–4544.

227 Y. Zeng, S. Tamhankar, N. Ramprasad, F. Fitch, D. Acharya and R. Wolf, *Chem. Eng. Sci.*, 2003, **58**, 577–582.

228 V. García, M. T. Caldes, O. Joubert, E. Gautron, F. Mondragón and A. Moreno, *Catal. Today*, 2010, **157**, 177–182.

229 A. G. Bhavani, W. Y. Kim and J. S. Lee, *ACS Catal.*, 2013, **3**, 1537–1544.

230 N. Galinsky, M. Sendi, L. Bowers and F. Li, *Appl. Energy*, 2016, **174**, 80–87.

231 B. Bulfin, J. Vieten, C. Agrafiotis, M. Roeb and C. Sattler, *J. Mater. Chem. A*, 2017, **5**, 18951–18966.

232 V. Moshnyaga, K. Samwer, Moshnyaga and Samwer, *Crystals*, 2019, **9**, 489.

233 M. M. Nair and S. Abanades, *Sustain. Energy Fuels*, 2018, **2**, 843–854.

234 G. Luciani, G. Landi, A. Aronne and A. Di Benedetto, *Sol. Energy*, 2018, **171**, 1–7.

235 Q. Jiang, H. Zhang, Y. Cao, H. Hong and H. Jin, *Energy Convers. Manag.*, 2019, **187**, 523–536.

236 N. Gokon, T. Yawata, S. Bellan, T. Kodama and H. S. Cho, *Energy*, 2019, **171**, 971–980.

237 F. He and F. Li, *Energy Environ. Sci.*, 2015, **8**, 535–539.

238 H. Jiang, H. Wang, S. Werth, T. Schiestel and J. Caro, *Angew. Chemie - Int. Ed.*, 2008, **47**, 9341–9344.

239 Y. Cao, B. Lin, Y. Sun, H. Yang and X. Zhang, *J. Alloys Compd.*, 2015, **624**, 31–39.

240 C. Barry Carter and M. G. Norton, in *Ceramic Materials*, Springer New York, New York, NY, 2007, pp. 400–411.

241 S. H. Feng and G. H. Li, in *Modern Inorganic Synthetic Chemistry: Second Edition*, eds. R. Xu and Y. Xu, Elsevier, Second Edi., 2017, pp. 73–104.

242 Y. Y. Luo, D. S. Jo, K. Senthil, S. Tezuka, M. Kakihana, K. Toda, T. Masaki and D. H. Yoon, *J. Solid State Chem.*, 2012, **189**, 68–74.

243 R. Ramaseshan, S. Sundarrajan, R. Jose and S. Ramakrishna, *J. Appl. Phys.*, 2007, **102**, 111101.

244 A. Riaz, P. Kreider, F. Kremer, H. Tabassum, J. S. Yeoh, W. Lipiński and A. Lowe, *ACS Appl. Energy Mater.*, 2019, **2**, 2494-2505.

245 M. Zhi, A. Koneru, F. Yang, A. Manivannan, J. Li and N. Wu, *Nanotechnology*, 2012, **23**, 305501.

246 R. Yensano, S. Pinitsoontorn, V. Amornkitbamrung and S. Maensiri, *J. Supercond. Nov. Magn.*, 2014, **27**, 1553–1560.

247 Y. Shen, K. Zhao, F. He and H. Li, *J. Energy Inst.*, 2019, **92**, 239–246.

248 M. C. Biesinger, B. P. Payne, A. P. Grosvenor, L. W. M. Lau, A. R. Gerson and R. S. C. Smart, *Appl. Surf. Sci.*, 2011, **257**, 2717–2730.

249 Q. H. Wu, M. Liu and W. Jaegermann, *Mater. Lett.*, 2005, **59**, 1980–1983.

250 S. Dey, B. S. Naidu, A. Govindaraj and C. N. R. Rao, *Phys. Chem. Chem. Phys.*, 2015, **17**, 122–125.

251 A. Demont, S. Abanades and E. Beche, *J. Phys. Chem. C*, 2014, **118**, 12682–

12692.

252 J. T. Mefford, W. G. Hardin, S. Dai, K. P. Johnston and K. J. Stevenson, *Nat. Mater.*, 2014, **13**, 726–732.

253 W. Wang, J. Geng, L. Kuai, M. Li and B. Geng, *Chem. - A Eur. J.*, 2016, **22**, 9909–9913.

254 F. Zhang, S. W. Chan, J. E. Spanier, E. Apak, Q. Jin, R. D. Robinson and I. P. Herman, *Appl. Phys. Lett.*, 2002, **80**, 127–129.

255 D. S. Su, M. Wieske, E. Beckmann, A. Blume, G. Mestl and R. Schlögl, *Catal. Letters*, 2001, **75**, 81–86.

256 A. Riaz, M. U. Ali, W. Lipiński and A. Lowe, *J. Mater. Chem. A*, 2019, **7**, 27347–27360.

257 V. Panchal, S. López-Moreno, D. Santamaría-Pérez, D. Errandonea, F. J. Manjón, P. Rodríguez-Hernandez, A. Muñoz, S. N. Achary and A. K. Tyagi, *Phys. Rev. B - Condens. Matter Mater. Phys.*, 2011, **84**, 1–12.

258 Z. Wu, M. Li and S. H. Overbury, *ChemCatChem*, 2012, **4**, 1653–1661.

259 Z. Wu, A. J. Rondinone, I. N. Ivanov and S. H. Overbury, *J. Phys. Chem. C*, 2011, **115**, 25368–25378.

260 M. V. Martínez-Huerta, J. M. Coronado, M. Fernández-García, A. Iglesias-Juez, G. Deo, J. L. G. Fierro and M. A. Bañares, *J. Catal.*, 2004, **225**, 240–248.

261 J. Mendialdua, R. Casanova A' and Y. Barbaux, *J. Electron Spectros. Relat. Phenomena*, 1995, **71**, 249–261.

262 Y. J. Park, N. G. Park, K. S. Ryu, S. H. Chang, S. C. Park, S. M. Yoon and D. K. Kim, *Bull. Korean Chem. Soc.*, 2001, **22**, 1015–1018.

263 M. V. Martínez-Huerta, G. Deo, J. L. G. Fierro and M. A. Bañares, *J. Phys. Chem. C*, 2007, **111**, 18708–18714.

264 J. Matta, D. Courcot, E. Abi-Aad and A. Aboukaïs, *Chem. Mater.*, 2002, **14**, 4118–4125.

265 M. Abbasi, A. A. Mirzaei and H. Atashi, *J. Alloys Compd.*, 2019, **799**, 546–555.

266 D. R. Mullins, S. H. Overbury and D. R. Huntley, *Surf. Sci.*, 1998, **409**, 307–319.

267 G. Xu, X. Wang, X. Chen and L. Jiao, *RSC Adv.*, 2015, **5**, 17782–17785.

268 A. Riaz, M. U. Ali, T. G. Enge, T. Tsuzuki, A. Lowe and W. Lipiński, *Research*, 2020, **2020**, 1–12.

269 H. Bosch, B. J. Kip, J. G. Van Ommen And P. J. Gellings, *Chem. Informationsd.*, 1984, **15**, 2479–2488.

270 R. Kapoor and S. T. Oyama, *J. Solid State Chem.*, 1995, **120**, 320–326.

271 Z. Zhao, H. Zuo, Y. Liu, W. Song, S. Mao and Y. Wang, *Int. J. Refract. Met. Hard Mater.*, 2009, **27**, 971–975.

272 E. Bêche, P. Charvin, D. Perarnau, S. Abanades and G. Flamant, *Surf. Interface Anal.*, 2008, **40**, 264–267.

273 D. J. Keene, W. Lipiński and J. H. Davidson, *Chem. Eng. Sci.*, 2014, **111**, 231–143.

274 C. A. Carrero, C. J. Keturakis, A. Orrego, R. Schomäcker and I. E. Wachs, *Dalt. Trans.*, 2013, **42**, 12644–12653.

275 N. Das, H. Eckert, H. Hu, I. E. Wachs, J. F. Walzer and F. J. Feher, *J. Phys. Chem.*, 1993, **97**, 8240–8243.

276 E. Abi-aad, R. Bechara, J. Grimblot and A. Aboukaïs, *Chem. Mater.*, 1993, **5**, 793–797.

277 M. V. Martínez-Huerta, G. Deo, J. L. G. Fierro and M. A. Bañares, *J. Phys. Chem. C*, 2008, **112**, 11441–11447.

278 C. Popa, M. V. Ganduglia-Pirovano and J. Sauer, *J. Phys. Chem. C*, 2011, **115**, 7399–7410.

279 C. Lu, K. Li, H. Wang, X. Zhu, Y. Wei, M. Zheng and C. Zeng, *Appl. Energy*, 2018, **211**, 1–14.